

X-RAY SPECTROSCOPIC DIAGNOSTICS OF
MAGNETICALLY CONFINED PLASMAS.
INSTRUMENTATION AND TECHNIQUES

Robin Barnsley

A thesis submitted to the University of Leicester
for the degree of Doctor of Philosophy.

September 1993

UMI Number: U550115

All rights reserved

INFORMATION TO ALL USERS

The quality of this reproduction is dependent upon the quality of the copy submitted.

In the unlikely event that the author did not send a complete manuscript and there are missing pages, these will be noted. Also, if material had to be removed, a note will indicate the deletion.



UMI U550115

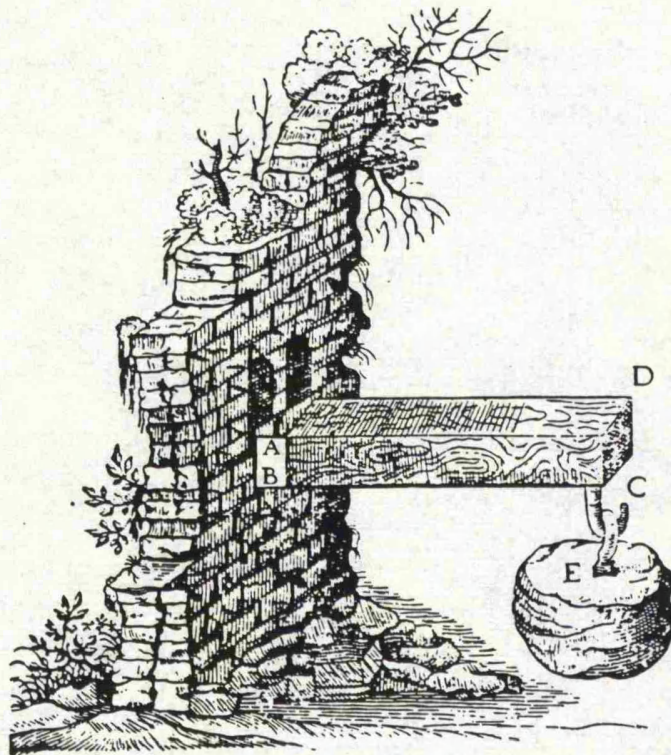
Published by ProQuest LLC 2015. Copyright in the Dissertation held by the Author.
Microform Edition © ProQuest LLC.

All rights reserved. This work is protected against
unauthorized copying under Title 17, United States Code.



ProQuest LLC
789 East Eisenhower Parkway
P.O. Box 1346
Ann Arbor, MI 48106-1346





Ultimate strength of a beam (woodcut).
Discorsi e dimostrazioni matematiche
 Galileo (Leyden 1638)

Lyte Lowys my sone, I aperceyve wel by certeyne evidences thyn ability to lerne sciences touching nombres and proporciouns; and as wel considre I thy besy praier to lerne the tretys of the Astrelabie.

Than for as mochel as a filosofre saith, "he wrappith himself in his frend, that condescendith to the rightfulle praier of his frend," therefore have I yeven the a suffisant Astrelabie as for oure orizonte, compowned after the latitude of Oxenforde; upon which, by meditation of this litel tretys, I purpose to teche the a certain nombre of conclusions aperteyning to the same instrument.

A Treatise on the Astrolabe
 Geoffrey Chaucer 1393

Abstract

This thesis reports several advances in x-ray crystal spectroscopic techniques for the diagnosis of high-temperature magnetically confined plasmas.

Two complementary spectrometers have been developed, and have been demonstrated in a wide range of experiments on the Culham Laboratory DITE and COMPASS tokamaks, and on the Joint European JET tokamak.

A Bragg rotor spectrometer uses a combination of crystals and multilayers to give complete coverage of the spectrum between 1 Å and 100 Å. It measures absolute intensities of line radiation from all impurities, with resolving power of typically $\lambda/\delta\lambda \sim 500$ (except above 25 Å, where $\lambda/\delta\lambda \sim 50$). Developments were made to extend the coverage from 25 Å to 100 Å, using multilayer mirrors and organic crystals. The success of the instrument depends largely on the development of a high-rate ($>10^7$ count/s) gas proportional counter system, capable of covering the energy range from 100 eV to 10 keV.

A Johann spectrometer uses a novel four-pillar jig to bend crystals to typically 1 m radius. A large-area cooled x-ray CCD array is used in the focus, resulting in a compact high-resolution instrument ($\lambda/\delta\lambda \sim 10^4$). This allows line profile and ratio measurements with a time resolution of ~ 1 ms.

Observations using the Bragg rotor spectrometer include impurity monitoring under various plasma and limiter configurations. Temperature and density sensitive line ratios were measured under known plasma conditions and compared with theory, adding confidence to their use for less well diagnosed plasmas such as those observed in astrophysics.

A major application has been the study of a switch (controlled by the refuelling rate) between long and short impurity confinement times in the DITE tokamak. Trace impurities were injected by laser ablation, and their subsequent temporal and spatial behaviour studied spectroscopically. Weak lines, due to radiative recombination into excited states of H- and He-like ions, were observed in the outer plasma. The radial profiles of these "radiative recombination lines" were governed by a balance between transport and recombination, and allowed the effective diffusion coefficient to be measured locally. It was shown that the transport changes occurred in the outer half of the plasma, and that conditions in the core were unchanged.

The suitability of Bragg spectroscopy for a reactor-relevant plasma was demonstrated during the JET preliminary tritium experiment (PTE). A double-reflection instrument was used, with a tritium-compatible radiation-shielded beamline. Based on this operational experience, a soft x-ray spectroscopy system for a next-step device such as ITER is proposed.

Introduction	1
1 Soft x-ray spectroscopic diagnostics	
1.1 Introduction	7
1.2 Magnetically confined plasmas	7
1.3 The soft x-ray spectrum	16
1.4 Atomic processes	21
1.5 Spectroscopic diagnostics	25
1.6 Implications for instrumentation	29
1.7 Conclusion	32
2 Soft x-ray absolute flux measurements	
2.1 Introduction	35
2.2 Absorption and scattering	35
2.3 Bragg analysers	37
2.4 Beam geometry	48
2.5 Spectrometer types	51
2.5 Absolute flux measurements	57
2.6 Conclusions	60
3 A Bragg rotor spectrometer	
3.1 Introduction	63
3.2 Optical design	68
3.3 Engineering design	70
3.4 Calibration	75
3.5 Results	81
3.6 Conclusion	83
4 A high count-rate gas proportional counter	
4.1 Introduction	85
4.2 Theory of gas proportional counters	85
4.3 Operation at high count-rates	95
4.4 Detector development	99
4.5 Mk1 detector system design	100
4.6 Performance and comparison with theory	104
4.7 Mk2 detector	107
4.8 Conclusion	109
5 Plasma spectroscopy beyond 25 Å using Bragg diffraction	
5.1 Introduction	112
5.2 Theory	114
5.3 Diffractor selection	117
5.4 Laboratory results	119
5.5 Tokamak results	121
5.6 Conclusion	126
6 A compact high-resolution Johann spectrometer	
6.1 Introduction	129
6.2 Engineering design	129
6.3 Optical performance	132
6.4 CCD detector	134
6.5 Results	137
6.6 Conclusion	143

7 Impurity monitoring	
7.1 Introduction	145
7.2 Impurity Surveys	145
7.3 Absolute Measurements	152
7.4 Conclusion	156
8 Control of impurity confinement in the DITE tokamak	
8.1 Introduction	158
8.2 Impurity transport theory	159
8.3 Ionization and excitation	164
8.4 The experiments	168
8.5 Data reduction and validation	172
8.6 Central-chord measurements	179
8.7 Radially resolved measurements	187
8.8 Conclusion	190
9 Spectroscopic diagnostics of temperature and density	
9.1 Introduction	194
9.2 Electron Temperature	193
9.3 Electron Density	201
9.4 Ion Temperature	205
9.5 Conclusion	207
10 The JET preliminary tritium experiment	
10.1 Introduction	209
10.2 Instrumentation	210
10.3 Calibration and alignment	213
10.4 Background radiation	213
10.5 Tritium containment and clean-up	222
10.6 Results	226
10.7 Future experiments	227
10.8 Conclusion	229
11 Diagnostics for reactor conditions	
11.1 Introduction	231
11.2 Neutron and tritium factors	233
11.3 Preselectors	234
11.4 Spatial resolution	238
11.5 Spectrometers	241
11.6 Conclusion	243
Conclusion	244

Acknowledgments

During the course of this work, I have been privileged to work with many colleagues from several institutions, and it is a pleasure to acknowledge their contributions here. I wish to thank in particular the technicians with whom I have spent many long hours, days, nights and weekends, and on whom the success of an experimentalist depends.

The work has grown from the expertise of several groups in the Department of Physics and Astronomy at Leicester University. I am grateful to Kenton Evans for recruiting me, and for giving the project a flying start by always seeing through any mass of details, problems or options, to separate the critical from the clutter. Richard Willingale, my recent tutor, has helped to shape this thesis with many valuable observations and suggestions on successive drafts.

I am especially grateful to the late Earnest Mathieson, former leader of the Nuclear Electronics Group, and earlier my patient MSc tutor. His interest and theoretical contribution was important for the development of the detector system for the Bragg rotor spectrometer. The electronics for that system were designed and built by Trevor Harris, supported by members of the electronics workshop. The Mk1 Bragg rotor spectrometer and the prototype crystal jig were built in the Leicester Physics Department workshop by Eric Peake.

The Johann spectrometer project was taken up by Jim Dunn, with whom I spent a fruitful and enjoyable period conducting experiments at various laboratories. His thesis (Leicester 1990) is complementary to this work. The addition of the CCD array was carried out in collaboration with Stephen Lea.

Throughout, progress has depended on the support and interest of many members of the X-ray Astronomy Group, led by Professor Ken Pounds. Their expertise in x-ray optics, crystals, detectors, and remote control has been indispensable. In the early days, availability of many existing components from space projects greatly speeded the development of the prototype Bragg rotor spectrometer. Recently, support from the CCD group, particularly from Tony Abbey, has been important in expanding the potential of the Johann spectrometer.

Most of the early experimental work took place at the UKAEA Culham Laboratory. There the enthusiasm and support of Nicol Peacock was essential to the inception and progress of the Bragg rotor and Johann spectrometer projects. Nick Hawkes helped a great deal during the initial experiments on DITE. I was very fortunate to have the technical support and company of Harry Jones for most of the work covered here. I am also grateful to Paddy Doyle for his technical assistance.

The experimental results at Culham were made possible by the DITE and COMPASS tokamak groups. The Bragg rotor spectrometer for JET was designed, built and commissioned in collaboration with Culham staff, particularly Richard Smith, Ash Patel and Trevor Dodd.

My work at JET has benefitted from the active cooperation of very many colleagues, from almost every division. I would like to thank my division head Paul Thomas and group leader Ruggero Giannella for their support, particularly of the JET Bragg rotor spectrometer. The technical support of John Ryan and Bernard Viacoz has been essential for the commissioning and continuing operation of all the instruments for which I have been responsible.

The commissioning of the JET double-crystal monochromator were aided by the experience and advice of Uwe Schumacher, Elisabeth Källne and Helmut Morsi. Measurements during the PTE, and subsequent data analysis, were additionally assisted by Jerzy Brzozowski, Ivor Coffey and Kerry Lawson, and Tarang Patel.

I am grateful to Diana Lewis for many helpful and clarifying suggestions during the final editing of the text, and to the JET graphics department for many of the figures included here.

INTRODUCTION

ENCOURAGEMENT!

I set out very industriously to learn all these different crafts. And then, of course, there was the exquisite art of enamelling!

Enamelling is an extraordinarily difficult business, because in the finishing process the fire very often completely ruins the work; but all the same I bent all my energies to learning the craft. I found it very hard going but got so much pleasure out of it that I looked on my exertions as a kind of relaxation. This attitude was the result of a special gift from God of a temperament so healthy and well-balanced that whatever I took it into my head to do I could always accomplish.

*The Life
Benvenuto Cellini c1558*

CAVEAT!

The first man I saw was of meagre aspect, with sooty hands and face, his hair and beard long, ragged, and singed in several places. His clothes, shirt, and skin were all of the same colour. He had been eight years upon a project for extracting sunbeams out of cucumbers, which were to be put into vials hermetically sealed, and let out to warm the air in raw, inclement summers.

He told me that he did not doubt in eight years more he should be able to supply the Governor's gardens with sunshine at a reasonable rate; but he complained that his stock was low, and entreated me to give him something as an encouragement to ingenuity, especially as this had been a very dear season for cucumbers.

*Visit to the Grand Academy of Lagardo
Gulliver's Travels
Jonathan Swift 1726*

Objective

The soft x-ray band is important for thermonuclear plasmas because it contains the peak of the radiated power, and a wealth of diagnostic information about the temperature and density of electrons and impurity ions. Prior to this work, however, instruments were not available which could fully exploit the diagnostic potential of the complete spectrum between about 1 Å and 100 Å (~100 eV to ~10 keV). This need was addressed by developing crystal spectrometers with high sensitivity optics and high count-rate detectors, which were then used in a wide range of measurements on magnetically-confined plasma experiments.

History

The work began in October 1981 with a design study for crystal spectroscopy on the Joint European Torus (JET) Tokamak, in a collaboration between UKAEA Culham Laboratory and the Radiation Physics group at Leicester University. A Bragg rotor spectrometer was proposed for the early phases of JET operation, followed by a range of optical and shielding configurations to be phased in as neutron yields increased over the years. After the initial failure of the proposal for JET, existing crystal spectrometers at the UKAEA Culham laboratory were commissioned and operated over a period of one year. In mid-1983 the design began of a Bragg rotor spectrometer for the Culham DITE Tokamak. The prototype was commissioned on DITE in September 1985 and operated almost continuously, monitoring impurities and taking part in many experiments, until the end of the DITE project early in 1988.

Two years were then spent at JET commissioning and operating the active-phase double-crystal monochromator, and aiding the commissioning of the spatially-scanning double-crystal monochromator. In 1990 an upgraded Bragg rotor spectrometer was commissioned on JET. It was used, together with the double-crystal monochromator, to monitor impurities during the JET preliminary tritium experiment (PTE).

In parallel with these activities, from 1982, a compact high-resolution Johann spectrometer was developed, and was used to observe various sources of highly ionized atoms. In 1990 it was equipped with a large-area cooled CCD array, and was demonstrated on JET.

Design context

The designer of crystal spectrometers soon learns that soft x-rays give up easily. In most other regions of the electromagnetic spectrum, photons can be reflected, refracted, focused, guided, transmitted, and otherwise taken advantage of. Apart from grazing-angle reflection from mirrors and gratings, which is costly and inefficient, diffraction by crystals and multilayers is at present the only satisfactory means of deflecting and dispersing soft x-rays, and even then the diffractor manages to absorb most of the incident beam. Collimation must rely on brute-force methods such as slits, slots and grids, and there is a constant struggle to minimize absorption losses in thin windows and their support structures. It seems a good rule of thumb that the most painstaking count-rate estimates for a given source and instrument always exceed by an order of magnitude the eventual results. An important exception to these negative factors is the Johann spectrometer, which not only "focuses" a relatively wide spectral range simultaneously, but does so without the need for an entrance slit; a feature which greatly simplifies the design, and increases the versatility of such an instrument.

Diagnostic installations at large fusion experiments such as JET are far removed from the type of laboratory instrument where the physicist can see all the components and make manual adjustments and readings. The system must record data automatically, and operate unattended under remote control with high reliability. Often the equipment is inaccessible except overnight or at longer intervals, and must endure adverse conditions such as high background radiation and high magnetic fields. The design, commissioning and operation of such a system is a major project, and involves most branches of engineering including mechanical, electrical, electronic, control, vacuum, software and safety.

Unlike the visible and UV spectral regions, where instruments suitable for plasma diagnostics have been commercially available for many years, most x-ray spectrometers have been unique custom-built devices. The main reason for this is that the grating instruments used at longer wavelengths are adaptable to many other sources. By contrast, fluorescence analysis - the main market for x-ray spectrometry - requires instruments that are not suitable for plasma diagnostics, in that the source (the specimen) is internal, and the photon fluxes are much lower. Several high-resolution narrow-band spectrometers have been built, usually benefitting from local expertise at each laboratory, particularly in position-sensitive detectors. Prior to the present work, however, broad-band flat-crystal instruments had not been optimized for magnetically confined plasmas.

Instrumentation

The instruments described here arose from an appraisal of spectrometer configurations and detector options, in the light of the priorities for the various measurable parameters. The aim was to produce general-purpose instruments which need not be dedicated to any particular source or beam-line. It is not practical to monitor the complete soft x-ray spectrum between about 1 Å and 100 Å with the spectral, temporal and spatial resolution required by some measurements, and compromises are therefore necessary. Two complementary plasma spectrometers have resulted: a broad-band medium-resolution Bragg rotor instrument, and a narrow-band high-resolution Johann instrument. They will be supported by an x-ray calibration facility.

The Bragg rotor spectrometer was designed for routine impurity monitoring and is described in chapter 3. It covers the full spectrum between about 1 Å and 100 Å with medium spectral resolution and has absolute calibration for intensity and wavelength. The instrument is a direct descendant of the Bragg spectrometers built at Leicester University for the x-ray astronomy space programme. In fact, the prototype Bragg rotor spectrometer used many existing components which either were recovered from sounding-rockets, or were replicas from satellite instruments. Chapter 4 describes the theoretical and developmental work necessary to build a detector system capable of handling in excess of 10^7 photon/s, made necessary by the bright source and high-throughput optics. Extension of the long-wavelength coverage of the instrument to 100 Å was a valuable improvement, described in chapter 5.

A Johann instrument is the natural choice where high resolution is required because, unlike flat-crystal configurations, there is no need to trade sensitivity with resolution. A compact high-resolution Johann spectrometer was therefore developed, whose main novel feature is a four-pillar crystal bending jig that uses flexures to position the crystal. The incorporation of a large-area cooled CCD array (developed at Leicester University primarily for x-ray astronomy) has resulted in a powerful and versatile instrument, described in chapter 6.

Soft x-ray spectrometry relies on absolute calibration data, particularly of the diffractor reflection integral. A new two-axis diffractometer using robot-motor technology is under construction and will speed up the hitherto tedious process of diffractor and filter calibration. The instrument, together with techniques for making such measurements, is outlined in chapter 2.

Techniques

By exploiting the high sensitivity and the wide spectral and dynamic ranges of the Bragg rotor spectrometer, several new or improved measurements were possible. In most cases, the ability to make spatially resolved measurements, albeit on a shot-to-shot basis, was crucial to the success of the experiments.

With the long-wavelength coverage of the instrument extended to about 100 Å, it is now possible to identify all the plasma impurities, and monitor them on a routine basis. We can also go some way toward answering the all-important question: "What is the composition of the plasma?". Techniques are being developed for deriving components of the impurity radiated-power and concentrations, and are discussed in chapter 7.

A good example of the importance of spatially-resolved data is shown by the studies of a long impurity-confinement mode in the DITE tokamak, described in chapter 8. The radial profile information was used, not only to validate the central-chord measurements, but also to reveal the region of the plasma where a transport change took place. It was then possible to make local measurements of impurity transport by analysing the weak recombination-excited line-radiation from the outer plasma.

The easy access to a wide spectral range made it possible to investigate temperature and density sensitive line ratios of several ions in the range between neon and chlorine (chapter 9). For magnesium and silicon, it was possible to measure electron temperature and density sensitive line ratios under plasma conditions suitable for a test of the atomic theory. These tests of theory will be useful for astrophysical plasmas, for which independent temperature and density measurements are not normally available.

Bragg spectroscopy of a reactor-relevant plasma requires shielding of the instrument against high fluxes of neutrons and gamma-rays, and safe operation in the presence of tritium. Techniques to allow monitoring of all impurities, and implementation of procedures to contain tritium, are described in chapter 10.

This work began with a design study for JET, and ends with some ideas which might find application on a future reactor-like plasma such as ITER, where the problem of making spatially-resolved measurements will be even more difficult than usual. A partial solution is proposed in chapter 11.

1 SOFT X-RAY SPECTROSCOPIC DIAGNOSTICS

1.1	Introduction	7
1.2	Magnetically confined plasmas	7
1.3	The soft x-ray spectrum	16
1.4	Atomic processes	21
1.5	Spectroscopic diagnostics	25
1.6	Implications for instrumentation	29
1.7	Conclusion	32

(400) *The great mystery, however, is to conceive how so enormous a conflagration (if such it be) can be kept up. Every discovery in chemical science leaves us completely at a loss, or rather, seems to remove farther the prospect of probable explanation. If conjecture might be hazarded, we should look rather to the known possibility of an indefinite generation of heat by friction, or to its excitement by the electric discharge, than to any actual combustion of ponderable fuel, whether solid or gaseous, for the origin of the solar radiation.*

Footnote

The prismatic analysis of the solar beam exhibits in the spectrum a series of "fixed lines" totally unlike those which belong to the light of any known terrestrial flame. This may hereafter lead us to a clearer insight into its origin. But, before we can draw any conclusion from such an indication, we must recollect, that previous to reaching us it has undergone the whole absorptive action of our atmosphere, as well as that of the sun's. Of the latter we know nothing, and may conjecture every thing; ...

Outlines of Astronomy
Sir John F W Herschel
Longman, Green and company, London 1893.

1.1 INTRODUCTION

Broad-band soft x-ray spectroscopy has been common for x-ray astronomy, and can be complementary to the high-resolution techniques that are more commonly applied to low density laboratory plasmas. Wide spectral coverage makes it possible to observe all plasma impurities and allows a wide range of diagnostic measurements, some of which are not possible with a narrow-band high-resolution instrument. This discussion concentrates on broad-band spectroscopy, while high-resolution work has been covered in a review by Bartiromo¹.

In a hot plasma relevant to nuclear fusion research, the main plasma ions are fully stripped except near the boundary, and passive spectroscopy must rely on radiation from impurities. This falls into two main areas: firstly their detection and monitoring, and secondly the derivation of plasma parameters from various effects on their spectra. At electron temperatures between 100 eV and 10 keV all impurities are highly ionized and radiate most strongly in the soft x-ray band between about 1 Å and 100 Å. In addition, all common impurities have significant fractional abundances in He-like and H-like ionization stages, for which the atomic physics is relatively simple and theoretical wavelengths and rate coefficients are usually adequate.

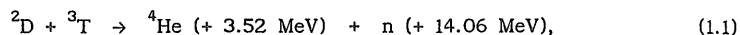
Although all common impurities have transitions in the XUV band between about 50 Å and 1000 Å, there are many lines and groups of lines with various diagnostic potential at shorter wavelengths, and a broad-band soft x-ray spectrometer can provide a useful complement or even alternative to an XUV grating instrument.

Spectroscopic observations are possible and necessary that have time-scales of 10 μ s, spatial extents of 1 mm, and bandwidths of 10^{-4} . To record this in full over the soft x-ray band for a typical tokamak discharge would require about 10^{13} bits of data, and it is hardly worth contemplating what the instrumentation would look like. Nevertheless, we do need to make such measurements and so must study what observations are possible, and what are the priorities, before designing a diagnostic system.

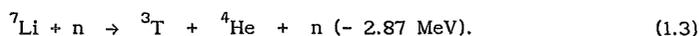
1.2 MAGNETICALLY CONFINED PLASMAS

Controlled thermonuclear fusion is a potential long-term source of energy that would have several advantages over nuclear fission. It is inherently safe because it can operate with a low fuel inventory in a low pressure reactor, where the need to maintain a high temperature means that any failure will quench the reaction. Fusion has a potential advantage over fission, in that the absence of fission products means that no high-level nuclear waste will be

created. Fusion reaction products are not radioactive, and there is scope to build the reactor from materials that minimize its activation. There is a sufficient supply of the fuels deuterium and lithium in water and the Earth's crust to last for thousands of years. The deuterium-tritium (D-T) reaction has the highest cross-section at the lowest temperature²:



and tritium may be bred by the reactions:



Even at their peak, the cross-sections for fusion reactions are very low (of order 1 barn) due to the Coulomb repulsion of the nuclei, and the fuel particles must be confined at high temperature with sufficient density for long enough to achieve a useful reaction rate. At the required temperature of about 20 keV, the fuel, together with any impurities, forms a highly ionized plasma.

For the fusion power output to exceed the radiation and particle losses, the "triple product" figure of merit must exceed

$$n_1 \tau_E T_1 \geq 5 \cdot 10^{21} \text{ m}^{-3} \cdot \text{s} \cdot \text{keV} \quad (1.4)$$

where n_1 and T_1 are the fuel ion density and temperature respectively, and τ_E is the energy confinement time.

The confinement can be gravitational, as in the Sun and stars where, although the ion temperature is only about 1 keV and the main fusion reactions are many orders of magnitude slower than the D-T reaction, the confinement time is quasi-infinite. Inertial confinement at near-solid density and with sub- μs confinement time is exploited in the hydrogen bomb, and is being investigated for controlled energy production via laser and ion-beam heating of mm-sized fuel pellets.

A fully ionized plasma can be confined by magnetic fields, for which the simplest closed geometry is toroidal, and where the most successful implementation to date has been the tokamak³. The tokamak principle is shown in figure 1.1, where a toroidal magnetic field is created by a set of coils around a toroidal vacuum vessel. A transformer drives a toroidal plasma current, which is connected with a poloidal magnetic field component so that the resultant B-field lines spiral around a centre line inside the vessel. The plasma must be shaped and stabilized by additional external coils. The efficiency of Ohmic heating decreases with electron temperature T_e , as the plasma becomes almost collisionless, and so auxiliary heating by neutral-particle beams and various forms of RF and micro-wave absorption is

Recent tokamak experiments with deuterium plasmas have achieved $n_i \tau_E T_i$ values close to the equivalent of $Q=1$ "breakeven" for a D-T plasma⁴, where the total fusion energy production would be equal to the total input power (fig.1.2). Ignition will occur when heating from the α -particles is sufficient to maintain the reaction.

Each of the three main current areas of research, namely plasma purity, confinement and heating, is related to the respective term in the $n_i \tau_E T_i$ product. The latter two areas are believed to be largely solved, in that additional heating has produced the necessary T_i , with a τ_E scaling that would be acceptable for a reactor. The use of low-Z wall materials has allowed high plasma purity to be achieved, but in all present machines reactor-relevant high-Q conditions are terminated after a few seconds by an impurity influx or "bloom" from the highly loaded regions of the plasma limiter. Impurity production and control, together with the related problem of helium "ash" removal, is therefore a major area of current research.

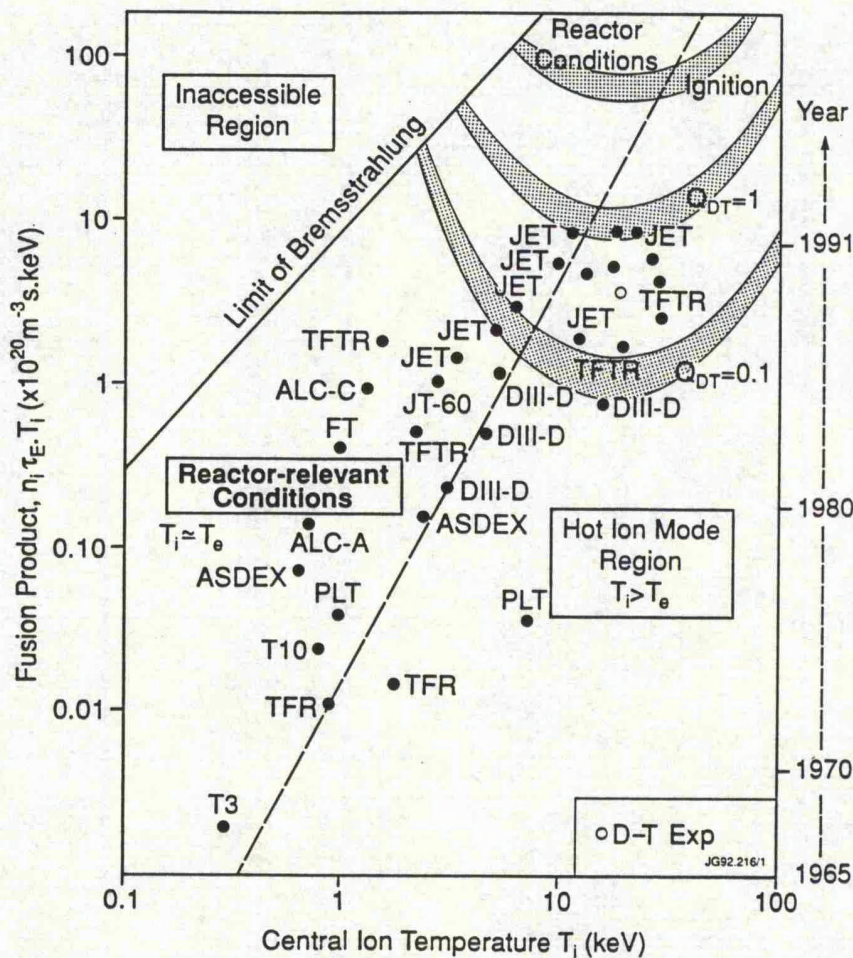


Fig.1.2 The fusion figure of merit $n_i \tau_E T_i$ versus ion temperature T_i ,

Figure 1.3 shows the evolution of the main parameters in a JET discharge. In the early Ohmically heated part of the discharge, the stable plasma density $\langle n_e \rangle$ and current I_{plasma} are established. About 14 MW of additional heating from neutral beams causes the central electron temperature T_e and ion temperature T_i to rise to a peak at about 13 s. This phase is terminated by an influx of impurities at about 14 s, indicated by an increase in the effective charge-state Z_{eff} and an increase in the radiated power P_{rad} .

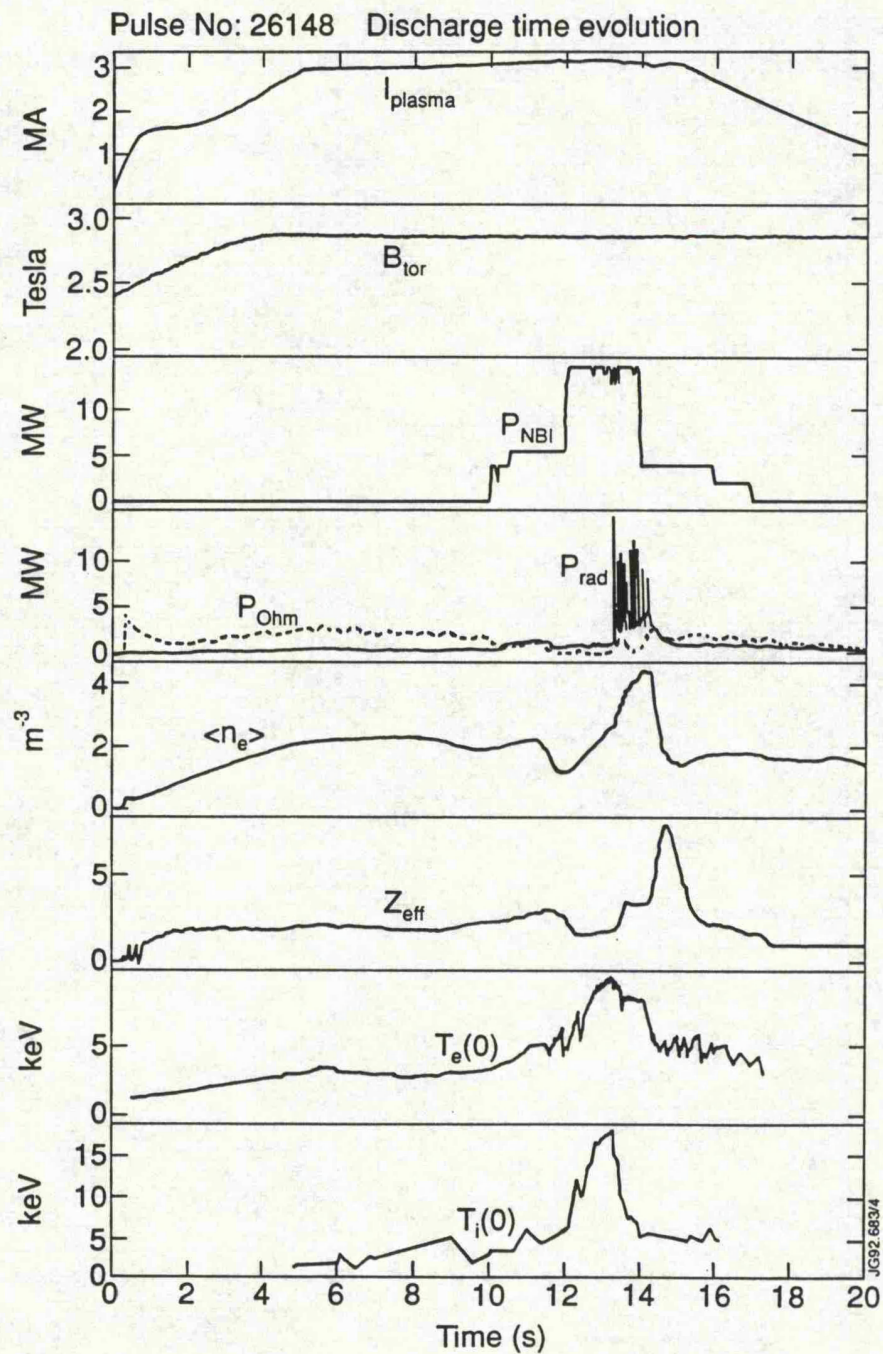


Fig.1.3 Evolution of the main parameters of a JET discharge.

Plasma diagnostics

Plasma diagnostics is a rich field^{5,6}, involving measurements of radiation in almost every part of the electromagnetic spectrum, of neutral and charged particles, and of magnetic and electrostatic fields. The primary diagnostic requirements of a plasma are: (a) radial profiles of density and temperature for the ions and electrons respectively, (b) energy balance diagnostics to compare radiated and particle power losses with power input, (c) magnetics for plasma position control and mode-structure measurements, (d) impurity monitors, usually spectroscopic, and (e) fusion product monitors.

The main JET diagnostics are shown in figure 1.4 and listed in table 1.2. Since the main plasma physics problem is not so much one of adding energy to the plasma, as one of maintaining a gradient between the reacting centre and the outside world, diagnostics that can make spatially resolved measurements are crucially important.

An important factor for reactor-relevant machines is the need for diagnostic installations to be compatible with tritium and with high levels of neutrons and gamma-rays. The operation of such an instrument during the JET preliminary tritium experiment is described in detail in chapter 10.

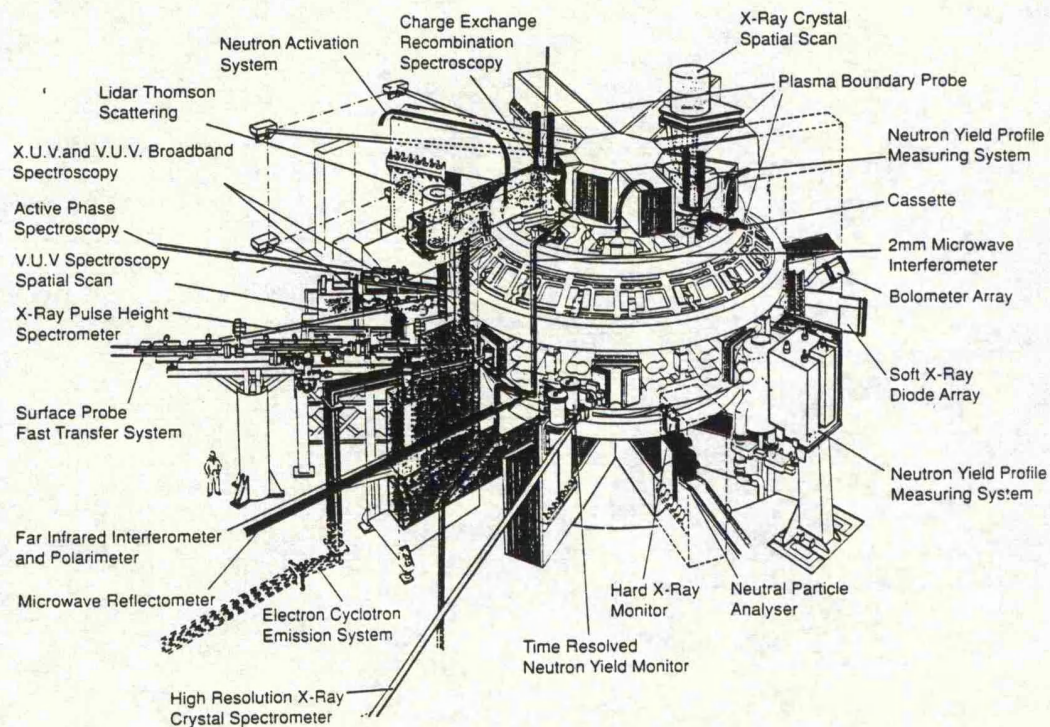


Fig.1.4 Schematic of the main diagnostic installations at JET.

System	Diagnostic	Purpose	Association	Status
KB1	Bolometer array	Time and space resolved total radiated power	IPP Garching	Modified
KC1	Magnetic diagnostics	Plasma current, loop volts, plasma position, shape of flux surface, diamagnetic loop, fast MHD	JET	Upgraded
KE3	Lidar Thomson scattering	T_e and n_e profiles	JET and Stuttgart University	Upgraded
KF1	High energy neutral particle analyser	Ion energy distribution up to 3.5MeV	Purchased from Ioffe St Petersburg	Upgraded
KG1	Multichannel far infrared interferometer	$\int n_e ds$ on six vertical chords and two horizontal chords	CEA Fontenay-aux-Roses	Modified
KG3	Microwave reflectometer	n_e profiles and fluctuations	JET and FOM Rijnhuizen	Modified
KG4	Polarimeter	$\int n_e B_{\theta} ds$ on six vertical chords	JET and CEA Fontenay-aux-Roses	Upgraded
KH1	Hard X-ray monitors	Runaway electrons and disruptions	JET	
KH2	X-ray pulse height spectrometer	Monitor of T_e , impurities, LH fast electrons	JET	
KK1	Electron cyclotron emission spatial scan	$T_e(r,t)$ with scan time of a few milliseconds	NPL, UKAEA Culham and JET	Modified
KK2	Electron cyclotron emission fast system	$T_e(r,t)$ on microsecond time scale	FOM Rijnhuizen	
KK3	Electron cyclotron emission heterodyne	$T_e(r,t)$ with high spatial resolution	JET	Upgraded
KL1*	Limiter viewing	Monitor hot spots on limiter, walls, RF antennae, divertor target tiles	JET	Upgraded
KL3	Surface temperature	Surface temperature of target tiles	JET	Upgraded
KM1	2.4MeV neutron spectrometer	Neutron spectra in D-D discharges, ion temperatures and energy distributions	UKAEA Harwell	
KM3	2.4MeV time-of-flight neutron spectrometer		NFR Studsvik	Modified
KM7	Time-resolved neutron yield monitor	Triton burnup studies	JET and UKAEA Harwell	
KN1	Time-resolved neutron yield monitor	Time resolved neutron flux	UKAEA Harwell	
KN2	Neutron activation	Absolute fluxes of neutrons	UKAEA Harwell	Modified
KN3*	Neutron yield profile measuring system	Space and time resolved profile of neutron flux	UKAEA Harwell	Upgraded
KN4	Delayed neutron activation	Absolute fluxes of neutrons	Mol	
KR2	Active phase neutral particle analyser	Ion distribution function, $T_i(r)$	ENEA Frascati	
KS1	Active phase spectroscopy	Impurity behaviour in active conditions	IPP Garching	
KS2*	Spatial scan X-ray crystal spectroscopy	Space and time resolved impurity profiles	IPP Garching	
KS3	H-alpha and visible light monitors	Ionisation rate, Z_{eff} , impurity fluxes from wall and limiter	JET	Upgraded
KS4	Charge exchange recombination spectroscopy (using heating beam)	Fully ionized light impurity concentration, $T_i(r)$, rotation velocities	JET	Modified
KS5	Active Balmer α spectroscopy	T_D , N_D and $Z_{eff}(r)$	JET	Modified
KS6*	Bragg rotor X-ray spectrometer	Monitor of low and medium Z impurity radiation	UKAEA Culham	Upgraded
KS7*	Poloidal rotation	Multichannel spectroscopic measurement of poloidal rotation	UKAEA Culham	Modified
KT2*	VUV broadband spectroscopy	Impurity survey	UKAEA Culham	Upgraded
KT3	Active phase CX spectroscopy	Full ionized light impurity concentration, $T_i(r)$, rotation velocities	JET	Modified
KT4*	Grazing incidence-visible spectroscopy	Impurity survey	UKAEA Culham	Upgraded
KX1	High resolution X-ray crystal spectroscopy	Central ion temperature, rotation and Ni concentration	ENEA Frascati	
KY3*	Plasma boundary probes	Vertical probe drives for reciprocating Langmuir and surface collector probes	JET, UKAEA Culham and IPP Garching	Modified
KY4	Fixed Langmuir probes (X-point belt limiter)	Edge parameters	JET	Modified
KZ3*	Laser injected trace elements	Particle transport, T_e impurity behaviour	JET	Upgraded
Ky1	Gamma rays	Fast ion distribution	JET	Modified

* Not compatible with tritium

JG93.131/1

Table 1.2 JET Diagnostic systems December 1992.

The role of impurities

Impurities degrade fusion plasmas by diluting the fuel, and by increasing the radiation losses relative to a pure hydrogen plasma. Ignition of a D-T plasma can be prevented by the presence of 3% of low-Z elements (oxygen), 1% of medium-Z elements (iron), or 0.1% of high-Z elements (tungsten)⁷. On the other hand, many diagnostic techniques rely on the presence of intrinsic or injected impurities. Isler⁸ has reviewed observations and the effects of impurities in tokamaks.

The radiation from impurities in a low density (hence optically thin) magnetically confined plasma is dominated by the effect of the electron temperature profile; it causes the ions to exist in a series of overlapping shells, increasing in ionization from the neutral atom at the plasma edge, to the highest stage produced by the central T_e . Transport phenomena shift these shells, usually inward, from the locations they would have in a steady-state plasma. The interpretation of impurity radiation is therefore inextricably linked to plasma particle transport, either negatively when it complicates concentration measurements, or positively when it allows transport effects to be measured. Figure 1.5 shows a typical JET temperature profile, and the calculated abundances of various chlorine ions, with and without inclusion of transport effects.

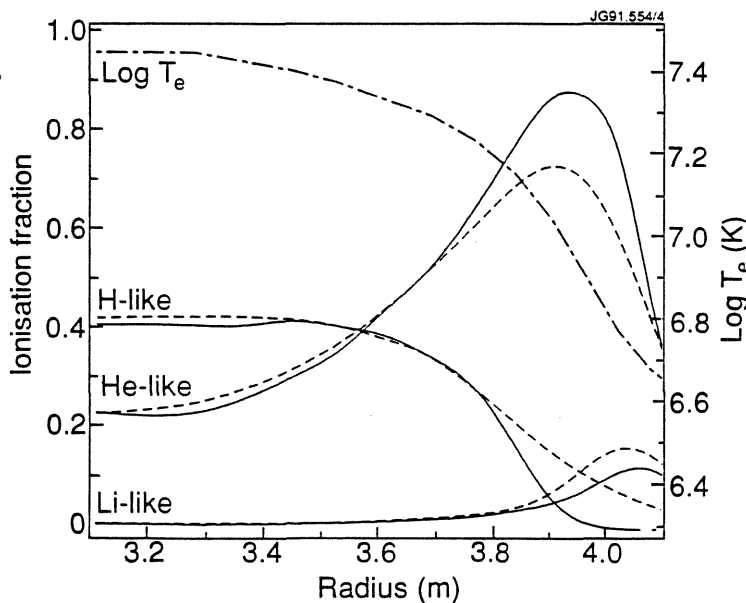


Fig.1.5 Chlorine ion abundances in JET calculated with (dashed) and without (solid) transport effects.

Impurity transport

Classical diffusion

Classical theory considers only two-body collisions as a mechanism to allow migration of particles across magnetic field lines. The scale length for diffusion is the relatively small ion gyro-radius, giving a coefficient D_{\perp} perpendicular to the field lines of⁹

$$D_{\perp} = \frac{2 n_e k T_e \eta_{\perp}}{B^2} \sim 5 \cdot 10^{-4} \text{ m}^2/\text{s} \quad (1.5)$$

for typical tokamak parameters ($T_e=1\text{keV}$, $B=3\text{T}$, $n_e=5 \cdot 10^{19} \text{ m}^{-3}$), where the plasma resistivity η_{\perp} is similar to that of metallic conductors.

However, most magnetic confinement experiments fail to follow the $1/B^2$ dependence, and exhibit a much higher diffusion than the classical prediction.

Bohm diffusion

Bohm's semi-empirical formula¹⁰ considers transport due to collective processes, such as convection and MHD instabilities, which can have scale lengths of the same order as the plasma size. Bohm diffusion predicts much higher values for D_{\perp} than classical diffusion, and has only a $1/B$ dependence:

$$D_B = \frac{1}{16} \frac{k T_e}{B} \sim 20 \text{ m}^2/\text{s} \quad (1.6)$$

for the same plasma parameters as above, which is over four orders of magnitude higher than classical diffusion.

The diffusion coefficients for tokamaks lie between classical and Bohm diffusion, in the range $0.01 < D_{\perp} < 10 \text{ m}^2/\text{s}$.

Neoclassical diffusion

The toroidal geometry of a tokamak results in an increasing B -field with decreasing major radius. This can result in a magnetic mirror effect, whereby particles can be trapped in "banana" orbits which do not fully circulate around the torus, resulting in a much reduced diffusion scale-length. The "neo-classical" theory that describes this has been reviewed by Hirshman and Sigmar¹¹. It is difficult to test since it requires information on the gradients of several parameters (such as ion temperature) which are themselves difficult to measure.

Anomalous transport

Most transport is described as anomalous, in that it does not obey classical, neoclassical or any other theory. The anomalous transport formulation is an empirical description which includes diffusive and convective terms. It was first suggested to describe the anomalous fluxes of the main plasma ions¹²

$$\Gamma_z = -D(r) \frac{\partial N_z}{\partial r} - V_o f(r) N_z. \quad (1.7)$$

This was later adapted to describe the impurity transport in ASDEX¹³, and was incorporated into the STRAHL¹⁴ impurity transport code

$$\Gamma_z = -D(r) \frac{\partial N_z}{\partial r} - \frac{2rD}{a^2} N_z. \quad (1.8)$$

This description of transport allows the emission-shells of the ions to be calculated by an impurity transport code, thus making it possible to derive their concentrations from central-chord observations. The reverse procedure - using the code to derive transport parameters from central-chord observations - must be treated with great care if any physically meaningful solution is to be found. Most impurity transport codes now have the provision to specify D and V as radial functions, effectively creating a large number of free parameters, and making it impossible not to find a set of D and V profiles that reproduces the experimental data.

1.3 THE SOFT X-RAY SPECTRUM

The soft x-ray spectrum is relatively simple compared with the visible, UV and XUV regions. As shown in the sketch of figure 1.6 and in a detail in figure 1.7, it consists mainly of lines from H- and He-like ions, usually well separated by continuum radiation. There is a crowded region between about 8 Å and 16 Å (fig.7.2) containing L-shell lines from medium-Z ions such as Fe and Ni. H- and He-like ions have few possible transitions, so the line radiation is concentrated into a few strong and easily identifiable lines.

The Si spectrum in figure 1.7 contains most of the features which make the soft x-ray region so fruitful for plasma diagnostics, and from which the following parameters can be derived:

- Impurity identification, from the absolute wavelength.
- Impurity concentration, from the absolute intensity.
- Ion temperature, from the Doppler widths.
- Plasma mass-motion, from Doppler shifts.
- Electron temperature, from line ratios of the same (Rydberg series) or different (H/He or satellite ratios) ionization stages.
- Electron density, from the "R" line-ratio of He-like ions.
- Effective charge-state, from the continuum spectrum.
- Proton density from the Lyman $\alpha_{1,2}$ ratio.
- Supra-thermal electrons, from a satellite/resonance-line ratio.

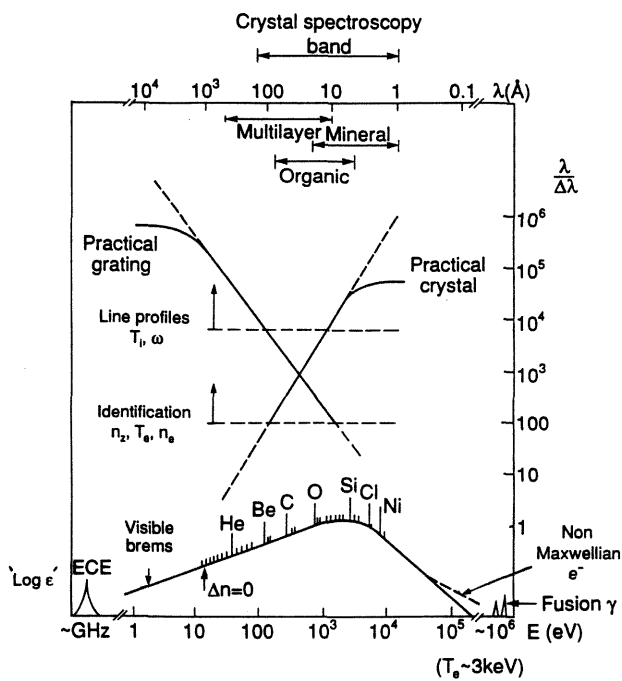


Fig.1.6 Sketch of the line and continuum spectrum from a tokamak, with a comparison of the typical resolving power achieved by grating and crystal spectrometers.

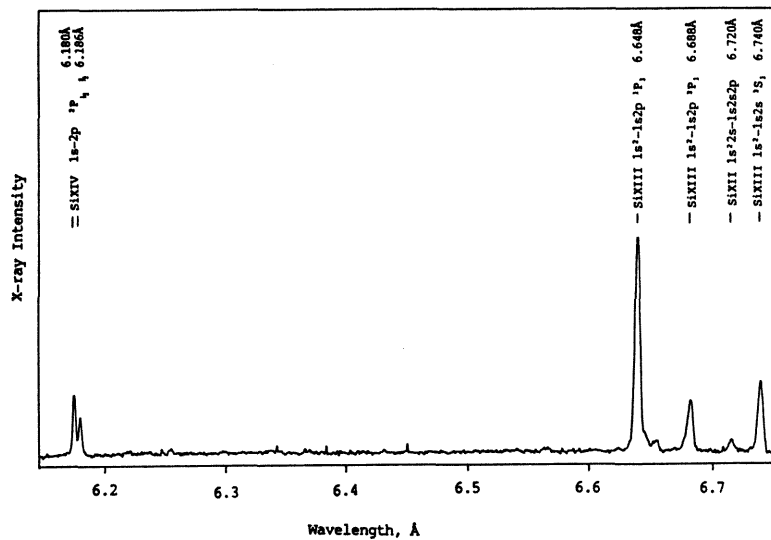


Fig.1.7 A typical section of the soft x-ray spectrum, containing well isolated H- and He-like lines, with the possibility to diagnose a wide range of plasma parameters (Dunn, unpublished).

Since one aim of this chapter is to specify the instrumental features necessary to monitor a wide range of impurities, it is useful to consider the bandwidth, resolving power and other features needed to measure each parameter. This is summarized in table 1.3, and will be discussed below where relevant.

H-like ions

As far as simple identification of impurities is concerned, we can go a long way before we need to look beyond the Bohr model of the Hydrogen atom.

The energy E_n of an electron in the n^{th} principal quantum level of an H-like atom of nuclear charge Z is:

$$E_n = - \frac{R_y Z^2}{n^2} \quad (1.9)$$

where

$$R_y = \frac{m_r e^4}{8 \epsilon_0^2 h^2}, \quad (m_r = \frac{m}{1 + m/M}) \quad (1.10)$$

where $R_y = 13.60$ eV is the Rydberg constant (the ionization energy of the hydrogen atom), and m_r is the electron mass reduced due to the orbit about its centre of gravity with the nucleus of mass M .

The photon energy from a transition between initial and final quantum states is:

$$E = h\nu = R_y Z^2 \left(\frac{1}{n_f^2} - \frac{1}{n_i^2} \right). \quad (1.11)$$

The energy is related to the wavelength by:

$$\lambda (\text{\AA}) = \frac{h c}{E} = \frac{12\,399}{E (\text{eV})} \quad (1.12)$$

and for the $n=2 \rightarrow n=1$ Ly α transition we obtain:

$$\lambda_{(\text{Ly}\alpha)} \cong \frac{1216}{Z^2} (\text{\AA}). \quad (1.13)$$

This sets the scene for the soft x-ray spectroscopy of high temperature plasmas, where the Ly α wavelengths for some typical impurities are given below.

Element	λ Ly α (Å)
Be	75.9
C	33.7
O	19.0
Si	6.18
Cl	4.20
Ti	2.50
Ni	1.53

Now, armed with eq.1.13 and a spectrometer covering from about 1 Å to 100 Å, we can identify and monitor all likely impurities very easily. This is an over-simplification, of course, but it does give an illustration of the relatively uncomplicated soft x-ray spectrum, which in practice facilitates the detection and identification of impurities.

Fine-structure splitting

On closer inspection, Lyman-series lines are doublets, due to the electron spin-orbit coupling. To first order, this fine-structure splitting can be derived from¹⁵

$$E_r = E_n \left(\frac{Z \alpha}{n} \right)^2 \left(\frac{n}{j + 1/2} - \frac{3}{4} \right) \quad (1.14)$$

where E_n and n are as in eq.1.9, the electron spin can be $j=1/2$ or $j=3/2$ and where α the fine-structure constant is:

$$\alpha = \frac{1}{4 \pi \epsilon_0} \frac{e^2}{\hbar c} = \frac{1}{137.0377} \quad (1.15)$$

The energy difference ΔE_{FS} between the $2P_{3/2}$ and the $2P_{1/2}$ levels is then:

$$\Delta E_{FS} = \frac{Ry Z^4 \alpha^2}{2 n^3} \quad (1.16)$$

When expressed as a wavelength difference, the splitting is almost constant at $\Delta \lambda_{FS} \approx 5.4$ mÅ. For neon this is about 1 part in 2300, which is just resolvable with a crystal spectrometer, while for nickel, at about 1 part in 300, it is easily resolvable.

The intensity ratio ${}^2P_{1/2}/{}^2P_{3/2}$ should be equal to 0.5, according to their statistical weights, but the ratio can be increased by population transfer from the metastable ${}^2S_{1/2}$ level to the ${}^2P_{1/2}$ level. The energy difference between the two levels is very small, so that collisions with ions are more important than with electrons. This offers the possibility to diagnose the fuel ion density from the $Ly\alpha_{1,2}$ ratio, and the effect has been calculated¹⁶. However, although anomalies in the ratio have been observed, they cannot be unambiguously attributed to proton excitation. Such measurements of the $Ly\alpha_{1,2}$ splitting and intensity ratios are discussed in detail by Dunn¹⁷.

He-like Ions

He-like ions are by far the most studied ions in tokamak soft x-ray spectra, and have been the subject of a large amount of theoretical work. This is because they are stable over a wide temperature range, and the spectrum has several features that can be used as plasma diagnostics. It is not a trivial point that the bandwidth of the spectrum conveniently matches that of the high-resolution spectrometers that have generally been used in the soft x-ray band. The energy levels of the ground state and first excited states of a He-like ion are shown in figure 1.8. The four main transitions to the ground state are, after Gabriel¹⁸:

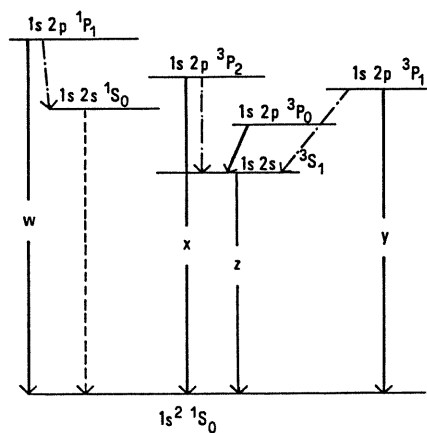


Fig.1.8 Energy levels and transitions from the first excited state of a He-like ion.

- the resonance line w , $1s2p(^1P_1) \rightarrow 1s^2(^1S_0)$; an electric dipole transition with transition rate scaling as Z^4 ,
- two intercombination lines: x $1s2p(^3P_2) \rightarrow 1s^2(^1S_0)$; a magnetic quadrupole transition scaling as Z^8 , and y $1s2p(^3P_1) \rightarrow 1s^2(^1S_0)$, an electric dipole transition with spin-orbit coupling, scaling as Z^{10} .
- the forbidden line z $1s2s(^3S_0) \rightarrow 1s^2(^1S_0)$; a relativistic magnetic dipole transition scaling as Z^{10} .

Of the remaining two states, the $1s2s(^1S_0)$ decays to the ground state by two-photon emission, and the $1s2p(^3P_0)$ decays radiatively to $1s2s(^3S_1)$ with the emission of a low energy photon. These main lines are accompanied by several satellite lines resulting either from dielectronic recombination or inner-shell excitation, which become more prominent with increasing Z .

1.4 ATOMIC PROCESSES

The interpretation of spectroscopic data requires knowledge of ionization, recombination, and excitation processes, as well as transition energies. Recent theoretical and experimental work has been extensively reviewed by De Michelis and Mattioli¹⁹. Summers has compiled a data base at JET²⁰, consisting of the most recent atomic data, with interpolation routines to cover incompletely documented ions.

Ionization Balance

In a plasma with a Maxwellian electron energy distribution, atoms exist in a range of ionization stages, with the balance being determined by the ionization and recombination rates into and out of each stage. The coronal equilibrium model (CE) is the simplest and assumes that all ionization is by electron impact and that all recombination is radiative. CE is a model of the low-density optically-thin limit, where photo-ionization and three-body recombination are negligible. The equilibrium of an ionization stage Z^{+q} results from electron impact ionization of the stage $Z^{+(q-1)}$ and recombination from the stage $Z^{+(q+1)}$. Figure 1.9 shows the results of an ionization balance calculation²¹ for aluminium.

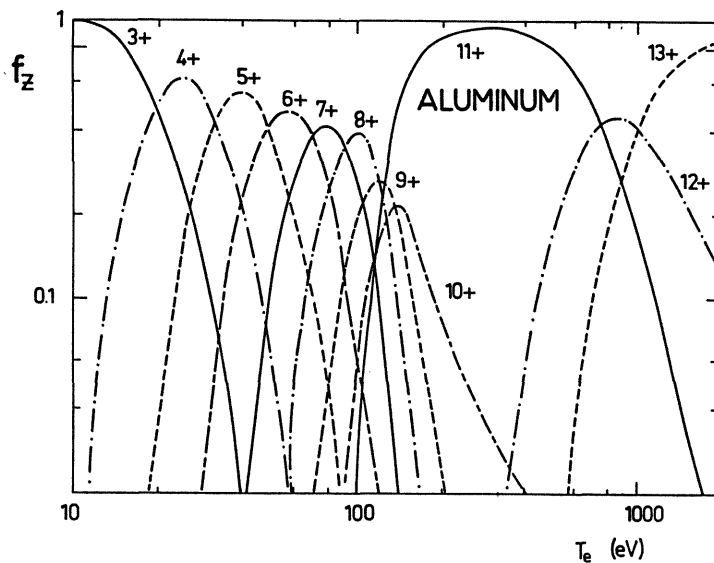


Fig.1.9 Coronal ionization balance for aluminium.

Ionization

The main process leading to impurity ionization is the direct detachment of a valence electron by a free-electron collision. A commonly-used semi-empirical formula for the ionization coefficient S (cm^3/s) is given by Lotz^{22,23}

$$S = 3.0 \cdot 10^{-6} \sum_m \frac{r_m}{I_m (kT)^{1/2}} E_1(I_m/kT) \quad (1.17)$$

where r_m is the number of electrons in the m -th subshell with ionization potential I_m , and E_1 is the first-order exponential integral. Both I_m and kT are expressed in eV.

Electron impact excitation

The simplest approximation for the cross-section of an optically allowed transition between states i and j was given by Van Regemorter²⁴

$$\sigma_{ij} = \frac{8\pi}{\sqrt{3}} \frac{Ry^2}{E_{ij} E} f_{ij} \bar{g}_{(E)} \pi a_0^2 \quad (1.18)$$

where E_{ij} is the transition energy, f_{ij} is the optical oscillator strength, a_0 is the classical Bohr radius and the Gaunt factor $\bar{g}_{(E)}$ is a semi-empirical factor that varies slowly with the energy E of the incident electron. By integrating the cross-section over a Maxwellian electron energy distribution, the excitation rate C_{ij} (cm^3/s) is obtained

$$C_{ij} = 3.15 \cdot 10^{-7} f_{ij} \bar{g} \frac{Ry}{E_{ij}} \left(\frac{Ry}{T_e} \right)^{1/2} \exp\left(-\frac{E_{ij}}{T_e} \right) \quad (1.19)$$

where $\bar{g} \cong 0.2$ is the Maxwellian average of $\bar{g}_{(E)}$. For transitions to the ground state in H- and He-like ions, the Van Regemorter approximation is within a factor two of more rigorous calculations. Examples are shown in figure 1.10 for H- and He-like Al, together with the emission function G , the product of the excitation rate and the coronal fractional abundance f_z

$$G_{ij} \equiv f_z C_{ij} \quad (1.20)$$

The volume emissivity ϵ_{ij} ($\text{photon}/\text{cm}^3 \cdot \text{s}$) in the transition is then given by

$$\epsilon = n_e n_z C_{ij} \quad (1.21)$$

where n_e is the electron density and n_z is the density of the ionization stage.

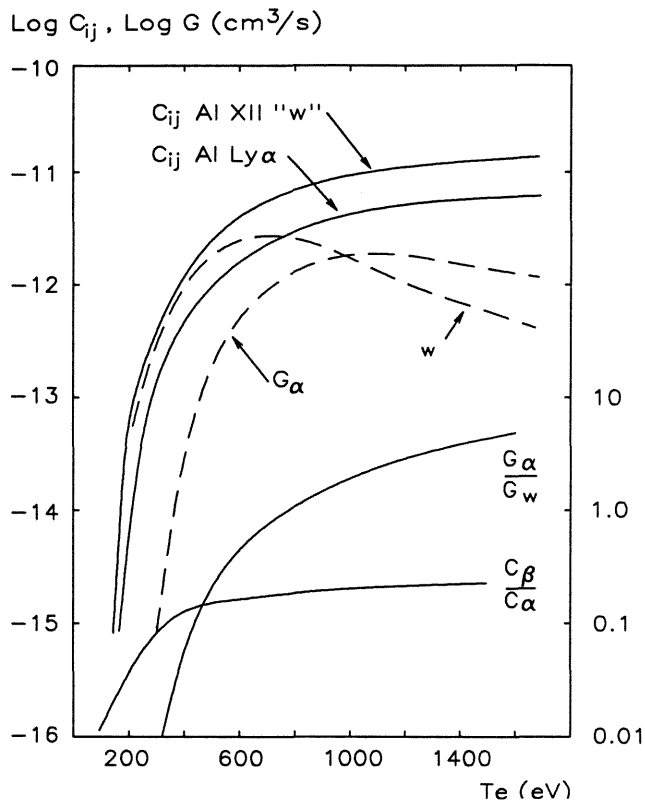


Fig.1.10 Excitation rates C_{ij} , emission functions G , and T_e -sensitive line ratios for H-like Al XIII and He-like Al XII.

Radiative recombination

Radiative recombination is a relatively slow process, and is particularly important for H-like ions, which can be transported well away from the region where they were ionized, before recombining. This phenomenon was used as a diagnostic of transport in the outer plasma, described in chapter 8. A semi-empirical formula for the radiative recombination rate α_{rad} is given by²⁵

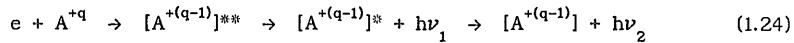
$$\alpha_{\text{rad}} = 5.197 \cdot 10^{-14} Z \lambda^{1/2} \left(0.4288 + \frac{\ln \lambda}{2} + 0.469 \lambda^{-1/3} \right) \quad (1.22)$$

where

$$\lambda = \frac{Ry Z^2}{T_e} \quad (1.23)$$

Dielectronic recombination

Dielectronic recombination²⁶ is the most important mechanism for ions that have more than two electrons, is significant for recombination leading to He-like ions, but cannot occur onto a fully-stripped ion. An electron recombines with an ion in the ground state, leaving it in a doubly excited state



where the superscripts * and ** indicate respectively that the ion is singly or doubly excited. The energy $h\nu_1$ of the first photon is reduced, relative to the analogous transition in the ion A^{+q} , by the presence of the "spectator" electron, resulting in dielectronic satellite lines to the long-wavelength side of the main transition.

Charge-exchange recombination

In this resonant process an electron is captured, usually from a neutral atom, into an excited state of an impurity ion. The peak charge-transfer cross section occurs for capture into an excited state whose energy below the continuum is equal to the the binding energy of the electron in the neutral atom²⁷. Charge transfer from neutral hydrogen in the ground state peaks at a value of the principal quantum number n , such that $\bar{n} = Z^{0.77}$.

Charge-exchange recombination is an important process, both for low energy neutral atoms at the plasma edge, and for high energy atoms from neutral beams in the core plasma. Although most charge-exchange spectroscopy uses high- n visible-light transitions of low- z ions²⁸, some x-ray lines of low and medium- z ions are strongly excited, and have been used to investigate neutral-beam penetration²⁹ and edge neutral particle densities^{30,31}.

Continuum Spectrum

The free-free (bremsstrahlung) spectrum is given by¹⁹

$$I_{ff}(\nu) = 6.4 \cdot 10^{-40} \frac{n_e Z_{eff} \bar{g}_{ff} e^{-h\nu/T_e}}{T_e^{1/2}} \quad (1.25)$$

($\text{erg/cm}^3 \cdot \text{s} \cdot \text{Hz}$, eV , cm^{-3}) where $\bar{g}_{ff}(\nu, Z, T_e)$ is the average free-free Gaunt factor.

This can be extended to include the free-bound continuum resulting from radiative recombination, where it is necessary to sum over all the energy levels $\chi_n \leq h\nu$. The continuum spectrum (photons/ $\text{cm}^3 \cdot \text{s}$) emitted in a frequency range $d\nu$ can be expressed as³²

$$dP = \frac{K N_e}{(T_e)^{1/2}} \sum_{Z,a} N_{Z,a} \left(Z^2 g_{ff}^Z + Z^2 g_{fb}^Z \sum_{n \geq n_0} \frac{\zeta}{n^3} \frac{\chi_n}{T_e} \exp\left(\frac{\chi_n}{T_e}\right) \right) \exp\left(-\frac{h\nu}{T_e}\right) \frac{d\nu}{\nu} \quad (1.26)$$

where

$$K = 128 \left(\frac{\pi}{3}\right)^{3/2} \frac{(\alpha a_0)^3 R_y^{3/2}}{h} = 9.63 \cdot 10^{-14} \quad (1.27)$$

with T_e in eV and n_0 in cm^{-3} , and where α is the fine-structure constant, a_0 the Bohr radius, and where ζ is the number of vacancies in the states characterized by n . To obtain the complete free-bound spectrum it is necessary to sum the above expression for each n -level of each ionization stage for all impurities.

1.5 SPECTROSCOPIC DIAGNOSTICS

The soft x-ray spectral region between 1 Å and 100 Å covers either K or L-shell radiation from all likely tokamak impurities, and contains a wide range of diagnostic information. The main derivable plasma parameters are shown in table 1.3, which also gives an indication of the spectral coverage and resolving power needed for each measurement.

Impurity monitoring

As discussed above, the observation of mainly H- and He-like ions in the soft x-ray band simplifies the detection and identification of impurities. The real challenge is to make quantitative measurements, especially of impurity concentrations. The main problem is one of plasma physics, since even if the instrument calibration and atomic physics were known perfectly, it would still be difficult to derive the central concentrations of the light impurities.

Light impurities such as Be and C in medium and large tokamaks are fully stripped except for a narrow region near the plasma edge, so that even if we can measure their radial profiles, some sort of extrapolation is necessary in order to say anything about their central concentrations. The situation is aggravated since it is mainly the light impurities that are responsible for the fuel dilution in most machines, and to estimate their concentrations within a factor two is not good enough; we really need an accuracy within 20%. This problem is discussed in more detail in chapter 7.

Concentrations

The ideal measurement is a radial profile $I_\lambda(r)$ ($\text{ph}/\text{cm}^2 \cdot \text{s}$) of the chordal intensities of a chosen transition, from which an Abel inversion will yield

the radial emissivity profile $\epsilon_{\lambda}(r)$ ($\text{ph}/\text{cm}^3 \cdot \text{s}$). This can be combined with measured T_e and n_e profiles to derive the abundance of each ion stage without any major uncertainty from

$$n_z(r) = \frac{\epsilon_{\lambda}}{n_e(r) C_{ij}(T_e, r)} \quad (1.28)$$

Unless all the possible ionization stages have been measured, which is almost never possible for experimental reasons, derivation of the total abundance of an impurity requires some assumption about the ionization balance and the fractional abundance f_z of the observed ionization stage

$$n_{\text{imp}}(r) = \frac{n_z(r)}{f_z(T_e, r)} \quad (1.29)$$

where the error in n_{imp} is minimized when f_z is as large as possible and is not a strong function of other parameters such as T_e . This is true for He-like ions, whose fractional abundance is high and almost constant over a wide T_e range, as shown for Al in figure 1.9. Such ions are thus suitable for abundance measurements over a wide range of T_e and Z. A further reduction in uncertainty can be achieved by adding together as many ionization stages as possible; for example

$$f_{(\text{Al } 11+)} + f_{(\text{Al } 12+)} > \sim 0.9 \quad \text{for } 300 \text{ eV} < T_e < 800 \text{ eV} \quad (1.30)$$

making gross errors due to shifts in the ionization balance unlikely. A further advantage of observing two or more ionization stages is that their abundance ratio can be compared with that predicted by the relevant ionization model, to check that approximate ionization equilibrium exists, and if so over what spatial extent of the plasma. This check is necessary because transport effects can seriously distort the ionization balance. It was carried out for all the Al ablation experiments described in chapter 8.

Thus, given independent T_e and n_e profiles, and profiles of preferably two or more ionization stages, it is possible to derive impurity abundance profiles without recourse to computer modelling, at least for the regions of the plasma where there is measurable emission in at least one ionization stage.

If only central-chord observations are available, some degree of modelling of the signal, usually by a transport code, will be inevitable. One partial solution to this problem would be to measure the ratios of transitions with very similar emission functions, such as Be IV and C V, since both will be radiating from the same plasma region, even if that region cannot be known exactly. This would give us a reliable measure of the Be/C ratio, which could be combined with other data, such as an independent Z_{eff} measurement, to

derive Be and C concentrations. This approach has been used to show that the O/Ne ratio in the Solar corona is the same as that in the photosphere³³.

Electron density and temperature

Several processes give rise to density and temperature sensitive effects in the spectra of H- and He-like ions. Some of these occur between different transitions of the same ion, and are thus (to first order at least) independent of the ionization balance. Others depend on the relationship between different ionization stages, and must be used with care if plasma transport is able to shift the ionization balance.

By far the strongest effect is that of the electron temperature on the ionization balance, and hence on the ratios of lines from different ionization stages. Figure 1.10 shows the Ly α /He"w" ratio of Al, for example, which changes by two orders of magnitude for a factor two in temperature. This will be discussed in more detail in chapter 9.

The dependence of the electron impact excitation rate C_{ij} on the transition energy means that the intensity ratios of transitions within a Rydberg series are temperature dependent. This will be strongest when the energy difference between the transitions is the greatest, such as the Ly β /Ly α ratio of an H-like ion. By combining eqs 1.11 and 1.19 we obtain

$$\frac{\epsilon_{\beta}}{\epsilon_{\alpha}} = \frac{f_{\beta}}{f_{\alpha}} \frac{27}{32} \exp - \left(\frac{5}{36} \frac{Ry}{T_e} Z^2 \right) \quad (1.31)$$

where³⁴ $f_{\beta}/f_{\alpha} \cong 0.19$. This ratio is plotted for aluminium in figure 1.10, and although it does not have such a strong temperature dependence as the H/He ratio, it is independent of the ionization balance. It is of greatest value at the threshold for excitation, as it tends to an asymptotic value at high temperature, where the transitions are more strongly excited. This ratio, or the equivalent ratio for He-like ions, has not been used routinely because its measurement requires a relatively large bandwidth of about 0.16, while to observe a complete Lyman series requires a bandwidth of 0.25. Such observations are possible with the broad-band instrumentation discussed in chapter 3. Even with transitions in a single ionization stage, care must be taken to ensure that they are excited mainly by electron impact, and not recombination which can predominate in the outer plasma.

The He-like spectrum contains the "R" ratio of the forbidden line z, to the sum of the intercombination lines x and y. The long life-time of the forbidden line means that it is collisionally de-excited at high density and, given a Z-number to suit the density range, this results in a valuable density diagnostic. Observations of this ratio for several impurities are discussed in chapter 9.

The collision strength has a different behaviour (as a function of incident electron energy) for the intercombination, forbidden and resonance lines of He-like ions³⁵. This results in a temperature dependence of the "G" ratio $(x + y + z)/w$.

Related to electron temperature is the effect of suprathermal electrons on the ratio of dielectronic satellites to the w line, in He-like ions^{36,37}. Dielectronic recombination is only excited by electrons whose energy is equal to the difference between the Li-like excited state and the ground state of the recombining ion. The resonance line is excited by all electrons whose energy is greater than its excitation energy, so that suprathermal electrons, whose energy is typically well above the dielectronic excitation energy, will preferentially excite the resonance line.

Impurity transport

A major use of spectroscopic diagnostics is in the study of impurity transport, by measuring the time evolution and radial profiles of impurities, usually injected by laser ablation. Although a wide wavelength range is not essential for this, it does give some flexibility in the choice of injected impurity. More important is good time and spatial resolution, since the signal rise-times can be of order 1 ms, and it is only the availability of spatial resolution that allows transport phenomena to be localized in the plasma. This subject is discussed in detail in chapter 8.

Doppler measurements

The measurement of impurity ion temperature from Doppler broadening of lines in the soft x-ray region is one of the most reliable spectroscopic techniques, and its first demonstration using crystal dispersion was by Bitter in PLT³⁸. The equipartition time between impurity ions and the main plasma ions is only a few μ s and, provided there is no mass motion of the plasma along the line of sight, the fuel ion temperature can be deduced.

The intrinsic line-widths of resonance lines are related, via the uncertainty principle, to their life-times, which are approximately $1.6/Z^4$ ns. This results in intrinsic Lorentzian line-widths which, being in the region of 10^{-5} , are usually at least 10 times less than the thermal Doppler broadening.

The Gaussian full-width at half-maximum intensity (FWHM) of a Doppler-broadened line is related to the ion temperature T_1 by³⁹

$$\frac{\Delta\lambda}{\lambda} = 2 \left(\frac{2 k T_1 \ln 2}{M_1 c^2} \right)^{1/2} = 7.71 \cdot 10^{-5} \left(\frac{T_1 \text{ (eV)}}{M_1 \text{ (amu)}} \right)^{1/2} \quad (1.32)$$

which can be conveniently expressed as

$$\frac{13000}{\lambda/\delta\lambda} = \left(\frac{T_1 \text{ (eV)}}{M_1 \text{ (amu)}} \right)^{1/2}. \quad (1.32)$$

A good *aide memoir* is that for Titanium ($Z = 22$), $\lambda/\delta\lambda = 2000$ when $T_1 = 2000$ eV.

A related Doppler measurement is the wavelength shift produced by bulk plasma rotation, usually during neutral beam injection. The relative wavelength shift $\Delta\lambda/\lambda$ for a non-relativistic velocity v is given by

$$\frac{\Delta\lambda}{\lambda} = \frac{v}{c} \cos \gamma \quad (1.33)$$

where c is the speed of light and γ is the angle between the velocity vector and the line of sight.

The He-like w line is most commonly used for these observations, as it is almost always the strongest line in the spectrum, and because other parameters can be diagnosed from simultaneous monitoring of the complete He-like spectrum. However, this observation is complicated by the presence in the long-wavelength wing of the w line of unresolvable $n \geq 4$ dielectronic satellites whose relative intensity is a function of T_e . This effect can result in erroneous T_1 measurements, and apparent Doppler shifts, and so considerable efforts have been made to model the spectrum^{40,41}. The fit to the data is then usually biased toward the short-wavelength side of the line. At some expense to sensitivity, this problem could be greatly reduced by observing another line, such as the He-like $1s^2-1s3p$.

1.6 IMPLICATIONS FOR INSTRUMENTATION

When trading off spectral coverage, time resolution and space resolution, the information (and hence instrumentation) requirements for impurity monitoring, impurity transport studies, and Doppler measurements are all very different. The bandwidth, resolving power and other factors required by the various techniques are summarized in table 1.3.

For all of the above parameters, the ability to take radial profiles, either by scanning the line of sight or by having multiple lines of sight, vastly improves the quality of the derived results and reduces dependence on code modelling.

Bragg diffraction is the best technique for spectroscopy in the band between 1 Å and 30 Å, allowing wavelength resolving powers ($\lambda/\delta\lambda$) of between 10^3 and 10^5 with good sensitivity, signal-to-noise ratio, and absolute

calibration for wavelength and intensity. Between 30 Å and 200 Å, synthetic multilayer structures are routinely used for fluorescent elemental analysis, and occasionally for plasma spectroscopy. Gratings have superior resolving power to Bragg diffractors above 30 Å, and have been preferred for plasma spectroscopy because the spectrum is usually more complex. Work described in chapter 5 has shown that it is possible to extend the useful coverage of Bragg spectroscopy to about 100 Å.

Table 1.3 Parameters derivable by soft x-ray spectroscopy.

Parameter	Principle	Bandwidth $\Delta\lambda/\lambda$	Res. Power $\lambda/\delta\lambda$	Other
Impurity ident.	Line ident.	1Å - 100Å,	~500,	Abs. λ .
Impurity conc.	Line intens.	Abs. intens.
Ion temperature	Dopp. broad.	0.002 - 0.1	~5000	$\Delta t \approx 10\text{ms}$
Plasma rotation	Dopp. shift	0.002 - 0.1	~5000	
Imp. transp.	Laser abl.	Monochrom.	~500	$\Delta t \approx 1\text{ms}$
Electron temp.	Ly α /w ratio	~0.15	~500	
Electron dens.	R-ratio	~0.01	..	
Fuel ion dens.	Ly $\alpha_{1,2}$	~0.005	~2000	
Non Maxw. elec.	dielec/w	~0.01	~1000	
CX neutrals	Lyman decr.	~0.15	~1000	
Z _{eff}	Continuum	1Å - 10Å	~100	Abs. intens.

Monitoring

The instrumentation requirements are for a spectrometer with a resolving power of $\lambda/\delta\lambda \sim 500$ and absolute intensity calibration, over a range from about 1 Å to 100 Å. Unbroken coverage of the spectrum is not absolutely necessary, since a few sub-regions can be found that still contain representative transitions of all the impurities, but it is a definite advantage. A resolving power of 500 is almost always adequate to avoid blending problems for routine monitoring. Most Lyman lines and He-like groups can be isolated with as low as 100.

Some form of spatial resolution, either on a shot-to-shot basis or from a scanning or imaging system, is almost essential. For monitoring purposes, the time resolution should ideally be less than the impurity confinement time of the plasma in question, otherwise the occasionally observed "UFOs" will remain just that.

General spectroscopy

Most of the line-ratio measurements described above can be made with a resolving power of about 500 and a bandwidth of about 0.15, so that any instrument designed for the basic monitoring function will also be suitable for general spectroscopy.

Transport studies

To study transport we need the best possible time and space resolution, and for many phenomena 1 μ s and 1 cm would not be too small. Here we have four options, summarized in the table below:

System	Space resolution	Time resolution
Full imaging	Best, ~ 1 cm	Adequate, ~10 ms depending on detector
Multichord	Needs ~10 chords	Best, ~10 μ s, count-rate limited
Scanning mechanism	~2 cm	~100 ms, good only for steady state
Shot-to-shot scan	~2 cm	< 1 ms given series of identical shots

It is not really necessary to have full spectral coverage on a space-resolving instrument designed for transport studies; in fact some of the best results to date have been obtained by sacrificing spectral resolution and wavelength coverage in order to get good time and space resolution of a single spectral line⁴². On a smaller machine it is usually possible to run a series of identical discharges, in which case the construction of a profile on a shot-to-shot basis has some attractions, because the effective time resolution can be as good as the signal intensity will allow. Such a technique was used for the transport studies described in chapter 8.

Doppler measurements

Doppler measurements, preferably of a single unblended line, require an instrumental resolving power $\lambda/\delta\lambda$ not much less than 10^4 , and this can be achieved with a high-resolution crystal spectrometer. The bandwidth need not be greater than $\Delta\lambda/\lambda \sim 0.005$, necessary to encompass a single line and some continuum, whereas a $\Delta\lambda/\lambda \sim 0.02$ will cover a typical He-like spectrum.

Most tokamaks have at least a central-chord measurement⁴³, while some have an array of several instruments to obtain radial profiles⁴⁴. High resolution is difficult to combine with coverage from 1 \AA to 100 \AA , and really these measurements need a separate instrument such as that described in chapter 6. However, it is shown in chapter 9 that a broadband Bragg spectrometer can be adapted to make useful Doppler measurements.

1.7 CONCLUSION

A soft x-ray spectrometer with coverage between about 1 Å and 100 Å would obtain a wide range of diagnostic information on all plasma impurities. The spectrum is relatively simple and the atomic physics are well understood. All the essential diagnostic measurements can be made with a resolving power $\lambda/\delta\lambda \sim 500$, except for Doppler measurements, which need $\lambda/\delta\lambda \sim 10^4$. An integrated impurity spectroscopy system would then consist of three systems:

- 1) A single fixed-chord broad-band instrument able to monitor all possible impurities with modest spectral ($\lambda/\delta\lambda \sim 500$) and time resolution (~ 10 ms).
- 2) A two-dimensional multi-chord or imaging system with not greater than 1ms time resolution, between 10 and 50 chords or resolution elements, and two or three simultaneous wavelengths. A 100 μ s fast window would be advantageous.
- 3) A multi-chord or imaging system for Doppler line-profile and line-shift measurements of at least one spectral line. About 10 chords would be required, with about 128 resolution elements per chord, and about 10 ms time resolution.

Functions 2) and 3) could be performed by the same system, by binning the line profile information in real time in order to improve the time resolution.

Without some provision for spatial resolution, we shall be condemned to (and probably by) the use of impurity transport codes for much of our data analysis.

References

- ¹ R Bartiromo, in Basic and Advanced Diagnostic Techniques for Fusion Plasmas. Varenna (1986) Publ. by International School of Plasma Physics, "Piero Caldirola" Milano, Italy.
- ² K S Krane, Introductory Nuclear Physics, Wiley, New York. (1988).
- ³ J Wesson, Tokamaks, Oxford Clarendon Press. (1987).
- ⁴ JET Team, Proc. 13th IAEA Conf. on Plasma Physics and Control. Nucl. Fusion Research, (Washington 1990) IAEA Vienna (1991), Vol 1, p27.
- ⁵ I H Hutchinson, Principles of plasma diagnostics., Cambr. Univ. Pr. (1991).
- ⁶ P E Stott, Reports on Progress in Physics. to be publ. (1993).
- ⁷ R V Jensen, D E Post et al, Nucl. Fusion, 17, (1977) 1187.
- ⁸ R C Isler, Nuclear Fusion, 24 no12, (1984) 1599-1678.
- ⁹ F F Chen, Introduction to Plasma Physics, Plenum Press, (1974).
- ¹⁰ N A Krall and A W Trivelpiece. Principles of Plasma Physics. McGraw-Hill (1973)
- ¹¹ S P Hirshman, D J Sigmar, Nuclear Fusion, 21 No9, (1981) 1079-1201.
- ¹² B Coppi and N Sharky, Nucl. Fusion, 21, (1981) 1363.

- ¹³ K Behringer, W Engelhardt, and G Fussmann.
in Divertors and impurity control. (Proc. IAEA Techn. Comm. Meeting.
(Eds. M Keilhacker, V Daybelge) IPP Garching, (1981) 42.
- ¹⁴ K Behringer, JET Report R(87)08.
- ¹⁵ L Schleinkofer et al, Phys. Scripta. 25, (1982) 917.
- ¹⁶ N N Ljepojevic et al, J. Phys. B. 17 , (1984) 3057.
- ¹⁷ J Dunn, PhD Thesis, Leicester University, (1990).
- ¹⁸ A H Gabriel, Mon. Not. R. Astr. Soc. 160 , (1972) 99.
- ¹⁹ C De Michelis, M Mattioli. Nuclear Fusion 21 no6, (1981) 677-754.
- ²⁰ H Summers, M von Hellerman. in: Atomic and plasma-material interaction
processes in controlled thermonuclear fusion. Ed. R K Janev,
Elsevier, Amsterdam. Publ. by IAEA (1993).
- ²¹ C Breton, C De Michelis. EUR-CEA-FC-948, Fontenay-aux-Roses rept.
- ²² W Lotz, Z. Phys. 216 , (1968) 241.
- ²³ W Lotz, Z. Phys. 220, (1969) 466.
- ²⁴ H Van Regemorter, Astrophys. J. 136,(1962) 906.
- ²⁵ M Arnaud et al, Astron. Astrophys. Suppl. 60, (1985) 425-475.
- ²⁶ J Dubau, S Volonté, Rep. Prog. Phys. 43 (1980) 199.
- ²⁷ H Ryufuku, H Watanabe, Phys. Rev. A, 20 (1979) 1828.
- ²⁸ M von Hellerman et al, Rev. Sci. Instrum. 61 (1990) 3479.
- ²⁹ B P Duval, N C Hawkes, S J Fielding, R C Isler, N J Peacock.
Nucl.Inst. Meth. B9 (1985) 689-697.
- ³⁰ J E Rice, E S Marmor, E Källne and J Källne.
Phys. Rev. A 35no7 (1987) 3033-44.
- ³¹ M Mattioli, N J peacock, H P Summers et al, JET-P(89)06.
- ³² H R Griem, Plasma Spectroscopy. McGraw-Hill, New York, (1964).
- ³³ J H Parkinson, Solar Physics, 42 no1 (1975) 183.
- ³⁴ H G Kuhn, Atomic Spectra, Longman and Green, London, (1962).
- ³⁵ F Bely-Dubau et al, Mon. Not. R. Astr.Soc. 198 (1982) 239.
- ³⁶ A H Gabriel, K J H Philips, Mon. Not. R. Astr. Soc. 189 (1979) 319.
- ³⁷ R Bartiromo et al, Phys. Rev. A, 32 (1985) 386.
- ³⁸ M Bitter et al, Phys. Rev. Lett., 42 (1979) 304.
- ³⁹ B E Shore, D H Menzel. Principles of Atomic Spectra, Wiley, NY, (1968).
- ⁴⁰ F Bely-Dubau et al, Mon. Not. R. Astr. Soc. 189 (1979) 801.
- ⁴¹ M Bitter et al, Phys. Rev. Lett. 47 (1981) 921.
- ⁴² V A Vershkov et al, (in Russ.) Soviet Journ. Instr. Tech. Exp. 6 (1987) 171
- ⁴³ R Bartiromo, F Bombarda, R Giannella, S Mantovani, L Panaccione,
G Pizzicaroli, Rev. Sci. Instrum. 60 (1989) 237.
- ⁴⁴ M Bitter, H Hsuan, J E Rice et al, Rev. Sci. Instrum. 59(10) (1988) 2131.

2 SOFT X-RAY ABSOLUTE FLUX MEASUREMENTS

2.1	Introduction	35
2.2	Absorption and scattering	35
2.3	Bragg analysers	37
2.4	Beam geometry	48
2.5	Spectrometer types	51
2.5	Absolute flux measurements	57
2.6	Conclusions	60

*Oure Hooste saugh wel that the brighte sonne
Th'ark of his artificial day had ronne
The ferthe part, and half an houre and moore,
And though he were nat depe ystert in loore,
He wiste it was the eightetethe day
Of April, that is messenger to May;
And saugh wel that the shadwe of every tree
Was as in lengthe the same quantitee
That was the body erect that caused it.
And therefore by the shadwe he took his wit
That Phebus, which that shoon so clere and brighte,
Degrees was fyve and fourty clombe on highte;
And for that day, as in that latitude,
It was ten of the clokke, he gan conclude.*

*Prologue to the Man of Law's Tale
The Canterbury Tales
Geoffrey Chaucer c1392*

2.1 INTRODUCTION

An important feature of a crystal spectrometer coupled to an energy resolving detector such as a proportional counter, is that the combination is doubly dispersive. In common with other doubly dispersive systems such as the gas-chromatograph mass-spectrometer (GCMS), the sensitivity, selectivity and signal-to-noise ratio of such a combination is difficult to improve upon. This point is not often emphasized, as proportional counters are in any case usually a natural choice, because of their high quantum detection efficiency (QDE) and relative simplicity. But in high-background applications the role of the energy resolution of a proportional counter in signal diagnosis, data validation and noise reduction is almost indispensable. The recent availability of cooled CCD arrays, which have sufficient energy resolution to be used as spectrometers in their own right, has further increased the value of such a combination.

A major reason for the reliability and stability of calibration is that all the relevant phenomena are volume effects. The absorption in windows and detectors, as well as being easily calculable from highly accurate data, is largely immune to the surface effects that plague the calibration of such components as mirrors, gratings and photocathodes. Crystals are relatively pure and simple structures whose Bragg diffraction properties are stable over periods of years and can often be calculated exactly. Also, for wavelengths around 10 Å, the angular dispersion offered by Bragg diffraction is about 100 times greater than can be achieved with a grating, leading to a general simplification in construction and alignment.

Another factor that contributes to very stable calibration is the photon-counting nature of the gas proportional counter. In a pulse-counting system, the QDE is stable against drifts in the detector gas-gain, the amplifier gain, or the electronic noise level. This is a great improvement on, for example, a micro-channel electron multiplier coupled to a phosphor.

The factors that influence the sensitivity and calibration of a crystal spectrometer divide into three areas: (a) absorption in windows and detector, (b) the diffractor reflection integral and (c) the beam geometry. These factors are discussed below, the most important item being the absolute calibration of diffractors.

2.2 ABSORPTION AND SCATTERING

Scattering factors

At photon energies between 100 eV and 10 keV, the main interaction with matter is with atomic electrons. Experimental measurements of photo-absorption cross-

sections over this energy range, for the full range of atomic Z-numbers, form the fundamental data for the analysis of x-ray scattering processes.

Accurate calculations for filters, mirrors, multilayers and crystals can be based on the atomic scattering factors ($f_1 + if_2$) of their constituent atoms. These factors have been derived from experimental photo-absorption data, for instance by Henke^{1,2}, using the Kramers-Konig dispersion relations

$$f_1 = Z + C \int_0^{\infty} \frac{\epsilon^2 \mu_a(\epsilon) d\epsilon}{E^2 - \epsilon^2} \quad (2.1)$$

and

$$f_2 = \frac{\pi}{2} C E \mu_a(E) \quad (2.2)$$

where

$$C = 1 / \pi r_0 h c \quad (2.3)$$

and where Z is the total number of electrons, r_0 is the classical electron radius, h is Planck's constant, c is the velocity of light, $\mu_a(\epsilon)$ is the atomic photo-absorption cross-section, and E is the incident photon energy.

The scattering factor f_1 is effectively the ratio of the scattering amplitude of all the electrons in the atom to that of a single electron. Similarly the crystal structure factor F determines the equivalent ratio for the unit cell of a crystal.

Refractive index

At x-ray wavelengths the refractive index n is less than unity by a small amount

$$n = 1 - \delta - i\beta \quad (2.4)$$

where the real and imaginary components δ and β are given by

$$\delta = \alpha/2 = K f_1 \quad (2.5)$$

and

$$\beta = \gamma/2 = K f_2 \quad (2.6)$$

where

$$K = \frac{r_0 \lambda^2 N_A}{2 \pi A} \rho \quad (2.7)$$

and where ρ is the density, A is the atomic weight, and N_A is Avogadro's number.

We may obtain the complex dielectric constant

$$\epsilon = 1 - \alpha - i\gamma \quad (2.8)$$

Mass absorption coefficients

The mass absorption coefficient μ is needed, to calculate the absorption of filters, windows and detectors, and is related to the atomic photo-absorption cross-section μ_a , by

$$\mu = (N_A / A) \mu_a . \quad (2.9)$$

Similarly, for the linear absorption coefficient μ_1

$$\mu_1 = \mu \rho . \quad (2.10)$$

The transmission T of a slab of material of density ρ and thickness x is given by

$$T = I / I_0 = \exp -(\mu \rho x) . \quad (2.11)$$

The transmission of typical window materials is shown in figure 2.1, where the most difficult spectral region is on the short-wavelength side of the carbon-K absorption edge. The 1/e absorption lengths for Argon and Xenon, the most common detector gases, are shown in figure 2.2. Argon gives adequate sensitivity over most of the required band, although below about 2 Å the denser gases krypton and xenon are more suitable.

2.3 BRAGG ANALYSERS

It is remarkable that there exists any region of the electromagnetic spectrum for which the best analysers have to be dug out of the ground. In spite of continuing improvements in the manufacture of microstructures, either gratings or multilayers, for diffraction at around 10 Å, parts of the soft x-ray spectrum are still safely in the (semi-precious) Stone Age.

Even though silicon, germanium and other crystals can be manufactured, and large organic molecules such as ADP and PET can be crystallized, there are parts of the x-ray spectrum where naturally occurring crystals such as Beryl are preferred or may even be the only practical choice. A review of theory, techniques and results for soft x-ray crystals is given by Burek³.

Theories of Bragg diffraction

The two main models of Bragg diffraction are the mosaic or ideally imperfect crystal with zero extinction, and the ideally perfect crystal with absorption. These models set limits for reflectivity and diffraction-profile width between which the properties of real crystals usually lie. Comparison of these models with measurements allows the quality and mosaicity of real crystals to be assessed, the latter being important when applying polarization corrections to two-crystal results.

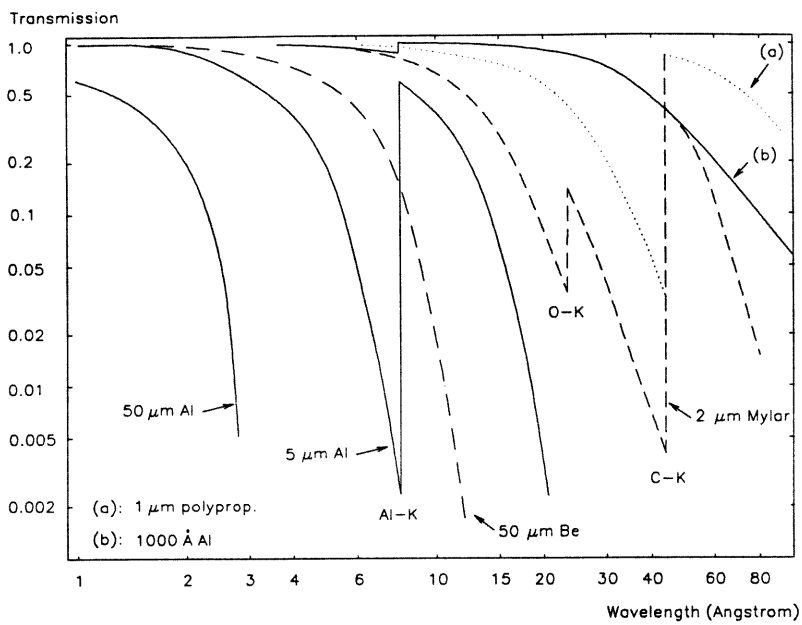


Fig.2.1 Soft x-ray transmission of typical window materials.

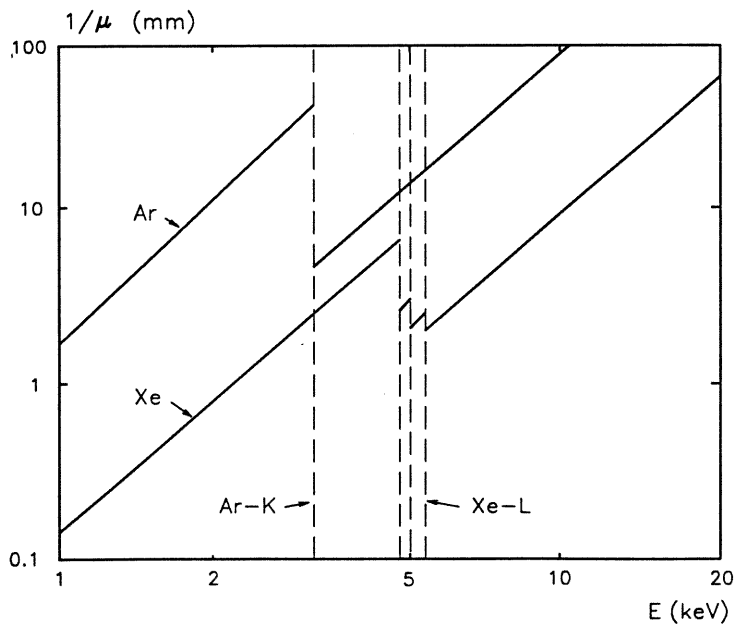


Fig.2.2 $1/e$ absorption lengths of Argon and Xenon.

Bragg dispersion function

The simplistic Bragg relation for a reflection of a wavelength λ , in diffraction order n , at Bragg angle θ_B , from a crystal of lattice spacing d is

$$n \lambda = 2 d \sin \theta_B \quad (2.12)$$

It requires corrections for thermal expansion, for refractive index, and for anomalous dispersion at wavelengths close to absorption edges of constituent atoms in the crystal. The necessary Bragg angle corrections are typically of the order of the diffraction width. They must be included in order to allow the accurate setting of a monochromator, and the fitting of a wavelength scale to a recorded spectrum.

The lattice spacing d_T , at temperature T ($^{\circ}\text{C}$), is given by

$$d_T = d_{18} (1 + \alpha (T - 18)) \quad (2.13)$$

where α is the linear expansion coefficient perpendicular to the diffracting planes. For accurate work the temperature at which the lattice spacing was measured should be quoted, and the temperature of the spectrometer should be measured, and controlled if necessary.

The effect of refraction is to bend the incident ray away from the normal inside the crystal, thereby reducing the angle at which diffraction takes place, by a small angle $\Delta\theta$ relative to the measured Bragg angle.

The refractive index decrement δ , is related to $\Delta\theta$ by

$$\delta = \Delta\theta \sin \theta_B \cos \theta_B \quad (2.14)$$

which can be combined with eq. 2.12 to give

$$n \lambda = 2 d \left(1 - \left(\frac{2 d}{n} \right)^2 \frac{\delta}{\lambda^2} \right) \sin \theta. \quad (2.15)$$

This is in a convenient form, since for wavelengths not close to an absorption edge, the factor δ/λ^2 is substantially constant for a given crystal. Including the influence of absorption edges, δ/λ^2 is given by Compton and Allison⁴ as a semi-classical analytical approximation

$$\frac{\delta}{\lambda^2} = \frac{N_A \rho r_0}{2\pi 10^{18} M} \left(Z_m + Z_k \left(\frac{\lambda}{\lambda_k} \right)^2 \ln \left| 1 - \left(\frac{\lambda_k}{\lambda} \right)^2 \right| \right) \quad (2.16)$$

where the crystal material density ρ , the number of electrons Z_m per molecule, and the gram molar weight M , can all be readily obtained. N_A is Avogadro's constant, Z_k is the number of electrons per molecule in the relevant K-shell, and λ_k is the wavelength of the absorption edge. For wavelengths far from an absorption edge, the multiplier of Z_k is negligible, and eq.2.16 simplifies to

$$\frac{\delta}{\lambda^2} = 2.701 \cdot 10^{-6} \frac{\rho Z_m}{M} . \quad (2.17)$$

Mosaic model

The basic assumption of the mosaic model is that the crystal is made up of discrete crystalline blocks, each of which is small enough for primary extinction to be ignored. The blocks are assumed to have some distribution function $W(\theta)$ in orientation angle that is wide compared to the diffraction width of each block, so that the blocks reflect independently. Under these assumptions the reflection integral of the entire crystal can be calculated without knowledge of $W(\theta)$, and is given by⁵

$$R_c = \frac{N^2 \lambda^3 r_o^2}{2 \mu_1 \sin 2\theta} |F|^2 \frac{1 + \cos^2 2\theta}{2} \quad (2.18)$$

where μ_1 is the linear absorption coefficient for the crystal, N is the number of unit cells per unit volume, r_o is the classical electron radius and F is the structure factor of the unit cell.

Although this model does not give any information about the diffraction profile, which here is determined by the mosaicity and not diffraction, the concept of ideal mosaicity does give an upper limit to the reflection integral that can be expected from a given crystal.

Ideally perfect model

The theory that is most widely used for the treatment of Bragg reflection from ideally perfect crystals, and which agrees well with experiment, is commonly called Darwin-Prins. Darwin⁶ developed a dynamical theory that took account of the interaction between the incident and diffracted beams in the crystal, but which did not include absorption - one of the main determiners of crystal performance, particularly at long wavelengths. Darwin theory was extended by Prins⁷ who included the complex refractive index to allow for absorption.

The theory accounts for the two competing processes that attenuate the incident beam in the crystal, namely extinction, where the beam is reduced by reflections from preceding planes (elastic scattering), and photoelectric absorption (inelastic scattering).

The zero extinction and zero absorption limits provide boundaries for the prediction of the performance of real crystals. A useful parameter, which quantifies the relative importance of extinction and absorption, is ξ the ratio between the number of planes that would be penetrated due to extinction alone to the number that would be penetrated by absorption alone

$$\xi^{-1} = \frac{N_{abs}}{N_{ext}} = \frac{\pi}{2} N \lambda r_o \frac{|F|}{\mu_1} . \quad (2.19)$$

Zero extinction limit

For large ξ , where absorption dominates, the reflection integral becomes equal to the mosaic case⁸ (eq. 2.18). The theoretical diffraction profile is a Lorentzian with peak P_c , of

$$P_c = \left(\frac{N \lambda r_0 |F|}{\mu_1} \right)^2 (1 + \cos^2 2\theta) \quad (2.20)$$

and FWHM W_c , of

$$W_c = \frac{\mu_1 d}{\pi \cos \theta} \quad (2.21)$$

where d is the lattice spacing, and from which the resolving power is

$$\frac{\lambda}{\Delta\lambda} = \frac{\pi \sin \theta}{\mu_1 d} \quad (2.22)$$

Zero absorption limit

In this approximation the reflection integral is given by³

$$R_c = \frac{8}{3\pi} N r_0 \lambda^2 |F| \frac{1 + |\cos 2\theta|}{2 \sin 2\theta} \quad (2.23)$$

Diffraction calibration

There is no entirely satisfactory way to measure the reflection integral and line-spread function of crystals, as we can rarely obtain an x-ray beam that is sufficiently monochromatic to reveal the diffraction profile. This is because the natural widths of x-ray lines tend to be broader than the crystal profile to be measured, and the only way to produce a beam of narrower bandwidth is to use a crystal. The use of one or more additional crystals to monochromate an x-ray beam is a partial solution that gives good control over the beam characteristics, but which must rely on some theoretical modelling to deconvolve the two-crystal profile.

The problem of deconvolving a two-crystal diffraction profile is less open to error than that of deconvolving x-ray lines from single-crystal profiles, and mainly for this reason the two-crystal technique is preferred, even though the calibration apparatus is necessarily more complicated.

The full characterization of a crystal requires the measurement of its Bragg dispersion function (largely determined by its lattice spacing) and of its diffraction profile P_θ , throughout the Bragg angle range for which it is to be used. At least the peak reflectivity P_0 , the FWHM W_c and the integral R_c of the single-crystal response are normally required.

In cases where the accurate deconvolution of a line-profile is being attempted, it is necessary to derive the detailed shape of the diffraction profile, usually by a combination of measurement and theory. Figure 2.3 shows calculated single crystal diffraction profiles for PET (002). At the shorter wavelengths the profile has the "top-hat" shape dominated by extinction, while at longer wavelengths the profile tends toward the absorption-dominated Lorenzian.

In view of the importance of crystal calibration, particularly for absolute flux measurements of astrophysical observations, a two-axis diffractometer was built at Leicester University in about 1970 to aid the selection and characterization of crystals for the x-ray astronomy space programme. In addition to the calibration facility, computer codes were developed to aid the assessment of crystal properties and to allow derivation of such results as are not obtainable by measurement alone.

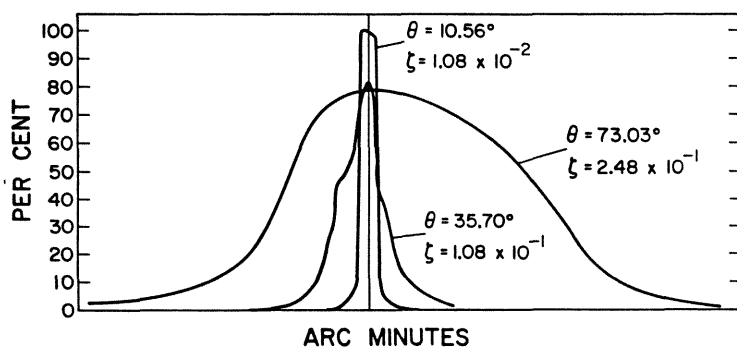


Fig.2.3 Calculated Darwin-Prins profiles for PET(002) (Burek³).

Thorough treatments of the principles and techniques of crystal calibration, as well as detailed calibrations of many crystals useful between about 2 Å and 26 Å, are to be found in the theses of Hall⁹ (ADP, PET, EDdT, SHA), Lewis¹⁰ (most acid phthalates), and Willingale¹¹ (Lead Stearate, Beryl, Gypsum). More widely available, with detailed discussion of the techniques and theories used (and further references), are Evans et al¹² (single-crystal techniques), Lewis et al¹³ (double-crystal measurements of KAP) and Hall et al¹⁴ (PET). This previous work has been invaluable, and the author has made what seems to be daily reference to it during the course of this project.

Bragg Dispersion Function

Determination of the Bragg dispersion function entails measuring the Bragg angle for a range of known¹⁵ wavelengths, with the aim of deriving a consistent value for the spacing of the reflecting planes. The standard technique is shown in fig 2.4, where the incident beam can either be directly from a source or from a monochromating crystal. By measuring the angle $(180^\circ - 2\theta)$, uncertainties in the source alignment can be eliminated.

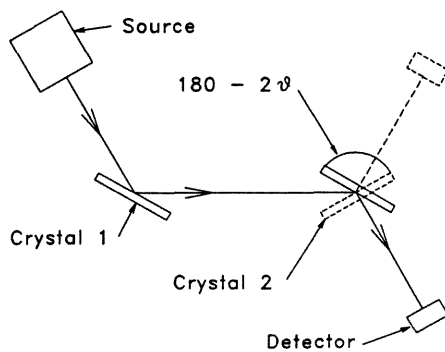


Fig.2.4 Measurement of the diffractor lattice spacing.

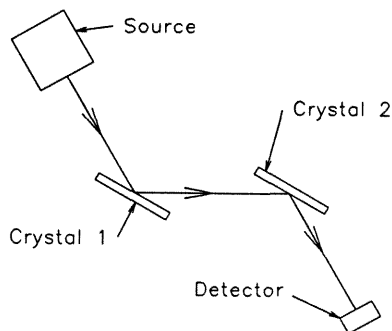


Fig.2.5 The (1,-1) configuration of a diffractometer.

Single crystal reflection integral

The single crystal reflection integral R_c is defined by

$$R_c = \int_0^\pi P_\theta d\theta \quad (2.24)$$

where the intensity P_θ of the diffraction profile rapidly tends to zero on either side of the peak.

Without requiring any knowledge of the detailed shape of the diffraction function, R_c may be measured from

$$E = \frac{I R_c}{\omega} \quad (2.25)$$

where E is the energy reflected into a detector from a parallel monochromatic beam of power I , as the crystal is rotated through the diffraction peak at angular velocity ω . This is independent of the divergence and spectral distribution of the input beam, provided they are small compared with the angular and spectral range over which diffraction occurs.

A reliable single reflection technique for measuring the reflection integral only was demonstrated by Evans and Leigh¹². The main challenge of their method is to minimize the error introduced by the continuum radiation produced by a direct electron excited x-ray tube. When using a proportional counter to measure the incident beam-power, the continuum makes a significant contribution, because the detector has insufficient energy resolution to reject all of the broad-band continuum. Hence the intensity I'_0 measured by the detector is greater than the intensity I_0 present in the desired emission line, leading to underestimation of the integrated reflectivity of the crystal.

Optimization of the source excitation energy, the beam filtration and the proportional counter energy window all help to minimize the contribution of the continuum to the measured incident beam. The principle of the method is to limit with filters the entire bandwidth of the incident beam within a wavelength interval such that the reflection interval is slowly varying over that bandwidth. The crystal itself is then used to measure the strength of the desired line relative to the continuum and other contaminating lines. Provided that the relative strengths of all the components in the beam have been measured, their total strength must equal I'_0 . The absolute power I_0 of the desired line can then be calculated once the total flux I'_0 has been measured.

Two-crystal reflection integral

The main advantage for two-crystal measurements is that in the parallel (1,-1) non-dispersive configuration, the two-crystal diffraction profile or "rocking curve" is independent of the profile of the source spectrum or of the vertical or horizontal beam divergence⁴. This condition is only true if the change crystal properties throughout the bandwidth of the beam is negligible, a condition that can easily be satisfied when using typical beam collimation of about 0.2° .

Compared with the single crystal method, the problem of contamination of the incident beam with continuum and unwanted lines effectively disappears, because I_0 is now measured after the first reflection, where the bandwidth is

narrow compared with the energy resolution of the proportional counter.

The other major advantage is that the two-crystal profile is a function only of the profiles of the individual crystals and is independent of the source spectrum. This makes it possible to obtain two-crystal rocking curves down to the arc-second level (given suitable crystals) even though the natural line-width of the source may be orders of magnitude greater.

The disadvantage is that it is not possible to derive the single-crystal response directly from the two-crystal measurement, for two reasons. Firstly, due to the symmetry of the parallel configuration, the two-crystal curve from a correctly aligned instrument is always itself symmetrical, whereas the diffraction profiles of many crystals are asymmetrical. This makes it impossible to derive the single-crystal line profile from the two-crystal measurement without relying on a model of the single-crystal profile shape. Secondly, the incident beam is partially polarized by the first crystal, and the contributions of the σ and π components cannot be separated by a parallel two-crystal measurement alone.

Two-crystal measurements do, however, give results that can be directly compared with theory, and hence allow the theory to be extended with confidence to predict the single crystal response.

The technique for measuring the two-crystal diffraction profile is shown in figure 2.5. The first crystal, A, is set at a fixed Bragg angle θ_m relative to a source X, to produce a quasi-monochromatic beam whose intensity I_0 may be measured by placing the detector, D, between the two crystals. The second crystal, B, is then scanned through the parallel position at constant angular velocity ω , through a range that includes all the significant reflected intensity.

The two-reflection integral R_{cc} is then given by

$$R_{cc} = \frac{E \omega}{I_0} = \frac{\sum_p E_p \omega}{\sum_p I_p} \quad (2.26)$$

where the p refers to the polarization components.

If the crystals are identical, parallel and are reflecting in the same diffraction order, the configuration is known as the (1,-1) position and the two-reflection integral is related to the single crystal integral by⁹

$$R_{cc} = 2 R_c \frac{(1 + k^2)}{(1 + k)^2} \quad (2.27)$$

where;

$$k_\theta = \frac{R_{c\pi}}{R_{c\sigma}} \quad (2.28)$$

The value of k_{θ} , the polarization ratio, depends in a complex manner on crystal properties such as absorption, extinction and defect density, but two limiting cases can be identified, based on Darwin theory⁵ (figure 2.6). For a perfect crystal with zero absorption, $k_p = |\cos 2\theta|$, while for a mosaic crystal, $k_m = \cos^2 2\theta$, and the values for real crystals normally lie within these limits. The correction applied to R_{cc} is a maximum at 45° , and the maximum error due to uncertainty in the choice of k_p or k_m is about 30% and occurs near to 35° and 55° .

Unless k_{θ} is known, it is impossible to obtain the single-crystal reflection integral from a two-crystal measurement, but in practice a good estimate of the polarization correction can be made, or its effect minimized. This can be done by comparing the measured and calculated two-crystal reflection integrals, and using the extent of agreement to justify applying the theoretical polarization corrections. Evans¹² showed that errors due to uncertainty in the polarization correction can be minimized by using a monochromating crystal whose 2d spacing is much larger than that of the second crystal. Thus the Bragg angle at the first crystal can be low, say about 15° to 20° , where k_{θ} , and the difference between k_p and k_m are both small.

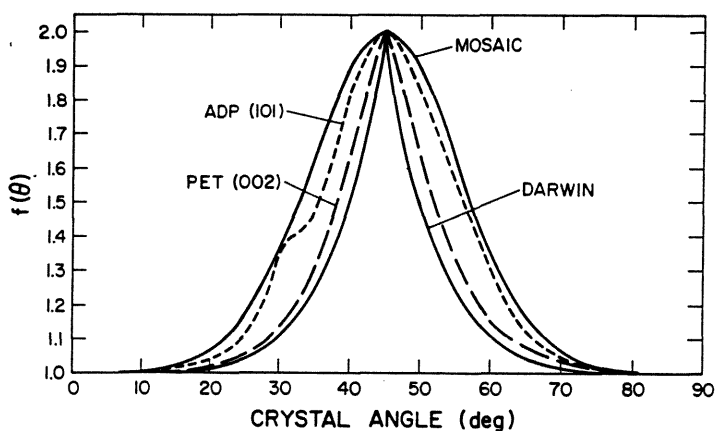


Fig.2.6 Darwin-Prins calculated polarization corrections for PET(002) and ADP(101) (Burek³).

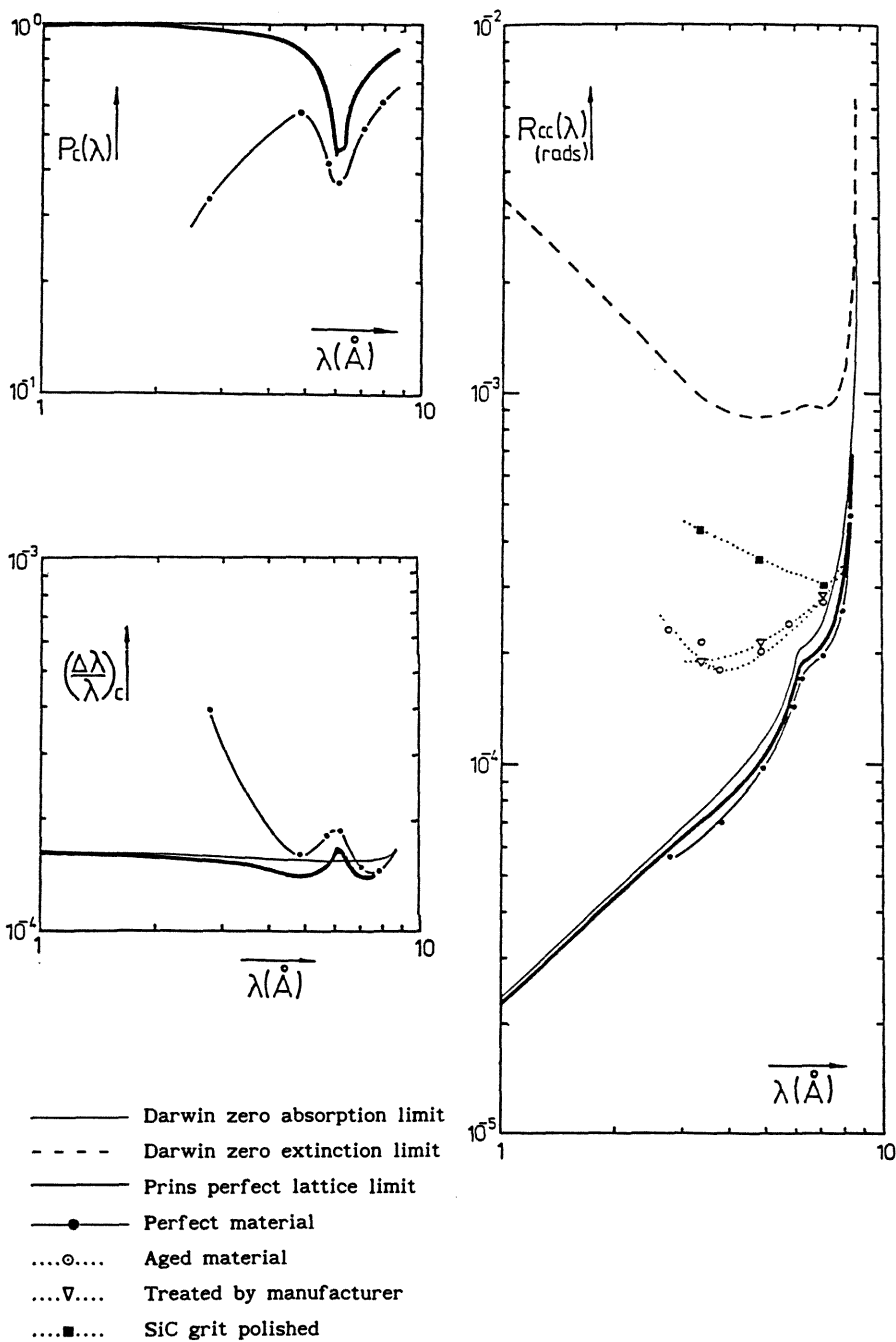


Fig.2.7 Calibrations of (a) peak reflectivity, (b) resolution and (c) reflection integral, for PET (002) $2d = 8.742 \text{ \AA}$. These single-crystal values are derived from two-crystal measurements (Hall⁹).

Calibration data⁹ for PET (002), a typical organic crystal, are shown in figure 2.7, derived from two-crystal measurements. This type of data is indispensable for accurate flux measurements and credible line-profile deconvolutions, and is the result of a large investment in effort and instrumentation.

2.4 BEAM GEOMETRY

Collimators

The simplest collimator (apart from infinite distance from the source) is a pair of slits, and although the sensitivity is necessarily low, such an arrangement still has an advantage for the most accurate flux measurements, because the beam geometry can be controlled and measured with greater precision than is possible with collimators. In most cases, however, some form of multiple-aperture collimator is used to make the most of the available aperture, by serving as a large number of pairs of slits in parallel.

Soller collimators

A simple large-area collimator with high transmission can be made by clamping together a stack of thin foils of thickness f , and length L , separated at their long edges by shims of thickness s , (fig 2.8). This arrangement has a triangular line-spread function, with a FWHM $\Delta\theta$ given by

$$\Delta\theta = s / L \quad (2.29)$$

and geometrical transmission by

$$T = f / (f + s). \quad (2.30)$$

The minimum absorption depth D_{abs} , seen by an x-ray incident at angle θ_1 , occurs when $\theta_1 = 2 \Delta\theta$, and hence

$$D_{\text{abs}} = \frac{f}{\sin 2\Delta\theta} \approx \frac{f L}{2 s}. \quad (2.31)$$

Typical values of the above dimensions ($L = 250$ mm, $f = 0.05$ mm, $s = 0.5$ mm) give $\Delta\theta = 1/500 \approx 7$ arcmin, $D_{\text{abs}} = 12.5$ mm, and $T = 0.91$; so that even when using polymer foils, the absorption depth is more than adequate for x-ray energies up to 20 keV.

Such collimators are useful down to angles of a few arcmin, but at smaller angles grazing incidence reflections from the large number of foils can produce extended wings to the line-spread function. This phenomenon can be largely overcome by using a matt material such as polyester drafting film for the foils. Though not relevant to this work (where collimation in a single plane only is required), a further disadvantage of this type of collimator is

that it is not possible to make a two dimensional version, except by placing two such collimators coaxially with their planes orthogonal.

The Soller collimator is almost ideal for flat crystal spectrometers of moderate resolving power ($\lambda/\Delta\lambda \sim 1000$): the angular divergence both in and perpendicular to the plane of dispersion can be optimal, and the geometrical transmission for typical dimensions can approach unity.

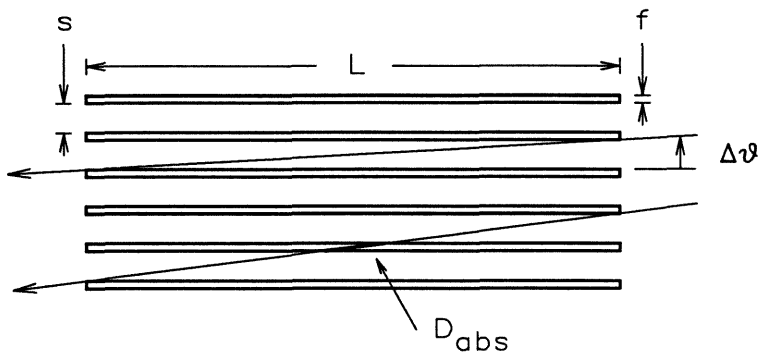


Fig.2.8 Schematic of a Soller collimator.

Gridded collimators

An alternative method to define a beam of small divergence is to position a series of grids such that their combined effect is to obstruct all but the desired rays (fig 2.9). If t is the grid size and w the grid spacing, then the position l_N of the grid number N , is given by¹⁶

$$L - l_N = \frac{w}{w + t} (L - l_{N-1}). \quad (2.32)$$

The angle θ_M , of the first side-lobe is

$$\theta_M \cong \tan \theta_M = \frac{t}{L - l_N} = \left(\frac{w + t}{w} \right)^N \frac{t}{L}. \quad (2.33)$$

The above equation can be solved for the necessary number of grids to be placed between the two end grids¹⁷

$$N = \frac{\log \left(\frac{L \theta_M}{t} \right)}{\log \left(\frac{w + t}{w} \right)}. \quad (2.34)$$

Since $\Delta\theta = w/L$, and the geometrical transmission is $T = w/(w+t)$, we can rewrite the above eq. 2.34 as

$$N = \frac{\log \left(\frac{\theta_M}{\Delta\theta (1 - T)} \right)}{\log (1 / T)} \quad (2.35)$$

where it can be seen that attempts to improve the collimation, the side-band angle or the transmission, are all at the expense of a larger number of grids. This function is very unfavourable for transmissions greater than 50%, and for a collimator with $\Delta\theta = 1$ arcmin and $\theta_M = 1^\circ$, the number of grids for transmissions of 50%, 70% and 80% would be 7, 15, and 26 respectively.

In a practical collimator, imperfections in the individual grids and in their collective alignment necessitate a larger number of grids than the theoretical minimum, and also lead to a lower transmission than the theoretical. In addition, even when only single axis collimation is required, some supporting material must be left in the grid perpendicular to the plane of collimation, further reducing its transmission. For these reasons it is difficult to make a gridded collimator with a transmission much greater than 50%, and for a high resolution model with $\Delta\theta \sim 10^{-4}$ the transmission will be nearer to 30%.

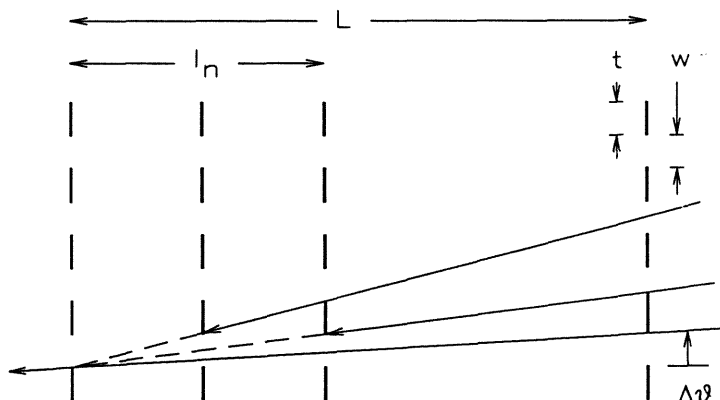


Fig.2.9 Schematic of a gridded collimator.

The use of a collimator is not obviously beneficial below 10 Å, where an additional crystal operating in the antiparallel dispersive configuration may offer superior sensitivity and resolving power. The peak reflection of an additional crystal is higher than the collimator transmission, and given the relatively low cost of modern rotation tables and control systems compared to a sub-arcmin collimator, it is probably no longer worth considering a collimator for high-resolution work.

2.5 SPECTROMETER TYPES

Spectrometers can be classified according to the crystal curvature (convex, flat, or concave) or the type of collimation (slit, collimator or focusing), but the single most important design feature is whether or not the optics require a position-sensitive detector.

Configurations that produce a spatially dispersed image are polychromators, and require no moving parts except to change the wavelength range if necessary between measurements. Monochromators need to be scanned to acquire a spectrum and run the risk of not being able to follow the time evolution of the source. They have the advantage that the wavelength scale can be fitted simply, usually by recording a single angle during the scan. For a fast-scanning system and an intense source, the time to scan a spectrum is comparable with the readout time of many position-sensitive detectors, and so the distinction between polychromator and scanning monochromator is less clear than might appear. The principles of most types of crystal spectrometer are covered by Thomsen¹⁸.

The sensitivity of a crystal spectrometer may be obtained by expanding eq 2.25 to describe the source emissivity, beam geometry and the efficiencies of the detector and other elements. The number of counts N integrated in a scan at angular velocity ω across a spectral line is then

$$N = I_{\lambda} A \frac{\Omega}{4\pi} \frac{Rc}{\omega} \eta \quad (2.36)$$

where I_{λ} (photon/cm²s) is the source irradiance, Ω (sr) is the solid angle subtended at the effective crystal area A , and η is the combined efficiency of the detector, filters and structural elements. Depending on the optics, Ω is defined by some combination of slits, collimators aperture stops, and the crystal diffraction width. The effective crystal area depends on its curvature, which may be flat, convex or concave, and on the input optics, which may have slits, collimators or be slitless.

For a monochromator scanning a Bragg angle range $\theta_2 - \theta_1$ ($> \Delta\theta$) at a frequency f (Hz), the count rate \dot{N} in a line is

$$\dot{N} = N f = \frac{N \omega}{\theta_2 - \theta_1} = I_{\lambda} A \frac{\Omega}{4\pi} \frac{Rc}{\theta_2 - \theta_1} \eta. \quad (2.37)$$

By differentiating the Bragg relation we obtain the spectral resolving power $\lambda/\Delta\lambda$

$$\frac{\lambda}{\Delta\lambda} = \frac{\tan \theta}{\Delta\theta} \quad (2.38)$$

where $\Delta\theta$ is the instrumental line-spread function, which may be limited by the collimation, diffractor or detector.

The Bragg spectrometer

This instrument¹⁹ (fig.2.10) allows a wide Bragg angle range to be covered simply by rotating the crystal about a fixed axis. The spectrum is obtained by integrating the detector count-rate in suitable time intervals. The photon flux is best measured by integrating the counts in a line scan, since this duplicates the conditions by which the diffractor reflection integral is defined (eq.2.25). If the crystal is rotated at angular velocity ω (rad/s), the integrated count N is independent of the instrument or source line profiles, and by expanding eq. 2.36 we obtain

$$N = I_{\lambda} \frac{h_x h_y}{4 \pi} \frac{\psi_x \psi_y}{\omega} \frac{R_c \eta_s \eta_{\lambda}}{\omega} \quad (2.39)$$

where if ϵ_{λ} (ph/cm³s) is the plasma emissivity and Δz is the effective plasma column depth, then $I_{\lambda} = \epsilon_{\lambda} \Delta z$. Other terms are: the crystal projected area $h_x h_y$, the respective slit or collimator angles $\psi_x \psi_y$ in, and perpendicular to, the plane of dispersion, and the efficiencies η_s of structural elements and η_{λ} of wavelength dependent elements, including the detector.

If the crystal is kept fixed, this instrument has high monochromatic sensitivity, because the full crystal area is sensitive to a single wavelength. The scan range can be chosen to suit a particular observation, a very useful feature when trading off sensitivity and bandwidth and, the collimation being quasi-parallel, close access to the source is not necessary.

The detector is usually scanned at twice the crystal angle in order to intercept the diffracted ray, but can instead be made long enough to accept a wide range of Bragg angles, as was done for the Bragg rotor spectrometer described in the next chapter.

Double-crystal (antiparallel)

This configuration (fig.2.11b,d) is dispersive, since a ray that makes an angle $\theta + \delta\theta$ with the first crystal makes an angle $\theta - \delta\theta$ with the second crystal. For a given pair of crystals, the dispersion is fully defined by the angle between them, which is the only quantity that must be measured. The resolution is governed only by the convolution of the two diffraction profiles, and in most cases is the optimum that can be achieved with a crystal spectrometer, particularly since the flat crystals contribute no errors due to focusing, or to bending stresses. The detector need only be a simple counter. The disadvantages for plasma diagnostics are that the sensitivity is low compared with a Johann instrument, and that a complicated mechanism is required if a large Bragg angle range is required. However, useful results can be obtained with this configuration, as demonstrated in chapter 9.

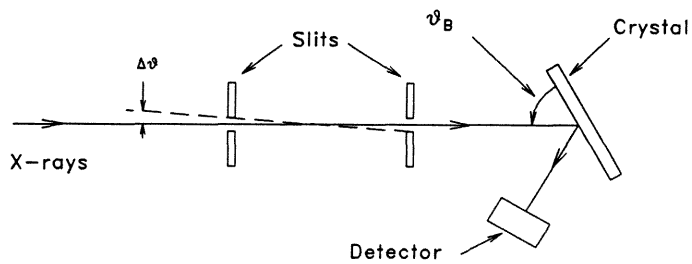
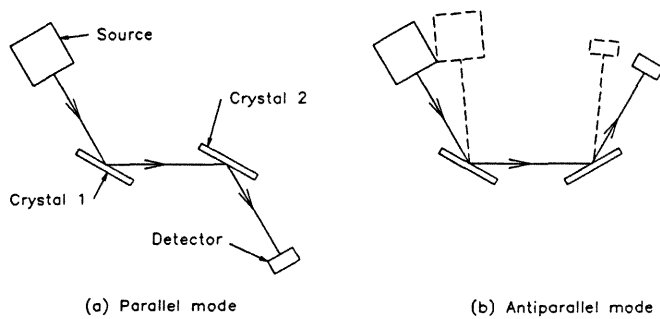


Fig.2.10 The Bragg spectrometer.

Standard Two-Axis Diffractometer



Fixed-Source Two-Axis Diffractometer

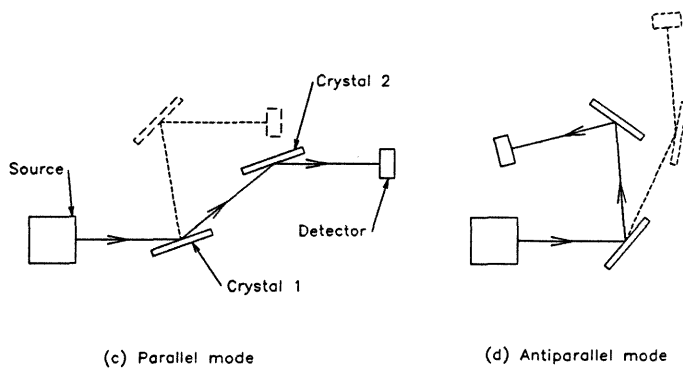


Fig.2.11 The principal configurations of a two axis diffractometer.

Double-crystal (parallel)

This configuration (fig.2.11a,c) is non-dispersive, since any ray that makes an angle $\theta + \delta\theta$ with the first crystal also makes an angle $\theta + \delta\theta$ with the second crystal, so that all off-axis rays that can pass through the optical path will be reflected. This is an unfavourable configuration for spectroscopy: the crystals must be kept parallel well within the diffraction widths, yet a collimator is still necessary to define the spectral resolution. However, the detector is in a fixed position, remote from the input beam, and this is a great advantage where shielding is required. Such an instrument was specially developed at IPP Garching for tritium experiments at JET, and its operation is discussed in detail in chapter 10.

De Broglie

A simple broad-band instrument can be made by bending a crystal round a former, and viewing an extended source via a single slit²⁰ (fig.2.12). The global sensitivity is equal to that of a scanning flat crystal of the same projected area and covering the same Bragg angle range. A position sensitive detector is required, and this has almost always been photographic film, since anyone with a photoelectric detector of the necessary spatial resolution would surely find a better use for it.

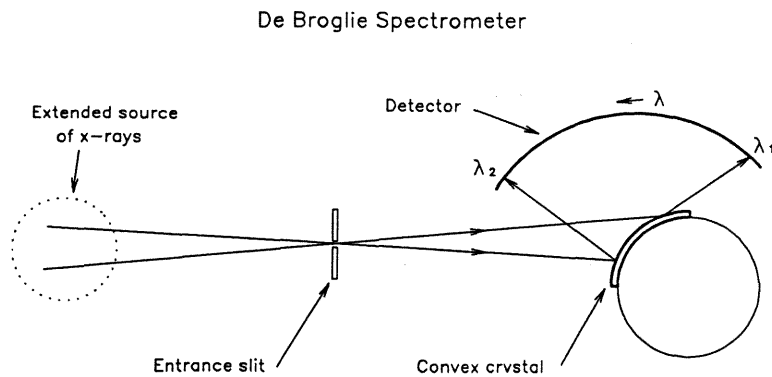


Fig.2.12 The De Broglie spectrometer.

Johann

This instrument²¹ (fig.2.13) has a great advantage over other types in that the full crystal area can simultaneously diffract a range of wavelengths. A thin crystal is bent to a radius R , with the result that x-rays from an extended polychromatic source pass through a virtual aperture to be focused onto a position sensitive detector on the opposite side of the Rowland circle of diameter R . The sensitivity advantage compared to a flat-crystal/collimator combination is the ratio of the beam-line divergence to the collimator divergence, and can exceed 100 for a high-resolution instrument. A compact and versatile example of this type of instrument is described in detail in chapter 6.

The related Johansson spectrometer²² (where the aberrations are reduced by pre-grinding the crystal to a cylindrical surface, which lies on the Rowland circle after bending) has not been found necessary for tokamak diagnostics, because the relatively large Rowland circle diameters used to date have kept the crystal f-number too low for the Johann aberrations to be significant.

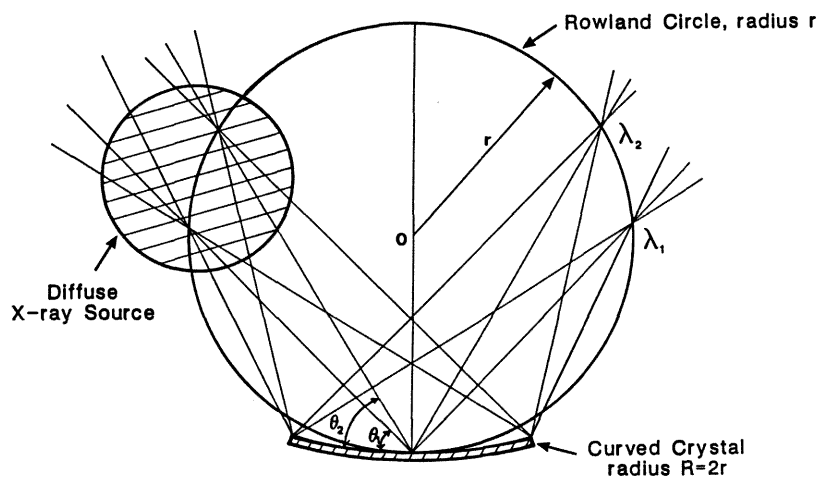


Fig.2.12 The Johann Spectrometer

Von Hamos

This configuration (fig.2.14) is similar to the De Broglie, except that the bandwidth is reduced by keeping the crystal flat in the plane of dispersion²³. The crystal is bent perpendicular to the plane of dispersion, resulting in vertical focusing which images a point source as a point on the detector. This can be used either to concentrate the intensity onto a narrow 1-D detector, or to spatially resolve the source onto a 2-D detector. Again, the global sensitivity is equal to that of a scanning flat crystal of the same projected area and covering the same Bragg angle range. The usable Bragg angle range is limited to about 2° by the angle subtended by the source or sight-tube. This is narrow for a survey instrument but usefully wider than can be achieved with most Johann spectrometers. High resolution must be achieved at the cost of sensitivity, by reducing the slit width. E Källne et al²⁴ have made extensive use of such an instrument on Alcatraz-C, and Alcatraz-C-Mod is being fitted with an array of about four similar instruments.

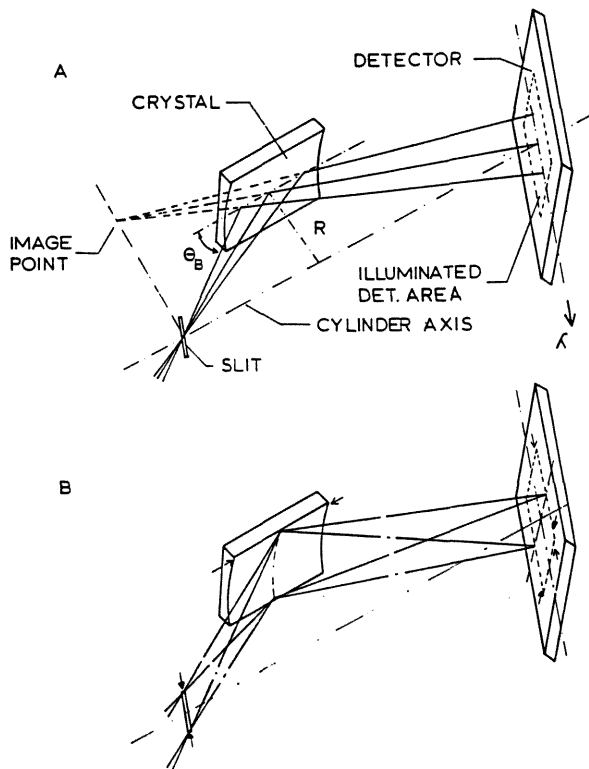


Fig.2.14 The Von Hamos spectrometer.

2.6 ABSOLUTE FLUX MEASUREMENTS

Any quantitative spectroscopy system must rely on calibration data, preferably of the individual components, and access to a calibration facility is essential. A two-axis diffractometer can be used to calibrate diffractors, filters, detectors and mirrors, and is an indispensable laboratory tool. A new two-axis diffractometer, incorporating recent technological developments, is under construction at the time of writing and is described in outline below. It is also useful to consider which instrument configuration would give us the most precise flux measurements of a plasma source.

A new two-axis diffractometer

The main aim of a two-axis diffractometer (fig.2.11a,b) is to measure the combined x-ray reflectivity of a pair of diffractors as a function of the angle between their lattice planes. This calls for different degrees of precision in the various motions that align the source, diffractors and detector. Broadly speaking, to locate a diffraction peak requires positioning at the level of one arc-minute, whereas to measure a diffraction profile requires a scan at the arc-second level. Traditionally, the motions have been provided by a combination of micrometer drives and worm-and-wheel drives, using stepping motors. The angles have been measured either by electro-optical encoders, or visually from optical graduated discs. It has been expensive to design, build and operate a high precision instrument. A major disadvantage of the configuration shown in figure 2.11a,b is that the choice of source and flexibility of the instrument are limited by the source being mounted to the "2 θ " drive of the first goniometer.

The new instrument (fig.2.11c,d) is an improvement on previous designs in that it takes advantage of state-of-the-art technology developed for robotics. Compact direct-drive servo-motors with closed-loop operation from built-in arc-second optical encoders have been used. These drives greatly simplify the design and operation of instruments that require precision rotary tables, and their mass production for industrial use has resulted a major cost saving compared to specialized systems available a few years ago²⁵.

A further improvement that follows from the new technology is that it is now possible to build a two-axis diffractometer that uses a fixed line of sight to the source instead of mounting the source to the "2- θ " drive of one turntable. This feature gives great freedom in the choice of source, with the instrument functioning either as a diffractometer (in the parallel non-dispersive mode, figure 2.11a) or as a spectrometer (in the anti-parallel dispersive mode, figure 2.11b).

Accurate plasma measurements

Some of the measures taken to improve sensitivity inevitably compromise the accuracy of the intensity calibration, and if each of the n elements in calibration has only a 5% uncertainty, the cumulative uncertainty of 0.95^n soon becomes large. A simple Bragg spectrometer with two pairs of slits and a "2 θ " scanning detector (fig.2.10) cannot be improved upon for the most accurate soft x-ray radiometry, because its principles of operation and data reduction are identical to the way that the crystal integrated reflectivity R_c is defined (eq.2.25). The three factors - geometry, absorption and diffractor reflectivity - would then limit the accuracy as follows.

Geometry

Perhaps surprisingly, measurement at the few percent level of the solid-angle.volume product of a large aperture instrument is one of the most difficult parts of its calibration.

A Soller collimator, although up to a hundred times more sensitive than a pair of slits, introduces uncertainties due to imperfections in the flatness of the foils and to grazing incidence reflections from their surfaces. Large-aperture beam-line and detector windows, with their necessary support-ribs, are another factor, and if the beam-line is used as part of the limiting aperture, as is almost always the case, the vignetting function can be difficult to derive with the required precision. The long stationary detector used for the Bragg rotor spectrometer, while allowing a high scan-speed for the crystal, has several extra calibration factors. These can be included but not without some additional uncertainty.

The ideal is to define completely the x-ray beam geometry by two pairs of slits, thus avoiding any interference from the sight-line, crystal or detector. It is possible to measure the four slit apertures and the distance between them to at least 1 part in 1000, giving an error in the geometry of not more than 0.5%.

Window transmission

The main uncertainty here is not the measurement of the transmission of a sample window, which should be done using the calibration facility as a monochromator, but ensuring repeatability between different samples, particularly if they are stretched polypropylene. The most accurate method is to remove the detector window after use, and measure the exact region illuminated by the optics, by which means we would expect to know the transmission at the relevant wavelength to better than 1%.

Diffraction

The reflection integral of a given diffractor sample can be measured¹² to about 3%, while the variability in different fresh samples from the same source is usually less than 5%.

Detector

The detector should be a simple single-wire gas proportional counter, with sufficient gas-depth to give a QDE of about 0.9. The main advantage of the high QDE, apart from the greater sensitivity, is that the high gas-absorption can be calculated much more accurately than if it were only, say, 0.1. The single wire gives the best energy resolution, and eliminates the possibility of counts being shared with, or lost to, adjacent anodes.

A " $\theta/2\theta$ " mechanism for the detector keeps its area as small as possible, thus reducing the background, and maintains normal incidence of the diffracted ray onto the detector window.

Pulse counting

It is necessary to operate at count-rates low enough to make dead-time and pulse pile-up negligible, and to store the detector energy spectrum as well as the wavelength spectrum. This enables selection of suitable angular (wavelength) and pulse-height (energy) limits for the integration of counts in the spectral line. With a few thousand counts in the line, and given low background, the accuracy of this measurement should be better than 3%.

Overall accuracy

Adding the expected errors quadratically gives a best expectation of about 4%. Such a technique would have rather low sensitivity for routine plasma monitoring, and would be best used as a reference against which to calibrate an instrument optimized for high sensitivity.

Calibration sources

An alternative to synthesizing the calibration from its individual elements is to use a calibration source. The most accurately known x-ray source at present is a synchrotron, whose spectrum may be calculated exactly from the beam energy and current, but whose geometry is unsuitable for testing large-aperture plasma-diagnostic instruments. Another possibility is to use an x-ray tube with an anode large enough to fill the instrument aperture, where the problem becomes one of calibrating the source. This returns to the problem of finding a radiometer with sufficient energy resolution to distinguish the x-ray line emission from the continuum, as discussed in section 2.3 above. At energies above a few keV, a solid-state detector has sufficient sensitivity

and energy resolution, but there is no suitable detector for the 100 eV to 1 keV range.

A large-area source with interchangeable anodes was built at IPP Garching²⁶ for this purpose, and was calibrated with a Ge-Li detector that had been calibrated on a synchrotron. At lower energies, corresponding to the L-lines of medium-Z metals such as Cr and Ni, the error bars are greater than should be achievable using the optimized Bragg spectrometer described above. In future it is hoped to improve the accuracy of the low-energy calibration of this source, so that large-aperture instruments can be calibrated directly, as well as by synthesis.

2.7 CONCLUSIONS

The theoretical and experimental techniques necessary to make accurate absolute flux and wavelength measurements in the soft x-ray band are well developed.

The Bragg spectrometer is very versatile, since it easily covers a wide spectral range, yet still has high monochromatic sensitivity when required. The relatively simple optical configuration is well suited to absolute flux measurements, and the quasi-parallel input beam means that close access to the plasma is not essential. The design of such an instrument, the development of a high-rate detector system, and the extension of the coverage to longer wavelengths, are discussed in chapters 3, 4 and 5 respectively.

The high sensitivity and crystal-limited resolving power of the Johann spectrometer have made it the standard choice for high-resolution measurements over a narrow band. The recent availability of CCD arrays with high spatial resolution have made it possible to design a new generation of compact Johann spectrometers, and such an instrument is described in chapter 6.

References

- ¹ B L Henke, AIP Conference Proceedings No. 75: Low Energy X-Ray Diagnostics. Eds. D T Attwood and B L Henke (1981).
- ² B L Henke et al, Atomic Data and Nucl. Data Tables 54/2 (Jul.1993) 181-343.
- ³ A Burek. Space Sci. Instrum. 2 (1976) 53-103.
- ⁴ A H Compton and S K Allison, "X-Rays in Theory and Experiment", Van Nostrand, New York, (1935).
- ⁵ R W James, The Optical Principles of the Diffraction of X-rays, Bell and sons, London (1948).
- ⁶ C G Darwin, Phil. Mag. 27, (1914) 315.
- ⁷ J A Prins, Zeit. f Physik, 63 (1930) 477.
- ⁸ P B Hirsch and G N Ramachandran, Acta Cryst. 3 (1950) 187.
- ⁹ R Hall, PhD Thesis, University of Leicester, (1980).
- ¹⁰ M Lewis, PhD Thesis, University of Leicester, (1981).
- ¹¹ R Willingale, PhD Thesis, University of Leicester (1979).
- ¹² K D Evans and B Leigh, Space Sci. Instrum. 2 (1976) 105-123.
- ¹³ M Lewis, P A Maksym, K D Evans. Astron. Astrophys. 87 (1980) 213-223.
- ¹⁴ R Hall, B Leigh, M Lewis, K D Evans. X-ray Spectrometry, 8 (1979) 19.
- ¹⁵ J A Bearden, X-Ray Wavelengths, U S Atomic Energy Commission, (1964).
- ¹⁶ J F McGrath Jr., Rev. Sci. Instrum. 39 (1968) 1036.
- ¹⁷ D L McKenzie, P B Landecker and J H Underwood, Space Sci. Instrum. 2 (1976) 125-139.
- ¹⁸ J S Thomsen, in X-ray Spectroscopy, ed. L A Azároff. McGraw-Hill (1974).
- ¹⁹ W L Bragg, Proc.Camb. Phil. Soc. 17 (1912) 43.
- ²⁰ M de Broglie, F A Lindeman. C R Acad Sci (Paris) 158 (1914) 944.
- ²¹ H H Johann, Z. Phys. 69 (1931) 185-206.
- ²² T Johansson, Ziet. f. Phys. 82 (1933) 507-528).
- ²³ L von Hamos, Ann d Physik, 17 (1933) 716.
- ²⁴ E Källne, J Källne, E S Marmar, J E Rice. Physica Scripta, 31 (1985) 551.
- ²⁵ R Barnsley, U Schumacher, et al, Rev. Sci. Instrum. 62(4) (1991) 889-98.
- ²⁶ H W Morsi, H Röhr, U Schumacher. Z. Naturforsch. 42A (1987) 1051.

3 A BRAGG ROTOR SPECTROMETER

3.1	Introduction	63
3.2	Optical design	68
3.3	Engineering design	70
3.4	Calibration	75
3.5	Results	81
3.6	Conclusion	83

*Have you heard of the wonderful one-hoss shay?
That was built in such a logical way,
It ran a hundred years to a day,
And then, of a sudden, it-*

*The Deacon's Masterpiece - The One Horse Shay
Oliver Wendell Holmes (1857)*

3.1 INTRODUCTION

The Bragg rotor spectrometer was originally designed as part of a study¹ for the JET tokamak. The aim was to provide a relatively simple monitor of all impurities, with wide spectral coverage and absolute calibration. The original version (Mk1) was first operated on the DITE tokamak at UKAEA Culham Laboratory, where it played a major role in several experiments described in this thesis. It was later operated on the Culham COMPASS tokamak, where the extended wavelength range was first demonstrated.

A Bragg spectrometer offers a simple means to cover a wide wavelength range with large dispersion, by recording the detector signal correlated with the rotation of a single flat crystal. By using slotted collimators and gas proportional counters, high throughput, large-aperture instruments with stable absolute sensitivity calibration can be built.

Count rates in the region of 10^7 s^{-1} can be expected in the strong lines, so that the Bragg angle can be scanned rapidly while retaining good counting statistics in each line. In view of this, and the relatively short discharge duration ($\sim 1\text{s}$) of medium-sized tokamaks, it is impractical to use a reciprocating crystal and scanning "20" detector as used in rocket, satellite and fluorescence analysis spectrometers. The crystal was therefore given the freedom to rotate continuously, while the detector was made stationary and of sufficient aperture to accept the full range of diffracted rays, a principle used previously by Von Goeller². Figure 3.1 shows a ray diagram of the basic instrument³, and a block diagram is shown in figure 3.2.

This chapter concentrates on the main features of the instrument, but to achieve an integrated design that could fully exploit the potential broad-band and high-sensitivity of a Bragg spectrometer, developments were required into high-rate proportional counters and long-wavelength diffractors. These are discussed in chapters 4 and 5 respectively.

Mk1 instrument

After the initially unsuccessful proposal for JET, the original instrument was built during 1984-5 for the Culham Laboratory DITE tokamak⁴ (Bundle-Diverter Neutral-beam-Injection Tokamak Experiment) and produced most of the the results presented in chapters 7, 8 and 9. It was equipped with a self-contained spatially-scanning vacuum chamber and beam line, and a stand-alone control and data acquisition system (SADA). When later operated on Culham COMPASS tokamak⁵ (COMPact ASSembly), its long wavelength coverage was extended to about 90 Å. In mid-1993 its mechanism and control system were upgraded to the same specification as the Mk2 instrument.

Table 3.1

Breakdown of terms in sensitivity equation (at $\sim 7.5 \text{ \AA}$)			
Term	Constraint	Optimum	
R_c : Crystal integrated reflectivity	PET (002)	2.10^{-4} rad	
ψ_x : Collimator acceptance angle in plane of dispersion	Resolving power	0.002 rad (1:500)	
ψ_y : Collimator acceptance angle perp. to plane of dispersion	Sight-tube f-number	~ 0.03 rad ($\sim 2^\circ$)	
h_x : Crystal/Collimator height	Spatial resolution	1-3 cm	
h_y : Crystal/Collimator width	Sight-tube clearance	5-10cm	
η_λ : Efficiency of windows and detector	Window technology	0.82 net	
	-Vacuum isolation window	1 μ m Polyprop.	0.97
	-Detector window	1 μ m Polyprop.	0.97
	-Detector window	500 \AA Al	0.97
	-Detector gas absorption		0.9
η_s : Transmission of structural elements	Mechanical design	0.58 net	
	-Beam Collimator slots		0.9
	-Anti-fluorescence collimator		0.95
	-Detector window support mesh		0.8
	-Detector window support frame		0.85

$$\text{Integrated count, } N = \epsilon_\lambda \Delta_z \frac{\psi_x \psi_y R_c h_x h_y \eta_s \eta_\lambda}{4 \pi \omega}$$

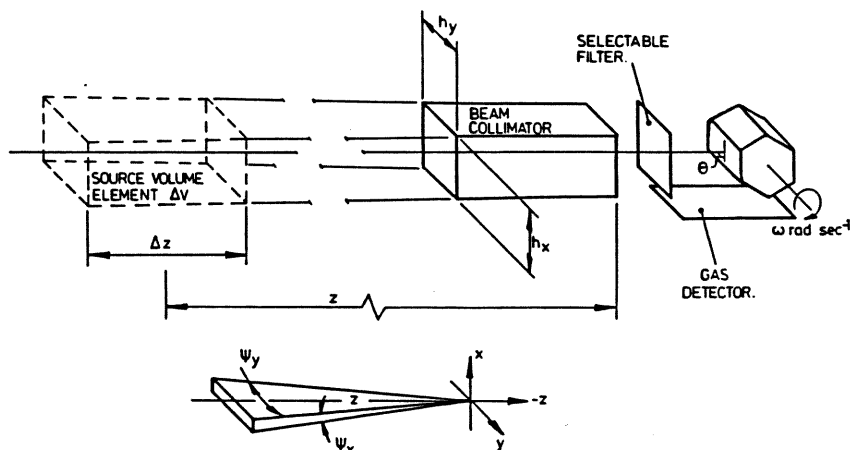


Fig.3.1 Ray diagram of a Bragg rotor spectrometer.

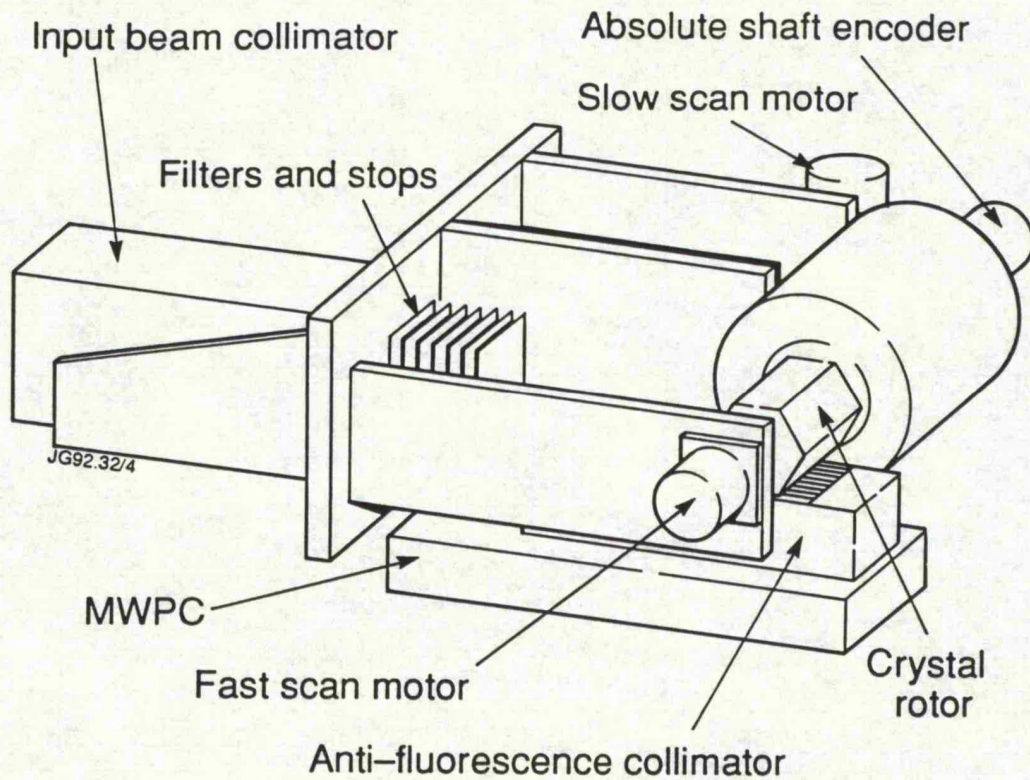


Fig.3.2 Schematic of the Mk1 Bragg rotor spectrometer.

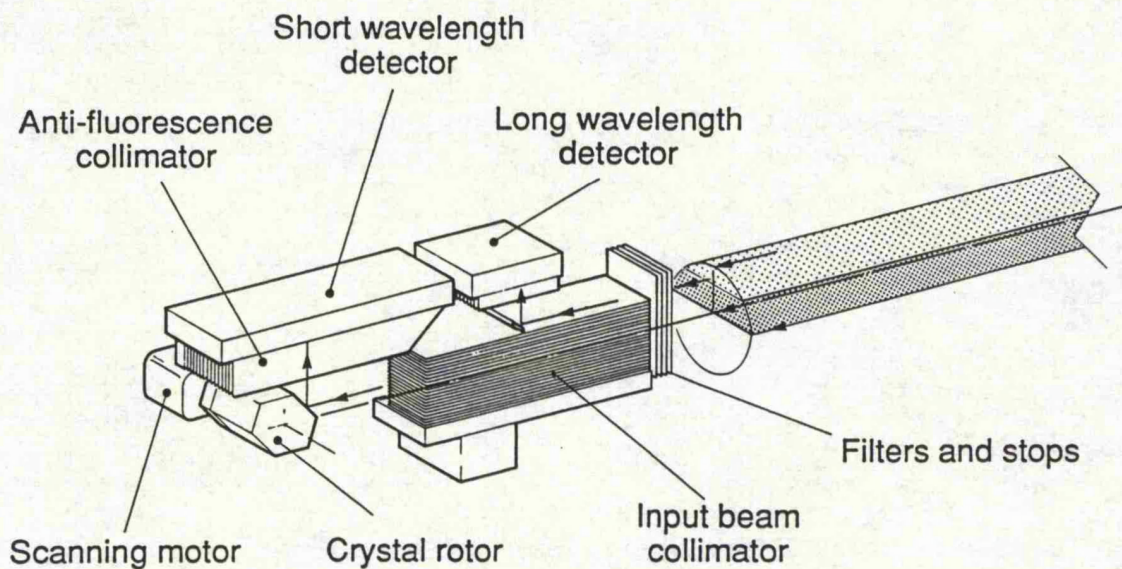


Fig.3.3 Schematic of the Mk2 Bragg rotor spectrometer, with parallel-channel monitor.

Mk2 instrument

With a history of successful results from DITE and COMPASS, and after yet more proposals, a Mk2 Bragg rotor spectrometer with an extended wavelength range (1 Å - 100 Å) was eventually developed in 1991 for the JET Tokamak. The extension to longer wavelengths was particularly useful at JET, where radiated power and fuel dilution were usually dominated by light impurities such as beryllium and carbon, whose H- and He-like transitions lie between about 25 Å and 100 Å. Although there is no fundamental necessity for all the impurities to be monitored by a single instrument, it is of great practical value to have a standardized set of data.

The instrument was built to share the sight-line and vacuum system of the active-phase double-crystal monochromator at JET (chapter 10), where the space available for the vacuum chamber was restricted, and the available aperture was a 50 mm diameter semi-circle (fig 3.3). This led to design compromises which have been remedied in the upgrade of the Mk1 instrument, which is more suited to general use on a circular sight-line (fig 3.4). The main improvement for the Mk2 instrument was the inclusion of a separate parallel-channel section for routine impurity monitoring, thereby freeing the main rotor for more specific spectroscopy, such as impurity injection studies.

In the light of experience with the Mk1 Bragg rotor spectrometer, and the grazing incidence instruments on JET, a design philosophy for the new instrument was arrived at, based on the type of data that was required by the interested parties. There was considerable conflict between the need for a complete and consistent set of data for all impurities on every discharge, and the need to set up the instrument in a monochromatic or narrow scan mode for specific experiments such as laser ablation of impurities. The three main design criteria for the Mk2 instrument can be summarized as follows.

- (a) Full coverage of the soft x-ray spectrum, to monitor a range of ionization stages of any possible impurity.
- (b) High monochromatic sensitivity, to monitor trace impurities and give good time resolution for the study of transient events such as impurity injection.
- (c) The best possible time resolution for representative lines of the few main impurities, combined with stable short-term and long-term sensitivity, for routine analysis of radiated power components.

These conflicting design aims were resolved by dividing the aperture into two closely integrated sections (fig 3.3), which could be operated independently.

Aims (a) and (b) were fulfilled by a hexagonal rotor that occupied about 70% of the 40 cm² aperture, and carried a selection of diffractors ranging from LiF (420) (2d = 1.8 Å) to a multilayer mirror (Ni-C 2d = 117 Å). Moderate

resolving power was provided by a 1:550 Soller collimator. A large area gas proportional counter (GPC) was fixed in position to cover a Bragg angle range from 20° to 75° . Each of the ten detector anodes was connected to an independent amplifier-discriminator chain, allowing count-rates up to 20 MHz to be processed. By scanning the diffractors sequentially, a large and continuous spectral range could be covered with a time resolution of about 300 ms. With the rotor kept stationary, a high monochromatic sensitivity was achieved, allowing a time resolution as short as 10 μ s.

Aim (c) was met by a smaller rotor or "paddle" that was mounted with a side-by-side array of four small diffractors. These reflected into a second GPC, which had eight anodes, connected in pairs to four parallel single channel analysers, each with its energy window set to suit the particular diffractor. The rotor was reciprocated over a relatively small Bragg angle range to give a time resolution of 20 ms for about 10 representative lines. The beamline provided a relatively coarse collimation of 1:150, which is suited to the line-widths of the multilayers and did not unnecessarily decrease the sensitivity.

Development work

Before completing the design of the detectors and the newly conceived parallel-channel monitor, valuable operating experience was gained with the prototype instrument on the COMPASS and JET tokamaks. The initial long-wavelength development was carried out first in the laboratory using a large area x-ray source, and later on the COMPASS tokamak at Culham Laboratory.

In May 1991 the original rotor, collimator and detector were installed on a temporary mount inside the chamber of the double-crystal active-phase monochromator on JET. The main reason for this was to assess the signal and noise of the instrument *in situ*, particularly above 25 Å where problems had been encountered on DITE. This would also allow time to modify the final design if found necessary. In fact, due to unreliability during 1991 of the grazing incidence instruments, this temporary installation itself became an essential impurity monitor on JET, albeit with rather limited time resolution.

During 1991 the new instrument was constructed, and the main rotor section was used to monitor the JET preliminary tritium experiment (Chapter 10). By the end of JET operations in February 1992, the instrument had been completed and its full capacity realized.

3.2 OPTICAL DESIGN

Crystal rotor

A study of the possible number of rotor faces showed that a six-sided rotor is a good compromise between covering a useful Bragg angle range and avoiding a dead period between crystal scans. Crystals pass every 60° allowing the detector to be apertured to cover Bragg angles from about 15° to 75° . There is little to be gained by increasing the coverage in either direction, since above 75° the remaining bandpass is very small, and below 15° the wavelength resolution is poor, and a crystal having a smaller lattice spacing would normally be available.

The next choice, that of crystal/collimator aperture (h_x, h_y), follows from table 3.1 where h_x is limited by the desired spatial resolution and h_y by the sight-tube aperture. Since the spatial resolution can always be controlled if necessary by aperture stops, the aperture was made to be $70 \times 70 \text{ mm}^2$ to match the 100 mm diameter sight-tube. The rotor hexagon was made 70 mm across its corners, fixing the maximum possible crystal size at $32 \times 70 \text{ mm}^2$, and dividing the available aperture into upper and lower halves, which could then be shared between different detectors and collimators.

Input collimators

Two existing collimators that had been flown on sounding rockets were used initially, one slotted (Soller) and made up from Mylar foils clamped between shims, the other having tungsten grids. The Soller collimator was of less than ideal aperture, but was adequate for commissioning and early results. A larger Soller collimator was later built to suit the available aperture.

Anti-fluorescence collimator

The siting of a large area detector close to the crystal introduces a strong noise source due to scattering of the input beam, mainly by fluorescence, at the crystal. To minimize this effect, it was found necessary to place a collimator, with an acceptance angle of 5° (perpendicular to the plane of dispersion), between the crystals and the detector. This collimator (fig 3.2) eliminates most of the scattered radiation, and could be reduced to about 2° before beginning to reduce the vertical divergence ψ_y , and therefore overall sensitivity (eq 3.2). The residual fluorescence-induced noise is the major noise source (unless there is high background due to runaway electrons) and this must be accepted in exchange for the ability to rotate the crystals at high speed. The more usual "2 θ " scanning detector would be about two orders of magnitude less sensitive to fluorescence, as it would be much smaller and could be collimated in two planes as opposed to one with the present design.

Filters and stops

Experience has shown the need for interchangeable filters and aperture stops to modify the sensitivity and spatial resolution, and to minimize the effect of crystal fluorescence and spurious orders of diffraction. To give the instrument greater versatility than would be offered by a simple filter wheel, it was decided to provide between four and six independently selectable filters.

Detector

The x-ray detector is a critical item, especially as a very wide energy range (100 eV - 10 keV) must be accommodated, with photon rates approaching 10^8 s^{-1} . Several types are usable at soft x-ray energies, but for this application a multiwire proportional counter (MWPC) was chosen (see chapter 4).

Briefly, the MWPC has several overriding advantages, particularly when positional resolution is not required. A MWPC detector can be built with large apertures at relatively low cost, and the QDE, which is limited mainly by the entrance window transmission, can approach unity. It also has a very useful energy resolution ($\Delta E/E$) of about 20%. Techniques for the construction of the chamber, anode array, window support system, and pulse processing electronics are well established, although for this project some further development was necessary to allow operation at count rates exceeding 10^7 s^{-1} .

In the context of the optical design, the main detector parameter to define is its aperture which, since it must be fixed, should be able to intercept the diffracted rays from a suitable range of Bragg angles. It follows that the detector width is governed simply by the crystal width ($h_y = 70 \text{ mm}$), while its length is determined by the maximum and minimum Bragg angles that it is required to intercept. As discussed above, a practical Bragg angle range is from 15° to 75° , implying a detector length of about 250 mm.

The detector used for the Bragg rotor spectrometer was a replica of the medium energy detector of the UK5 x-ray satellite. Originally it had a window area of $300 \times 56 \text{ mm}^2$ and a depth of 50 mm. Its aperture was close to the optimum, and although it required much modification during the course of the project, its availability at an early stage facilitated the development of the final system.

3.3 ENGINEERING DESIGN

Having defined the aperture and optical components, we can consider the engineering design of the spectrometer; that is, the support structure, and the various drives and mechanisms. All mechanisms were remotely controllable and were designed, where possible, not to require continuous energization.

Below is a summary of the main features of the Mk2 instrument.

Main rotor

- Collimator:* 75 μm Mylar foils on 0.45 mm pitch, $\delta\theta = 1:550$,
aperture 90 x 30 mm²
- Diffraction:* Six freely selectable diffractors, 90 x 34 mm²,
on hexagonal rotor, ranging from LiF (420) ($2d = 1.8 \text{ \AA}$)
to a multilayer mirror (Ni-C $2d = 117 \text{ \AA}$).
- Detector:* 10 identical anodes, 25 μm dia. l 200 x w 9 x d 20 mm³.
- Scan modes:* Programmable sequence to combine continuous rotation,
reciprocation over an arbitrary angle range, and monochromatic
pauses during a 25 s discharge.

Parallel-channel monitor

- Collimator:* Provided by beam-line, 1:150
- Diffraction:* 4 diffractors side by side, 16 x 25 mm², on reciprocating mount
to give representative lines of main impurities.
- Detector:* 8 anodes, 25 μm dia. l 100 x w 8 mm².
six with 4 mm gas depth for low energy, two with 25 mm depth.
- Scan modes:* Full Bragg angle scan ~100 ms, Line-scan ~10 ms,
Monochromatic ~ 1 ms

Structure

The Mk1 instrument (fig 3.2) was based on a vertical plate, with the collimator assembly mounted to one side, and the crystal drives, filters, and detector to the other. The unit could be assembled and aligned on the bench before being mounted to a bulkhead in the vacuum chamber.

In the Mk2 instrument (fig 3.3) all the components were mounted to a base-plate which was placed in the vacuum chamber from above, and rests on kinematic mounts. The upgraded Mk1 (fig 3.4) employs all the improvements of the Mk2, but with the aperture centred on a 100 mm diameter circle rather than a semicircle.

Rotor drives

The requirement was to spin the rotor at several revolutions per second in survey mode, to scan with a step size of a few arcsec, (small compared with the instrument line width of about 3 arcmin), and to lock the rotor within one

encoder division (2.6 arcmin) in monochromatic mode. At the time of the original design, it was difficult to fulfil these requirements with a single motor and gear combination, and so it was decided that the fast and slow drives would be performed by separate "spin" and "scan" motors whose action was selected by a clutch mechanism (fig. 3.2). The MkII version uses newly available 50 000 step micro-stepping motor controllers to perform all scan functions with a single, direct drive, motor.

The use of a stepper motor for the spin motor provides much better starting characteristics than could be obtained with a synchronous motor of similar size, and allows easy variation of the rotor scan speed. Also the phasing of the crystal scans can be synchronized over a long series of plasma discharges.

Rotary encoders

Following Leicester University sounding-rocket practice, the MkI instrument was fitted with an optical absolute rotary encoder, on the grounds that measurement of the Bragg angle is too important to trust to the counting of pulses sent to a stepper motor, or even to the counting of pulses from an incremental encoder. However, recent experience has shown that microstepping motor controllers, which can incorporate closed-loop feedback from an incremental encoder, are a reliable alternative to absolute encoders. (The safest way to operate with an incremental encoder is to reset to its reference marker before each discharge.)

Filter mechanism

It is common for filters to be mounted on a wheel, but for the chosen aperture of 70 x 70mm² even a wheel with only four apertures would take up considerable space, and compromise the layout of the other main components within the relatively cramped vacuum chamber. To save space, and to allow a more versatile filter system than would be offered by a filter wheel, the filters were made to be individually selectable.

In the MkI instrument, a novel filter mechanism operated three filters by a single cam, the arrangement of lobes being such that during a single revolution of the cam, all combinations of the filters were selected. The cams were driven by cheaply available geared miniature induction motors, with index and datum positions being indicated by micro-switches. There were two sets of three filters, which completed a full cycle in about two minutes, and did not need power once selected. This mechanism was designed with high vacuum in mind and could, if necessary, be actuated by a single rotary feed-through. The ability to use any combination of up to six filters proved very useful, and the total of six was adequate in practice.

In the Mk2 instrument, there are four filter mechanisms, each actuated by a separate geared DC motor.

Control system

The control and data acquisition for the Mk2 instrument is effected via CAMAC modules (Computer Automated Measurement And Control), as shown in figure 3.5. The two stepper motor controllers are programmed via a CAMAC serial link module (RS232), and triggered from a 24-bit digital input/output port, which also controls and reads the filter positions. Discriminated pulses from the signal processing chain, together with the encoder up/down pulses, are counted in a programmable multichannel scaler before being transferred to memory.

Vacuum system

The vacuum system is a major item in any x-ray spectroscopic system, usually accounting for about 25% of the cost of the project.

Diagnostic installations are naturally expected to have sight-line pressures that are at least as low as the torus base pressure of between 10^{-7} and 10^{-8} mbar. This is almost impossible to achieve when using a flow proportional counter with a thin polymer window. Because this type of spectrometer uses a large aperture instead of a slit, differential pumping of the sight line is not sufficient, and a vacuum isolation window must be used. In practice this has proved a thoroughly workable system, removing the need for UHV conditions in the main spectrometer chamber, and resulting in a significant cost saving and increased operational flexibility.

The self-contained vacuum system built for the Mk1 instrument consists of independently pumped sight-line and spectrometer chambers separated by a gate-valve and a $1\ \mu\text{m}$ polypropylene window. The window is protected by a by-pass valve that must be opened when the gate-valve is closed. The two valves must be controlled with great care, since a small pressure difference across the window will burst it. If this occurs, the spectrometer must be removed from the chamber to allow access to the window, and several hours of pumping will be necessary before a satisfactory sight-line pressure can be regained. After a few days under vacuum, the sight line pressure is usually well below 10^{-7} mbar and the spectrometer chamber is at about 10^{-5} mbar. An unsupported window has been tested at 1 mbar differential pressure without failure.

During nearly three years of operation on DITE, only one window failure occurred when, during the first radial profile scans, the backing line to the spectrometer chamber was disturbed. There was no degradation of the torus vacuum because the DITE sight-line valve was only open during a discharge, and was interlocked to the sight-line pressure.

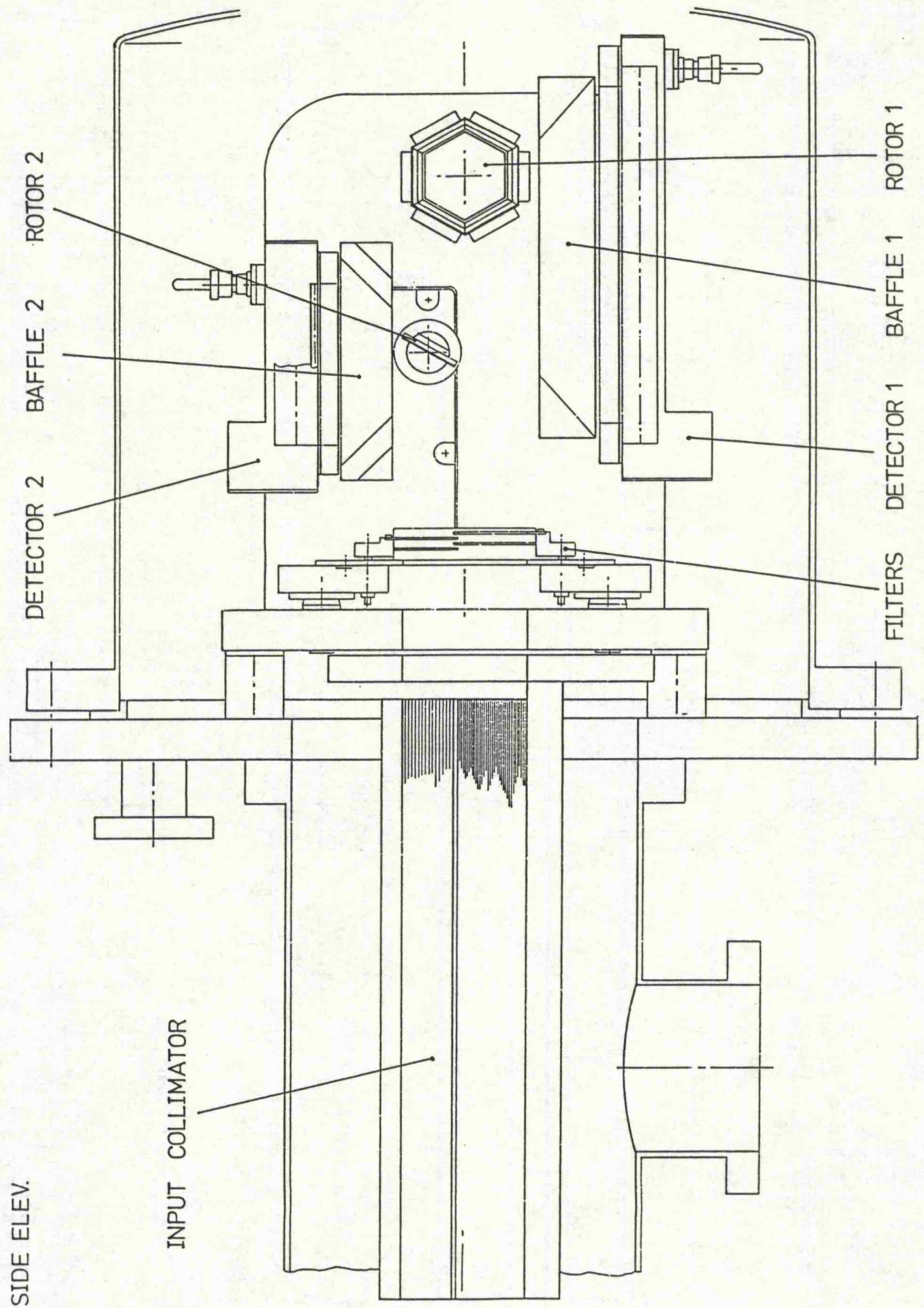


Fig.3.4 Side elevation of the upgraded Mk1 Bragg rotor spectrometer.

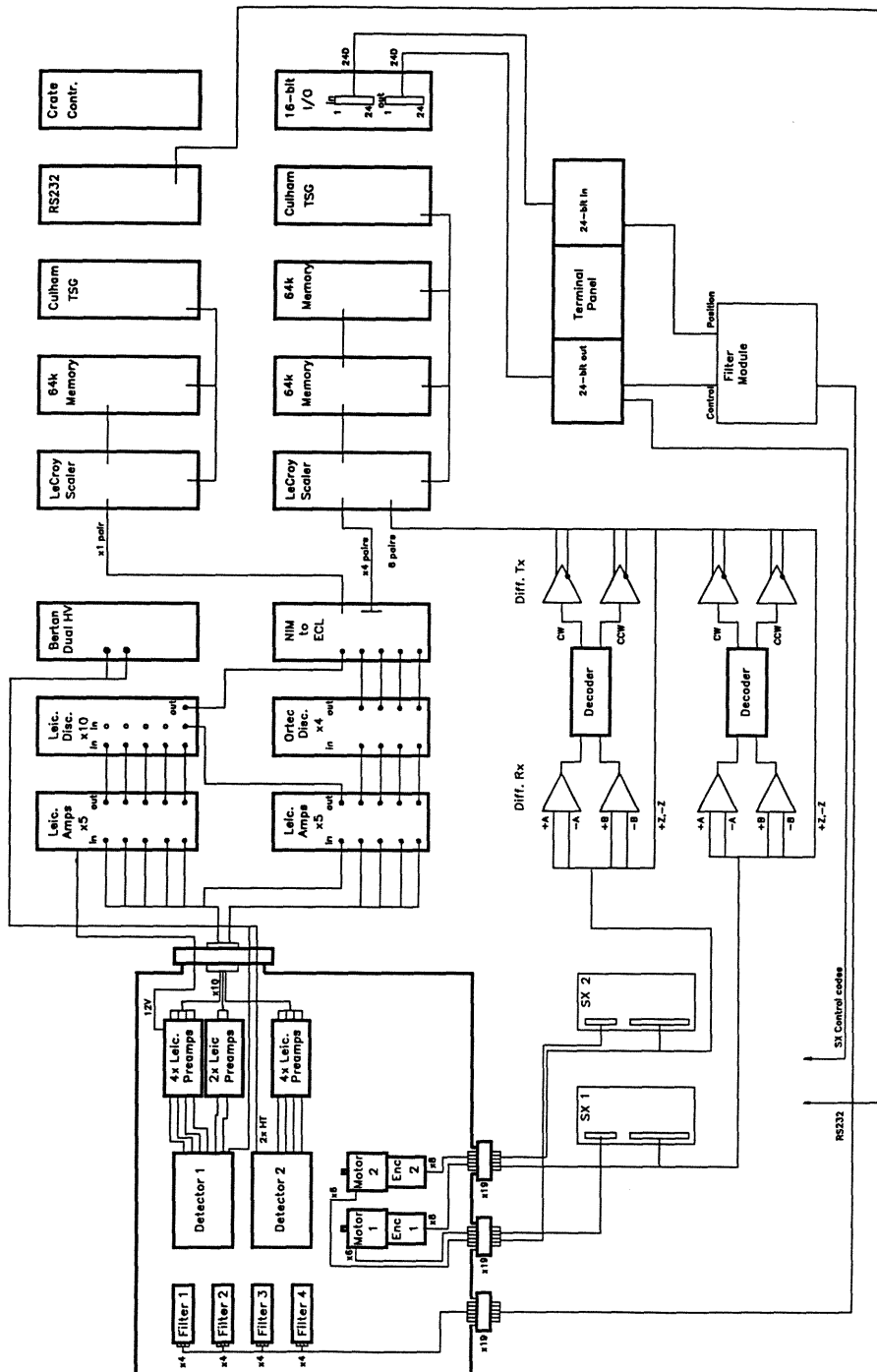


Fig.3.5 Block diagram of the control and data acquisition system.

3.4 CALIBRATION

This section discusses all the factors necessary to obtain $\epsilon_{(\lambda,t,r)}$, that is, the spectral, time and space resolved emissivity of the source. The features peculiar to a Bragg rotor spectrometer, and which affect the calibration, are the hexagonal rotor and the long stationary gas proportional counter. An additional feature of the Mk2 instrument was the coarse collimation of the monitor section, which was chosen to be limited to about 150 by the beamline divergence. This optimized the sensitivity of the multilayer diffractors without compromising their resolving power.

Wavelength calibration

The procedure for calibrating wavelengths was that used for aligning sounding rocket spectrometers (described in detail by Evans et al.⁶). The collimator collimator axis was aligned perpendicular to, and intersecting, the crystal rotational axis, setting the crystal at some known angle to the collimator axis (in this case 90°) and then recording the encoder angle to give a reference. The encoder reading corresponding to a Bragg angle of 90° was measured for each of the six crystals because although they are nominally at 60° intervals there is no independent fine adjustment for each crystal. With the Soller collimator, the 90° position was found by shining a tungsten lamp down the collimator onto the crystal and observing the maximum reflection back through the collimator as the crystal was rotated. An average of ten such readings gave the 90° position accurate to one encoder division (2.6 arcmin.).

Resolving power

The resolving power $\lambda/\delta\lambda$ is derived by differentiating the Bragg relation

$$\lambda/\delta\lambda = \tan \theta / \delta\theta \quad (3.1)$$

where $\delta\theta$ is the instrumental line-width, determined by the convolution of the collimator and diffractor line-spread functions. Below 25 Å this is usually dominated by the collimator, and above 25 Å by the diffractor.

Sensitivity

As discussed in chapter 2, the photon flux is best measured by the integrated count method where the crystal is rotated at angular velocity ω (rad/s), and where the integrated count N is given by

$$N = \epsilon_{\lambda} \Delta_z \frac{\psi_x \psi_y}{4\pi} \frac{R_c}{\omega} h_x h_y \eta_s \eta_{\lambda} \quad (3.2)$$

where ϵ_λ (ph . cm⁻² . s⁻¹) is the plasma emissivity, Δz (cm) is the effective plasma column depth. The other terms are as listed in table 3.1, which also shows the impact on sensitivity of various other constraints. Grouping together the terms that are constant or can be calibrated, we can write

$$I_\lambda = \epsilon_\lambda \Delta z = \frac{N \omega}{C_\lambda} \quad (\text{ph.cm}^{-2}.\text{s}^{-1}) \quad (3.3)$$

where C_λ (count.rad.cm².ph⁻¹) is defined as the instrument calibration function. An example of C_λ for a PET crystal is shown in figure 3.7.

As discussed in chapter 2, the critical term in the calibration is the crystal reflection integral R_c , while the other terms may be relatively simply calibrated or calculated.

Sometimes it is necessary to measure the photon flux from the peak count rate in a line, as for example with monochromatic data. This is an inferior method because the peak intensity can be dependent on the source line-shape, whereas the line integral is conserved. However, this is not a serious problem where the line profile is dominated by the instrument.

Using the same calibration function C_λ , we may write

$$I_\lambda = \frac{\dot{N} P_\lambda}{C_\lambda} \quad (3.4)$$

where \dot{N} is the peak count rate in a line and P_λ (radian) is a line profile factor that relates the peak to the integral of the line, and which must be determined empirically for each wavelength-collimator-crystal combination.

The derivation of C_λ from the terms in eq. 3.2 is now discussed.

Bragg reflection integral (R_c)

Where possible, experimental measurements of reflection integrals have been used, as discussed chapter 2.

Collimator acceptance angles (ψ_x, ψ_y)

The Soller collimator acceptance angle $\psi_x = 0.0026$ rad (6.9 arcmin.) in the plane of dispersion was defined by the ratio of slot spacing to collimator length (0.4 mm / 200 mm). The angle $\psi_y = 0.021$ rad (1.2°) was defined by the angle subtended at the crystal by the sight-tube (62 mm / 3000 mm for the DITE installation)

The gridded collimator had $\psi_x = \psi_y = 0.00083$ rad (2.85 arcmin.) defined by the ratio of grid aperture to collimator length (0.25 mm/300 mm), and so its sensitivity was about 50 times lower than that of the Soller collimator.

Transmission of structural elements (η_s)

Input Collimator: $T_{lc} = 0.9$ (slots of 0.05 mm Mylar on 0.45 mm pitch)

Detector Window Support Frame: $T_{df} = 0.75$ (2 mm ribs on 8 mm pitch)

Detector Window Support Mesh: $T_{dm} = 0.56$ at normal incidence

(25 μm stainless steel wires on 100 μm pitch. The correction for other angles of incidence is discussed below in the section on geometrical effects.)

Anti-fluorescence Collimator: $T_{ac} = 0.92$.

(0.5 mm Al sheets on 4 mm pitch, alternate sheets coinciding with the window support ribs.)

Filter and window transmissions (η_λ)

Ideally, samples of filters should be calibrated throughout the desired wavelength range using, for example, a two-axis diffractometer as a monochromator. Alternatively, filters have been calibrated in the Bragg rotor spectrometer using the plasma as a source, and relying on the repeatability of a suitable series of discharges to compare the spectrum with and without the filter. Measured transmissions for a range of wavelengths (taken from prominent lines) can then be plotted onto theoretical absorption curves to allow interpolation and extrapolation of the filter transmission function (chapter 2)

Geometrical Effects

This spectrometer has several features peculiar to its design which need to be accounted for in its calibration:

a) Change of optical axis with Bragg angle. A crystal mounted on a multi-faced rotor does not rotate about an axis that lies on its surface. While this does not affect the Bragg diffraction, it does cause the crystal to scan across the collimator aperture (fig. 3.1). This means that the effective centre line shifts by about 1 cm through the Bragg angle range, which can be significant for radial profiles.

b) Effect of long stationary detector. This feature, dictated by the need to rotate the crystals at high speed, means that the diffracted beam passes through the detector window at a range of incident angles. This affects the sensitivity in the following three ways.

i) There is a purely geometrical effect due to the finite thickness of the window support mesh ($2r = 25 \mu\text{m}$ wires on $2d = 100 \mu\text{m}$ pitch) as shown in figure 3.6, where

$$T = \frac{a'}{a} = \frac{d \cos (2 \theta_B - 90^\circ) - r}{d - r} \quad (3.5)$$

ii) The effective window thickness and gas depth (fig. 3.6) is given by

$$t' = \frac{t}{\cos (2 \theta_B - 90^\circ)} \quad (3.6)$$

and is most pronounced at long wavelengths and large Bragg angles (e.g. RbAP 23 Å, $\theta_B = 61.7^\circ$, where the window absorption is almost doubled).

iii) The possibility arises that the detector, which is permanently open to a wide range of Bragg angles, will be simultaneously sensitive to reflections from other sets of planes in the crystal. One such possibility is where the PET(002) planes with $2d = 8.742 \text{ \AA}$ are at a Bragg angle of 21.8° , while the (022) planes with $2d = 6.181 \text{ \AA}$ behave as an asymmetric cut and diffract at a Bragg angle of $45^\circ + 21.8^\circ = 66.8^\circ$. This has been observed when a line detected at a nominal Bragg angle of 21.8° was identified as Si XIII $1s^2-1s^3p$ (5.68 Å) from the (022) planes. The detector energy resolution is the ultimate safeguard against the misidentification of spurious reflections, and in practice these have not been a problem.

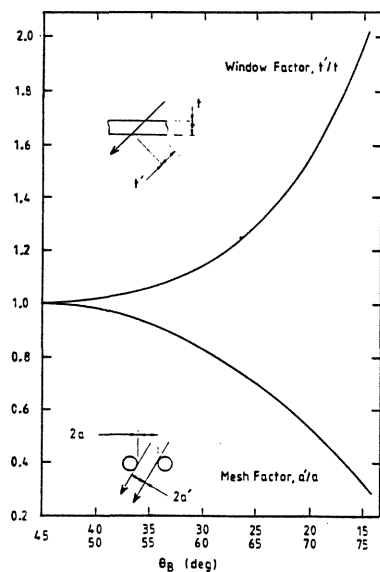


Fig.3.6 Effective depth of detector gas and window, and mesh transmission.

Spatial resolution

The spatial resolution Δr is defined by the projected crystal height, which is typically about 14 mm. To this must be added the collimator divergence projected to the plasma ($z \cdot \psi_x = 3000 \text{ mm} \times 0.002 = 6 \text{ mm}$ for the Soller collimator on DITE). Aperture stops can be used to reduce the projected crystal height and thus improve the spatial resolution, but with the Soller collimator, 10 mm would be the practical minimum.

Thickness and colour of stretched polypropylene

When stretching polypropylene film, a series of coloured interference fringes appears. The sequence of colours has been recorded to facilitate the stretching process and to help save material and time by giving a guide as to when to stop. The thickness was estimated by drawing a grid on the unstretched film, and measuring the area change after stretching, assuming the density to be constant. The angle of incidence of the light source (fluorescent room-light), and the viewing angle of the observer relative to the foil, were both about 45° . Several rings of magenta appear during stretching, but the pea-green only occurs once and is a good indication that the process is nearing its limit. The final thickness of about $0.5 \mu\text{m}$ agreed well with x-ray transmission measurements.

COLOUR	BOUNDARY	THICKNESS	COMMENT
		22.5 μm	Original thickness
Any		$\sim 1.7 \mu\text{m}$	First colours to appear
Scarlet Red	Pale		
Blue-Green	Dark		
Magenta			
Pea-Green		0.6 μm	Only occurs once
Deep Blue	Dark		
Deep Magenta			
Pale Magenta			
Buttercup Yellow			
Pale Blue		0.5 μm	Best to stop here

Detector quantum efficiency and energy resolution

The quantum detection efficiency (QDE) of a gas proportional counter is calculated using the measured window transmission and published absorption data for the fill-gas constituents so that

$$\eta_d = T_{\text{window}} (1 - T_{\text{gas}}) \quad (3.7)$$

Being a function of Bragg angle as well as wavelength, the detector QDE has not been evaluated separately but is included in the overall calibration such as that shown in figure 3.6.

The fraction of detector pulses that is counted depends on the discriminator upper and lower limits relative to the pulse height distribution, and this must be taken into account if a narrow pulse-height window is used. However, it is only for monochromatic work that the SCA might be narrow enough to exclude a significant fraction of the signal, as normally it is set quite wide (at least 0.5x and 1.5x the central voltage) to suit the energy range of the chosen wavelength scan.

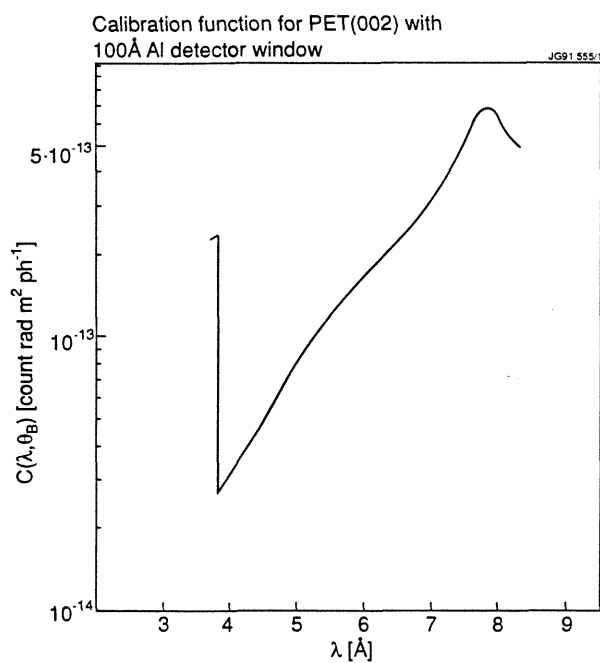


Fig.3.7 Full instrument calibration for a PET crystal.
(This is the sensitivity per anode; five were normally used)

3.5 RESULTS

Mk1 instrument

This instrument monitored impurities in the DITE Tokamak between 1985 and 1988, and was also used for several specific experiments described in chapters 7, 8 and 9. It was later installed on the COMPASS Tokamak, where the some of long-wavelength developments described in chapter 5 were carried out.

Mk2 instrument

Main rotor

The main rotor was operated almost continuously during 1991 operations at JET, including the preliminary tritium experiment (PTE), which is described in detail in chapter 10. The full survey spectrum is shown in figure 3.8,

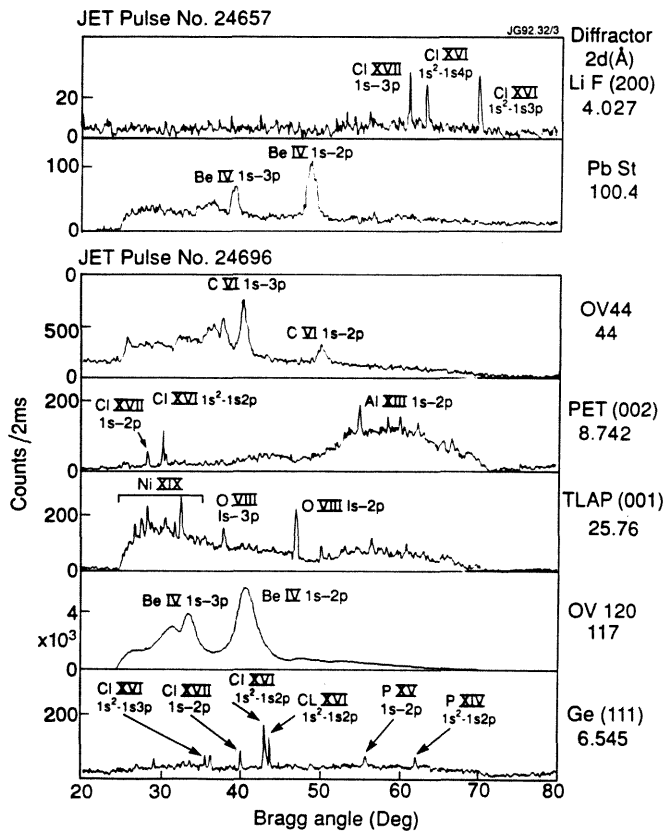


Fig.3.8 Typical survey spectra from JET, using a range of crystals and multilayers on the hexagonal rotor. Spectral coverage is almost complete between 2 Å and 100 Å, thereby monitoring all the main impurities.

Parallel-channel monitor

This new section of the instrument was commissioned in early 1992 and proved to be a valuable addition to the main rotor, allowing a time resolution of about 100 ms for a full Bragg angle scan (figs 3.8-9).

There is an unacceptably high background level from the Si (111) crystal, due to Si-K fluorescence at 7.13 Å (1.74 keV). It is impossible to remove this background completely, either by filtration or by pulse-height analysis, because it is so close in wavelength to the working range of the crystal ($2d=6.271$ Å). The problem is less serious, though still significant, for Ge-L fluorescence at 10.46 Å from a Ge (111) crystal ($2d=6.545$ Å). It is planned to overcome the problem by using Graphite (002) ($2d=6.708$ Å) because it has high reflectivity and its line-width is well matched to the coarse collimation of this section of the instrument.

In future, diffractors will be offset relative to each other in order to bring the main lines to the same rotor angle. This will allow a time resolution of about 10 ms for line scans and as short as 100 μ s in monochromatic mode, though in the latter case at the expense of a background measurement.

With some further development, this section of the instrument would be well suited to providing real-time impurity intensities, and could form an essential part of the diagnostic system for a long-pulse prototype reactor.

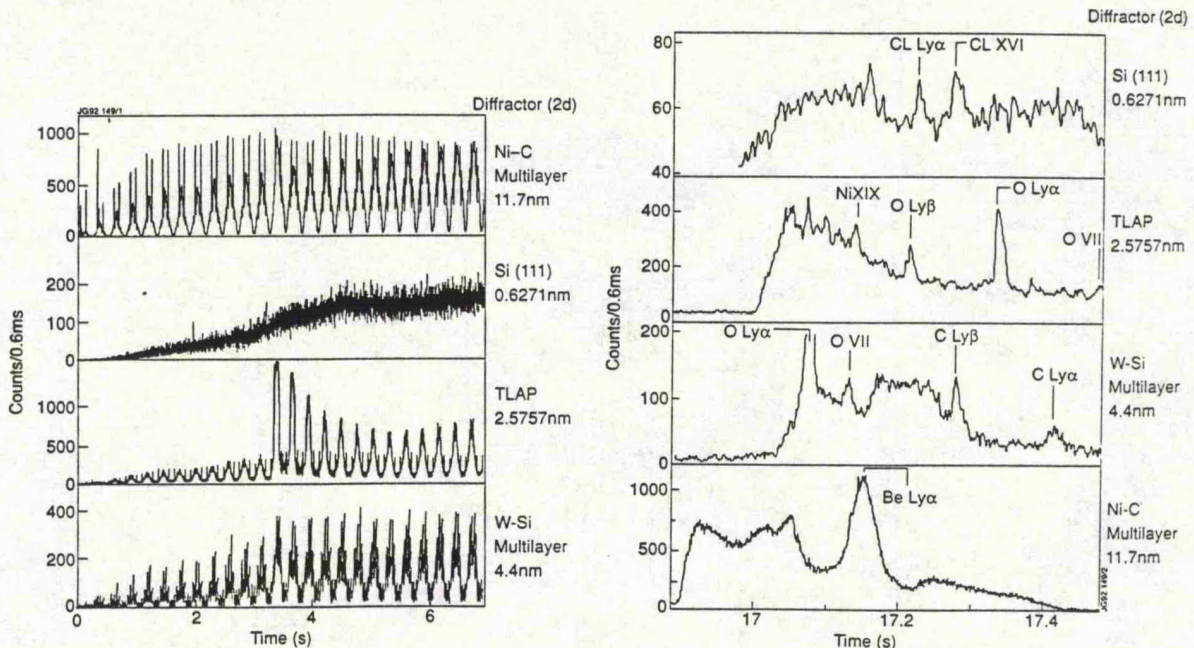


Fig 3.8 (left) Raw data from reciprocating scans of the parallel-channel monitor, for the first few seconds of a JET discharge.

Fig 3.9 (right) Detail of the spectra from the parallel-channel monitor, showing all the major impurities in JET.

The success of multilayers for monitoring C and Be was partly due to the low concentrations in JET of metals such as Cr, Fe and Ni, and the resulting lack of contamination from their strong transitions between 25 Å and 100 Å. For this reason, it should be fruitful to investigate the use of large organic crystals such as OAO, which have the potential for high resolution (see chapter 5).

3.6 CONCLUSION

This chapter has demonstrated the feasibility of using a combination of crystals and multilayers in a single instrument for routine monitoring of all the impurities in both large and small magnetically confined plasmas.

The improvement of the Mkl instrument to include the parallel-channel monitor provides a standardized set of impurity data from each discharge. This type of data will not be disturbed by the need to program the main rotor for more specific observations.

The main rotor is almost identical to the original 1982 proposal. Its easy access to a wide spectral range, with good monochromatic sensitivity and time resolution, has proved difficult to improve upon.

References

- ¹ R Barnsley, J E Bateman, K D Evans, M J Forrest, W G Griffin, N C Hawkes, N J Peacock. JET diagnostic design study 12-6. (1982).
- ² K W Hill et al, AIP Conf. Proc. 75, Low Energy X-ray Diagnostics, (1981) 8.
- ³ R Barnsley, K D Evans, N J Peacock, N C Hawkes, Rev. Sci. Instrum. 57(8) (1986) 2159.
- ⁴ J M Paul, Nucl. Fusion, 25 (1985) 1097.
- ⁵ R J Hayward et al, Proc. 15th symposium on fusion technology. Utrecht, Netherlands. Vol 1. North Holland. (1989).
- ⁶ K D Evans, R J Hutcheon, J P Pye, Space Sci Instrum. 2 (1976) 339-348.

4 A HIGH COUNT-RATE GAS PROPORTIONAL COUNTER

4.1	Introduction	85
4.2	Theory of gas proportional counters	85
4.3	Operation at high count-rates	95
4.4	Detector development	99
4.5	Mk1 detector system design	100
4.6	Performance and comparison with theory	104
4.7	Mk2 detector	107
4.8	Conclusion	109

Frank Barnsley (1911-), veteran of cats' whiskers and grid-bias batteries, is being x-rayed.

Ever-inquisitive patient:

"How many volts do you use on that x-ray set?"

Mildly indignant nurse:

"We don't use volts - we use kilovolts".

4.1 INTRODUCTION

A large fraction of the development work for the Bragg rotor spectrometer was devoted to the detector and pulse processing system. The combination of high source brightness and sensitive x-ray optics requires a detector capable of handling around 10^7 photon/s throughout an unusually large energy range of about 100 eV to 10 keV. It was decided to use a multiwire gas proportional counter (MWPC) if this performance could be achieved, since it has many favourable features. These include a high and predictable quantum detection efficiency (QDE) over a wide energy range, a very useful energy resolution, and relatively low cost of construction for large areas.

To achieve 10^7 count/s without serious pulse pile-up implies a pulse-pair resolution of around 10 ns, and while this is possible in principle with a single pulse processing chain, a system of multiple parallel channels was shown to be more practical.

Before arriving at the Mk1 system design, tests were made with an unmodified detector from an x-ray astronomy satellite experiment, combined with standard laboratory pulse processing electronics, complemented by a theoretical analysis of MWPC performance at high count rates. This work was followed by tests with a modified chamber and prototype fast electronics, resulting in the design and production of a system with up to ten parallel channels. Further development led to the Mk2 design, which is effectively an array of single-wire chambers.

4.2 THEORY OF GAS PROPORTIONAL COUNTERS

Much development of multiwire gas proportional counters has been performed by Charpak¹, and their theory and practice has been reviewed by Sauli². Their use in x-ray astronomy, which has many similarities with plasma diagnostics, has been reviewed by Fraser³, together with most other types of x-ray detector.

A gas proportional counter consists of a chamber, with a window through which photons enter before being absorbed in a suitable counting gas, causing ionization. The active gas volume is defined by the anode/cathode electric field such that the electrons and ions drift to the anode and cathode respectively. The anode is usually a wire of about 20 μm diameter, while the bias voltage of typically 2 kV allows the electrons to drift towards the anode without recombining or causing further ionization. When they reach the strong field within a few anode radii of the anode, a Townsend avalanche results, causing further ionization, and a multiplication of the original number of electrons. The resulting pulse of charge appears as a voltage across the capacitance of the anode/cathode and associated connections and is then

detected, amplified and shaped by a pulse processing amplifier.

The various steps in this process limit the performance of a multiwire proportional counter in different ways as discussed below:

- | | |
|-------------------------------|---|
| 1 Photon absorption | - Mainly photoionization for $E_x < 50$ keV. |
| 2 Ionization | - Creation of an initial electron cloud proportional to E_x . |
| 3 Electron Drift | - Initial electron cloud drifts most of the way to the anode, ideally without recombination or ionization. |
| 4 Multiplication | - Townsend avalanche in high field close to anode. Large multiplication of initial charge. |
| 5 Ion Drift | - Ions formed in avalanche drift to cathode, giving voltage pulse with fast initial rise, slower subsequent rise. |
| 6 Restoration of Bias Voltage | - Voltage drop due to pulse is restored from bias supply. |
| 7 Pulse Processing | - Simultaneous with ion drift. |

The relevant features of a MWPC and its associated pulse processing chain are shown in figures 4.1 and 4.2.

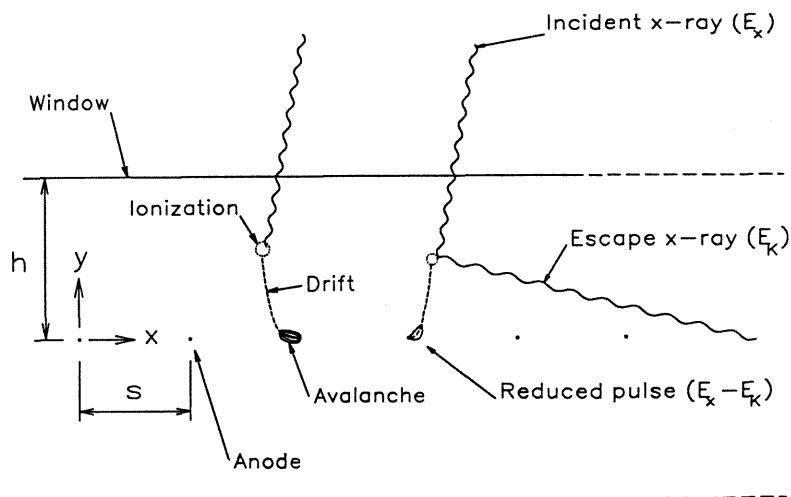


Fig.4.1 Cross section of a multiwire gas proportional counter, showing the dimensions and main events.

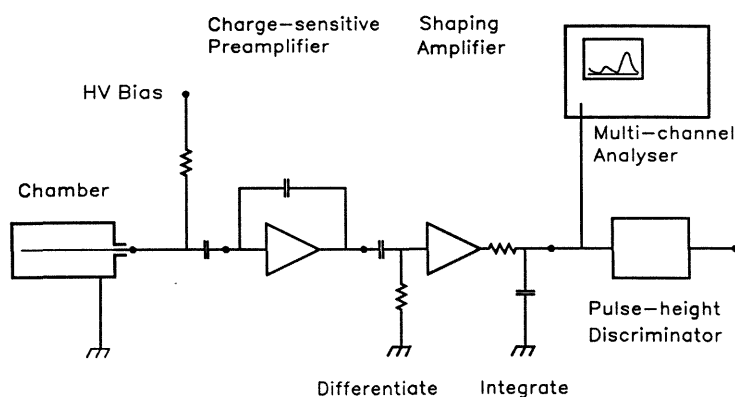


Fig.4.2 Pulse processing chain for a gas proportional counter.

Two parameters require definition:

a) For a planar multiwire chamber with inter-anode spacing s , and anode/cathode spacing h , the effective cathode radius r'_c is given by⁴

$$r'_c = 4h/\pi, \quad (\text{if } s \gg h) \quad (4.1)$$

or

$$r'_c = (s/2\pi) \exp(\pi h/s), \quad (\text{if } \exp(2\pi h/s) \gg 1). \quad (4.2)$$

b) A non-dimensional chamber parameter C is proportional to the anode/cathode capacitance, and simplifies most of the equations by eliminating $4\pi\epsilon_0$.

$$C = 1 / \ln (r'_c/r'_a)^2. \quad (4.3)$$

1 Photon absorption

For photon energies of interest for gas proportional counters ($100 \text{ eV} < E_x < 50 \text{ keV}$) absorption is mostly photoelectric, with a small contribution from the Compton effect, and can be calculated from the gas mass absorption coefficients (chapter 2).

2 Ionization

The initial photo-electron leaves a trail of N electron-ion pairs proportional to E_x the energy of the absorbed photon, so that

$$N = E_x/w \quad (4.4)$$

where w ($w = 26.2 \text{ eV}$ for Argon, 21.5 eV for Xenon) is the mean energy required to create an electron-ion pair. For typical x-ray energies, N lies in the range $20 < N < 500$, and the statistical variation in N sets a fundamental limit to the energy resolution achievable from a gas counter.

In practice the variance σ_N^2 in N is less than would be predicted by Poisson statistics, and can be described by

$$\sigma_N^2 = F N \quad (4.5)$$

where F , the Fano factor⁵, is typically about 0.2.

Some fraction of absorbed photons results in K or L-shell x-rays from the counter gas. The gas has low absorption at its own K-shell energy and many of these x-rays can escape from the detector without being absorbed. The resulting pulse is reduced by an amount equal to the K-shell energy, giving a secondary peak, the escape peak, in the pulse-height spectrum.

A mono-atomic gas is necessary for the main detector gas to ensure that the photon energy is converted into ionization rather than the dissociation which would also occur with a molecular gas.

Due to the absorption track of the initial photo-electron, the centroid of the initial charge-cloud is remote from the position of absorption of the photon by a distance

$$r \approx a \frac{E^n}{\rho} \quad (4.6)$$

where a (≈ 44) and n (≈ 1.7) are empirical constants, E is the photo-electron energy and ρ (g/l) is the gas density. This distance sets a fundamental limit to the positional resolution of a gas detector and for an 8 keV photon in Argon at atmospheric pressure ($\rho = 1.7$ g/l) we have $r \approx 0.9$ mm.

3 Electron drift

The electric field around the anode performs two distinct functions: firstly to cause the initial electron cloud to drift to the anode without recombining or causing further ionization, and secondly to produce an avalanche in the high-field region close to the anode. The electric field in a coaxial chamber is given by³

$$E = \frac{V_o / r}{\ln(r_c / r_a)} \quad (4.7)$$

The electric field in a MWPC is given by (with x and y defined in fig.4.1)

$$E = \frac{V_a}{h} K \left(\frac{\cosh(2\pi y/s) + \cos(2\pi x/s)}{\cosh(2\pi y/s) - \cos(2\pi x/s)} \right)^{1/2} \quad (4.8)$$

and where

$$K = \frac{1}{1 - \frac{s}{2\pi h} \ln \left(\frac{2\pi r_a}{s} \right)^2}$$

Knowledge of the electron drift process is particularly important when the best possible timing and positional information is required, and the process has been studied extensively theoretically⁶ and experimentally⁷. During the

drift, the presence of electronegative impurities such as oxygen (or deliberately added Freon) can capture electrons, causing an apparent gain reduction and a deterioration of the energy resolution (through the poorer statistics in the number of electrons that initiate the avalanche).

While drifting to the anode plane, the original charge-cloud expands by diffusion, the important parameter being D/μ , the ratio of electron diffusion D (cm²/s) to mobility μ (cm/Vs).

The variance σ , in the spreading charge-cloud is given by

$$\sigma = \sqrt{2 D t} = \sqrt{2 D \frac{d}{v}} = \sqrt{2 \frac{D}{\mu} \frac{d}{E}} \quad (4.9)$$

$$\sigma = \sqrt{2 \frac{(D/\mu)}{(E/p)} \frac{d}{p}} = \sqrt{2 \frac{d(\text{cm})}{p(\text{torr})}} \quad (4.10)$$

where E (V/cm) is the electric field in the drift region, p (torr) is the gas pressure, t (s) is the time to drift the distance d (cm) to the anode at drift velocity v (cm/s).

4 Multiplication

In the high-field region close to the anode the electrons are accelerated sufficiently to cause further ionization, leading to a Townsend avalanche which multiplies the original number of electrons by M , the gas gain.

A useful semi-empirical formula due to Zastawny⁸ for the gas-gain is

$$\ln M \approx 2 C V_a B \left(\ln \frac{2 C V_a}{S_o p r_a} - 1 + \frac{S_o p r_a}{2 C V_a} \right) \quad (4.11)$$

where for (Ar, 10% CH₄), $B \approx 0.03 \text{ V}^{-1}$, $S_o = 25 \text{ V.cm}^{-1}.\text{torr}^{-1}$, p : gas pressure (torr).

The fractional gain change with respect to anode voltage can be derived by differentiating eq.(4.11) to obtain

$$\frac{1}{M} \frac{dM}{dV} \approx 2 C B \ln \frac{2 C V_a}{S_o p r_a} \quad (4.12)$$

In a pure inert gas, the avalanche becomes a complete breakdown above a very low gain threshold ($M \approx 10$). This is due to UV photons, created by recombination, which release further electrons from the cathode. It can be prevented by the addition of a small proportion of a quench-gas (5 to 20% CH₄ or CO₂). The quench-gas molecules absorb UV photons, and allow operation at a gain of up to $M \sim 10^6$, which is adequate for most purposes.

The total charge q_o , per pulse is

$$q_o = N M e = \frac{E}{w} M e. \quad (4.13)$$

In addition to the statistical variance in N , a statistical variance occurs in M , resulting in a further uncertainty in the energy of the absorbed photon, and a lower limit to the achievable energy resolution $\Delta E/E$ of⁹

$$\frac{\Delta E}{E} \approx \frac{0.43 w}{\sqrt{E}} \text{ (eV)} \quad (4.14)$$

This is about 14% at 6 keV for Argon, which is adequate to give a very useful degree of background rejection and allows discrimination between different diffraction orders from crystal spectrometers.

Gas-gain / anode-voltage characteristic

The gas-gain as a function of anode bias voltage for a proportional counter is shown in figure 4.3. Below a threshold voltage the gain is negligible, after which it rises approximately exponentially according to eq (4.11). At higher voltages, depending on the gas mixture, there may be a partially saturated region where the gain is almost independent of V_a or the chamber may pass directly toward the Geiger region.

In the saturated region and beyond, the avalanche size becomes independent of the size of the initial electron cloud, and proportionality of the output pulse with the energy of the absorbed photon is lost. In practice a proportional counter will not behave as a Geiger counter at high voltage, since the anode impedance is too low to quench the discharge.

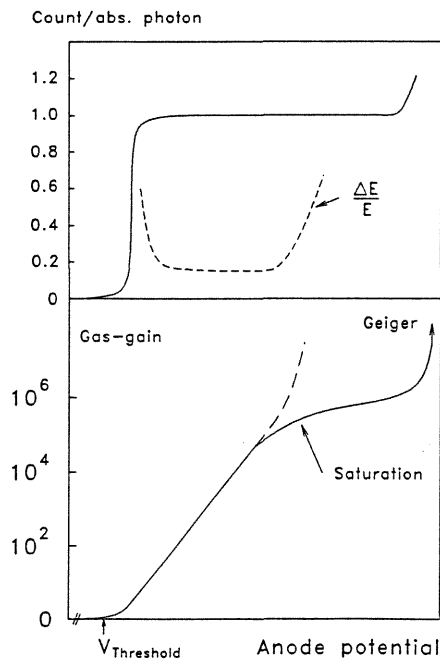


Fig.4.3 Typical gas-gain, energy resolution and counts per absorbed photon for a gas proportional counter.

5 Ion drift

The time history of the pulse as it appears across the anode/cathode capacitance is shown in figure 4.4 and is given by¹⁰

$$q = q_0 C \ln(1 + t/t_0) \quad (4.15)$$

where

$$t_0 = \frac{r_a^2}{4 \mu^+ C V} \quad (4.16)$$

and for a planar MWPC the ion collection time t is

$$t_c = \frac{hs/\pi - (s/\pi)^2 \ln 2}{2 \mu^+ C V_a} \quad (4.17)$$

These two characteristic times, t_0 and t_c , govern the maximum count rate that can be achieved from a gas proportional counter:

Rise-time. The time t_0 (≈ 1 ns typically) determines the rise-time of the pulse, and eq. 4.15 gives the fraction of the total charge that would be collected for a given pulse-shaping time-constant ($t = \tau_s$). For a typical chamber ($C = 0.05$, $t_0 = 1$ ns) and a fairly fast τ_s of 100 ns we get $q/q_0 = 0.25$, and for a very fast τ_s of 3 ns the charge collection efficiency is only 0.07. For $t \leq 1$ ns eq. 4.15 breaks down, because electron diffusion in the direction of drift causes a spread of about 1 ns in their time of arrival at the anode, and hence in the duration of the avalanche, which eq. 4.15 assumes to be instantaneous.

Ion collection time. The time t_c taken for the ions created by the avalanche near the anode to drift to the cathode is the slowest intrinsic time constant in the chamber and varies from a few μ s for a chamber designed for fast counting, to as long as 1 ms.

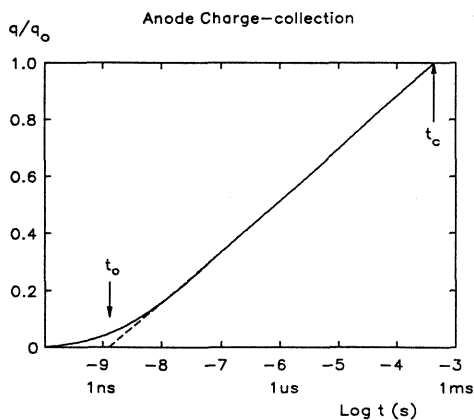


Fig.4.4 Anode pulse evolution for a proportional counter.

6 Restoration of bias voltage

The charge q_o causes an anode voltage drop q_o/C_a (≈ 1 mV typically) and this charge must be restored by the anode bias supply. An anode supply resistor R_a is necessary to give a time constant τ_a (for restoration of the anode voltage) that is much longer than the pulse-shaping time constant τ_s ; otherwise a significant fraction of q_o would be lost to the anode bias circuit. On the other hand τ_s must be short enough to re-supply the anode without causing a significant drop in V_a (and hence a gain reduction) at the maximum count-rate.

This effect can be trivially countered, and it is always the gain reduction due to space-charge that limits the maximum count-rate

The total anode current, I_a at a count-rate N count/s is

$$I_a = N q_o \quad (4.18)$$

the anode time-constant, τ_a is

$$\tau_a = R_a C_a \quad (4.19)$$

and the anode voltage drop, ΔV_a is

$$\Delta V_a = I_a R_a = \frac{N q_o \tau_a}{C} \quad (4.20)$$

Putting $\tau_a = 10 \mu\text{s}$, $q_o = 1 \text{ pC}$, $N = 10^7 \text{ s}^{-1}$, $C_a = 30 \text{ pF}$, we get $\Delta V_a = 3.3 \text{ V}$ which is acceptable, and implies $R_a = 330 \text{ k}\Omega$, which is typical of what is used in practice.

The combination of the fast rise given by eq. 4.15 and slow fall eq. 4.19 results in the "long-tail pulse" that is characteristic of a gas proportional counter. This is shown in figure 4.5 together with the capacitively coupled (and therefore differentiated) image which appears on an adjacent anode in a multiwire chamber. This image causes problems when dealing with signal pulses over an energy range as great as 100:1 (or even 1000:1 if large noise pulses are included) since it can produce a count in an adjacent channel. This is one reason why the Mk2 detector was divided up into individual single-wire chambers, as discussed below.

7 Pulse processing

With reference to figure 4.2, the anode is maintained at a positive voltage V_a of about 2 kV relative to the cathode by an external bias supply via the anode resistor R_a . Pulses appear as a charge across the capacitance of the anode and its associated connections to the preamplifier. A high voltage capacitor isolates the anode from the input of a charge-sensitive preamplifier which converts the collected charge to a voltage across its feedback capacitor. This feedback capacitor defines the charge calibration of the system, for

example a value of 1 pF gives 1 V/pC.

The pulse is then fed to a shaping amplifier and differentiated with a time constant τ_d to remove the long tail, while saving as much as possible of the rise consistent with the required pulse process time. This pulse is then integrated with a time constant τ_i where usually $\tau_i = \tau_d = \tau_s$, the pulse shaping time constant. The resulting pulse is approximately Gaussian and has an amplitude proportional to its area, which represents the collected charge. These pulses can then either be sorted by upper-level and lower-level discriminators (ULD/LLD) or fed to a Multichannel analyzer (MCA) to display a pulse-height spectrum. Discriminated counts are in the form of digital pulses and are stored in a memory via a scaler.

The analog pulse has a duration of $2\tau_s$ approximately, and this defines the minimum time between two pulses - the pulse process time τ_p - that will still produce two counts

$$\tau_p = 2 \tau_s . \quad (4.21)$$

The 3 dB bandwidth Δf of the pulse is

$$\Delta f = 1 / 2 \tau_s \quad (4.22)$$

and this has major implications for the whole detector/amplifier system, since time-constants less than about 100 ns are in the radio frequency range, and require that the detector, interconnections, amplifiers and screening be designed accordingly.

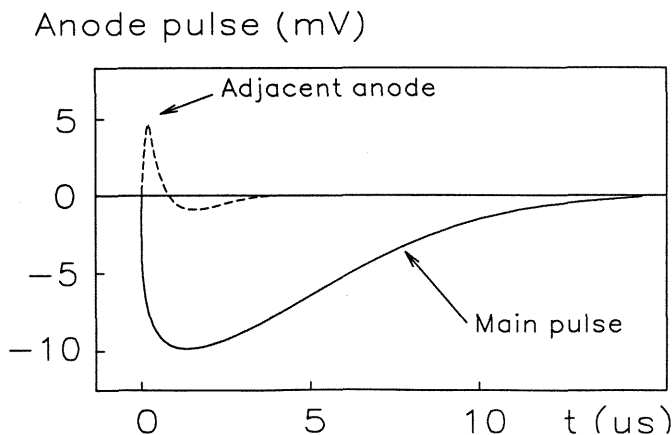


Fig.4.5 The "long-tail" anode pulse from a proportional counter, showing the capacitively coupled image on an adjacent anode of a multi-wire chamber

Stability of QDE with anode voltage

A precious feature of a well-behaved gas proportional counter is that the QDE is independent of the gas-gain, as shown in figure 4.3.

For this to be true, every electron cloud created by an absorbed photon must reach the anode and produce an avalanche. That is to say, there must be a one-to-one relationship between absorbed photons and counts, the critical factors being the electric field in the drift region and the electron drift properties in the counting gas. The magnitude of the gas-gain only affects the subsequent size of the pulse and should not influence the QDE (unless there is an unusually broad distribution in the number of electrons arriving at the avalanche region, so that increasing the gain raises more small pulses out of the noise). In order to achieve good energy resolution, there must be no net change in the number of electrons in the electron cloud during its drift to the anode; otherwise the pulse-height would depend on the distance from the anode of the position of absorption of the photon.

For normal counting gases such as P10 (90% Ar, 10% CH₄), the electron drift is stable for a wide range of drift fields (50 to 5000 Vcm⁻¹) and for most chambers this coincides with the range of anode voltages V_a necessary to give a gas-gain in the proportional region. The fact that changing V_a also changes the drift field is usually ignored, since the drift properties are a weak function of V_a . Hence the operating V_a is chosen primarily to give the required gas-gain and charge per pulse.

Electronegative gases

Electronegative gases such as Freon are sometimes added to multiwire chambers in order to prevent electrical breakdown at high voltages, but only at great cost to the stability of the gain, energy resolution and QDE. The Freon captures electrons during the drift, so that the charge reaching the anode becomes a function of the distance from the anode that the photon was absorbed, and also a function of the anode potential since it affects the drift velocity and electron attachment coefficient. The energy resolution is degraded by attrition of the drifting charge cloud, to the point where counts can be lost completely.

The effect of adding very small fractions of Freon to a single-wire flow counter¹¹ is shown in figure 4.6. Without Freon the count-rate is stable over a wide range of anode potential. The Freon allows a much higher anode voltage to be reached, with a consequently higher gas-gain and larger pulse, but there is no longer a region of stable QDE. At lower voltages counts are lost during the drift, while at higher voltages spurious counts are generated by single electrons since the gain has become saturated and independent of the size of the charge-cloud.

It is impossible to calculate the QDE of such a detector from the gas depth in the normal way, since it is now a strong function of the anode voltage, and it must be calibrated against a known detector. It need hardly be said that this is a pernicious effect to be avoided at all costs.

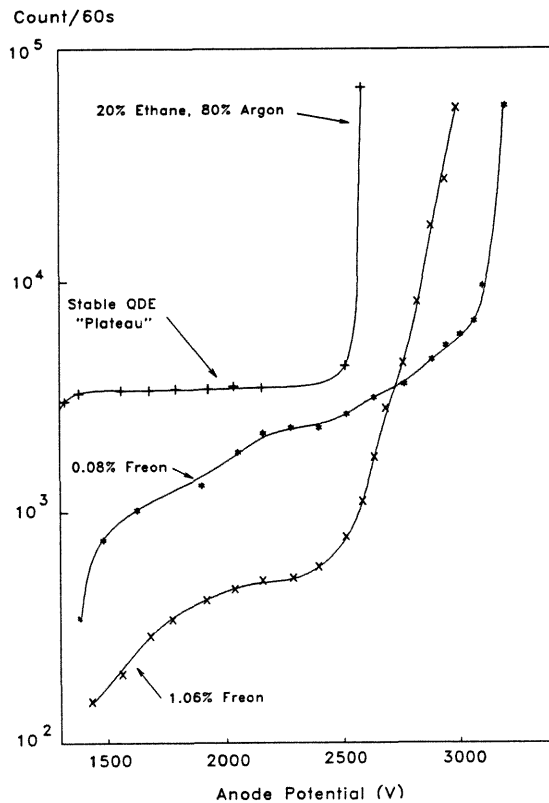


Fig.4.6 The effect of Freon on the QDE stability of a proportional counter. (Korgaonkar¹¹)

4.3 OPERATION AT HIGH COUNT-RATES

Two effects govern the maximum count-rate achievable from a proportional counter, namely the pulse-pair time-resolution, and the gain-reduction due to space-charge. For a particular chamber (and chosen acceptable levels of dead-time and gain-sag) the maximum achievable count-rate is determined ultimately by the noise level in the electronics. There is a minimum value of pulse process time τ_p , below which a higher count rate cannot be realized because of space-charge limitation. Indeed, further reduction in τ_p makes matters worse, since the charge collection becomes less efficient (eq. 4.15) and a bigger total charge q_0 is necessary to maintain the S/N ratio σ .

Theory

At high count rates, the space charge due to drifting ions can reduce the effective anode potential sufficiently to reduce significantly the gas-gain and thus the collected charge. If the gain reduction is greater than a few percent, severe corruption of recorded data can occur as the detector becomes non-linear or even saturates.

This problem has been studied theoretically and experimentally for co-axial proportional counters by Hendricks¹² and by Sipilä et al^{13,14}. This work has been extended to include multiwire chambers, theoretically by Mathieson¹⁵, and experimentally by Smith and Mathieson¹⁶.

Mathieson derived the following result in the general form

$$-\frac{\ln(q/q_0)}{q/q_0} = \frac{n_1 q_0}{I_m} \quad (4.23)$$

where (q/q_0) is the fraction of the low-count-rate charge q_0 , collected at specific count rate n_1 (ct s⁻¹.m⁻¹) per anode wire, and I_m (Am⁻¹) is a characteristic current for the chamber. For the case of a MWPC anode where the irradiation length is large compared with h , then

$$I_m = \left(\frac{R_m}{M} \cdot \frac{dM}{dV_a} \right)^{-1} \quad (4.24)$$

where

$$R_m = \frac{h^2}{2 \mu^+ V_a C_1} \quad (4.25)$$

and where

$$C_1 = 4\pi \epsilon_0 C \quad (4.26)$$

is the anode capacity per unit length.

For a coaxial chamber, the equivalent expression to eq.4.26 becomes

$$R_c = \frac{r_c^2}{4 \mu^+ V_a C_1} \quad (4.27)$$

The lower value of R_c compared to R_m (due to the factor 4 in the denominator) is partly offset by the need for a lower V_a in a coaxial chamber. However, in a rectangular single-wire chamber (which approximates a coaxial chamber), the effective cathode radius is dominated by the smaller dimension. Thus the gas absorption depth is not as constrained by the trade-off with ion drift time as in a multiwire chamber.

The reduced charge q/q_0 is shown plotted against the normalized count-rate nq_0/I_m in figure 4.7. Here the critical parameter is not just the count-rate n_1 , but the chamber current, which is the product $n_1 \cdot q_0$ of count-rate and charge per pulse. To maximize the count-rate capacity of a

given detector it is therefore important to minimize q_o , which is in turn ultimately limited by q_n the equivalent noise-charge in the pulse processing system.

It is clear from eqs.4.21 and 4.27 that since $\mu + V_a C_i$ is approximately constant for a given gas and gas-gain, the count-rate capacity is limited primarily through h^2 or r_c^2 . This implies that h or r_c should be minimized, consistent with providing sufficient photon absorption at the energy of interest. There is a lot to be gained by increasing the gas density, either by using a higher pressure or a denser gas, since it allows a corresponding reduction in h .

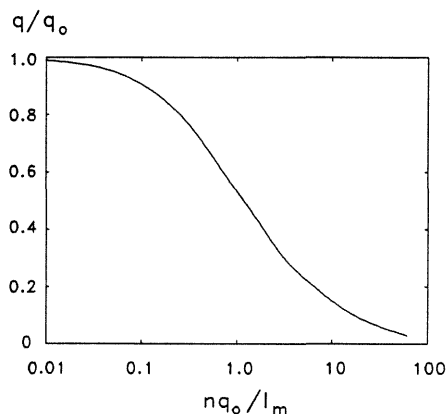


Fig.4.7 Reduced charge q/q_o as a function of normalized count-rate.

Parallel pulse processing channels

When aiming for high count-rate capacity, there is a clear electronic signal-to-noise advantage in using several signal channels in parallel, and three distinct factors contribute to this:

a) Sharing the capacitive loading of many anodes between several channels should reduce the equivalent noise charge q_n per channel in proportion to the number of anodes. In practice, due to other capacitances associated with the detector body and preamp leads, the improvement will not be so great.

b) Sharing the count-rate allows longer pulse shaping time-constants and hence more efficient charge-collection. For example, the use of ten parallel channels would allow a pulse shaping time-constant of 100 ns, compared with 10 ns for a single channel. This would more than double the charge collection efficiency given by eq.4.15, and allow a proportional reduction in the necessary gas-gain.

c) The reduction in bandwidth, resulting from the longer pulse-process time, is in proportion to the number of channels. This further reduces the noise, in proportion to the square-root of the number of channels.

These three effects allow the detector gas-gain to be reduced at least in proportion to the number of channels, while still maintaining the same signal-to-noise ratio, with a corresponding increase in the count-rate capacity for a given chamber current.

Count-rate summing

There are two ways of combining the counts from multiple channels: either hard-wired in real-time or by storing all the outputs in separate memory channels.

Real-time addition by means of an OR-gate gives automatic coincidence discrimination against multiple time-correlated counts. These can arise from either signal or noise events which may produce pulses on more than one anode. A signal photon can produce multiple pulses either by division of the drifting charge-cloud between adjacent anodes, or by the escape x-ray being absorbed over a different anode from the primary photon, or both. (The $1/e$ absorption length for an Ar-K x-ray in Ar at 1 atm. is about 3.5cm).

If the discriminators are set to a fairly wide energy range for broad band surveys, these multiple pulses can easily produce discriminated pulses in more than one channel, but still only give rise to a single count from the OR-gate, which clearly can only produce one count at a time. The same argument applies to background-induced events, some of which will lead to pulses in several channels (particles can leave a trail of ionization through the chamber).

Multiple counts due to signal photons will corrupt the sensitivity calibration, and multiple counts for background events will degrade the signal-to-background ratio. It is thus theoretically preferable to add the channels in real-time as opposed to storing the multiple-channel outputs separately. In practice there will also be a saving in memory space.

Pulses due to background radiation, even though most may be rejected, still have to be processed by the electronics and cleared through the chamber, contributing to dead-time and gain-sag. Thus the higher the count-rate capacity, the higher will be the tolerable background-count level and in some circumstances this may be critical.

4.4 DETECTOR SYSTEM DEVELOPMENT

In view of the above arguments relating to multiple-channel operation, it was decided to build a 10-channel preamp-amp-discriminator system with between 20 ns and 50 ns pulse-shaping, and with pulse addition by a fast OR-gate which would deliver 10ns pulses to a 100 MHz scaler and memory.

Early experience on the DITE Tokamak

The MWPC used for the Bragg rotor spectrometer was a replica of the medium energy detector for the UK5 x-ray astronomy satellite, and had an aperture of 56 x 300 mm². The original honeycomb collimator and beryllium window were replaced by a thin polymer window supported by a stainless steel mesh and aluminium grid (fig. 4.8). Originally, the full chamber depth of 5 cm was retained and two anodes were fitted, connected in parallel to a single pre-amplifier, Ortec 410 research amplifier and Canberra single-channel analyzer. This system was useful for commissioning and diagnosis of the signal and background radiation, and quickly led to the first results, and thence to a design for the final system.

Two sources of unwanted radiation both proved much larger than had been expected, and required careful attention to minimize their effects. These were hard x-ray background, and crystal fluorescence.

Hard x-ray background

Under most DITE operating conditions, there was a background noise count correlated with the readings on the DITE radiation monitors. This radiation was attributed to hard x-rays, generated by runaway electrons striking some part of the torus, probably the limiter. During conditions of only moderate runaway-induced background, the detector was paralyzed by events due to this background. This was not only because of the count-rate in the background, but also because many of the pulses were equivalent to energies above 200 keV, saturating the pulse-shaping amplifier for several μ s. Since these noise pulses deposited a charge equivalent to about 100 signal pulses, they also caused a large gain reduction due to space-charge, an effect magnified by the modest ion collection time of the rather large original chamber.

The solution to this problem was to make the chamber as shallow as possible consistent with adequate absorption of the signal. This minimized the sensitivity to background radiation (which can be expected to be a volume effect) and also reduced the charge-per-pulse of background events. The reduced gas depth also reduced the ion collection time and improved the count-rate capacity of the chamber as predicted by the theory of section 4.3. For the pulse-processing electronics, part of the pre-amplifier and amplifier

specification was the provision of a wide dynamic range so that noise pulses with amplitudes many times the signal pulse would not saturate the system and lead to an increase in dead-time. In addition, lead (Pb) shielding blocks and bags of lead shot were placed around the detector, both inside and outside the vacuum chamber.

Crystal fluorescence

As discussed in chapter 3.2, the siting of a large area detector close to the crystal results in a high sensitivity to scattered radiation, chiefly fluorescence of the crystal. This effect was reduced optically, though not completely eliminated, by placing an anti-fluorescence collimator between the crystal and detector. Further rejection of fluorescence-induced noise is provided by the energy resolution of the detector which, in many cases, allows almost complete discrimination against fluorescence. The count-rate due to fluorescence is greater when broad-band scans are performed, because the discriminators must be set correspondingly wider, but in practice this has not proved to be a problem.

4.5 Mk1 DETECTOR SYSTEM DESIGN

The above experience of making simple modifications to an existing detector (reducing the effective chamber depth) and using standard electronics (adding some resistive feedback to a standard charge-sensitive pre-amplifier to differentiate the pulse and reduce pile-up, and operating with 0.1 μ s shaping) showed that successful operation could be achieved with a gas proportional counter. Predictions based on this initial experience and on the foregoing analysis of count-rate maximization suggested that it was possible to build a MWPC detector system with good sensitivity, count-rate capacity and background rejection. In view of this it was decided to build an optimized MWPC system rather than a micro-channel electron multiplier (MCEM) system proposed originally.

An apparent advantage of the MCEM at the early design stage was its better vacuum compatibility compared to a MWPC with thin polymer window. However, experience showed that leakage from the MWPC into the spectrometer chamber could reliably be isolated from the beam-line by a 1 μ m polypropylene vacuum isolation window.

Detector chamber

The main choices to be made for an improved detector were the gas absorption depth (2h), and the anode spacing (s).

It is difficult to design a single chamber with a high efficiency throughout the range between 1 Å and 100 Å (≈ 100 eV to ≈ 10 keV), particularly if a high-count rate capacity (which implies minimum depth) is required.

A depth of 8 mm of Argon at atmospheric pressure was chosen as giving a reasonable compromise between broad-band detection efficiency, count-rate capacity and operational practicability. This depth gives a gas absorption greater than 50% over most of the band longer than 2 Å except for a dip near the Ar-K edge (fig 2.2). The option was retained to use Xenon if maximum sensitivity were required for a particular experiment, in which case the gas efficiency would be above 90% for wavelengths longer than 2 Å.

The results of calculations based on the foregoing theory, and listed in table 4.1, suggested that an anode spacing of $s = 8$ mm would give adequate high count-rate performance. This would avoid the complication of fitting a large number of closely spaced anodes, and allow each anode to be connected to an individual preamp. Indeed, later work on a detector at JET¹⁷ has shown that the connection of a large number of closely spaced anodes into groups can severely reduce the energy resolution, due to coupling between individual anodes and between adjacent groups of anodes.

To achieve the desired anode array dimensions, the existing detector was modified by fitting a raised cathode plane made of double-sided printed circuit board to the bottom of the chamber (fig. 4.8) to give a working gas depth of 8 mm. An array of 7 anodes of 25 μ m Tungsten wire was mounted with 8mm spacing to the circuit board. The conducting surface was removed where necessary to isolate the anodes from each other and from the cathode. The anode resistors and high voltage isolation capacitors were placed inside the chamber under the cathode board to save space outside the chamber. The anode signals were wired to miniature 50 Ω (LEMO) sockets inside a small screened box integral with one end of the detector. Gas could be flowed continuously through the detector via a vacuum feed-through. The preamplifiers were placed inside the vacuum chamber and connected to the detector by the shortest possible leads.

Analog pulse processing electronics

For the reasons discussed above, it was decided to build a multiple channel pulse-processing chain, using up to ten preamplifier-amplifier-discriminator chains whose digital outputs would be added by a fast OR-gate before being fed to a scaler and memory (fig. 4.9). The system was designed by Dr T J Harris and built in the Physics Department Electronics Workshop at Leicester University.

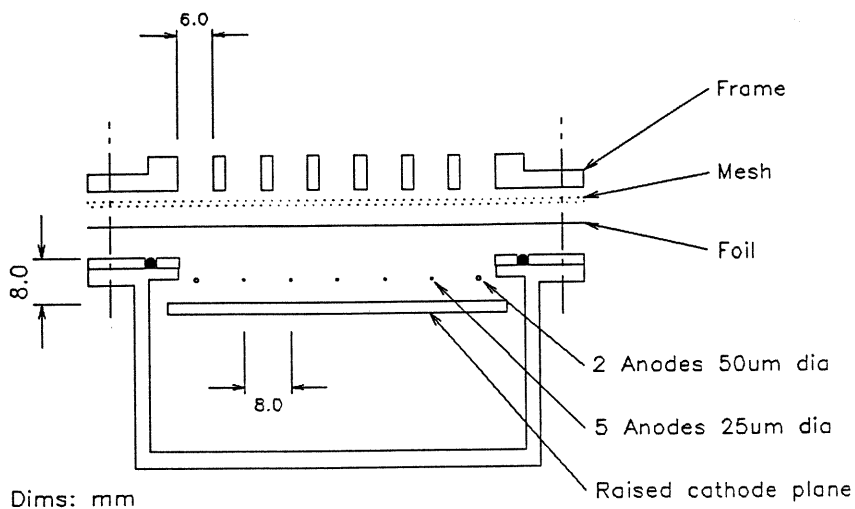


Fig.4.8 Cross-section of the Mk1 detector.

The specification of the system is shown in Table 4.2. The shaping amplifiers have sufficient bandwidth to run with 20 ns time constants but have been wired for 50 ns to date, giving a bi-polar pulse with a zero-crossing time of 100 ns. The discriminator outputs are 10 ns long, this being the effective pulse process time for the full system, so that count-rates of around 10^7 s^{-1} can be handled without unmanageable pile-up. The amplifiers and preamplifiers were designed to have as wide a dynamic range as possible, and to handle overload pulses without being paralyzed.

To minimize electrical interference, the preamplifiers were sited inside the vacuum chamber, with the shortest possible leads to the detector. This minimized the capacitive loading on the preamplifier inputs, and allowed the signals to be fed out through the vacuum system with low impedance. It was found more convenient to locate the shaping amplifiers and all subsequent items in the diagnostic control area, since they require occasional adjustment. This implied that the preamps would be up to 50 m away from the amplifiers.

In the early stages of commissioning, the preamps were fed with a screened supply from the NIM rack in the machine area next to the spectrometer, resulting in an unacceptable noise level. A screened preamp power supply fed from the the same NIM rack (in the control area) that contained the amplifiers, was found to be essential for low noise operation.

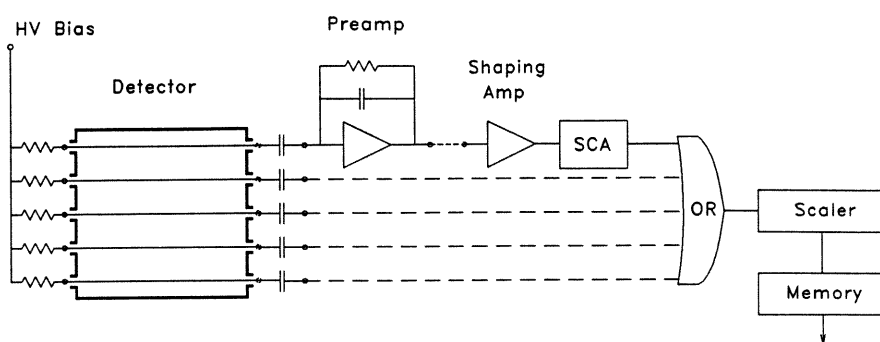


Fig.4.9 Pulse processing system for the Mkl detector.

Data acquisition

For count-rates exceeding 10^7 s^{-1} , a correspondingly fast scaler and memory were required. The scaler was a LeCroy dual-port scaler, capable of counting up to 100 MHz with a programmable sample time down to $1 \mu\text{s}$. The memory was a LeCroy with 64 kByte capacity for 14 bit words and was indexed in synchronism with the scaler by a Culham CPG3 time-sequence generator.

Table 4.2 Signal processing specification

Preamplifier (10 off in 3 die-cast boxes 4+4+2)	
Calibration (charge collected)	4 V pC^{-1}
RMS noise level	15 mV, $4 \times 10^{-3} \text{ pC}$
Linear range	3 V, 0.75 pC
Saturation	4 V
Dynamic Range	48 dB
Rise-time, fall-time	13 ns, 125 ns
Supply	0 V, + 12 V / 13 mA
Shaping amplifiers (10 off in 2 double-width NIM Modules 5+5)	
Voltage gain (variable)	0 to 5 V
Pulse-Shaping Time Constants	50 ns (20 ns possible)
Supply (NIM)	+12 V / 67 mA, -12 V / 67 mA
Discriminators (10 off in 1 double-width NIM Module)	
Upper/lower level Discriminator	0 to 5 V
Independent ULD/LLD settings with 5 channels each	
Output	- 0.8 V, 10 ns
Supply NIM	+ 5 V, $\pm 12 \text{ V}$

All units 50Ω input/output impedance

Table 4.1 Parameters of the Mk1 and Mk2 detector chambers.

	eq.	Symbol	Units	Mk1	Mk2
Chamber half depth		h	mm	4	10
Anode spacing		s	mm	8	n/a
Measured $\Delta E/E$ at 6 keV	(14)	$\Delta E/E$		~0.20	~0.16
Gas efficiency 1 keV		η_g		0.99	1.0
3 keV			0.18	0.4	
10 keV			0.08	0.2	
Anode radius		r_a	μm	12.5	12.5
Effective cathode radius	2	r'_c	mm	6.1	5.0
Chamber parameter	3	C		0.081	0.083
Capacitance/length	26	C_l	pF/m	9.1	9.3
Anode Volts for gain $\approx 10^4$	11	V_a	V	1350	1300
Chamber char. time	16	t_o	ns	1.7	1.6
Ion collection time	17	t_c	μs	130	125
Chamber resistivity	25	R_m	M Ω m	3.1	2.4
Fractional rate of change of gas gain	12	$\frac{1}{M} \frac{dM}{dV}$	V^{-1}	1/63	1/60
Char. current for gain reduction	24	I_m	$\mu\text{A}/\text{cm}$	0.20	0.26
Charge collection effy (50ns pulse shaping)	16	q/q_o		0.28	0.29
Ion mobility		μ_+	$\text{cm}^2/\text{V}\cdot\text{s}$		1.9
Gas density		ρ	mg/cm^3		1.6
Mass abs. coeff. 1 keV		μ	cm^2/g		3420
3 keV			"		176
10 keV			"		64

4.6 PERFORMANCE AND COMPARISON WITH THEORY

Having designed and built a detector system on the basis of initial trials and the above theory, it is now possible to compare its performance with predictions.

Gas-gain / anode-voltage characteristic

The charge per pulse was measured as a function of anode voltage at low count-rate, (using a ^{55}Fe source, which emits predominantly Mn-K x-rays at 5.9 keV, following electron capture). The charge was measured using the final design for the preamplifiers, which have a calibration of 4 V/pC. The results

are shown in figure 4.10 and show good agreement with the theoretical gain from eq. 4.13, particularly in the slope dM/dV . The absolute gain is about a factor 3 less than predicted, but this is a small discrepancy in view of the steepness of the curve, and is equivalent to a change of about 130 V in V_a . With the system noise level as shown at about $4 \cdot 10^{-3}$ pC, this gas-gain versus anode-voltage characteristic allows selection of a suitable anode voltage for a particular minimum x-ray energy (this curve is for 5.9 keV photons, and clearly the charge per pulse is changed in proportion for photons of other energies).

Once the detector gas has been flowing for about 24 hours, the gain is very stable, and can be checked regularly by means of a small ^{55}Fe source permanently placed in the spectrometer chamber. This source was positioned and attenuated to give a constant count-rate of about 100 s^{-1} per anode, which is enough to calibrate the system but too low to corrupt the data.

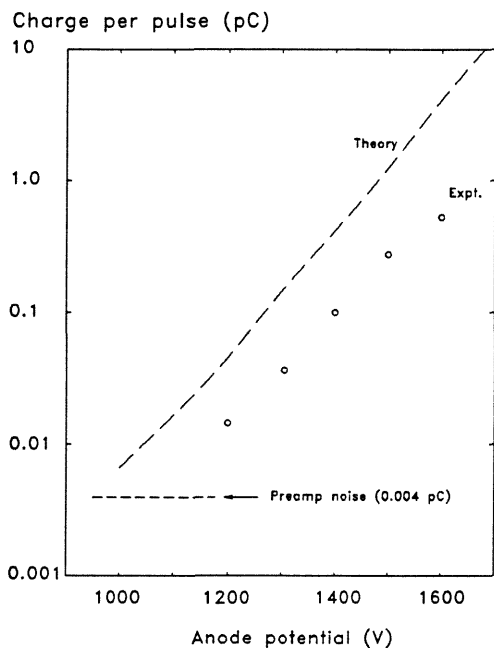


Fig.4.10 Gas-gain v. Anode voltage characteristic for the Mkl detector.

Energy resolution and linearity

Using Mn-K x-rays as a calibration, the linearity and energy resolution were assessed at a range of energies, recorded during plasma discharges, as plotted in figure 4.11. The linearity is quite good, and the energy resolution is well within what is acceptable for such a system.

High count-rate performance

Estimates of the gain reduction at a count-rate of about 1 MHz per anode were made by observing the pulses on the oscilloscope during a discharge. This was done on consecutive discharges at anode voltages of 1400 V and 1500 V, resulting in gain reductions of 13% and 33% respectively. These measurements can be compared with theory, as shown in table 4.3. The agreement is quite good in that the measured characteristic current is $0.35 \mu\text{A}/\text{cm}$, whereas the calculated value is $0.31 \mu\text{A}/\text{cm}$. In view of the approximate nature of the observed results, this level of agreement is possibly fortuitous, but clearly Mathieson's theory gives a good prediction of gain-reduction due to space-charge.

These results show that for pulses (q_0) of less than about 0.1 pC, count-rates greater than 10^6 s^{-1} per anode can be achieved, which is in line with the aim of a total count-rate exceeding 10^7 s^{-1} for 10 channels.

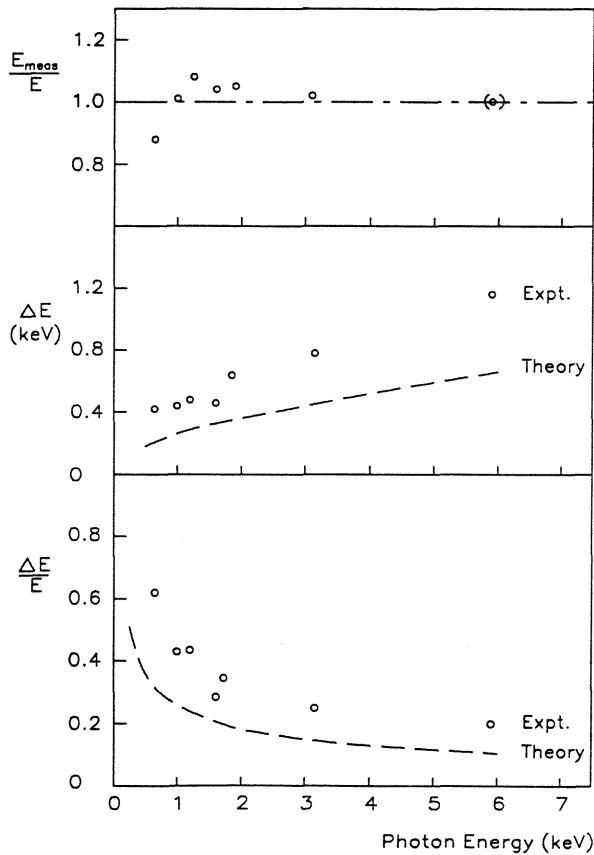


Fig.4.11 Energy resolution and linearity of the Mkl detector.

Table 4.3 Gain Reduction at 10^6 s^{-1} per anode for the Mk1 detector.

Wavelength, Energy	6.7 Å, 1.85 keV		
Irradiated Anode length, L	16 mm ($\therefore L/h = 4$)		
Corrected I_m to allow for $L/h=4$	I_{CE}	=	$I_m/0.7$
Chamber parameter	C	=	0.082
Anode Capacitance/length,	$4\pi\epsilon_0 C$	= C_1	= 9.1 pF/m
Characteristic Resistivity,	$h^2/2\mu_a V_a C_1$	= R_m	= $0.311 \times 10^9 \Omega\text{cm}$
Measured fractional gain-slope	$\frac{1}{M} \frac{dM}{dV}$	=	$1/63 \text{ V}^{-1}$

Observed				
Anode Voltage	V_a	V	1400	1500
Low-rate charge per pulse	q_o	pC	0.031	0.088
Low-rate pulse at amplifier		mV	150	600
High-rate " " "		mV	130	400
Fractional charge at high-rate	q/q_o		0.87	0.67
$(n_1 q_o / I_o) \text{exp. from fig 4.7}$			0.145	0.59
Experimental char. curr.	I_m	$\mu\text{A}/\text{cm}$	0.41	0.28
			mean 0.35	
Theoretical				
Chamber characteristic current	I_m	$\mu\text{A}/\text{cm}$	0.20	
Char. curr. incl. finite irradiation length	I_{CE}	$\mu\text{A}/\text{cm}$	0.31	
$n_1 q_o / I_{CE}$			0.065	0.18
Calculated gain reduction	q/q_o		0.92	0.85

4.7 Mk2 DETECTORS

The detectors for the Mk2 Bragg rotor spectrometer were further improved relative to the Mk1 detector by separating the anodes by cathode walls (fig 4.12). This results in an array of single-wire chambers rather than a MWPC since all the anodes are separated by cathode walls that coincide with the window support ribs. This design confers several advantages where high count-rate and wide energy range are required:

a) Since the effective cathode radius is governed mainly by the smaller of the chamber cross-sections, it can be smaller than gas depth. This makes it possible to provide a large gas absorption depth without an undue sacrifice in the ion drift time, as would be the case in a multiwire chamber.

- b) A lower anode voltage is needed for a given gas-gain, thus eliminating the breakdown problems often encountered with deep multiwire chambers.
- c) It is easier to achieve a uniform electric field around the anode than with a MWPC, so the energy resolution can be very close to the theoretical value.
- d) The absence of edge effects removes the need for field-defining anodes at each side of the array, leading to a compact detector design.
- e) There is no capacitive cross-talk between anodes. This reduces the number of spurious pulses and is a major advantage when operating with an energy range of 100:1.
- f) It is possible to provide different gas depths for adjacent anodes.

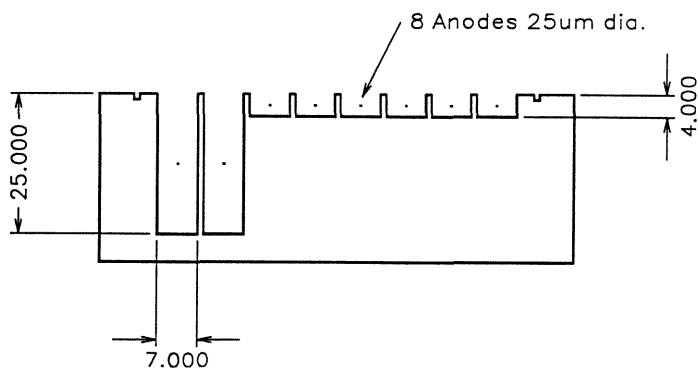


Fig.4.12 Cross-section of the detector for the parallel-channel section of the Mk2 spectrometer.

The calculated parameters for the Mk2 detector are compared with the Mk1 version in table 4.1. The improved QDE due to the increase in gas depth from 8 mm to 20 mm is achieved without an increase in the chamber resistance R_m : in fact this is slightly lower. A pulse-height spectrum from the Mk2 detector is shown in figure 4.13. The energy resolution is improved relative to Mk1, being as low as $\Delta E/E = 0.16$ at 6 keV (fig 4.13a). The same spectrum is plotted on a log scale in figure 4.13b, which shows that noise counts due to fluorescence of the aluminium chamber walls are negligible.

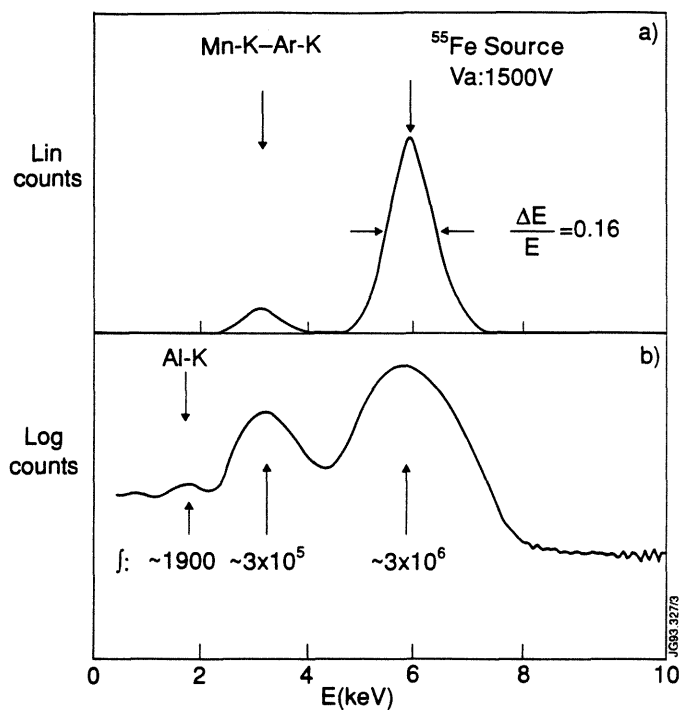


Fig.4.13 Pulse-height spectrum from the Mk2 detector (A Patel).
a) Linear scale, showing the Mn-K peak and Ar escape peak (Mn-K - Ar-K).
b) Log scale, showing negligible Al-K fluorescence in the chamber.

4.8 CONCLUSION

A combination of theoretical and experimental work on both the chamber and the electronics has achieved the required high-rate performance. Compared with the Mk1 model, the Mk2 detector has greater efficiency and lower inter-anode cross-talk over a wider energy range, and the Bragg rotor spectrometer can now benefit from a high QDE, high count-rate, energy resolving detector.

References

- ¹ G Charpak, Ann. Rev. Nucl. Sci. 20 (1970) 195.
- ² F Sauli, CERN report 77-09 (1977).
- ³ G W Fraser, X-ray detectors in astronomy, Cambridge Univ. Press, (1989).
- ⁴ E Mathieson. MSc lecture notes, University of Leicester, (1980).
- ⁵ V Fano, Phys. Rev. 72 (1947) 26.
- ⁶ V Palladino, B Sadoulet. Nucl. Inst. Meth. 128 (1975) 323-335.
- ⁷ N El-Hakeem, E M Mathieson. Nucl. Inst. Meth. 166 (1979) 447-450.
- ⁸ A Zastawny, J. Sci. Instrum. 43 (1966) 179-181.
- ⁹ M W Charles and B A Cooke, Nucl. Inst. Meth. 61 (1968) 31.
- ¹⁰ A G Michette, C J Buckley. X-ray Science and Technology. Publ. IOP (1993).
- ¹¹ A V Korgaonkar, JET internal group report (1989).
- ¹² R W Hendricks, Rev. Sci. Instrum. 40 no9 (1969) 1216-23.
- ¹³ H Sipilä, V Vanha-Honko. Nucl. Inst. Meth. 153 (1981) 461.
- ¹⁴ H Sipilä et al. Nucl. Inst. Meth. 176 (1980) 381.
- ¹⁵ E Mathieson, Nucl. Inst. Meth. A249 , (1986) 413-420.
- ¹⁶ G C Smith, E Mathieson. IEEE Trans. Nucl. Sci. NS-34 no1 (1987) 410.
- ¹⁷ M Wohlin, MSc dissertation, Royal Inst. of Technology, Stockholm. (1990).

5 PLASMA SPECTROSCOPY BEYOND 25 Å USING BRAGG DIFFRACTION

5.1	Introduction	112
5.2	Theory	114
5.3	Diffraction selection	117
5.4	Laboratory results	119
5.5	Tokamak results	121
5.6	Conclusion	126

9. To know the quantite of the day vulgar, that is to seyn fro spring of the day unto the verrey nyght.

Know the quantite of thy crepuscules, as I have taught in the 2 chapitre bifore, and adde hem to the arch of the day artificial, and tak there the space of all the hool day vulgar unto the verrey nyght.

18. To know the degrees of longitudes of fixe sterres after that they be determynat in thin Astrelabie, yif so be that thei be trewly sette.

Set the centre of the sterre upon the lyne meridionall, and tak kep of thy zodiak, and loke what degre of eny signe that sitte upon the same lyne meridionall at the same tyme, and tak there the degre in which the sterre stondith; and with the degre cometh that same sterre unto that same lyne fro the orisonte.

*A Treatise on the Astrolabe
Geoffrey Chaucer 1393*

5.1 INTRODUCTION

A wavelength of about 25 Å has usually been regarded as the cross-over point between the performance of grating and crystal instruments for plasma spectroscopy. Below 25 Å, large aperture crystals with good resolution can be combined with energy-resolving detectors such as gas proportional counters, resulting in sensitive instruments with good signal-to-noise ratio. Gratings, on the other hand require small slits and shallow grazing angles, and suffer from low sensitivity and internally scattered light. For these reasons, Bragg spectroscopy of plasma impurities is a well-established technique for high resolution line-profile measurements below about 10 Å^{1,2}, and for survey work up to about 25 Å^{3,4}. Above 25 Å, gratings have been the standard choice^{5,6}.

However, there is an incentive to extend the practical upper limit for Bragg spectroscopy of magnetically confined plasmas from about 25 Å to about 100 Å, since this would allow a single instrument to monitor the most highly ionized species of all impurities that have $Z \geq 3$ (Li). This is important for the light impurities Be, B, and C, which often dominate the radiated power, fuel dilution and effective charge state of tokamak plasmas.

Access to the 100 Å to 200 Å range can be considered more an interest than a necessity, since although it is a very fruitful band for plasma diagnostics using grating instruments, where $\Delta n = 0$ transitions of medium-Z ions are exploited, all impurities can be monitored at least as sensitively between about 1 Å and 100 Å, using $\Delta n = 1$ transitions.

A major part of the effort to extend the useful wavelength range of Bragg spectroscopy was concentrated on the selection of suitable diffractors, and included theoretical predictions, laboratory tests, and a successful demonstration on the COMPASS tokamak. A range of long-wavelength diffractors, together with conventional crystals, was then installed in the Bragg rotor spectrometer (ch 3) to cover the spectrum from about 1 Å to 100 Å, and to monitor the JET tokamak plasma throughout 1991 operations (ch 7, 10).

Background

The most common use of Bragg spectroscopy above 25 Å is for fluorescence analysis of low-Z elements, where the K-shell lines of elements such as Be, B and C are well isolated, and where the fluorescent yields are very low. Commercially available diffractors have been optimized for this type of application, where the main requirement is for the maximum possible sensitivity at the expense of resolving power. In contrast, the requirements for plasma spectroscopy are almost the opposite, since the intense source and crowded spectrum usually demand the best possible resolving power at the cost of sensitivity. Compared with fluorescence analysis, plasma spectroscopy above

25 Å is complicated by several factors that expose limitations in the x-ray optics and detectors. The main difficulty is that the signal-to-noise ratio is potentially much worse due to the wide energy range of the line and continuum spectrum in the beam incident on the diffractor, and the likelihood of background radiation due to neutron production or runaway electrons in the plasma. These sources give rise to noise counts, either directly in the detector or as fluorescence or scattering from the crystal.

The most difficult region to observe is between about 25 Å and 44 Å, just below the carbon-K absorption edge, where the presence of carbon in a diffractor such as lead stearate (PbSt) or tungsten-carbon (W-C) causes a severe drop in reflectivity. Since most thin windows, such as polypropylene, also contain carbon, the loss of sensitivity can be severe. The transmission of typical window materials is shown in figure 2.1, from which it is clear that even the thinnest practical windows cause a serious loss between 25 Å and 43.7 Å. A further problem arises if the higher-order reflections are strong, leading to contamination of the spectrum by lines at λ/n .

These effects are exacerbated by the naturally poor energy resolution of a gas proportional counter at low energies, which means that a larger fraction of the noise spectrum is added to the signal, and which can prevent the discrimination of higher-order reflections. The situation is nevertheless better than the case of a microchannel plate detector (which normally has no energy resolution) used with a grating spectrometer, where overlapping diffraction orders are accepted as a fact of life.

A further advantage of a pulse-counting system, as normally used with a proportional counter, is that the signal intensity can be immune to changes in the detector gain of at least a factor two (for typical discriminator settings). Although channel-plate detectors can be absolutely calibrated⁷ and will operate very well in pulse-counting mode with electronic readout (even exhibiting modest energy resolution), for simplicity they are frequently coupled to phosphors and optical readouts when used in grating instruments. This is a second-best system that makes absolute calibration very difficult, since the signal is now also a function of the detector gain, which is known to vary with instantaneous and integrated flux, as well as with more mundane factors such as vacuum quality and surface contamination.

Recent work

Langmuir-Blodgett films⁸, such as lead stearate, and sputtered⁹ or evaporated¹⁰ multilayers are now commercially available and can be used for Bragg spectroscopy up to about 200 Å. Lead stearate has been calibrated experimentally and modelled theoretically by Willingale¹¹, but is being superseded by synthetic multilayers, which are physically more stable and

offer high reflectivity in a wide range of $2d$ spacings¹². When considering their use for plasma spectroscopy, a serious drawback of these types of diffractor is their very poor resolving power ($\lambda/\Delta\lambda$), which declines from about 100 at 20 Å to about 10 at 200 Å.

The use of synthetic multilayers (or layered synthetic microstructures, LSM) for plasma spectroscopy has been reviewed recently by Moos¹³, where some results seem to highlight, rather than offer a solution to, the problems of working between 100 Å and 200 Å with a resolving power $\lambda/\Delta\lambda$ of about 40. A modelled fit to a group of Ti XV, XVI, XVII, XVIII and XIX lines from the TEXT tokamak is shown, where the experimental data from a Mo-B₄C multilayer consist of only six points between 138 Å and 175 Å. A spectrum from a Penning ionization discharge of Al IV and Al V between 115 Å and 135 Å using the same multilayer is more convincing, and shows a resolving power of about 43.

True crystals of large organic molecules such as potassium hydrogen phthalate (KHP or KAP) are used widely and successfully up to about 25 Å, but although there are many potentially suitable crystals with $2d$ values up to nearly 100 Å, they have been little used to date. Luck and Urch¹⁴ have demonstrated the production, and application in a commercial fluorescent analysis spectrometer, of octadecyl hydrogen maleate (OHM) $2d$ 62.5 Å and octadecyl adipate (OAO) $2d$ 91.2 Å, with significantly improved resolution compared with commercially available multilayers.

5.2 THEORY

As discussed above, this chapter is concerned primarily with achieving the best possible resolving power above 25 Å. At long wavelengths where absorption dominates, the perfect lattice with absorption model is a good approximation, and will be used here as a guide to the performance that can be expected from various diffractors.

Resolving power

From chapter 2 the absorption-limited resolving power is given by

$$\frac{\lambda}{\Delta\lambda} = \frac{\pi \sin \theta}{\mu_1 d} = \frac{\pi \lambda}{2 \mu_1 d^2} \quad (5.1)$$

where μ_1 is the linear absorption coefficient and d is the lattice spacing. Inspection of this equation shows that to maximize the resolving power at a given wavelength, we should choose a diffractor with the smallest practical lattice spacing and a small linear absorption coefficient.

A collection of calculations is shown in figure 5.1, together with previous results for an OAO crystal and various multilayers, where the references are those discussed above (except for Bobashev et al, which is as yet unpublished). The main feature of the diffractors containing carbon is the sharp drop in resolving power on the short wavelength side of the C-K absorption edge.

The most significant result is that the theory predicts better resolution at all wavelengths for the true crystals than for currently available synthetic multilayers, even for multilayers that contain no carbon. This is because, even for wavelengths below the C-K edge, μ_1 for Si, Ni and W is still greater than that of C, suggesting that a carbon-free synthetic multilayer may not be the best choice.

The curve for a possible Ge-Si multilayer with a 2d spacing of 53 Å predicts a resolving power better than 100 at C Ly α (33.7 Å). This is close to the predicted OHM performance, and is due to the smaller 2d rather than to reduced absorption.

A further striking feature of the theory is that for wavelengths longer than the C-K edge, very good resolution is predicted, comparable with that which can be obtained below 25 Å. The dashed curve which forms the upper envelope is not for any particular crystal, but is the perfect-lattice-with-absorption limit (ch. 2.3) for notional crystals having 2d values equal to the wavelength (by setting $2d = \lambda$ in eq 4). This forms a guide to the best resolution that can be expected at a given wavelength from a crystal, assuming a similar fractional elemental composition to that of OHM.

This curve is a very strong function of wavelength, and decays as $\lambda^{-3.3}$, with the result that $\lambda/\Delta\lambda$ falls by an order of magnitude for a doubling of the wavelength. Since it is unlikely that any practical diffractor, whether crystal or multilayer, could have a lower linear absorption than an organic molecule composed mainly of carbon and hydrogen, this curve probably represents the effective "laws of physics" limit for Bragg spectroscopy.

Using this criterion, the best resolving power close to 34 Å should be given by an organic crystal with a 2d of about 36 Å, for which a resolving power of about 350 is predicted.

Refractive index correction

The refractive index correction $\Delta\theta$ based on eq 2.23 has been calculated for the first three orders of OHM, including the influence of the carbon and oxygen edges, and is shown in figure 5.2. The first order corrections are very large, and may account for the differences in the published values of the 2d for this crystal (Luck and Urch 62.5 Å, Underwood 63.5 Å¹⁵). The value obtained here, based on C-K α and using the above correction, is 62.6 Å.

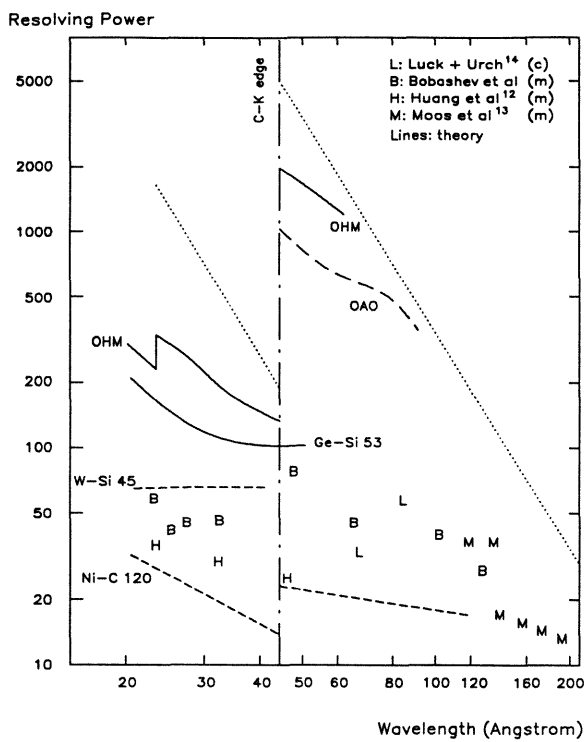


Fig.5.1 Theoretical resolving power for multilayers (m) and crystals (c), compared with previously achieved values.

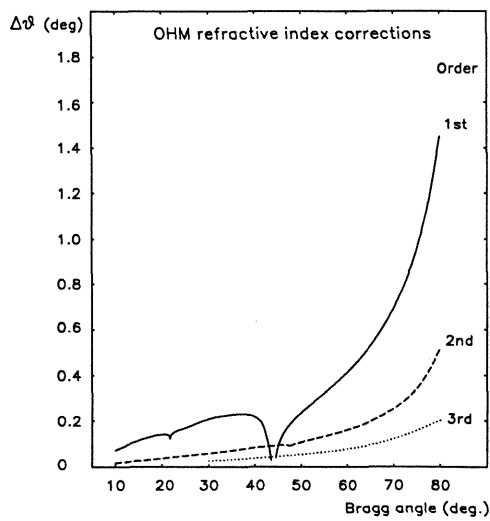


Fig.5.2 Refractive index corrections for the first three orders of octadecyl hydrogen maleate (OHM).

5.3 DIFFRACTOR SELECTION

The main motivation for extending the wavelength range of Bragg spectroscopy is to monitor the strong H- and He-like lines of beryllium, boron and carbon, which lie in the range 25.5 Å to 100.25 Å. Strong lines from Cl VIII, Fe XVI and Ni XVIII can also be expected to complicate the spectrum of most tokamaks in this band. Most of the important lines are listed below in Table 1, together with K- and L-shell lines that are suitable for calibration. As discussed above, operation in the band between 100 Å and 200 Å would be seen as an added bonus rather than a necessity.

Initially it was expected that the best performance below the carbon K-edge might be obtained from a carbon-free multilayer with a 2d spacing of between 40 Å and 50 Å, possibly using boron or silicon to replace carbon as the low-Z component. However, the theory (eq.5.1) suggests that an organic crystal may be superior. Details of the diffractors discussed here are given in table 5.2.

Test diffractors

Based on the above requirements, several different diffractors were obtained for evaluation, as described below:

OV-51A. This W-Si multilayer, with a 2d of 51 Å and an aperture of 70 x 30 mm², was supplied by Philips on a standard mount ready for use in a fluorescent analysis spectrometer. The original manufacturer was Ovonic. Philips also offer multilayers with 2d values of 120 Å and 200 Å.

Lead stearate. This is a Langmuir-Blodgett multilayer with a 2d spacing of 100.4 Å. Lead stearate has been given a full theoretical treatment by Willingale, who also calibrated samples from the same manufacturer (Quartz and Silice).

Octadecyl hydrogen maleate (OHM). This is a true crystal with a 2d of 63.5 Å, and a small sample of about 10 x 15 mm² was obtained from Quartz and Silice.

Calculations for the diffractors tested here are shown in figure 5.9, together with the experimental results. After some laboratory work, samples of three further Ovonic multilayers were obtained for evaluation on plasma sources:

OV-045A (W-Si) 2d 44 Å,
OV-070A (W-Si) 2d 70 Å,
OV-120N (Ni-C) 2d 117 Å.

Further calculations show that an OV-110L V-C 2d 110 Å multilayer should have a much better resolution than the OV-120N, and is also worth testing.

Table 5.1 Plasma lines and calibration lines in the band 20 Å to 100 Å.

Ion	Plasma line	"X-ray" line	λ (Å)	Diff-ractor	2d (Å)	$\sim\lambda/\Delta\lambda$
Be III	$1s^2-1s2p^1P^0$		100.255	↓ OV110	110	60
				↓ PbSt	100.4	50
	$1s^2-1s3p$		88.309	↓ OAO	91.2 ^a	400
		S L	83.4	↓	$\sim 94^b$	
	Series limit		80.564			
Be IV	$1s-2p$		75.928			
		Cl L	67.9	↓ OV70	70	40
		B $K\alpha$	67.6	↓		
	$1s-3p$		64.064			
	$1s-4p$		60.743			
	Limit		56.945	↓ OHM	62.5	600
B IV	$1s^2-1s2p^3P^0$		61.088			
	$1s^2-1s2p^1P^0$		60.3144			
	$1s^2-1s3p$		52.685			
	Limit		47.801	↓ PXI	51	50
B V	$1s-2p$		48.591			
		C $K\alpha$	44.7			
		C K edge	43.67	↓ OV45	45	70
	$1s-3p$		40.996			
	limit		36.442			
C V	$1s^2-1s2p^3P^0$		40.7306			
	$1s^2-1s2p^1P^0$		40.2680			
	$1s^2-1s3p$		34.9728			
	Limit		31.621			
C VI		Ca L	36.3			
	$1s-2p$		33.736			
		N $K\alpha$	31.6			
	$1s-3p$		28.466	↓ KHC	31.2	500
		Ti $L\alpha$	27.4	↓		
	$1s-4p$		26.357	↓ KAP	26.63	1000
	Limit		25.303			
	O $K\alpha$	23.6				
	Cr $L\alpha$	21.6				

Table 5.2 Diffractor Data

Diffractor	Type	2d (Å)	Formula	Supplier
OV-200H	SM	200	Mo-B ₄ C	Ovonics
OV-120N	SM	117	Ni-C	Ovonics
OV-110L	SM	110	V-C	Ovonics
Lead stearate (PbSt)	LBF	100.4	[CH ₃ (CH ₂) ₁₆ COO] ₂ Pb	Quartz & Silice
Diocetyl-adipate (OAO)	Xtal	91.2 ^a ~94 ^b	(CH ₂) ₄ [COO(CH ₂) ₁₇ CH ₃] ₂	(Q & S?)
OV-070	SM	70	W-Si	Ovonics
Octadecyl-Hydrogen-Maleate (OHM)	Xtal	62.5 ^a 63.5 ^b	CH ₃ (CH ₂) ₁₇ OOC-CH:CH-COOH	Q & S
Tetradecyl-Hydrogen-Maleate (THM)	Xtal	52.5	CH ₃ (CH ₂) ₁₃ OOC-CH:CH-COOH	
OV-51A	SM	51	W-Si	Ovonics
OV-045A	SM	44	W-Si	Ovonics

SM: Synthetic multilayer ^a Luck & Urch¹⁴
 LBF: Langmuir-Blodgett film ^b Underwood¹⁵

5.4 LABORATORY X-RAY SOURCE

The diffractors were first tested in the Bragg rotor spectrometer (chapter 3) which was coupled to a large-area x-ray source. The source had interchangeable anodes of area 100 x 300 mm² and could operate at up to about 2 mA and 30 kV. For these tests, either Inconel (Ni-Cr-Fe) or graphite anodes were fitted. This system was not optimized for testing small samples at long wavelengths, mainly because of the large fixed detector with its relatively thick window.

The results at C K α (44.7 Å) are shown in figure 5.3 and in table 5.3. The best resolving power ($\lambda/\Delta\lambda = 32$) was given by the OHM crystal, and the best reflectivity by the OV 51 multilayer. With only single-crystal measurements, it was not possible to make an absolute calibration of reflectivity.

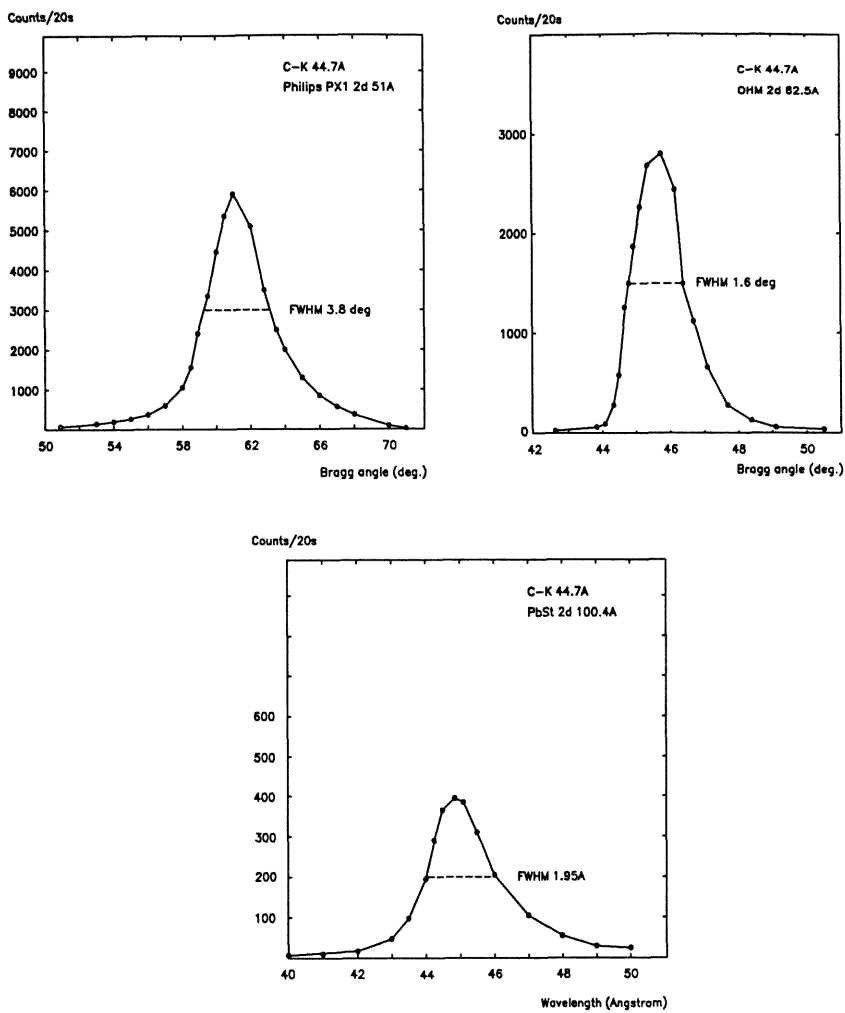


Fig.5.3 The carbon K-line at 44.7 Å, measured with various diffractors.

Table 5.1 Total line width and apparent resolving power of the test diffractors at C-K α (44.7 Å)

Diffractor	2d (Å)	FWHM (deg.)	$\lambda/\Delta\lambda$
Lead stearate	100.4	1.2	23
OHM crystal	62.5	1.9	32
PX1 multilayer	51	4.0	22.5

5.5 TOKAMAK RESULTS

After tests with the x-ray source, the lead stearate, OHM and OV-51 diffractors were mounted in the Mk1 Bragg rotor spectrometer during its operation on the COMPASS tokamak. The COMPASS vacuum vessel had recently been boronized, providing the opportunity to observe H-like and He-like boron lines in the 48 Å to 61 Å region. For these observations the detector was still fitted with a window of graphite-coated 2 μm Mylar, which had very low transmission below the C-K edge (fig.2.1), and which is therefore a prominent feature in all the spectra. This low transmission is responsible for the absence of any carbon lines in the 25 Å to 40 Å region, though at shorter wavelengths the oxygen lines at 18.97 Å and 21.6 Å were recorded on the OV-51 multilayer.

A further selection of multilayers was then obtained for use in the Mk2 Bragg rotor spectrometer on JET, results from which are also included here. The resolving powers obtained from the tokamak results are shown as points in figure 5.9, together with the theoretical curves for crystals and multilayers, and two-crystal measurements for lead stearate. Good sensitivity was also achieved, giving a spectrum in about 100 ms from any of the diffractors.

Lead stearate

The lead stearate spectra of boron between about 45 Å and 60 Å (fig.5.4) show a resolving power of between 40 and 50, which is slightly lower than the value of about 70 that would be predicted from Willingale's work. This diffractor, although it had been stored carefully, was four years old at the time these results were taken, and it is possible that it had deteriorated during this period. When used on JET to monitor beryllium, the PbSt gave similar performance at 76 Å, but as shown in figure 5.6, it had strong reflections in the higher orders, which led to spurious lines when neon was injected. This occurred only rarely, and would be greatly reduced by using a narrower detector energy window. Nevertheless, this sensitivity to higher orders was seen as risk to the data validity, and so the OV-117 multilayer was preferred, even though it had poorer resolving power

Multilayers

At the two extremities of its Bragg angle range, from O VIII Ly α at 18.97 Å up to B Ly α at 58.59 Å, the OV-51A Multilayer (fig.5.7) showed an almost constant resolving power of about 50, in agreement with the theoretical prediction as shown in figure 5.9. The absence of any carbon lines in the spectrum is due to the window absorption, but it can be expected that this carbon-free multilayer would give similar resolution throughout its Bragg angle range.

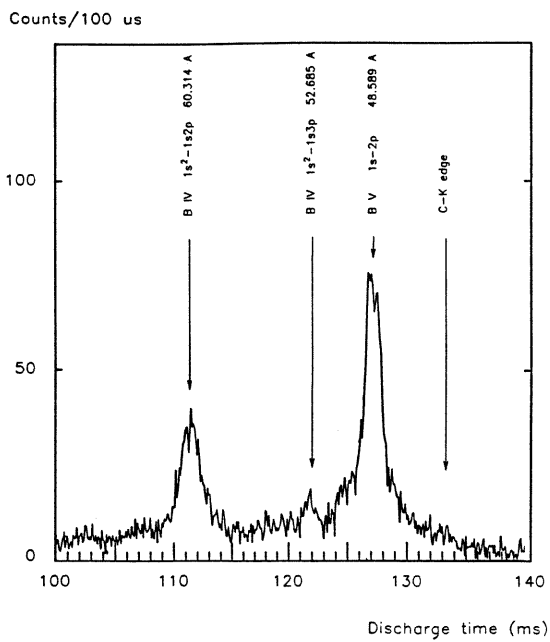


Fig.5.4 Boron spectrum from the COMPASS tokamak, obtained using lead stearate.

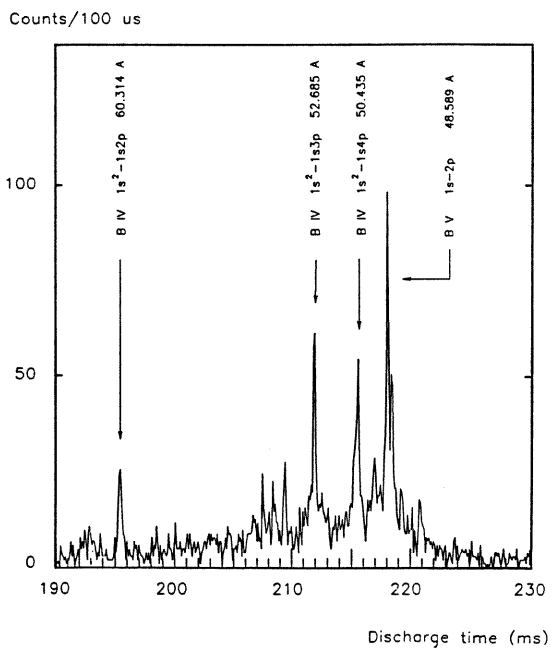


Fig 5.5 Boron spectrum from the COMPASS tokamak using an OHM crystal $2d = 62.5 \text{ \AA}$.

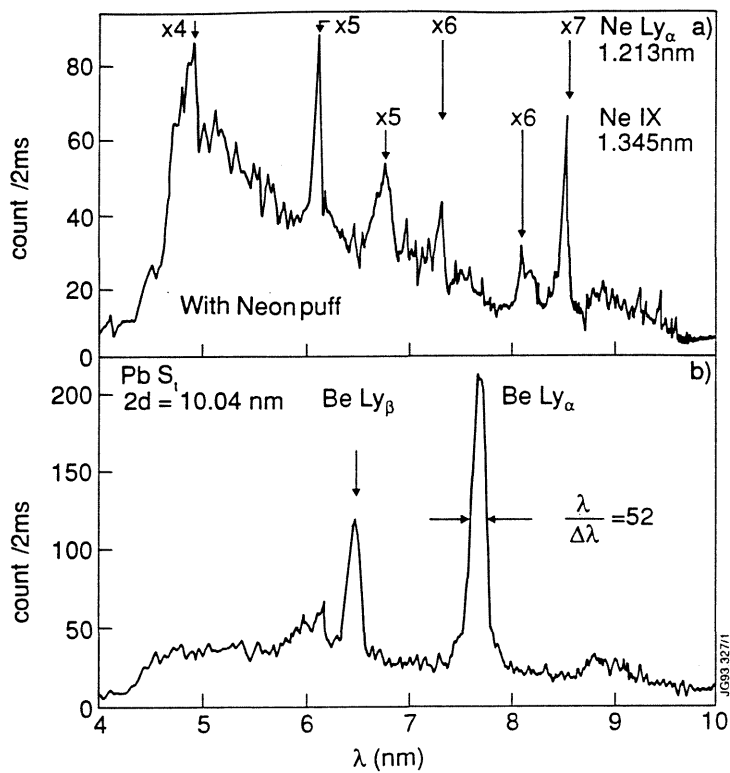


Fig.5.6 Spectra from the JET tokamak using lead stearate. a) With neon puff, showing higher order reflections, b) without neon.

Counts/250 us

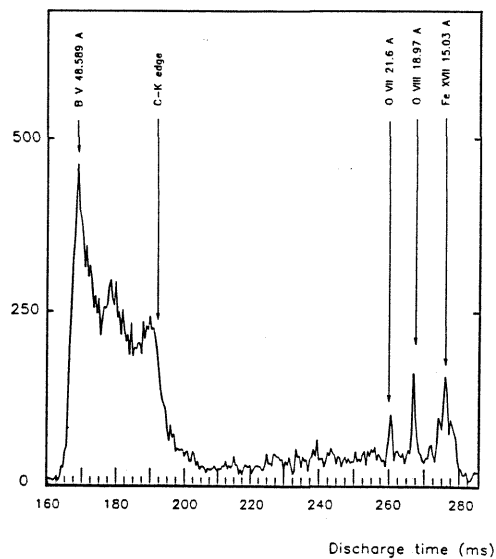


Fig.5.7 Spectrum recorded from the COMPASS tokamak using a W-Si multilayer, $2d = 51 \text{ \AA}$.

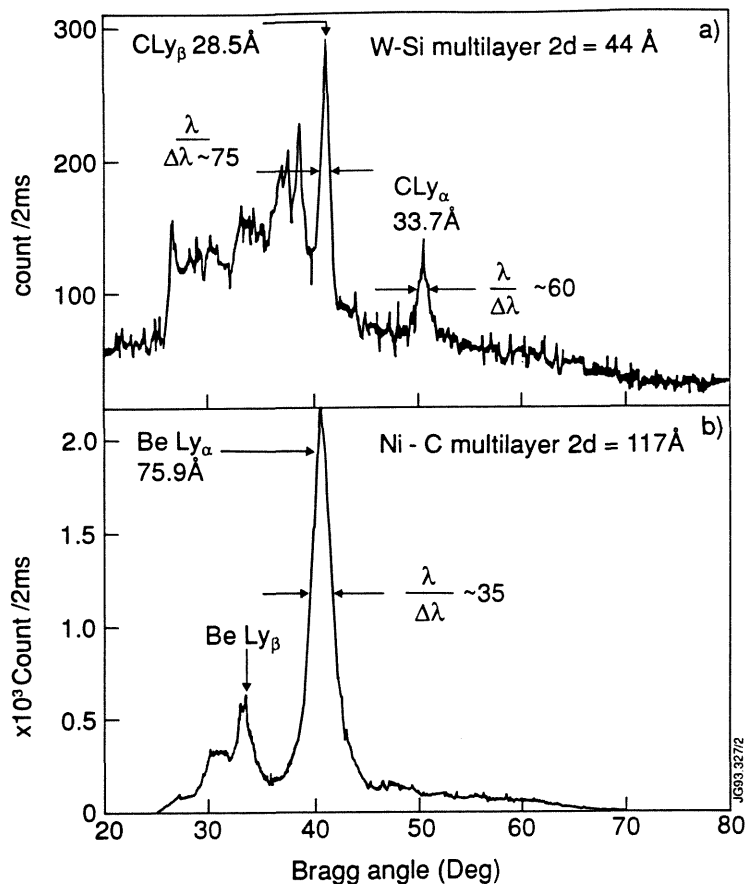


Fig.5.8 Carbon and beryllium spectra recorded from the JET tokamak using:
a) W-Si multilayer, $2d = 44 \text{ \AA}$. b) Ni-C multilayer, $2d = 117 \text{ \AA}$.

The **W-Si 44 Multilayer**, (fig 5.8a) was used on JET to monitor carbon $\text{Ly}\alpha$ 33.74 \AA and $\text{C Ly}\beta$ 28.47 \AA , and showed a better than predicted $\lambda/\Delta\lambda \approx 60$. The reversed $\text{Ly}\alpha:\text{Ly}\beta$ ratio in the data, and absence of the $\text{C V } 1s^2-1s2p \text{ } ^1P^0$ line at 40.27 \AA , are both due to the steeply-falling transmission of the $2 \text{ }\mu\text{m}$ Mylar detector window.

The **W-Si 70 Multilayer** was used on JET but not routinely, since it exhibited lower resolution than expected, and its wavelength range was not useful either for C or Be (fig 7.9).

The **Ni-C 117 Multilayer** (fig 5.8b) had a peak reflectivity about ten times higher than PbSt, and about twice the line-width. Under most circumstances its $\lambda/\Delta\lambda \approx 35$ was adequate to monitor Be $\text{Ly}\alpha$ at 75.93 \AA , and it was used throughout 1991 JET operations. Calculations suggest that a V-C multilayer $2d \approx 100 \text{ \AA}$, $\lambda/\Delta\lambda \sim 80$, would be more suitable.

Diffractor resolving power

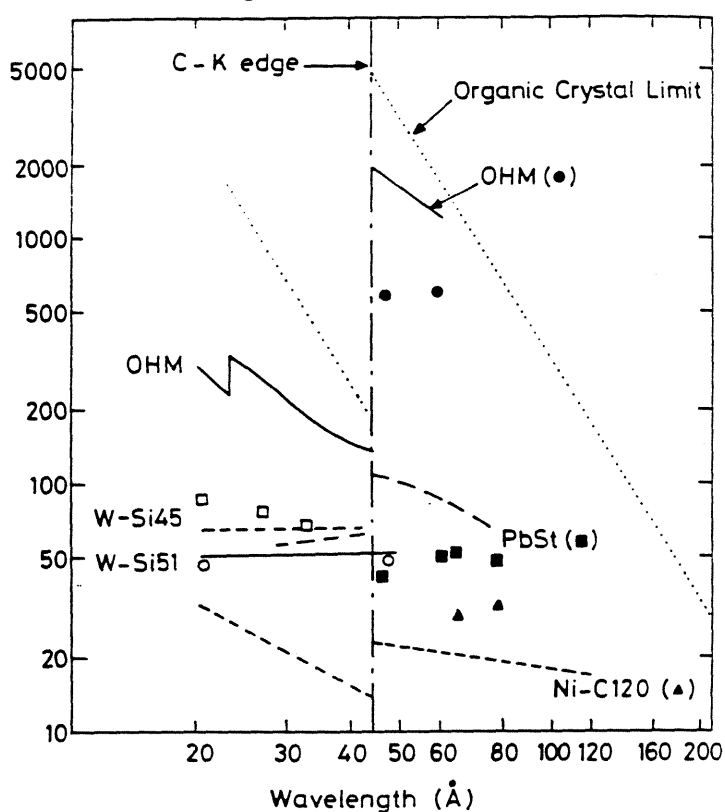


Fig.5.9 Theoretical and measured resolving powers for the crystals and multilayers tested in this work. The calculations for W-Si45 and Ni-C120 were made before the multilayers were ordered. On delivery they were found to be W-Si44 and NiC117: an insignificant difference.

OHM Crystal

By far the best resolution was obtained from the OHM crystal (fig.5.6); it gave a sensitivity and resolving power that compare favourably with grating spectrometers in this spectral region. Even though the active area of the OHM was only about 20% of the PbSt and OV-51 diffractors, similar peak count-rates (~2MHz) were recorded. The longest wavelength recorded was B IV $1s^2-1s2p^1P^0$ at 60.31 Å. It shows a line-width in the spectrum of about 0.23° , which for the Bragg angle of 72° gives an instrumental resolving power of 700. Assuming that the crystal diffraction profile is Lorentzian (as would be expected for a perfect crystal with absorption), it can be expected to add linearly with the collimator, which has a triangular line-spread function with a FWHM of 0.09° . This implies a resolving power for the crystal alone of about 1000, which is very close to the theoretical limit, and an impressive result for a true crystal at such a long wavelength.

5.6 CONCLUSION

As demonstrated above, operational experience with a plasma source is an effective way to evaluate diffractors, but this can never replace thorough laboratory calibrations supported by rigorous theoretical work, particularly where absolute flux measurements are required.

Single crystal results as described here are usually a poor substitute for double crystal measurements, which allow absolute calibration of reflectivity, and the measurement of diffraction profiles that are independent of the source line-broadening or beam geometry.

Double-crystal measurements, of the type described and referred to in chapter 2, are now required for these long wavelength diffractors. We require calibration data on diffraction profiles, reflection integrals and $2d$ values.

Although the OHM crystal gave very good results for plasma lines of boron, its $2d$ is not ideal either for beryllium or carbon, for which $2d$ values of about 110 Å and 45 Å respectively would be more suitable. Other possible true crystals are KHC $2d$ 31.2 Å (potassium hydrogen cyclohexane-1,2-diacetate), THM $2d$ 52.5 Å (tetradecyl hydrogen maleate) and OAO $2d$ 91.2 Å (dioctadecyl adipate).

This chapter has shown that when the best possible resolution is required, true crystals will out-perform either Langmuir-Blodgett films or synthetic multilayers by an order of magnitude. The particularly good results obtained with OHM make it important now to test a sample of OAO $2d$ 91.2 Å to determine whether or not the predicted resolving power of about 500 at 75.9 Å can be achieved. If it can, then the cross-over between practical crystal and grating instruments would extend to about 90 Å and the wavelength of 25 Å need no longer be regarded as the frontier between good and mediocre Bragg spectroscopy.

References

- ¹ R Bartiromo et al, Rev. Sci. Instrum. 60(2) (1989) 273.
- ² M Bitter et al, Rev. Sci. Instrum. 57 (1986) 2145.
- ³ R. Barnsley, K D Evans, N J Peacock and N C Hawkes,
Rev. Sci. Instrum. 57(8) (1986) 2159.
- ⁴ R Barnsley, U Schumacher, et al, Rev. Sci. Instrum. 62(4) (1991) 889-898.
- ⁵ R Fonck et al, Appl. Opt. 21 (1982) 2115.
- ⁶ J L Schwob et al, Rev. Sci. Instrum. 58 (1987) 1601.
- ⁷ G W Fraser et al, Nucl. Inst. Meth.
A219 (1984) 199, A224 (1984) 272, A261 (1987) 579.
- ⁸ B L Henke, Adv. X-Ray Anal. 7 (1964) 460.
- ⁹ E Spiller, in Low Energy X-ray Diagnostics-1981, Ed. D T Attwood and
B L Henke, AIP Conf. Proc. No 75, (1981) 124.
- ¹⁰ T Barbee, *ibid* p 131.
- ¹¹ R Willingale, PhD Thesis, Leicester University, (1979).
- ¹² T C Huang, A Fung and R L White, X-ray Spectrometry, 18 (1989) 53-56.
- ¹³ W Moos et al Rev. Sci. Instrum. 61(10) (1990) 2733-2737.
- ¹⁴ Sara Luck and David S Urch, Physica Scripta, 41 (1990) 749-753.
- ¹⁵ J H Underwood, in: X-ray data booklet, Publ. by Lawrence Berkeley Lab.
University of California (1986).

6 A COMPACT HIGH-RESOLUTION JOHANN SPECTROMETER

6.1	Introduction	129
6.2	Engineering design	129
6.3	Optical performance	132
6.4	CCD detector	134
6.5	Results	137
6.6	Conclusion	143

291. Edison's phonograph.-

Edison has devised an apparatus for reproducing sound, which is remarkable for the simplicity of its construction and for the striking character of the results which it produces. ... According to Edison's statement, as many as 40 000 words can be stored on a space not exceeding 10 square inches.

*Elementary Treatise on Physics,
Experimental and Applied.
Ganot and Atkinson.
Longman, Green and company. London 1883.*

6.1 INTRODUCTION

This Johann¹ spectrometer was designed to be sufficiently versatile and portable for use on any of a wide range of plasma, ion-beam, electron-beam and synchrotron experiments. In most such experiments there is a need to measure absolute and relative wavelengths, line profiles and line shifts; features that demand high resolving power and stability. The design aim was for a spectrometer giving access to a wide range of Bragg angles and crystal focal lengths without compromising the mechanical stability between the crystal and the detector. By using the Rowland circle radius as a free parameter, the resolving power need be limited only by the crystal.

The instrument has been used on Tokamak, beam-foil and laser produced sources, and has now been fitted with a large area CCD detector, which provides an almost ideal complement to its optical characteristics. Details of alignment, dispersion, aberrations, and sensitivity, together with the first results from a wide range of sources, are covered in detail by Dunn².

6.2 ENGINEERING DESIGN

Structure

High stability is achieved by mounting the crystal and detector to a single rigid beam, or "Rowland chord", which provides a reference axis for all the critical alignments of Rowland circle geometry (fig.2.12). The chord length can be varied between about 0.2 m and 5 m to match the band-pass, dispersion and aberrations to the source, and to suit the spatial resolution of whichever detector is in use. At the longer focal lengths, the central section of the chord is formed by a rigid tube that also serves as part of the vacuum chamber (fig.6.1). This tube is mounted to the chamber at the crystal end via a flexible bellows, allowing access to a range of Bragg angles while isolating the fixed chord from most of the stresses that would tend to distort the optical axis. The crystal chamber is sealed with quickly demountable lightweight clamp-flanges, and a choice of angled ports allows a wide Bragg angle range to be easily accessed.

Crystal bending-jig

Thin crystals of area up to $100 \times 30 \text{ mm}^2$ can be bent to a wide range of focal lengths by a novel four-pillar jig (fig.6.2), which uses flexures to transfer loads to the crystal from adjusting micrometers. The usual way to position the rollers is to use two pointed screws at each end, giving a total of up to 16 adjusters, depending on the jig design. That is an unsatisfactory system

because adjustment of a single screw tends to twist and translate the roller, giving rise to shear forces between it and the crystal. Although it is possible, in principle, to adjust the roller parallelism, in practice it is difficult to maintain it.

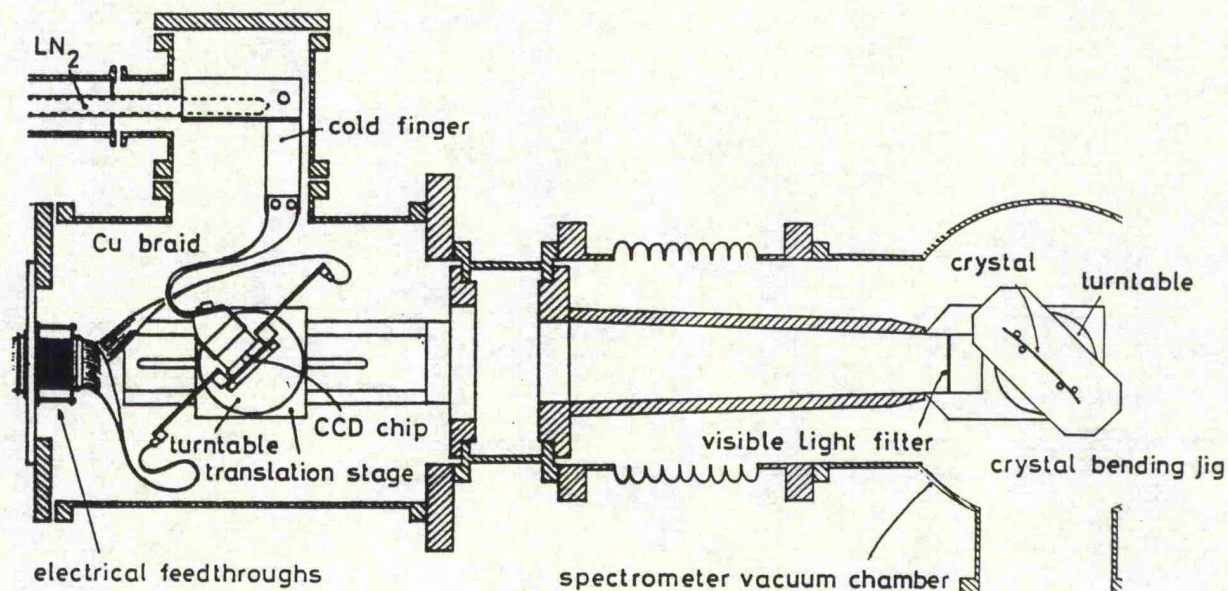


Fig 6.1 Schematic of the diffraction arm of the instrument. The tube connecting the crystal and detector stages can be varied in length between 70 mm and 3 m.

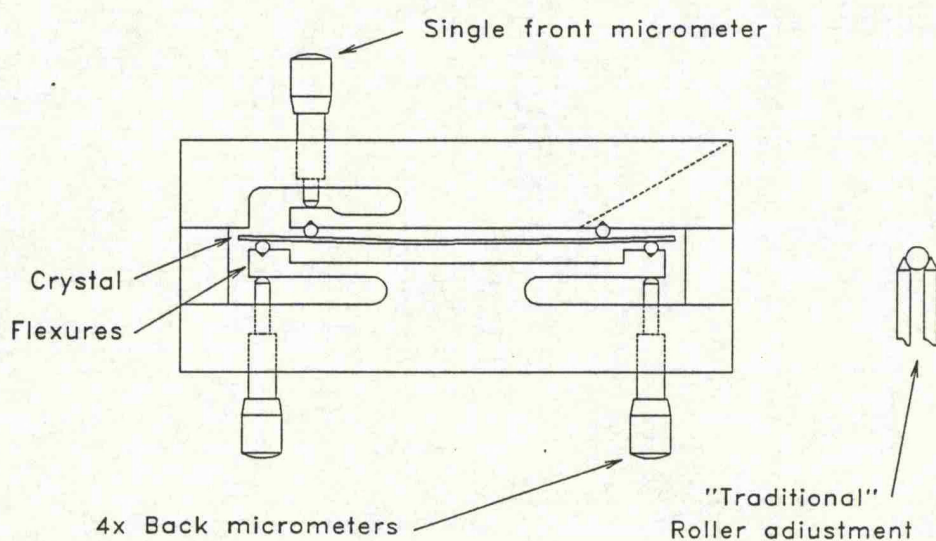


Fig 6.2 Flexure principle of the crystal bending-jig, with detail of the usual means of roller adjustment.

The use of flexures in the new jig means that the functions of support and adjustment can be separated, and the number of adjusting screws reduced to five. The front screw is to correct for any residual twist in the front plate, by setting the front rollers in the same plane. Once this has been set, focusing can take place using the back rollers only, and can usually be achieved in a few minutes. The key to holding a good focus is to tap the jig gently with, for example, a 3 mm Allen key to relax any stresses, until tapping no longer disturbs the focus.

Effect of bending the crystal

The result of bending a crystal is to strain the lattice, which can affect the diffraction process. We can estimate the significance of this by a simple strain analysis. Using the standard beam-bending relation, a uniform beam subject to a local bending moment M , takes up a local radius of curvature R , and develops a tensile stress σ_x at a height y above the neutral axis

$$\frac{M}{I} = \frac{\sigma_x}{y} = \frac{E}{R} \quad (6.1)$$

where we have: stress σ (N.mm^{-2}), strain ϵ , Young's modulus $E = \sigma/\epsilon$ (N.mm^{-2}), second moment of area I (mm^4). For a symmetrically loaded simply-supported beam such as the crystal in a four-pillar bending jig, the bending moment and hence the radius, is constant between the inner loads.

The change in the $2d$ value at the crystal surface is

$$\frac{\Delta 2d}{2d}(y) = \epsilon_y = -\nu \epsilon_x = -\frac{\nu \sigma_x}{E} = -\frac{\nu y}{R} \quad (6.2)$$

where ν (≈ 0.3) is Poisson's ratio. Taking $y = 0.15$ mm, $R = 300$ mm, which would be quite practical when using a high spatial resolution detector, we obtain $\Delta 2d/2d \approx -1.5 \cdot 10^{-4}$. This reduction in the lattice spacing is comparable to the diffraction width for typical high-resolution crystals.

The effective penetration depth of the incident x-ray beam normal to the crystal face is approximately

$$\delta y \approx \frac{\sin \theta_B}{\mu_1} \quad (6.3)$$

where μ_1 is the linear absorption coefficient. Now the $\Delta 2d/2d$ at the penetrated depth $y-\delta y$ is

$$\frac{\Delta 2d}{2d}(y-\delta y) = -\frac{\nu}{R} \left(y - \frac{\sin \theta_B}{\mu_1} \right) \quad (6.4)$$

Thus the relative change in $2d$ across the absorption depth is

$$\frac{\delta 2d}{2d} = \frac{\Delta 2d}{2d}(y) - \frac{\Delta 2d}{2d}(y-\delta y) = -\frac{\nu y}{R} + \frac{\nu}{R} \left(y - \frac{\sin \theta_B}{\mu_1} \right) \quad (6.5)$$

so that

$$\frac{\delta 2d}{2d} = - \frac{\nu \sin \theta_B}{\mu_1 R} \quad (6.6)$$

which interestingly is independent of the crystal thickness or Young's modulus, and is greatest for a low-Z crystal and high photon energy. For a near worst-case example of 12 keV x-rays in Si(440) crystal ($\rho = 2.3 \text{ g/cm}^3$, $\mu = 20 \text{ cm}^2/\text{g}$, $\mu_1 = 46 \text{ cm}^{-1}$) bent to a radius of 300 mm, the value is about 10^{-4} , which would cause additional broadening of the diffraction profile, comparable with the plane-crystal value.

A more rigorous evaluation³ has shown that the reflection integral and diffraction width are both increased by bending the crystal, with the critical radius being about 0.4 m.

6.3 OPTICAL PERFORMANCE

Alignment in visible light

A tungsten lamp, orange filter and variable slit provide a quasi-monochromatic line source which is focused onto a standard eye-piece to set the required crystal radius. The use of monochromatic light assists focusing, and allows assessment of the focus quality by measuring the fringe pattern produced by diffraction at the crystal aperture. A micro-densitometered photographic image of the optical focus is shown in figure 6.3. For the crystals used to date, no correction has been found necessary for any offset between the optical surface and the diffracting planes.

Resolving power

The optical focusing and alignment procedure allows absolute wavelength calibration accurate to about 1 part in 3000, and relative measurements to about 2 parts in 10^5 . The instrumental resolving power ($\lambda/\delta\lambda$) is limited mainly by the crystal diffraction width, and depending on the crystal is typically 10^4 in the wavelength range from 1 Å to 13 Å.

The best resolving power that has been demonstrated to date was of Ne X ions in a beam-foil source, produced by stripping a beam of 39 MeV Ne⁶⁺ ions in a 0.5 μm carbon foil, at the Oxford University Folded Tandem accelerator. For this observation - the first axial observation of such a source⁴ - the viewing direction was chosen to minimize Doppler broadening due to the source (fig.6.4). The resulting Ne X Ly $\alpha_{1,2}$ spectrum (fig.6.5) was recorded during a 30 hr exposure on photographic film, using a KAP (002) crystal ($2d=13.316\text{Å}$) bent to a radius of 1073 mm. It shows a resolving power of $\lambda/\delta\lambda = 4400$, which is about a factor two lower than the calculated single-crystal value⁵, and if recorded from a plasma would be equivalent to an ion temperature of 180 eV.

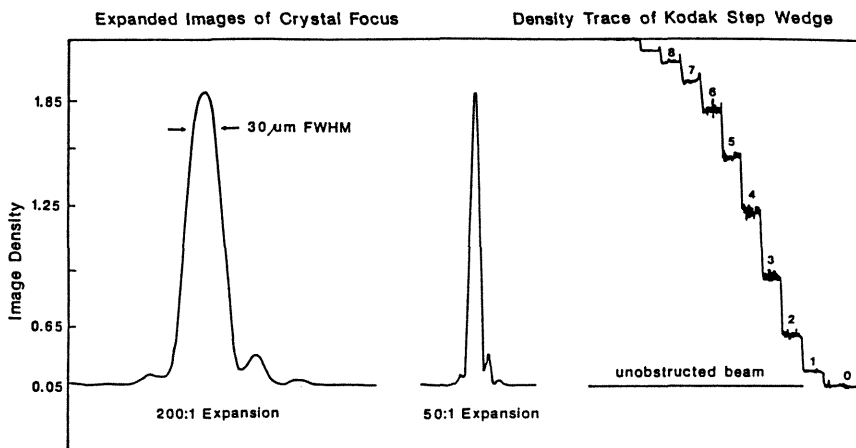


Fig 6.3 A calibrated densitometer trace of the optical focus (Dunn¹)
A FWHM of 30 μ m at 1 m radius is typical.

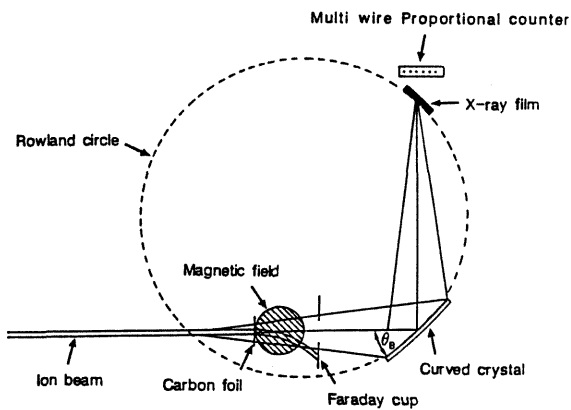


Fig 6.4 Schematic of the axial observation of a beam-foil source.

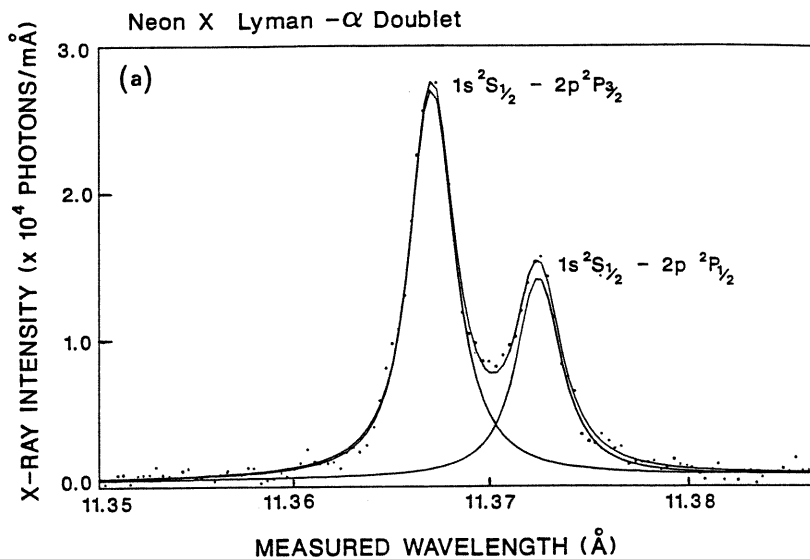


Fig 6.5 Ne X Ly α spectrum from the axial observation of beam-foil source. The wavelength is blue-shifted due to the ion-beam velocity.

6.4 X-RAY CCD DETECTOR

Like many other x-ray detectors, such as photographic film and micro-channel plates, the charged coupled device (CCD) was originally developed for the visible spectrum. It is also potentially the ideal imaging x-ray detector, offering high QDE, high spatial resolution and good energy resolution. Much of the development of CCDs as x-ray detectors has been led by the x-ray astronomy community, and has been reviewed by Fraser⁶.

A CCD is an array of metal-oxide-silicon (MOS) capacitors, formed by depositing parallel electrodes onto the oxidized surface of a silicon wafer. Most CCDs use the three-phase frame-transfer system developed for TV cameras, illustrated in figures 6.6 and 6.7. Photons absorbed during integration create electron-hole pairs, which are trapped in pixels formed by the depletion region under the electrodes. Each pixel is defined by a triplet of electrodes, whose clocking during readout is phased so as to transfer packets of charge along the array. After integration the image is moved in parallel onto the store section and thence line-by-line to the read-out register, from where it is read out serially via a single preamplifier.

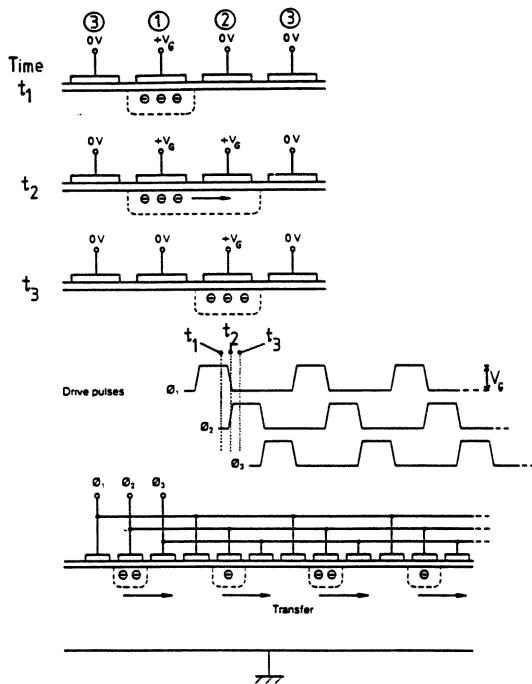


Fig.6.6 Charge transfer between pixels in a three-phase CCD. Each pixel is defined by a triplet of electrodes whose clocking is phased so as to transfer packets of charge along the array.

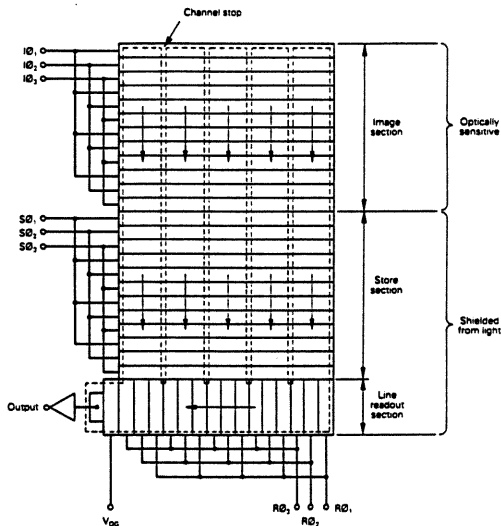


Fig.6.7 Operating principle of a frame-transfer CCD. After integration the image is moved in parallel onto the store section before being read out serially, line-by-line, from the read-out register.

The capacitance at the read-out node is only about 0.1 pF so that, by cooling the array to -100°C and using low noise electronics, it is possible to measure the charge created by single soft x-ray photons. The achievable energy resolution is about 150 eV, which is comparable with Si(Li) detectors, and makes the CCD an energy dispersive spectrometer in its own right. The currently achievable (standard electrode) and projected (open electrode) QDE of CCD detectors is shown in figure 6.8.

The CCD array has many advantages which make it the near-ideal detector for use with a Johann spectrometer:

- 22.5 μm 2-D spatial resolution with negligible spatial linearity error.
- High dynamic range with good intensity linearity.
- 20% to 80% quantum detection efficiency for soft x-rays.
- 150 eV energy resolution in low count-rate mode.
- ~ 10 ms time resolution (with on-chip binning).
- Wide range of read-out modes can be programmed.
- Solid state, no high voltage or need for high vacuum.

The CCD detector used on this instrument (fig.6.1) was developed by the X-ray Astronomy Group at Leicester University⁷, primarily for astrophysical observations. It has a 2-D spatial resolution of 22.5 μm (1152 x 1242 pixels, 26 x 28 mm^2) and a quantum detection efficiency (QDE) greater than 20% between 0.7 keV and 12 keV.

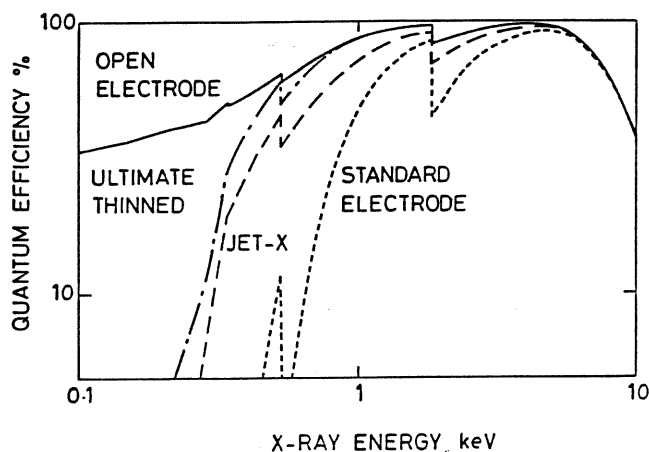


Fig 6.8 The soft x-ray quantum detection of CCD detectors. Present (standard electrode) and projected (open electrode).

Photon-counting with energy resolution

Cooling to -100°C with liquid nitrogen results in a noise per pixel of about 5 electrons RMS. By digitizing the collected charge, single x-ray photons can be detected with an energy resolution of about 150 eV, provided the count rate is low enough to avoid a significant number of pixels with multiple photons. This mode is important for low flux (and possibly high background) sources common with beam-foil, beam-gas and ion-trap experiments, where the low read-out noise will allow long integration times, and the energy resolution will give good background rejection. Using a 12-bit ADC, read-out time for the full image is about 5 s.

On-chip compression for high fluxes

To deal with count-rates typical of high-flux sources such as a Tokamak, it is necessary to sacrifice the energy resolution by collecting multiple photons per pixel. In order to obtain a time resolution of order 1 ms, the two-dimensional line spectrum can be binned on the frame-transfer region of the CCD to give a 1-D histogram. For an extremely intense source such as a synchrotron, a time resolution of $\sim 10\ \mu\text{s}$ could be achieved by masking all but a single line on the array, and operating in a quasi-streak-camera mode.

6.5 RESULTS

DITE Tokamak

The instrument was originally used on the DITE Tokamak, initially with photographic film, and later with a prototype CCD system which used a standard TV chip in video mode recording to video tape¹. Figure 6.9 shows the DITE installation, while figure 6.10 shows an Al XII spectrum recorded on film using an ADP ($2d = 10.648\ \text{\AA}$) crystal bent to a radius of 1250 mm. The line profiles are dominated by Gaussian Doppler broadening at the measured ion temperature of 950 eV.

Laser-produced plasma

Laser-produced plasmas from the Rutherford Appleton Laboratory VULCAN laser were diagnosed in order to derive electron densities⁸ from Al XI dielectronic satellites to the Al XII $1s^2-1s2p$ resonance line at $7.757\ \text{\AA}$ (fig.6.11). In this spectrum, which covers the same region as figure 6.7, the line profiles are mainly Lorentzian due to Stark broadening. The forbidden line z, present in the Tokamak spectrum, is absent due to the high density.

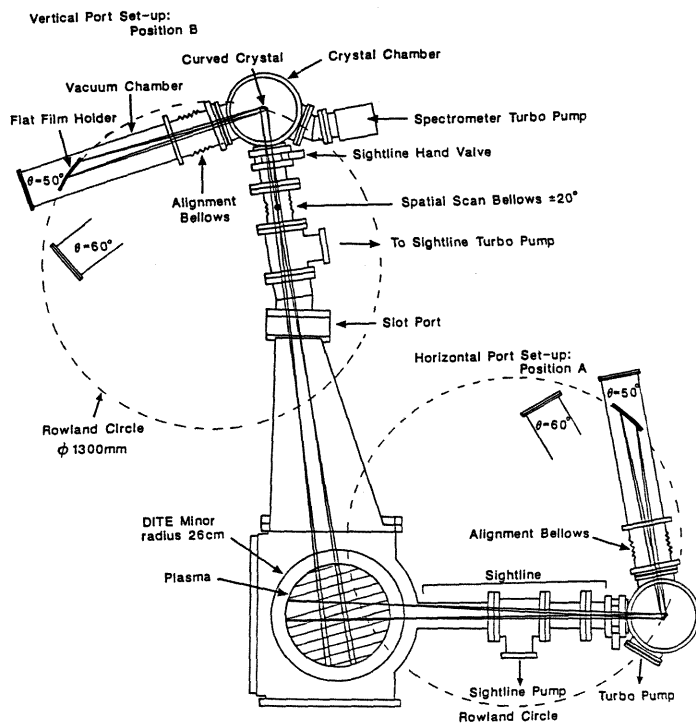


Fig 6.9 Two alternative installations on the DITE Tokamak. The vertical port allowed radial profile to be obtained.

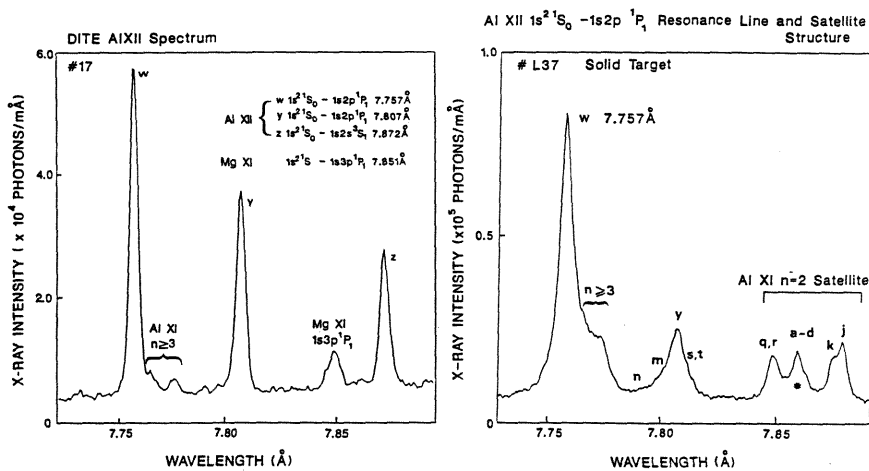


Fig 6.10 (left) Al XII spectrum from the DITE Tokamak. Recorded on film using an ADP crystal bent to a radius of 1250 mm. (Dunn¹).

Fig 6.11 (right) Laser-produced spectrum of Al XII. Recorded on film from a single laser pulse (7 J, 20 ps, 0.52 μ m). PET crystal, 300 mm radius. (Dunn¹).

For this observation the crystal jig and film holder were mounted to an optical bench inside the laser target chamber. The spectrum was recorded on film from a single green laser pulse (7 J, 20 ps, $\lambda = 0.52 \mu\text{m}$), using a PET(002) ($2d = 8.742 \text{ \AA}$) crystal at radius of 300 mm.

Results from the JET Tokamak

In two short demonstrations on the JET Tokamak, the instrument was set up initially in photon counting mode and later, in the on-chip compression mode.

A sequence of spectra was recorded throughout JET pulse no. 26938, using a Ge(220) crystal bent to a radius of 1400 mm. First and second order lines are superimposed (fig.6.12), but can be discriminated by using the energy information also stored in the image. The energy spectrum of all pixels on the CCD array, integrated during a single frame, is shown in figure 6.13. The photon flux was on the upper limit for single-photon counting, so that many pixels have more than one event, and almost every pixel had some charge due to events that were spread over more than one pixel.

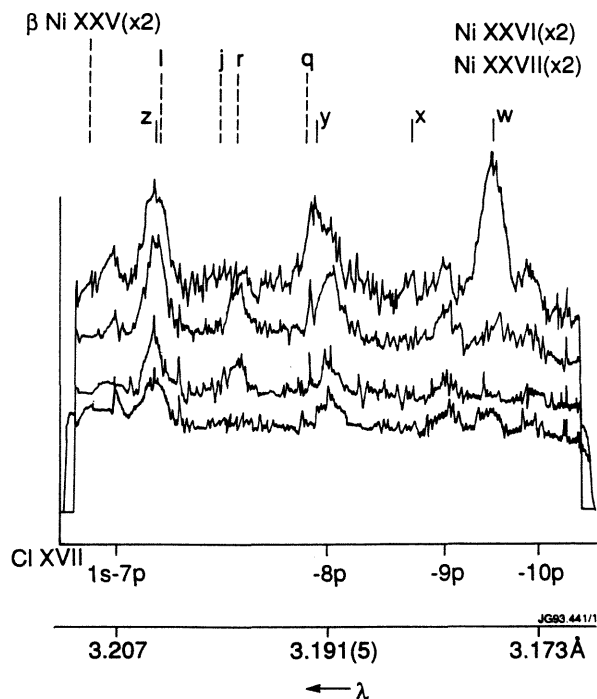


Fig 6.12 A sequence of spectra recorded throughout JET pulse no. 26938, using a Ge(220) crystal bent to a radius of 1400 mm. First and second order lines are superimposed, but can be discriminated by using the energy information also stored in the image.

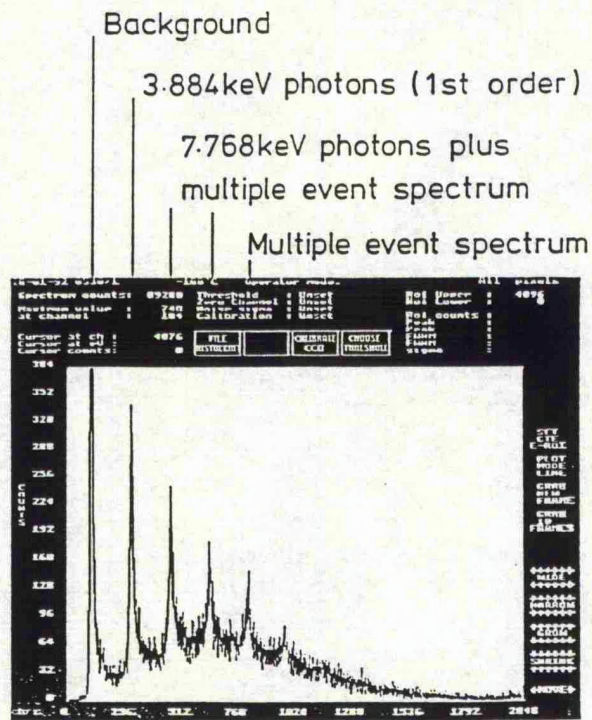


Fig 6.13 The energy spectrum of all pixels on the CCD array, integrated during JET pulse no. 26938. The photon flux was on the upper limit for single-photon counting, and many pixels have more than one event.

The spectrometer was later installed on JET for the last day but one of 1992 operations, this time to demonstrate the time-resolving mode of the CCD array. A Si(111) crystal, $2d = 6.271 \text{ \AA}$, was bent to a radius of 997 mm and set up to observe the spectrum of He-like Cl XVI. The frame-store half of the CCD array was masked, and the open area was protected against visible light by a graphite-coated $2 \mu\text{m}$ Mylar filter. A single exposure was made where the full 2-D image was saved, in order to check the position of the image on the CCD array, and the alignment of the spectral lines with the pixel columns (necessary for on-chip compression). All other discharges were recorded using the on-chip binning mode, which gave a time resolution of 40 ms for the full discharge duration of about 23 s.

The time-resolved spectrum of Cl XVI from a neutral-beam heated JET discharge is shown in figures 6.14 and 6.15, and a time-slice is shown in figure 6.16. The line profiles are dominated by thermal Doppler broadening at the ion temperature (relevant to the radial position in the plasma of the Cl XVI emitting region) of about 3 keV. A Doppler blue-shift due to beam-induced plasma rotation is visible during neutral-beam injection. A further demonstration of the time-resolution was made by injecting a mixture of Mo and Ge into the plasma by laser ablation, which caused several transient lines to be recorded. Time evolutions of the derived Doppler shifts and widths⁹ are shown in figure 6.17

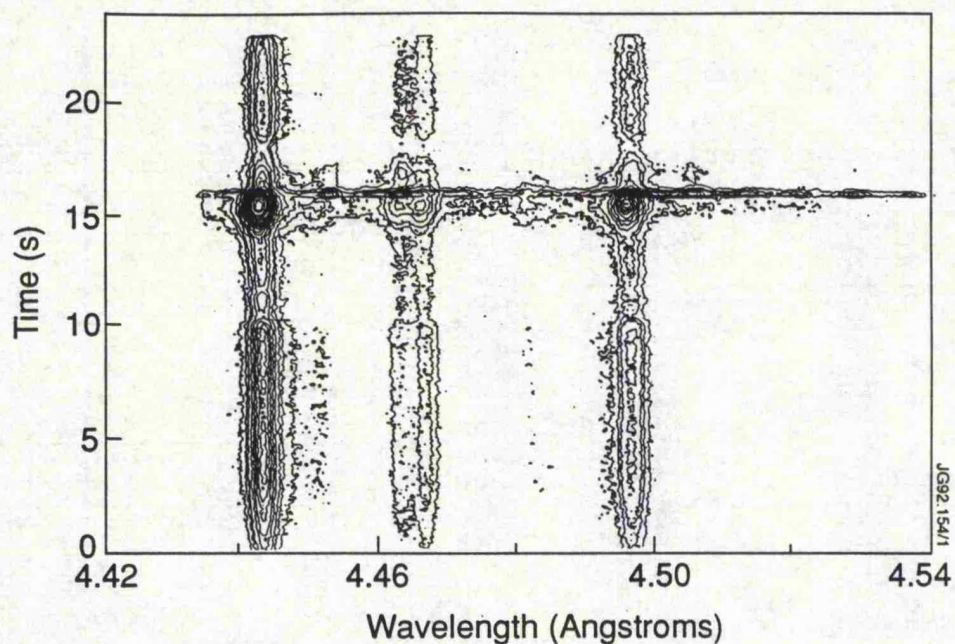


Fig 6.14 Contour plot of the time-resolved spectrum of Cl XVI.

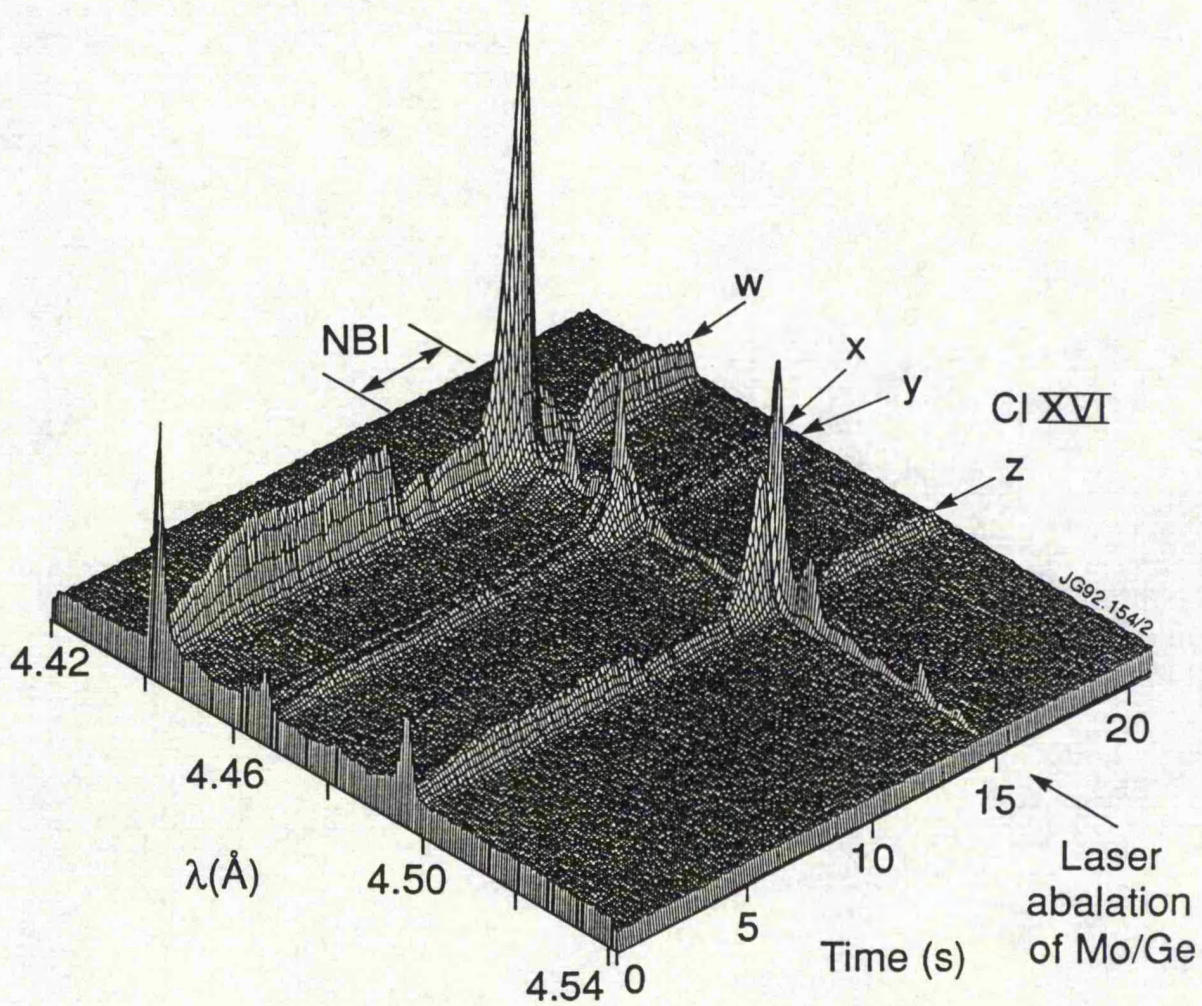


Fig 6.15 Isometric plot of the time-resolved spectrum of Cl XVI.

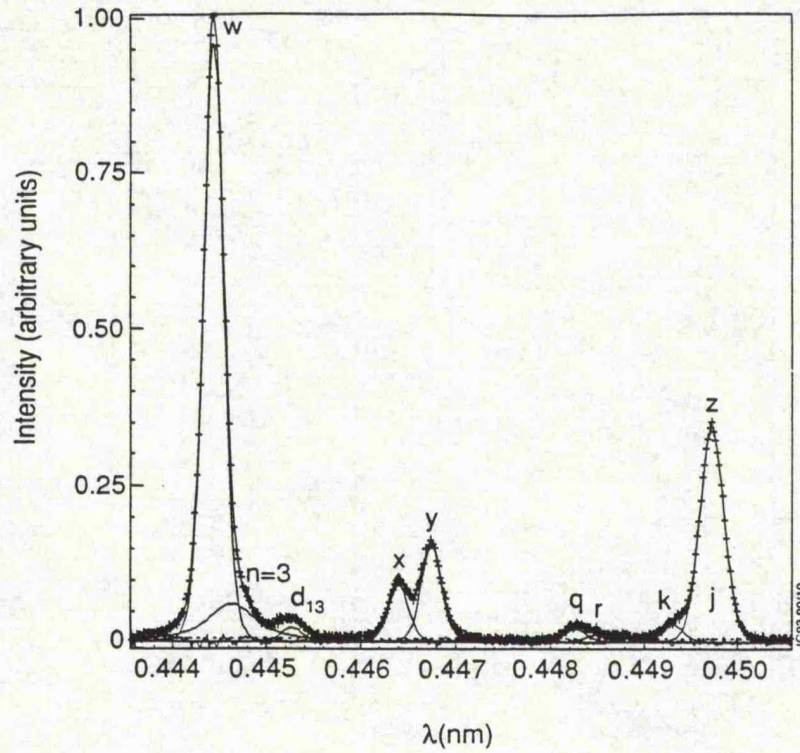


Fig 6.16 The spectrum of He-like Cl XVI, integrated over about 2 s.

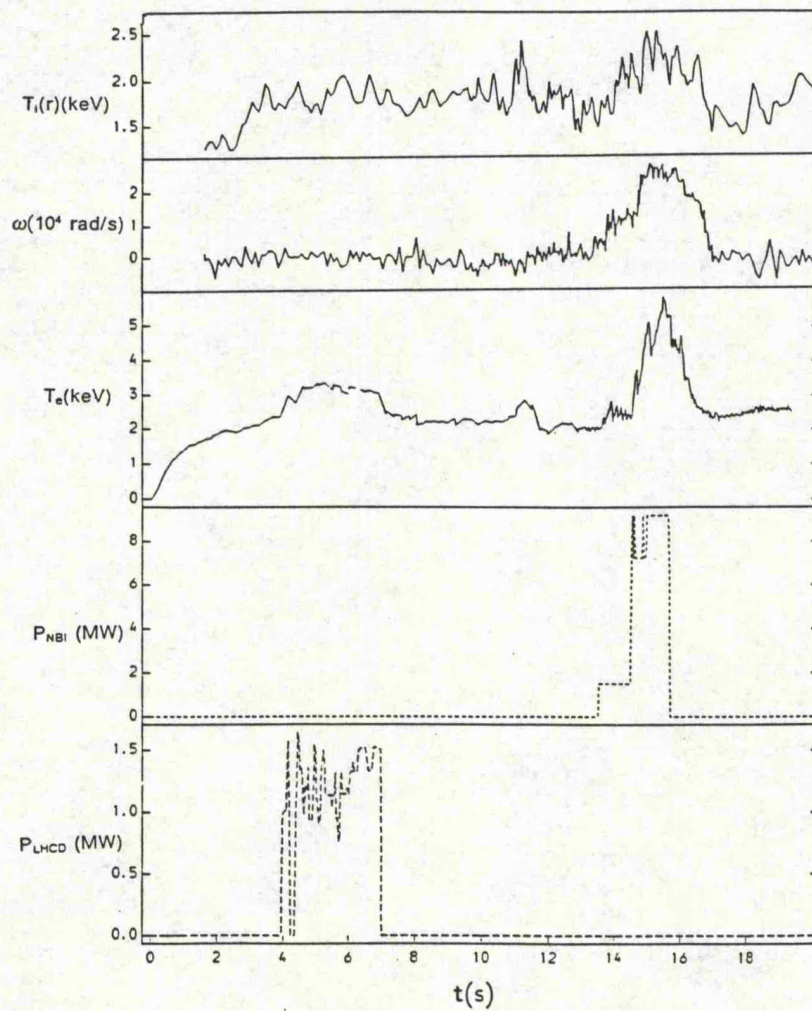


Fig.6.17 Time-resolved Doppler shifts and widths from figure 6.14. (Coffey⁸)

For the set-up used to record the Cl XVI spectrum from JET, a single pixel of 22.5 μm corresponded to a resolving power $\lambda/\delta\lambda$ of about 40 000. This was well-matched to the crystal resolving-power of about 7 000. The overall instrumental resolving power, including Johann aberrations, was about 5000; equivalent to a chlorine ion temperature of 250 eV. A Doppler shift of one pixel was equivalent to a velocity of 7.5 km/s, it being possible to find the line centroid to much better than one pixel, given good counting statistics. This is borne out by the rotational velocity plot in figure 6.17, where the scatter in the measurement during neutral-beam heating (when the line intensity was greatest) is about 7.5 km/s. Given that the beamline viewed only a $\sin 19.5^\circ$ (0.334) component of the toroidal rotation (fig 10.1), this is equivalent to a measureable shift of 2.5 km/s.

6.6 CONCLUSION

The main factors distinguishing this instrument from others are the easily-focused crystal-jig, the rigid mounting between the crystal and detector stages, and the compact portable construction. All these features have contributed to the success of experiments on a wide range of laboratory sources of highly ionized atoms.

The incorporation of an x-ray CCD detector with several programmable operating modes has greatly increased the suitability of the instrument for a large variety of both high-flux and low-flux experiments.

References

- ¹ H H Johann, Z. Phys. 69 (1931) 185-206.
- ² J Dunn, PhD Thesis, Leicester University, 1990.
- ³ R Caciuffo et al, Rev. Sci. Instrum. 61(11) 3467 (1990).
- ⁴ J M Laming et al, Phys Lett A, 126(4) 253-257 (1988).
- ⁵ M Lewis, PhD Thesis, Leicester University, 1980.
- ⁶ G W Fraser, X-ray detectors in astronomy, Cambridge University Press, 1989.
- ⁷ E G Chowanetz, D H Lumb and A A Wells, SPIE 597, 38 (1985).
- ⁸ G J Tallents et al, RAL Annual Report 1989.
- ⁹ I H Coffey, PhD Thesis, Queen's University Belfast, (1993).

7 IMPURITY MONITORING

7.1	Introduction	145
7.2	Impurity Surveys	145
7.3	Absolute Measurements	152
7.4	Conclusion	156

(397a) Another mode of expressing the heat generated and radiated off from the sun's surface, well calculated to impress us with an overwhelming idea of the tremendous energies there constantly in action, is that employed by Professor Thomson, who estimates the dynamical effect which would be produced in our manufacturies by a consumption of fuel competent to evolve the heat given out by each individual square yard of that surface, at 63 000 horse-power, to maintain which would require the combustion of 13 500 pounds of coal per hour.

*Outlines of Astronomy
Sir John F W Herschel
Longman, Green and company. London 1893.*

7.1 INTRODUCTION

The first task of an impurity spectroscopy system must be to monitor all possible impurities throughout every discharge, and this is now possible with the extended wavelength-range Bragg rotor spectrometer. This should end the frustration of having to explain to an unsympathetic session-leader that today's crystal doesn't happen to suit the impurity that might have just caused a disruption. Beyond this relatively straightforward task lies the severe problem of measuring absolute impurity concentrations.

There is a great need for absolute measurements of impurity data, particularly of their contributions to the radiated power and to plasma dilution. While there are problems for the light impurities, some progress has been made. The availability of time-resolved data for all the impurities means that a quantitative analysis of the complete impurity picture is possible, rather than of just a few impurities in isolation.

The main alternative to passive spectroscopy for deriving impurity concentrations is charge exchange recombination spectroscopy (CXRS)¹. This has the advantage of making local observations in the visible spectrum of the fully stripped light ions in the plasma core. A disadvantage is that a neutral beam is required, whose attenuation across the plasma must be measured or modelled. Furthermore, the charge-exchange cross-sections for visible transitions of medium and high-Z impurities are very low, limiting observations to about $Z \leq 8$ (O).

7.2 IMPURITY SURVEYS

The high instrumental sensitivity and the relatively uncomplicated spectrum mean that new occurrences of unplanned impurities are easily identified, and are normally detected by the crystal spectrometer before the XUV instruments.

DITE tokamak

The Mkl Bragg rotor spectrometer was the main monitor of core impurities in DITE from late 1985 until early 1988, when the project came to its end. During this period the instrument was used in several experiments, including transport studies (chapter 8), investigation of a new limiter design (chapter 7.3) and electron cyclotron resonance heating (chapter 9.2). The upper wavelength coverage was restricted to about 25 Å, limiting the observable impurities to $Z \geq 7$ (nitrogen).

As well as monitoring the intrinsic impurities, the continuous spectral coverage allowed the early detection of several unexpected impurities. The most notable of these was the initial detection of magnesium, followed by a rapid shot-to-shot increase. This was traced to the loss of insulation from a cracked sensor-coil, which eventually required an opening of the vacuum vessel to allow a repair. Other impurities were detected occasionally, including F, Si, K, and Ni.

Typical DITE survey spectra are shown in figures 7.1 and 7.2, which contain all the main intrinsic impurities except carbon. The presence in figure 7.1 of the Ar-K absorption edge is due to the detector gas, and shows that the background signal is mainly due to diffracted continuum signal and not scattered radiation. This spectrum is typical of the soft x-ray region, and consists mainly of easily-identified H-like and He-like transitions, separated by relatively wide bands of continuum. The sensitivity and signal-to-noise ratio of the instrument is such that the effective noise level for the detection of a trace impurity is the statistical variation in the continuum signal.

Spectra from two different radii, recorded with the rotor scanning at 3.33 Hz, are shown in figure 7.3. A radial scan of such a spectrum gives profiles of several different ionization stages: for example of O VIII, shown in figure 7.4, and Abel inverted in figure 7.5.

DITE impurity control limiter

The Bragg rotor spectrometer was used to monitor the effect on the intrinsic impurities of a novel divertor design². The main feature of the impurity control limiter (ICL) (fig.7.6) was the hollow shape facing the plasma, and the relatively sharp edge. This design meant that impurities sputtered from the limiter would be more likely to be lost in the scrape-off layer than to enter the plasma. The effect of the ICL on O VIII and Fe XVII is shown in figures 7.7 and 7.8 respectively, where the central-chord line intensities were normalized by the line-integrated density in order to reflect their concentrations. This is approximately valid, since the emission from the ions was peaked just off-axis and was relatively insensitive to temperature variations. In helium discharges the insertion of the ICL resulted in a 50% reduction in the total radiation and a 37-66% reduction in the impurity contribution to Z_{eff} compared with the values obtained with rail limiters of conventional geometry. In deuterium discharges, the reduction in the total radiation was only 20%; this was attributed to the greater importance of wall sources of carbon and oxygen in deuterium plasmas relative to those in helium.

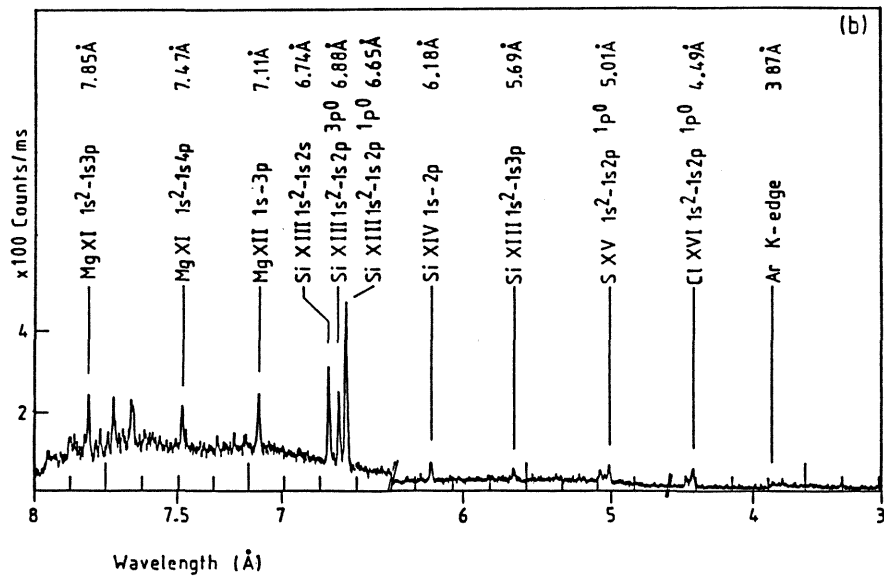


Fig.7.1 Survey spectrum from the DITE tokamak, obtained using a PET crystal.

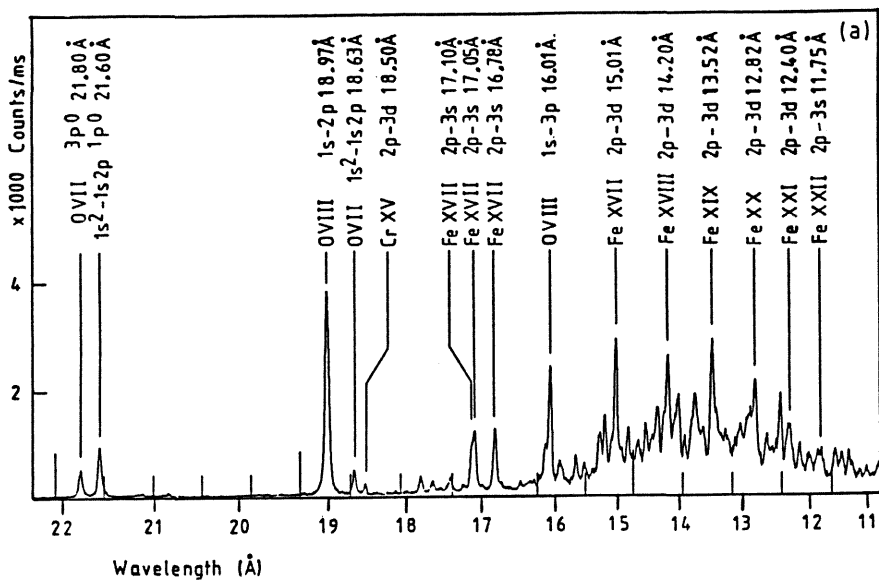


Fig.7.2 Survey spectrum from the DITE tokamak, obtained using an RAP crystal.

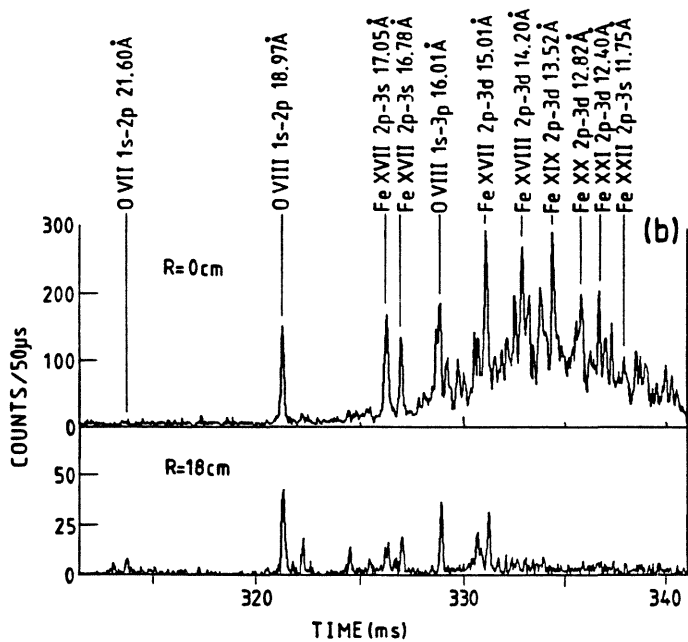


Fig.7.3 DITE survey spectra from two lines of sight.

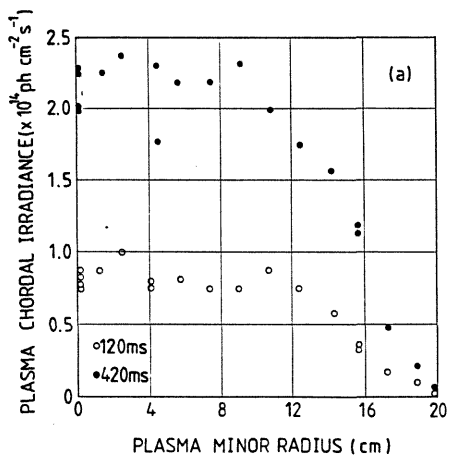


Fig.7.4 Line-of-sight profiles of O VIII, recorded during a sequence of identical DITE discharges.

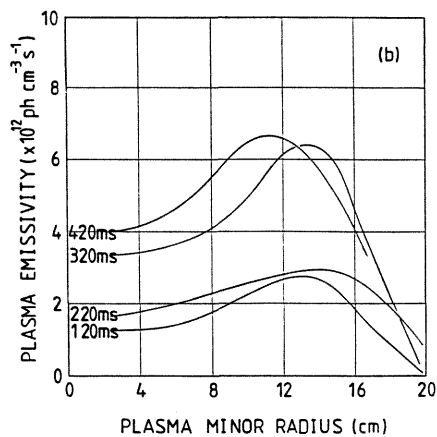


Fig.7.5 Abel inverted data from the profiles shown in figure 7.4.

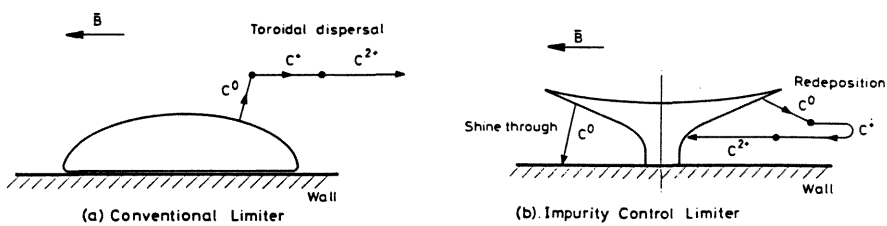


Fig.7.6 Schematic of the DITE impurity control limiter.

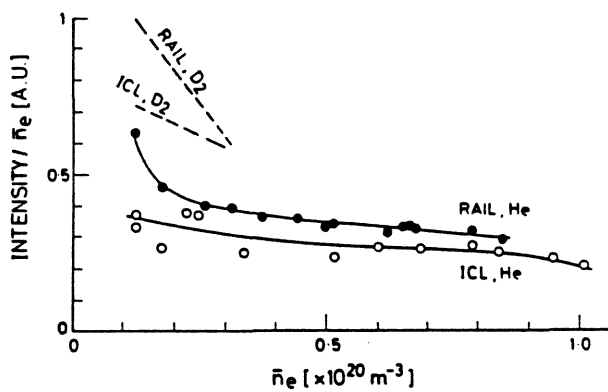


Fig.7.7 Showing the effect of the DITE impurity control limiter on O VII.

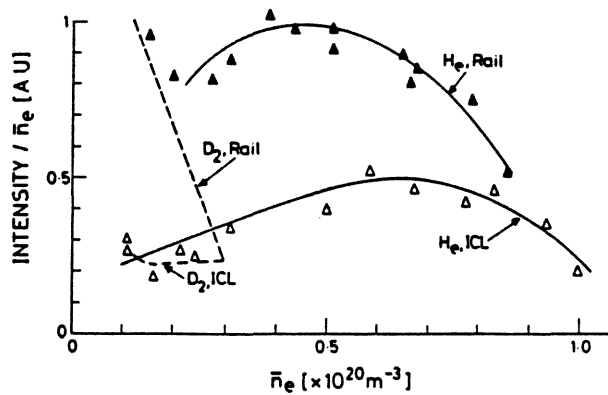


Fig.7.8 Showing the effect of the DITE impurity control limiter on Fe XVII.

JET tokamak

During 1991 the Mk2 Bragg rotor spectrometer with extended wavelength coverage was developed, and commissioned on JET (ch.3). Typical JET survey spectra are shown in figure 7.9, which shows all the main JET impurities, and has almost complete coverage from 2 Å to 100 Å. Spectra resulting from unexpected influxes of Al and Zn are shown in figures 7.10 and 7.11 respectively.

The stable calibration of the instrument made it possible to monitor the long-term impurity behaviour, as shown in figure 7.13, which shows the session-by-session mean impurity intensity for a month of JET operations.

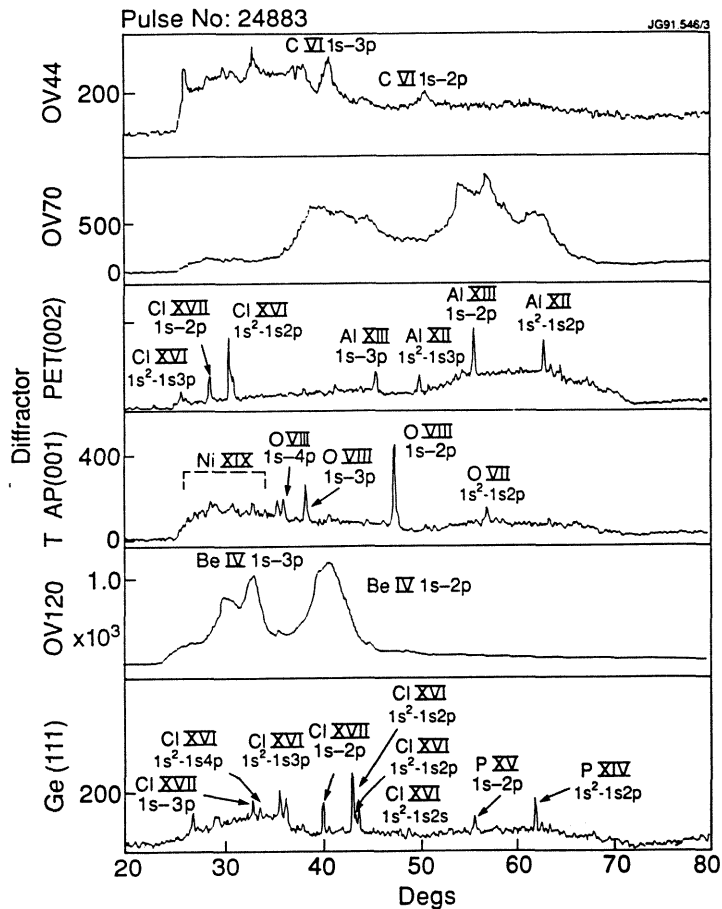


Fig.7.9 Typical survey spectra from JET, using a range of crystals and multilayers on a hexagonal rotor. Spectral coverage is almost complete from 2 Å to 100 Å, thereby monitoring all impurities.

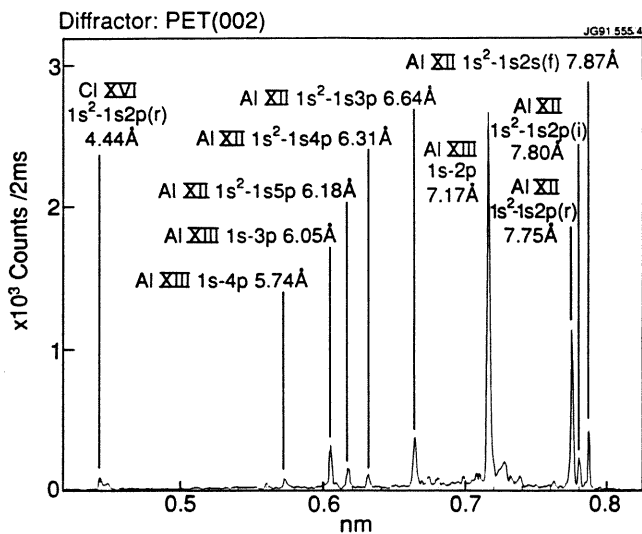


Fig.7.10 JET spectrum of H- and He-like Al, recorded using PET (002) $2d = 8.742 \text{ \AA}$.

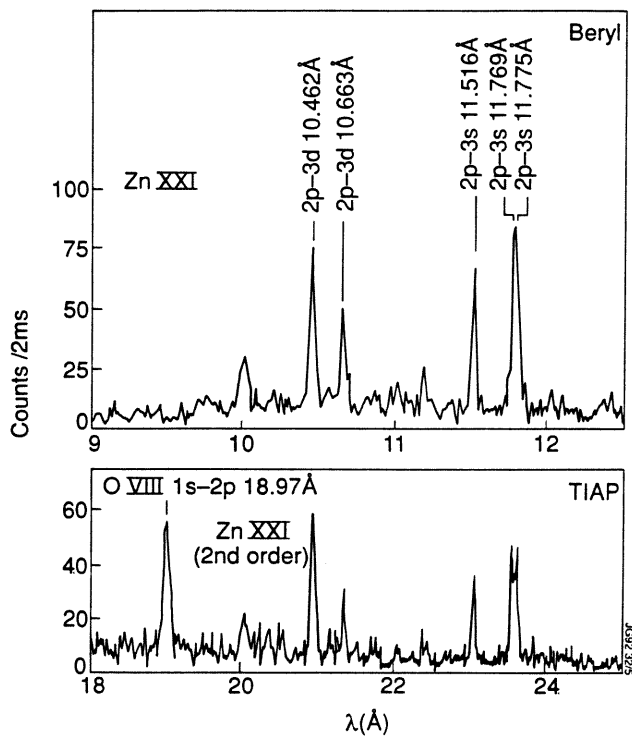


Fig.7.11 JET spectra of the main 2-3 transitions of Zn XXI, recorded with Beryl (1010) $2d = 15.954 \text{ \AA}$, and TIAP (002) $2d = 12.88 \text{ \AA}$.

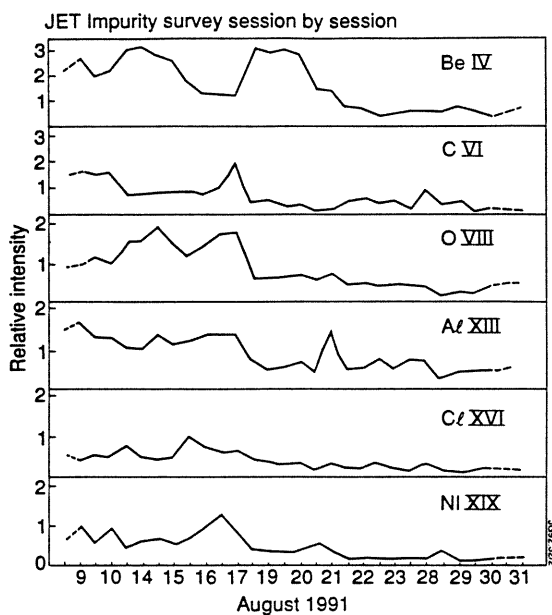


Fig.7.12 Line intensities of the main impurities, measured during the early Ohmic phase of each discharge, for one month of JET operation. Note the general anti-correlation between beryllium and carbon, and the long time-constant for the decay of chlorine.

7.3 ABSOLUTE MEASUREMENTS

In principle it is possible to derive P_{rad} components and impurity concentrations using a transport code together with an instrument absolute calibration, but for low-Z ions the uncertainties are too great at present to yield results that are consistent with independent P_{rad} and Z_{eff} measurements. Errors arise from uncertainties in the parameters of the outer region of the plasma, where low-Z impurities mostly radiate, from the atomic physics and from the instrument absolute calibration.

At the time of writing, absolute calibrations were not available for the multilayers used to observe Be and C, so it was not possible to make independent absolute measurements of the light impurities, which contribute most to the radiated power and fuel dilution. To overcome this problem, the intermediate step was taken of deducing the radiated power components for each impurity, and using these, instead of line intensities, as inputs to the transport code.

The results discussed in this section were obtained during the JET preliminary tritium experiment (PTE), and although this did not affect the analysis, they are unique since the grating VUV/XUV instruments were inoperable due to high neutron background and lack of tritium compatibility. Details of the techniques necessary to achieve these results during the JET PTE are discussed in chapter 10.

Radiated power

P_{rad} components were derived by fitting a set of coefficients k_z to the individual line intensities I_z , such that the sum $\sum_z k_z I_z = P_{\text{rad}}$: the total radiated power as measured by bolometry. This technique, developed by Lawson³, requires that the time evolutions of the impurity line intensities be sufficiently different from one another to identify their signatures on the bolometry, a condition that can usually be met by analysing a large enough number of pulses. An example of this technique applied to VUV/XUV data is shown in figure 7.13, where the very different time signatures of the various impurities, particularly Be and Cl, allowed their contribution to P_{rad} to be derived, even without any knowledge of the instrument calibration.

To minimize the sensitivity to profile effects, the best lines to monitor are those whose emissions peak neither on axis, where they would be temperature sensitive, nor near the separatrix, where they would be most sensitive to transport. The ideal for JET is ions with ionization and excitation energies around 1 keV, though this is not possible for the light elements such as Be and C.

The technique is open to the objection that it by-passes plasma and atomic physics, and that there is no reason why the intensity of any given line should be proportional to the power radiated by that impurity. In practice however, if lines are chosen whose emission is peaked off axis, their central chord integrated intensity is not unduly sensitive to the plasma parameters. This assumption can break down in some cases, such as the H-mode, where emission from the observed ion is confined to a thin shell at the plasma edge.

The results of the same technique applied to Bragg spectroscopic data are shown in figure 7.14 for the main radiating impurities Be, C, and Cl, in a D-T discharge. The agreement in the Ohmic phase of the discharge is good, but there is up to a factor two discrepancy in the beam-heated phase. The time resolution was limited to about 1 s by the scan speed available at the time. There is no data point for C at 12 s, and the resulting interpolation has overestimated the radiated power at that time.

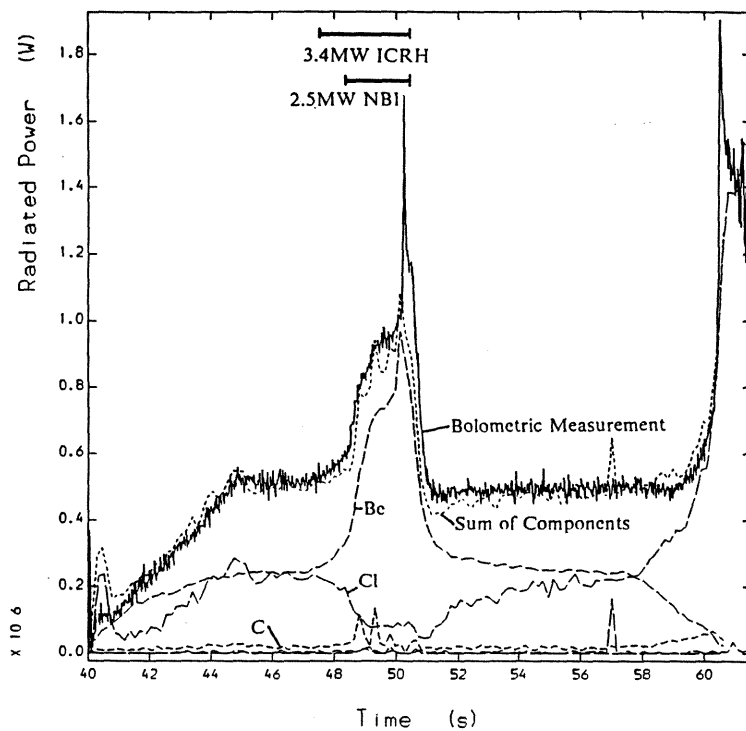


Fig.7.13 Radiated power components derived by fitting VUV/XUV grating spectrometer line intensities to the total radiated power P_{rad} (Lawson).

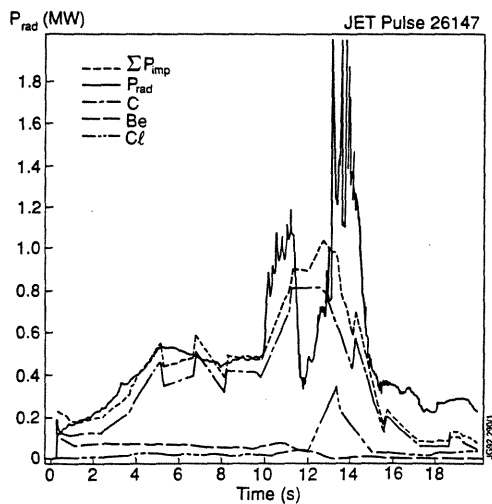


Fig.7.14 Radiated power components derived by fitting line intensities to the total radiated power (P_{rad}). The time resolution was limited by the scan time of the hexagonal rotor.

Impurity concentrations

The main feature of this part of the analysis was the use of P_{rad} components derived by the above technique as inputs to the SANCO time-dependent impurity transport code, which uses measured T_e and n_e profiles, and transport coefficients obtained from experiments at JET^{4,5}. The derived concentrations are about a factor two higher than needed for consistency with the visible bremsstrahlung value $Z_{\text{eff-vb}}$. This is considered to be good agreement in view of the uncertainties inherent in modelling central chord data.

These interim concentrations are then normalized to $Z_{\text{eff-vb}}$ at a time of 6 s, thus only relying on the code to model the relative impurity abundances. The results (fig. 7.15) are consistent with Z_{eff} up to about 12 s, but do not show the sharp increase at 13 s recorded by charge exchange spectroscopy. This is partly due to the scanning time resolution of the Bragg spectrometer data, but may also be due to the problems of modelling the light impurity radiation in the H-mode, where the edge profile effects are most severe.

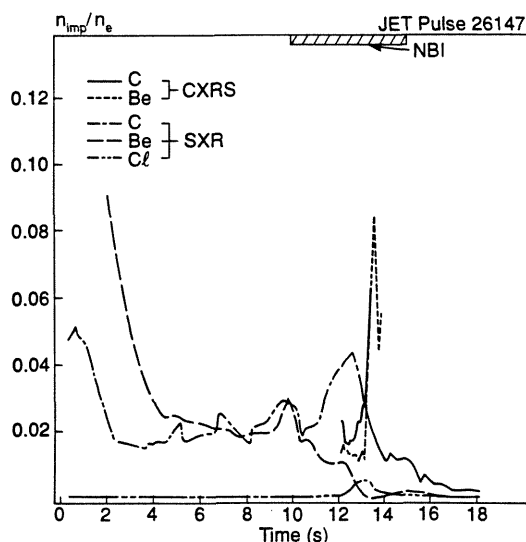


Fig.7.15 Impurity concentrations derived from soft x-ray spectroscopy (SXR) compared with charge exchange recombination spectroscopy (CXRS).

7.4 CONCLUSION

The Bragg rotor spectrometer, in the version now installed at JET, is able to monitor all impurities, and therefore offers a viable alternative to grating instruments.

At the present level of analysis, the derived components of P_{rad} and Z_{eff} are useful only in the Ohmic phase, and are thus complementary to charge-exchange recombination spectroscopy.

Further work on multilayer calibration can be expected to reduce the reliance on code modelling.

References

- ¹ M von Hellerman et al, Rev. Sci. Instrum. 61 (1990) 3479.
- ² G F Matthews et al, Nuclear Fusion, 28 no 12 (1988) 2209.
- ³ K D Lawson et al, Proc. 17th EPS Conf. Controlled Fusion and Plasma Physics, Amsterdam, III p1413-8, (1990).
- ⁴ D Pasini et al, Proc. 18th EPS Conf. Contr. Fus. and Plas. Physics, Berlin, (1991).
- ⁵ R Giannella et al, JET-P(91)33 (1991).

8 CONTROL OF IMPURITY CONFINEMENT IN THE DITE TOKAMAK

8.1	Introduction	158
8.2	Impurity transport theory	159
8.3	Ionization and excitation	164
8.4	The experiments	168
8.5	Data reduction and validation	172
8.6	Central-chord measurements	179
8.7	Radially resolved measurements	187
8.8	Conclusion	190

*Swift as any shadow, short as any dream,
Brief as the lightning in the collid night,
That, in a spleen, unfolds both heaven and earth,
And ere a man hath power to say, "Behold!"
The jaws of darkness do devour it up:
So quick bright things come to confusion.*

*A Midsummer Night's Dream
William Shakespeare 1600*

8.1 INTRODUCTION

There are two themes to this chapter: firstly, the study of a controllable switch between long and short impurity confinement modes in the DITE Tokamak, and secondly, the use of a novel technique, here called "Radiative-Recombination Spectroscopy", as a diagnostic of the phenomenon.

The main discovery of the DITE experiments was that the impurity confinement could be controlled by refuelling, as shown by the impurity-injection time-histories in figure 8.1, where the difference between the two discharges was the gas feed rate. For constant-density plasmas, the impurity confinement time τ_{imp} increased steeply (as a function of \bar{n}_e) from ~25 ms to ~250 ms in the density range $2 \times 10^{19} < \bar{n}_e < 8 \cdot 10^{19} \text{ m}^{-3}$. At high density, τ_{imp} could be reduced to about 30 ms by refuelling at the plasma edge. Radial profiles of impurity line radiation indicated that there was no change in the plasma core, and that a change in transport in the outer half of the plasma was responsible for the different impurity confinement.

The high sensitivity of the Bragg rotor spectrometer allowed diagnosis of weak Al XII and Al XIII line radiation in the outer radii. This was shown to be due to radiative recombination excitation of fully stripped and H-like ions, leaving the core in a time comparable with the recombination time. The same transitions can, of course, be excited by electron impact in the hotter regions of the plasma, but in the cooler outer regions they are excited predominantly by radiative recombination, and here will be called "radiative-recombination lines".

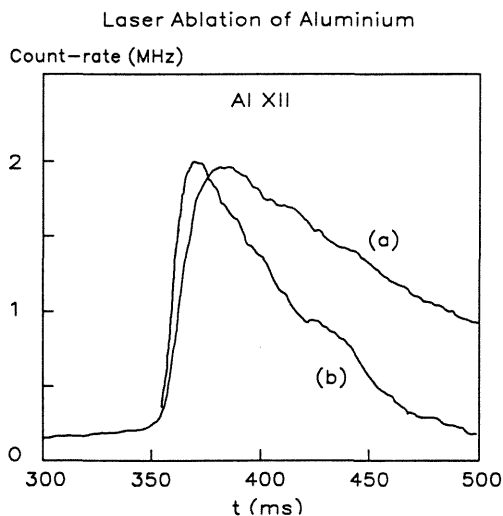


Fig.8.1 Time evolution of Al XII for:
(a) constant density and (b) density rising due to gas-puff.

Before these experiments, long impurity confinement times had been observed in some cases; for example, in deuterium discharges in ISX-B¹, in the absence of the sawtooth instability in Pulsator² and DIII³, in ASDEX H-mode discharges⁴ and after refuelling by pellets⁵, and in low current high density discharges in T-10⁶. In general, however, impurity confinement was relatively independent of density for a given machine, and the results of many machines⁷ showed good agreement with a scaling law based on impurity injection experiments at ALCATOR⁸.

Since the results from DITE were reported⁹, a similar phenomenon has been reported in several other Tokamaks, including TEXTOR¹⁰, where long impurity confinement was observed in low-current, high density detached plasmas. More significantly, improved energy confinement and/or fuel ion confinement have also been achieved as in ASDEX¹¹ and T10¹². The other side of the coin - impurity control by gas-puffing - has also been reported¹³.

In the DITE experiments, impurities were injected by laser ablation¹⁴, which has the advantage of introducing a small quantity of a non-intrinsic, non-recycling impurity whose subsequent transport can be monitored spectroscopically. The good sensitivity and wide dynamic range of the Bragg rotor spectrometer made it possible not only to observe the main effect on the central-chord signals but also to diagnose the changes in transport in the outer plasma.

The work described here began as a study of the effect of the Bundle Divertor (BDII) and neutral-beam injection (NBI) on impurity confinement. When the long confinement mode was discovered, the emphasis changed and the work became a more fundamental study of impurity confinement and transport. Most of the results analysed here are for Ohmic discharges in helium, with aluminium as the injected impurity.

8.2 IMPURITY TRANSPORT THEORY

As discussed in chapter 1, impurity transport in Tokamaks can usually be described by an anomalous transport equation containing diffusive and convective terms. Given the complications of accounting for the effect of the temperature and density profiles on the ionization balance, it is usual to interpret central-chord impurity radiation by comparing it with the output from a so-called impurity transport code. In fact, such a code spends most of its time calculating the ionization balance and excitation, while the transport theory it contains can be quite rudimentary.

A simple calculation for a typical laser ablation signal is shown in figure 8.2, where the influx and confinement of the impurity can be fitted by two time constants τ_{rise} and τ_{fall} . It is the aim of much of the following

discussion to demonstrate that for the data analysed here, $\tau_{\text{rise}} \cong \tau_1$ and $\tau_{\text{fall}} \cong \tau_0$, where τ_0 and τ_1 are time constants which result from an analytical solution of the anomalous transport equation.

For this experiment, we can establish that the central-chord signal originates from the core of the plasma, where there is approximate coronal equilibrium, and where $T_e(t)$ is constant during the measurement. We can also show that the emission from the observed ions is not unduly temperature sensitive, and that the ionization time is short compared with the rise-time of the signal. It is then only necessary to correct for any density variation during the measurement to be able to interpret the signals directly in terms of impurity concentration. Given such data, it is possible to make some progress by analytical methods, and that is the approach taken here.

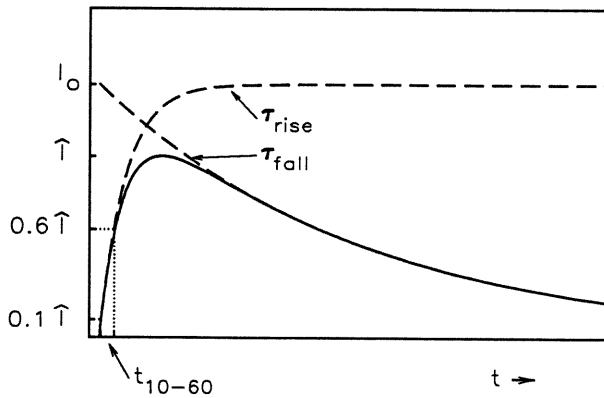


Fig.8.2 Convolution of the rise and fall times from equations 8.18 and 8.21. The rise-time was measured between 10% and 60% of the peak value, then converted to τ_{rise} .

Anomalous transport

Seguin et al¹⁵ derived an analytical solution of the radial transport equations

$$\frac{\partial N}{\partial t} = \frac{1}{r} \frac{\partial}{\partial r} \left(r \left(D \frac{\partial}{\partial r} + V \right) N \right); \quad N(r_L) = 0 \quad (8.1)$$

for the simple case

$$D \equiv D_a, \quad V \equiv V_a \frac{r}{r_L}, \quad S \equiv \frac{r_L V_a}{2 D_a} \quad (8.2)$$

where $N(r,t)$ is the total impurity density, r_L is the limiter radius, D_a and V_a are diffusive and convection-velocity constants respectively, and S is a dimensionless "convection parameter" that describes the relative importance of convection and diffusion.

The first eigenvalue τ_0 of their solution corresponds to the steady decay of an evolved profile, equivalent to the impurity confinement time τ_{imp} , and is approximated by

$$\tau_0 \cong \frac{77 + S^2}{56 + S^2} \cdot \frac{e^S - S - 1}{4 S^2} \cdot \frac{r_L^2}{D_a} \quad (8.3)$$

For the data used here it will be deduced that S lies in the range $0 > S > 3$, in which case eq. 8.3 can be further approximated, within about 5% to give

$$D_a \cong \frac{r_L^2}{(2.4^2 - 1.4 S) \tau_0} ; \quad (0 > S > 3). \quad (8.4)$$

This is now in the same form as a simplified solution¹⁶ to the diffusion equation neglecting convection, frequently used to estimate an effective diffusion coefficient from the observed confinement time

$$D_{eff} = \frac{r_L^2}{(2.4)^2 \tau_{imp}} \quad (8.5)$$

where 2.4 is the first root of a zero-order Bessel function. The Seguin formulation (eq 8.3) reduces to this as S tends to zero. For $S = 2$, then $D_{eff} \cong 0.5 \cdot D_a$, and so this simplified expression tends to underestimate diffusion in the presence of convection.

The second eigenvalue τ_1 , is the time scale for relaxation of an arbitrary profile toward the stable shape, and corresponds to the inflow time in an injection experiment. It is important to be able to measure τ_1 accurately, since without it we are limited to estimating an effective diffusion coefficient only, and will be unable to determine whether the transport has any convective component. The relationship between the ratio τ_0/τ_1 and S is shown in figure 8.3, adapted from Seguin et al. In the absence of convection, $\tau_0/\tau_1 = 5.3$ ($= p_2^2/p_1^2$ where $p_1=2.40$ and $p_2=5.52$ are the first two roots of a zero order Bessel function).

This analysis now enables us to derive anomalous transport coefficients D_a , V_a and S from the rise and fall times observed in a laser ablation experiment.

Particle transport and radiative recombination spectroscopy

It is not usually possible to derive an analytical expression for the radial profile of the impurity line radiation from a Tokamak plasma, since the ionization balance, and the emission from a given ionization stage, depend on the plasma temperature, density, transport and sources.

However, in this experiment, the radial dependence of spectral lines

excited by radiative recombination results from an almost ideally simple transport case. This approximates to a line source of impurities on axis, with the escaping ions recombining in the outer plasma. Interpretation of the emission is greatly simplified because radiative recombination is the only significant atomic process in the outer plasma that can lead to certain transitions. Figure 8.7 shows that the radiative recombination rates α_{rad} for Al^{12+} and Al^{13+} are remarkably constant in the temperature range of interest for DITE. When these rates are folded with the DITE density profile, the product $\alpha_{\text{rad}} n_e$ is practically independent of plasma radial position (fig 8.4). This is not a necessary condition for the analysis, but simplifies it considerably.

For this case, the diffusion equation can be written as¹⁷

$$\frac{\partial n_z}{\partial t} = D \nabla^2 n_z. \quad (8.7)$$

For ions leaving the core to recombine in the outer radii, the recombination rate R_r at radius r , is

$$\frac{\partial n_z}{\partial t} \equiv R_r = \alpha_{\text{rad}} n_e n_z. \quad (8.8)$$

Setting eq. 8.7 in cylindrical co-ordinates

$$\frac{R_r}{D} = \frac{\alpha_{\text{rad}} n_e n_z}{D} = \frac{\partial^2 n_z}{\partial r^2} + \frac{1}{r} \frac{\partial n_z}{\partial r} \quad (8.9)$$

or

$$\frac{\alpha_{\text{rad}} n_e R_r}{D} = \frac{\partial^2 R_r}{\partial r^2} + \frac{1}{r} \frac{\partial R_r}{\partial r}. \quad (8.10)$$

If we can measure experimentally R_r , (the radial dependence of the radiative-recombination line) we can then solve eq. 8.10 for D . By inspection of the radial profiles of radiative-recombination lines (figs 8.4 and 8.13), the profile in the outer plasma can be fitted by an exponential decay

$$R_r = R_o e^{-r/\lambda} \quad (r > 10\text{cm}) \quad (8.11)$$

where λ is the $1/e$ scale length of the radial decay of the recombination radiation. It follows that

$$\frac{\partial R_r}{\partial r} = - \frac{R_o e^{-r/\lambda}}{\lambda} = - \frac{R_r}{\lambda} \quad (8.12)$$

and

$$\frac{\partial^2 R_r}{\partial r^2} = \frac{R_o e^{-r/\lambda}}{\lambda^2} = \frac{R_r}{\lambda^2}. \quad (8.13)$$

Substituting for $\partial R_r / \partial r$ and $\partial^2 R_r / \partial r^2$ into (8.13) above, effectively defines the boundary conditions. These are a line source at $r = 0$, which is a fair approximation to the source of fully stripped ions in the core, and a plasma of infinite radius, which is almost the case for the recombining ions, since most have recombined before reaching the limiter radius. Thus

$$D = \frac{\alpha_{\text{rad}} n_e \lambda^2 r}{r - \lambda} \quad (8.14)$$

or, since $\lambda \ll r$,

$$D \cong \alpha_{\text{rad}} n_e \lambda^2. \quad (8.15)$$

In this way the diffusion coefficient may be deduced from the radial decay of the radiative-recombination line emission. This method only measures D_{eff} , which, as discussed above, will tend to underestimate the true diffusion if significant convection is present.

It should be emphasized that the measurement can be independent of the time dependence of the central-chord signal, and could also be used for an intrinsic impurity. It has an advantage over central-chord time-evolution measurements, in that both the spatial and time dependence of the transport can be diagnosed.

This type of recombination-excited line radiation has been observed previously¹⁸, though not analysed by the above technique. A similar analysis is possible for recombination edges in radially resolved soft x-ray pulse-height-analysis spectra¹⁹.

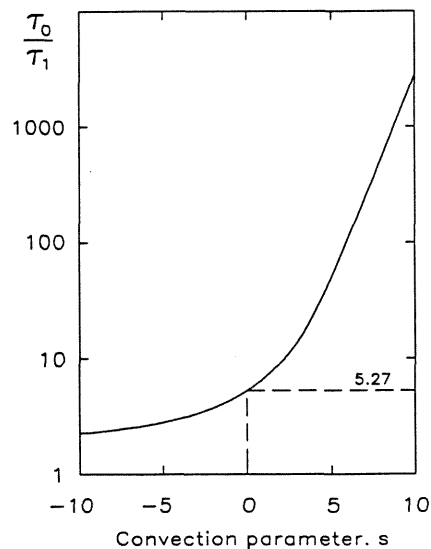


Fig.8.3 The theoretical fall/rise-time ratio τ_0/τ_1 as a function of the convection parameter S . Adapted from Seguin et al.

8.3 IONIZATION AND EXCITATION

Here we discuss the ionization, excitation and recombination mechanisms for Al XII and Al XIII in the context of the DITE plasma T_e and n_e profiles.

The emission from two distinct regions has been studied.

- a) The plasma core, extending to a minor radius of about 6 cm, where the ions are close to coronal equilibrium, and from where 95% of the central chord signal is radiated. This radiation was used for the measurement of τ_{imp} , based on the time decay of the central chord intensity.
- b) The plasma outside a minor radius of about 10 cm, where the excitation of Al XII and Al XIII is almost entirely due to radiative recombination, and which was used to diagnose the localized transport.

Excitation Mechanisms

As discussed in chapter 1, the excitation mechanisms that lead to radiation from the 1s-2p and 1s²-1s 2p resonance transitions of Al XIII and Al XII are: electron impact excitation, radiative recombination and charge-exchange recombination. Radial profiles of the excitation rates for electron impact excitation and radiative recombination were calculated using the DITE $T_e(r)$ and $n_e(r)$ profiles. Figure 8.4 shows the product of $n_e(r)$ with the relevant rate coefficient:

- a) $n_e(r) \cdot C_{1j}(T_e)$ (Van Regemorter electron impact²⁰)
- b) $n_e(r) \cdot \alpha_{rad}(T_e)$ (Summers radiative recombination²¹)

The error bars on C_{1j} and α_{rad} result from the errors in $T_e(r)$ and $n_e(r)$. Also shown are the predicted coronal abundances of H-like and fully stripped Al, (based on fig 8.5), the coronal emissivity of Al XIII 1s-2p, and the measured Al XIII profiles.

As shown in figure 8.4, for radii less than about 6 cm, electron impact excitation dominates by a factor of a few, while at radii greater than about 10 cm, radiative recombination dominates by several orders of magnitude. It is notable that, for the DITE T_e and n_e profiles, $\alpha_{rad} \cdot n_e(r)$ is almost constant outside 10cm, and is also relatively insensitive to errors in $T_e(r)$ and $n_e(r)$.

Some fraction of radiative recombinations onto fully-stripped Al ions result in the 1s-1p Ly α transition in Al XIII. This fraction (α_{2p}/α_{rad}) is estimated to be close to 0.3, based on calculations for radiative recombination of Oxygen²², and the resulting rate $\alpha_{2p} \cdot n_e$ is shown in figure 8.4. Derivation of the diffusion coefficient from this radiative recombination line is a relative measurement, and is not sensitive to the ratio (α_{2p}/α_{rad}).

The coronal abundances and electron impact excitation rates of Al XII and Al XIII are negligible for $r > 12$ cm, so that Al XIII line radiation will only be seen if the ion transport is fast enough for bare Al nuclei to reach the outer plasma on a time scale similar to the recombination time.

In a similar experiment, Marmar et al¹⁸ showed (fig 8.6) that charge-exchange recombination from neutral deuterium was only significant for the higher- n transitions of Ar XVII, and that in a helium plasma it had a negligible effect on the $1s^2-1s2p$ transition. Charge-exchange recombination has not yet been included in this analysis.

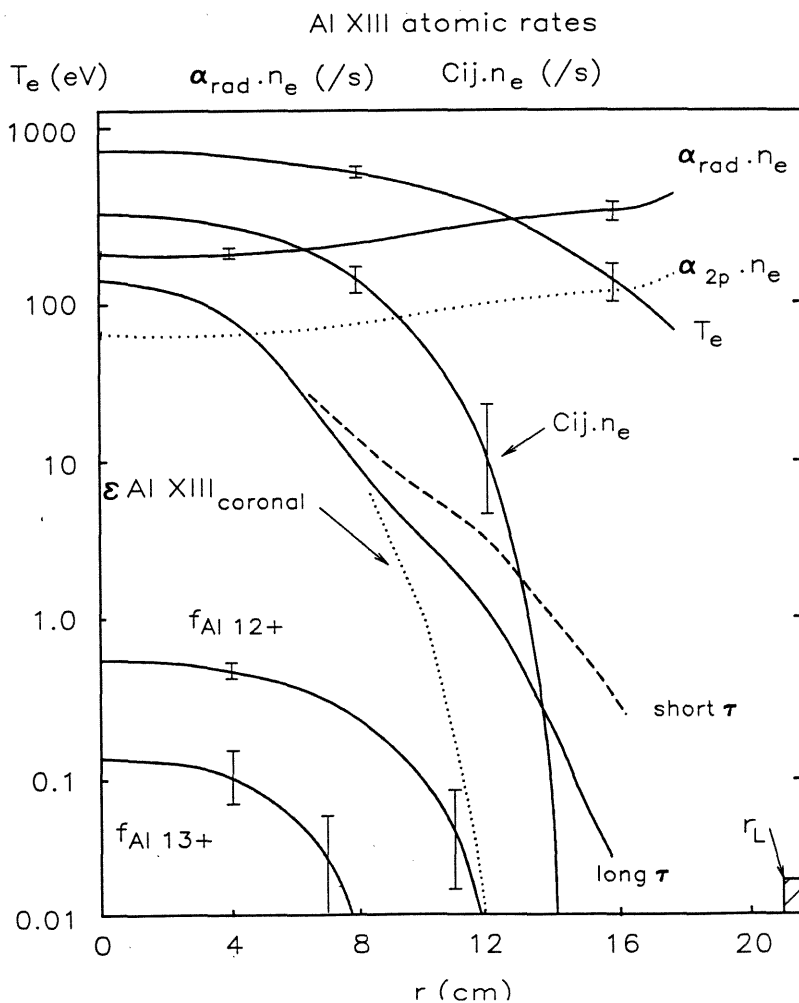


Fig.8.4 Atomic rates and ion fractional abundances, combined with the DITE electron temperature and density profiles.

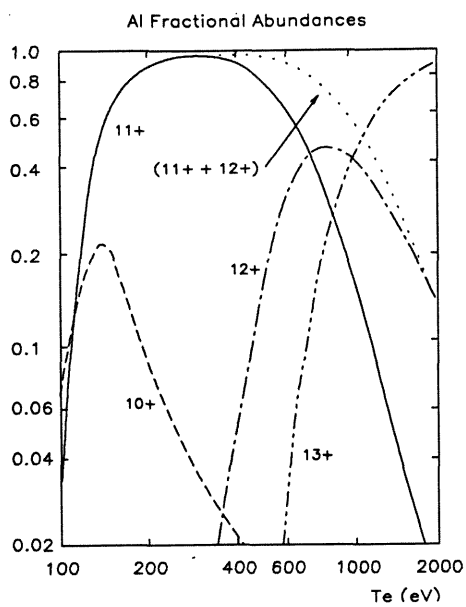


Fig.8.5 Coronal abundance fractions of Al. The sum of Al^{11+} and Al^{12+} accounts for over 80% of the total aluminium in the central DITE plasma.

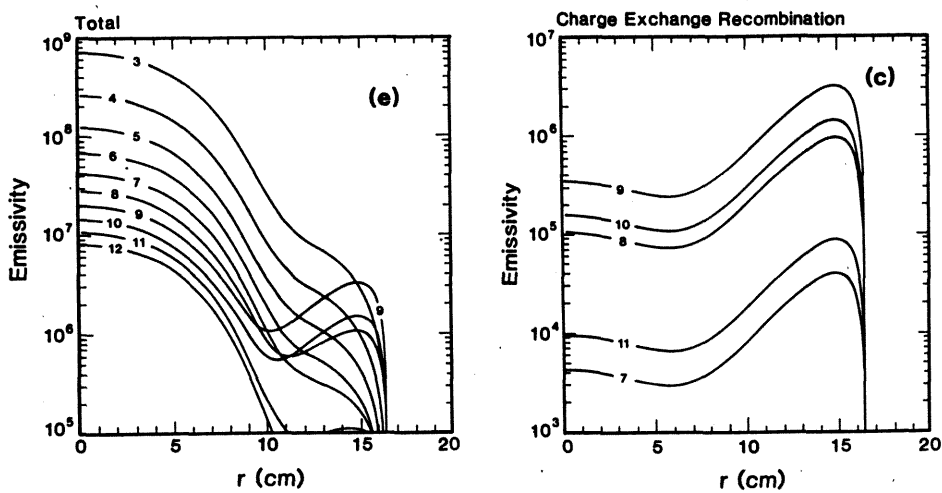


Fig.8.6 Modelled radial profiles of $1s^2-1snp$ transitions of Ar XVII for helium plasmas in Alcator-C. The excitation mechanisms are: electron-impact, radiative recombination and charge-exchange recombination. Charge-exchange has a negligible effect on the low- n transitions. (Marmar et al¹⁸).

Ionization time

It is important to get a good measurement of the impurity influx time τ_1 , preferably without the complication of its being folded with the ionization time. An estimate of importance of the ionization time can be made from the ionization rates shown in figure 8.7. (interpolated from Summers²¹).

The ionization rate, $I_{z \rightarrow z+1}$ ($\text{cm}^{-3} \text{s}^{-1}$) from ions in charge-state z to $z+1$ is given by

$$I_{z \rightarrow z+1} = n_z n_e s_z \quad (8.16)$$

where the ion and electron densities are n_z and n_e (cm^{-3}) respectively, and s ($\text{cm}^{-3} \text{s}^{-1}$) is the ionization rate coefficient.

Rearranging

$$\frac{n_z}{I_{z \rightarrow z+1}} = \frac{1}{(n_e \cdot s_z)} \text{ (seconds per ionization).} \quad (8.17)$$

The RHS vertical scale of figure 8.7 shows $1/(n_e \cdot s_z)$ for a typical DITE \bar{n}_e of $5 \cdot 10^{19} \text{ m}^{-3}$. The ionization time for Al XII is less than 1 ms for the T_e range from which the Al XII radiates, (90% of the central-chord Al XII signal is radiated from within $r = 8 \text{ cm}$ where $T_e > 500 \text{ eV}$) and therefore the "burn-through" time to He-like Al is small compared with the typical transport-limited rise-time of about 8 ms. Conversely, the time to ionize He-like to H-like Al is of order 10 ms at 800 eV and is also very sensitive to T_e . For this reason the analysis of rise-times was restricted to AlXII.

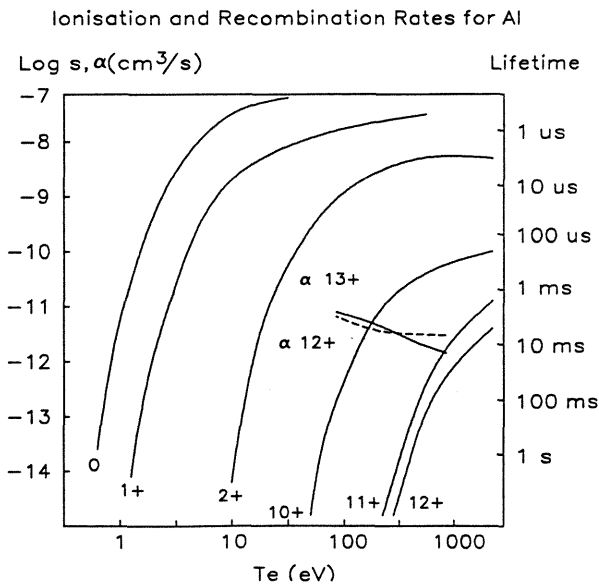


Fig.8.7 Ionization and recombination rates for Al.

8.4 THE EXPERIMENTS

Aluminium was chosen for most of the work on DITE because, for the central T_e of ~ 700 eV, almost all the Al in the plasma core was in either the H-like (Al XIII) or He-like (Al XII) state, as shown by the Coronal Equilibrium (CE) calculation²³ of figure 8.5. This made the atomic physics (ionization, excitation and recombination) relatively simple, reducing uncertainties in the derived ion concentrations and profiles. Also, the line radiation was concentrated into a small number of lines, which improved the S/N ratio for spectroscopic measurements. A further experimental advantage was that the line radiation from Al XII and Al XIII occurred at around 7 Å, which coincided with the peak in the sensitivity of the Bragg rotor spectrometer. A spectrum of Al XII and Al XIII is shown in figure 9.1, and the transitions used for the transport studies are listed in table 8.1, where $\lambda/\delta\lambda$ is the resolving power of the collimator/Bragg-angle combination as discussed in chapter 3.

Table 8.1 Al transitions used for impurity injection studies.

Ion	Transition	λ (Å)	$\lambda/\delta\lambda$ (inst.)
AlXII (He-like)	$1s^2-1s2p \ ^1P_0$	7.757	900
AlXIII (H-like)	$1s-2p$	7.173	700

Three main sets of data were obtained, all with the spectrometer in monochromatic mode (50 μ s time-resolution), during the study of injected impurities:

- a) Density scans b) Radial profiles c) Gas-puff scan

a) Density scans

Time evolution of the central-chord intensity, from which the impurity confinement was derived, was recorded for many sets of parameters. The most important result was that long or short impurity confinement could be achieved at high density, depending on whether the density was constant, or rising as the result of gas puffing (fig 8.1). An example of the central-chord Al XII signal is shown in figure 8.9 together with the gas feed and density behaviour. The gas feed was turned off at 440 ms, and by about 460 ms the density had begun to fall, resulting in a rapid increase in the impurity confinement time. Gas was again fed at 470 ms, leading to a return to short confinement as the density rose, although the absolute change in density during the switch was not very great.

It was necessary to correct results with the Bundle Diverter (BDII) for lost counts at count rates above about 3 MHz, due to detector gain-sag which

caused some of the pulses to fall below the lower-level discriminator. This was corrected by repeating a discharge with a grid of 12% transmission in place. For the results used here, the correction is not more than about 20% in intensity, and corrected rise and fall times are about 10% shorter than those taken from the raw data. The problem was eliminated in subsequent measurements by leaving the aperture stop in place whenever it was likely that the detector count-rate would approach 3 MHz.

b) Radial profiles

Radial intensity profiles were made of injection into the long confinement mode, followed by a gas-puff which caused a switch to short confinement. One aim of these profiles was to check that the Al XIII/XII ionization balance would allow the central-chord intensities to be interpreted in terms of impurity transport and confinement.

As well as this necessary function, the radiative-recombination lines from the outer plasma proved to be a valuable diagnostic of changes in impurity transport. Al XII signals at three representative chords are shown in figure 8.8 together with soft x-ray, T_e , \bar{n}_e and gas-puff data. The signals at 6 cm and 12 cm were multiplied by 5 and 25 respectively to normalize the plot. The signal at 12 cm is almost entirely due to radiative recombination, and is due to H-like ions that reach the outer radii after being formed in the core. The change in confinement following the gas-puff is abrupt, as shown by the rapid rise at 12 cm as the core ions suddenly lose confinement and stream outwards.

Throughout this series of about 20 discharges, the plasma behaviour was extremely repeatable, showing that the transport modes were repeatable and controllable. The Al intensity recorded by the soft x-ray diode array was constant to better than about 5%, and was not a limiting factor in the Abel inversion of the spectroscopic profiles. This reproducibility of the laser ablation system was also essential when comparing the amount of Al reaching the plasma core under different conditions.

c) Gas-puff scan

A further series of discharges was made, all at approximately constant density, but with a range of refuelling rates. The refuelling rate was controlled to be almost constant throughout the rise and fall phases of the ablation. This was an improvement on the original series, but meant that the maximum achievable \bar{n}_e was lower, due to the need to turn off the gas feed earlier for the constant \bar{n}_e measurement. This limited \bar{n}_e to about $6.5 \cdot 10^{19} \text{ m}^{-3}$, which was lower than the earlier density scans, and thus the difference between the long and short confinement times was smaller.

The results were consistent with those taken 10 months previously, and the better control of the refuelling allowed a direct comparison of the rise and fall times for each discharge. Since the rise-time for Al XIII would be complicated by the ionization time as discussed above, and since the fall times for Al XII and Al XIII were practically identical, this later observation was restricted to Al XII.

The $\bar{n}_e(t)$ plots of figure 8.10 show that $\dot{\bar{n}}_e$ was almost constant from ablation to decay. The τ_{imp} of 130 ms at constant \bar{n}_e agrees well with that measured with the same conditions in the original measurements. The AlXII intensity curves for $\dot{\bar{n}}_e = 0$ and $\dot{\bar{n}}_e = 11.7 (10^{19} m^{-3} s^{-1})$ are shown in figure 8.1 and the long confinement mode is clearly preceded by a slower rise.

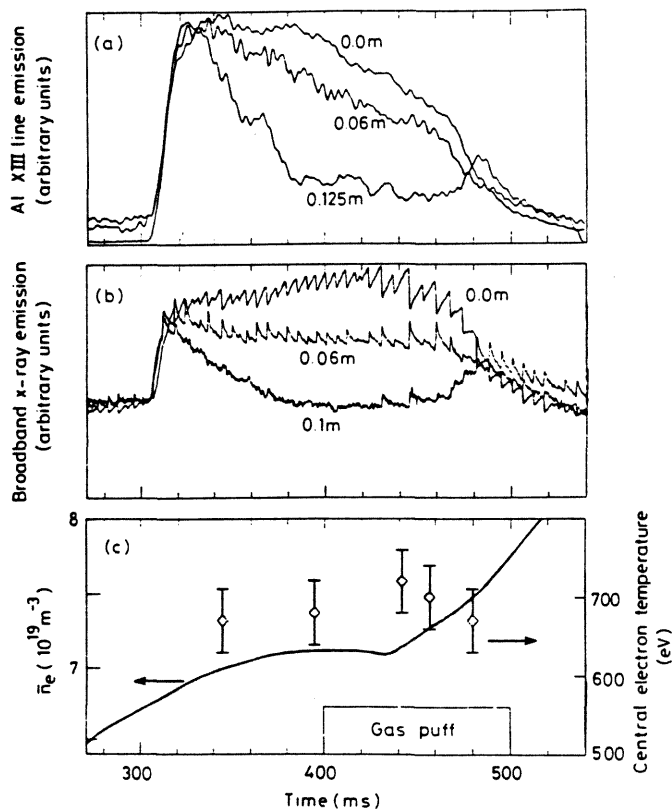


Fig.8.8 Data of the discharges used for the radial profile scan: (a) spatially resolved Al XII, (b) soft x-ray, and (c) time history of \bar{n}_e (solid line), $T_e(0)$ (points) and gas-puff.

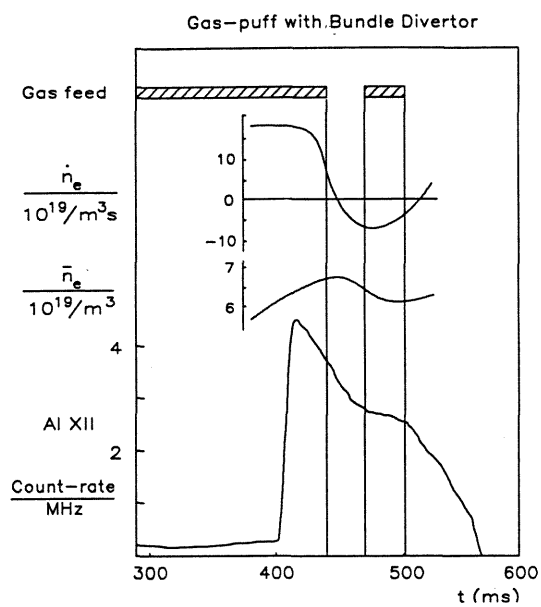


Fig.8.9 The effect of the gas feed on density, rate of change of density, and impurity confinement, with the bundle divertor.

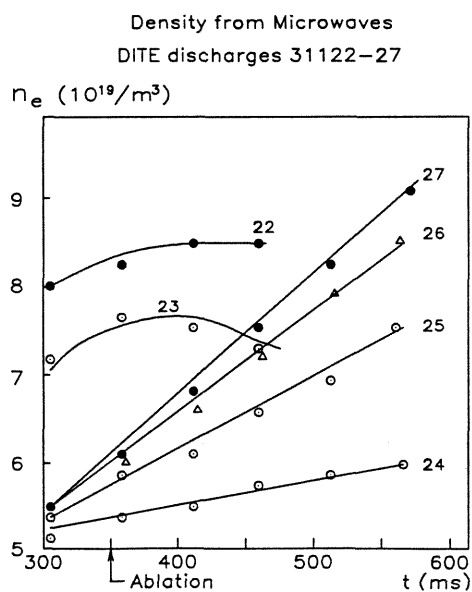


Fig.8.10 The density time histories for the \dot{n}_e -scan of AlXII ablation. This was more controlled from ablation to decay than earlier discharges, and provided the most reliable ratios of τ_0 to τ_1 .

8.5 DATA REDUCTION AND VALIDATION

Impurity confinement time τ_{imp}

Provided that T_o is constant, and \bar{n}_e is constant or measured with time, the confinement time of an injected, non-recycling impurity can be measured from the $1/e$ decay time of the emission from a suitably chosen core ion. Most of the τ_{imp} data presented here were derived by this method, and a large part of the following discussion is devoted to establishing that the above conditions hold, thus allowing a reliable measurement.

Rise and fall times

The observed impurity signal following laser ablation can be described by the convolution of two exponentials (fig 8.2)

$$I = I_o (1 - \exp(-t/\tau_1)) \exp(-t/\tau_o) \quad (8.18)$$

where τ_1 and τ_o are the respective rise and fall time constants discussed above, and I_o is the value the intensity would reach if τ_1 were zero. We are interested in the ratio k between the rise and fall time constants

$$k = \tau_o/\tau_1 . \quad (8.19)$$

By differentiating eq. 8.18, the time \hat{t} to reach the maximum intensity \hat{I} is

$$\hat{t} = \tau_1 \ln(1+k) \quad (8.20)$$

at which time

$$\hat{I} = I_o \frac{k}{1+k} \exp\left(-\frac{\ln(1+k)}{k}\right) . \quad (8.21)$$

The rise and fall times were measured according to the following definitions.

Rise-time

The time was measured for the signal to rise between specified fractions of the peak value. Various limits were used, with the time to rise from 10% to 60% of the peak (\hat{I}) being chosen as the most suitable (fig 8.2). These limits make use of a large fraction of the amplitude without unduly complicating the measurement by including the later part of the rise, when the convolution of the decay time is becoming significant. When $k \gg 1$ ($\tau_o \gg \tau_1$), the rise-time from 10% to 60% (t_{10-60}) is only weakly dependent on τ_o , and for the range of values relevant here ($5 > k > 15$) the following relation holds to about 2%

$$\tau_{rise} \equiv \tau_1 = 1.44 t_{10-60} . \quad (8.22)$$

Fall-time

This was taken as the $1/e$ decay time of the signal, and was measured, where possible, at a time after the peak when the decay was exponential. This was done both by measuring the time taken for the signal to fall by a factor two, and by extrapolating the gradient to the base level. Where possible this was measured at up to four points on a single decay curve. At the very long decay times (> 150 ms) the decay tended to be more linear than exponential. For the discharges where \bar{n}_e changed significantly during the decay period, the decay curves were first corrected for the changing \bar{n}_e , by scaling the values in inverse proportion to the relative \bar{n}_e change referred to \bar{n}_e at ablation.

Raw profiles

The Al XII and Al XIII profiles were obtained from a series of discharges (#29920 to #29941, 7th May 1986). The Al was injected at 300 ms into the constant density, long confinement, phase of the discharge, and at 400 ms additional helium was puffed, resulting in a rapid change to the short confinement mode. Profiles were taken at 11 different chords, at approximately 1.5 cm steps, from the central chord to a radius of 18 cm. For radii less than 8 cm, the signal was attenuated with a grid of 12% transmission to prevent saturation of the detector, allowing a dynamic range of about 10^4 (between the core and the edge) to be observed.

The radial profiles show a scatter that cannot be attributed to shot-to-shot variability in the amount of Al entering the plasma, since the signal from the soft x-ray diode array (SXR) was very repeatable throughout the series. The scatter is believed to be due to the inaccurate resetting of the spectrometer (in monochromatic mode) between the Al XII and Al XIII wavelengths at each chord*. This scatter, which complicated the Abel-inversion, was not random but was correlated with the sequence in which the chords were scanned. Figure 8.11 shows the peak signal and discharge number at each radius, where the later points in the series are systematically higher.

Abel inversion

Line-of-sight radial profiles of representative times during long and short confinement were smoothed logarithmically such that

$$\log N_r = (\log N_{r-\Delta r})/4 + (\log N_r)/2 + (\log N_{r+\Delta r})/4 \quad (8.23)$$

* In the Mk1 instrument, used for these observations, the Bragg angle was measured in divisions of 2.4 arcmin. Although this was much less than the instrumental line-width of about 8 arcmin FWHM, it left some uncertainty in setting to the exact peak of a line. This uncertainty has been much reduced for the Mk2 instrument, which has encoder divisions of 0.3 arcmin.

where N is the count rate at radius r . This method gave equal weight to each radius, and was in accordance with the type of scatter on the data, namely a scatter in the proportion of the signal rather than in its absolute error. Points from these smoothed profiles (fig 8.12) were then Abel-inverted to give radial profiles of Al XII and Al XIII volume emissivity for long and short confinement (figs 8.13-14). Because the profiles are peaked on axis, and have very steep wings, the Abel inversion is not thought to have introduced any significant errors.

Analysis of radial emission profiles

The calibrated and Abel-inverted emission profiles can now be used as follows.

- a) To locate the region of emission of each ion.
- b) To compare the ionization balance with Coronal Equilibrium (CE).
- c) Using the DITE $T_e(r)$ and $n_e(r)$ profiles, to calculate the ion ground state profiles, and hence the total Al profiles.
- d) To diagnose changes in transport, from differences in the radiation from radii outside 10 cm, where the excitation is mainly by radiative recombination.

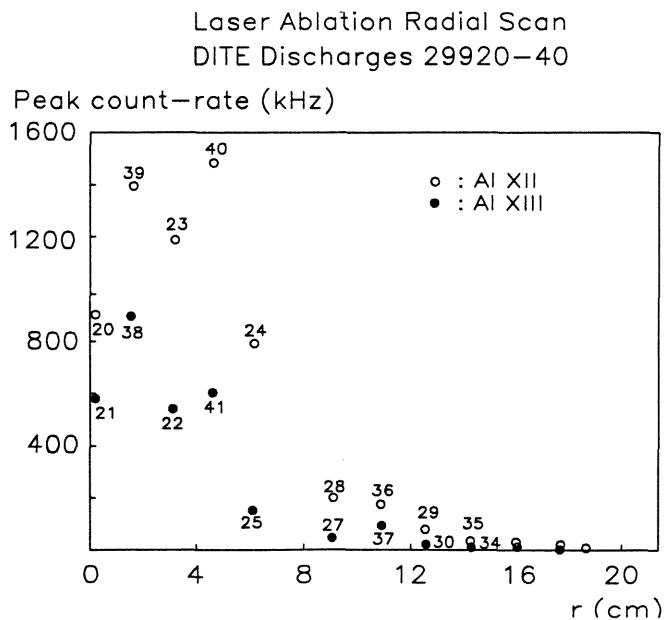


Fig.8.11 Peak count-rate for the radial profile series of discharges. The scatter is believed to be due to inaccurate resetting of the spectrometer in monochromatic mode between Al XII and Al XIII.

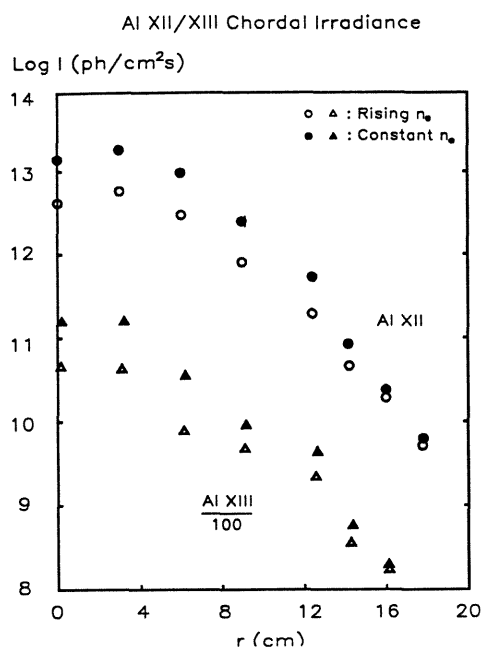


Fig.8.12 Line of sight profiles of Al XII and Al XIII irradiance for long and short confinement.

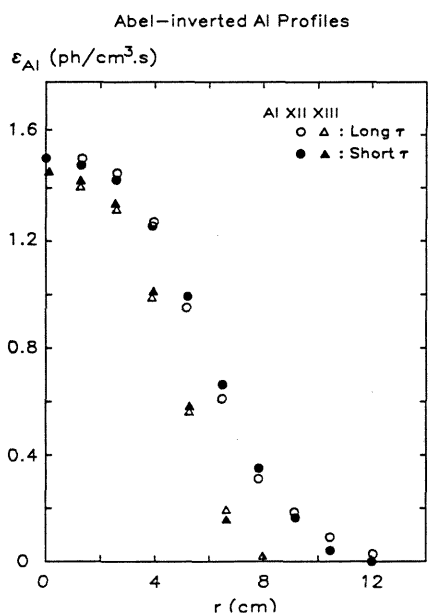


Fig.8.13 Abel inverted profiles Al XII and Al XIII emissivity. Most of the intensity is emitted from within 6 cm, and thus central-chord signals give a good representation of the total emission.

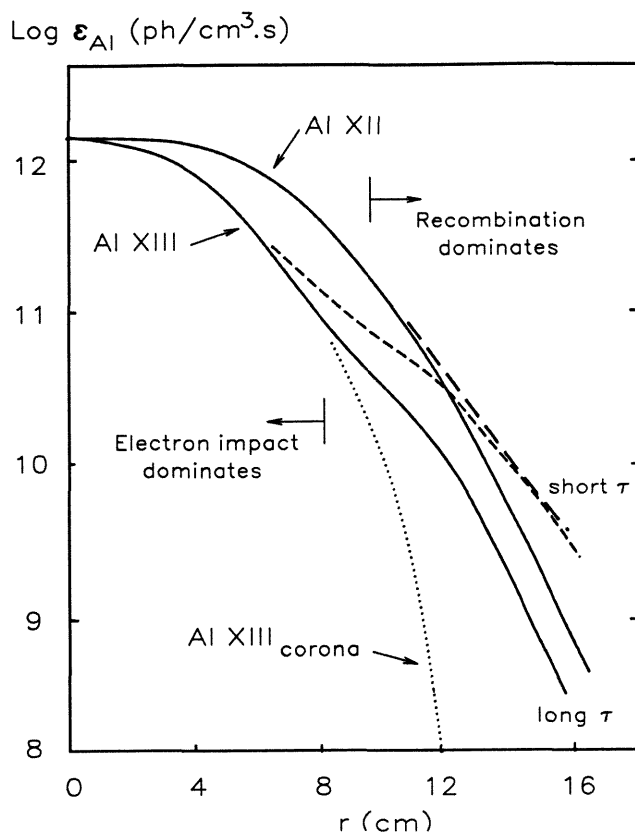


Fig.8.14 Abel inverted profiles Al XII and Al XIII emissivity. The radiative-recombination lines outside 12 cm have exponential radial decays, which can be interpreted in terms of diffusion.

a) Region of emission

There is very little difference in the shape of the core profiles between the long and short confinement modes (fig 8.13). The radiation from Al XIII (hwhm = 4.8 cm) and Al XII (hwhm = 6.0 cm) is strongly peaked on axis. This localization of the radiation means that the central chord observations (which were used for the majority of confinement time measurements) are essentially measurements of the central emission and are thus relatively insensitive to changes in the profiles $T_e(r)$ and $n_e(r)$. Therefore, given measurements of the central T_e and \bar{n}_e , the time evolution of the central chord intensity can be interpreted directly in terms of total aluminium content.

The emission profile from the outer half of the plasma (due to radiative recombination excitation) is broader in the short confinement mode (fig 8.14).

b) Ionization balance

Figure 8.15 shows the radial dependence of the Al XIII/Al XII emission ratio compared with a Coronal Equilibrium prediction based on the Thomson scattering T_e profile. Within 8 cm the agreement is very good, showing that here the Al ions are close to coronal equilibrium, and also that there is no significant difference in the core T_e profile, between long and short confinement. Outside about 10 cm the Al XIII/Al XII emission ratio is far from coronal, and differs greatly between the two confinement modes, implying very different ionization balances in the two cases.

c) Ground-state and total aluminium profiles

From the Abel-inverted Al emissivity profiles, and the Thomson scattering $T_e(r)$ and $n_e(r)$ profiles, the ion ground state abundance profiles (fig 8.16) can be calculated from

$$n_z(r) = \frac{\epsilon_r}{n_e(r) \cdot C_{IJ}(T_e, r)} \quad (8.26)$$

The total Al profile is then best calculated by adding together the Al XIII and Al XII ground states, since their sum accounts for at least 80% of the Al in this T_e range (fig 8.4)

$$Al_{tot} = \frac{n_{XII} + n_{XIII}}{f_{XII} + f_{XIII}} \quad (8.25)$$

This profile (fig 8.16) is peaked on axis, with the error bars not being strongly dependent on the $T_e(r)$ profile.

Summary of core profiles

The foregoing analysis of the radial profiles of Al XIII and Al XII emission has shown the following.

- a) Most of the radiation is emitted from within 8 cm, and therefore the central chord observations give a good measure of the total luminosity.
- b) The emission is from a region of approximate coronal equilibrium.
- c) The emission is from a region where the T_e and n_e gradients are not steep, and so measurements of central T_e and of \bar{n}_e are adequate.
- d) The total Al profile is peaked on axis.

These conclusions allow us to estimate the Al abundance from central chord observations alone, and to interpret the time evolution of the signal after ablation in terms of impurity transport and confinement.

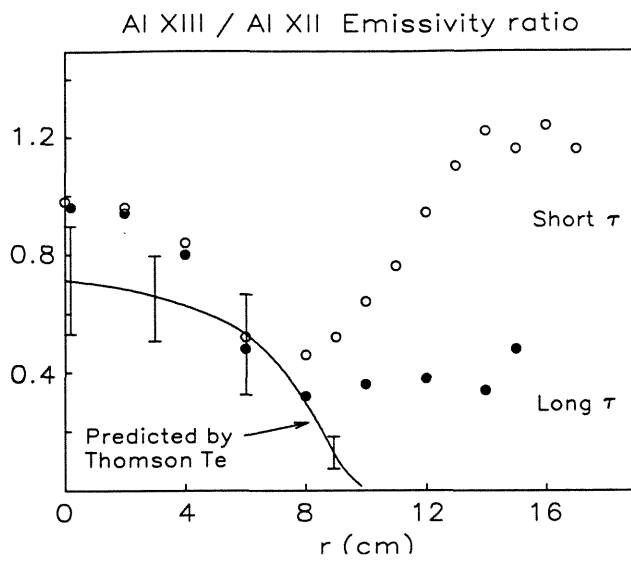


Fig.8.15 The measured AlXIII/XII emissivity ratios, compared with the steady-state coronal ratio predicted from the Thomson scattering profile.

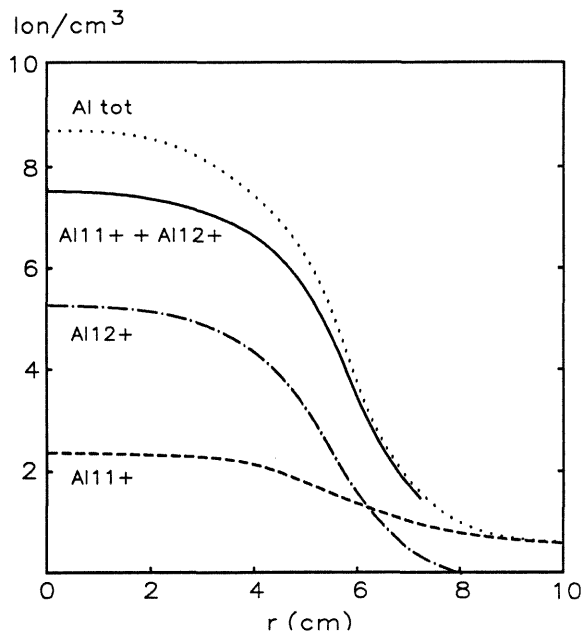


Fig.8.16 Derived ground-state abundances of Al^{11+} and Al^{12+} , and the deduced total Al profile assuming coronal equilibrium.

8.6 CENTRAL-CHORD MEASUREMENTS

Having established that the central-chord intensities are a reliable measure of the impurity content, and are not unduly sensitive to the $T_e(r)$ and $n_e(r)$ profiles, we can go on to analyse their time-evolution in terms of plasma impurity concentration.

Impurity confinement time

The confinement times for the rail-limiter discharges in helium are shown for 100 kA and 150 kA poloidal current in figure 8.17. The results for the bundle divertor (fig 8.18) show a similar pattern, but long confinement was not achieved until the density was falling.

The phenomenon of a change from long to short confinement looks rather like a bifurcation, since below a density of about $4 \cdot 10^{19} \text{ m}^{-3}$, the gas-puff has little or no effect. Above this density the reduction in confinement become increasingly greater, as if the refuelling might be driving an instability, and it may be significant that the maximum density used was close to the DITE density limit for helium.

However, there are not two distinct modes, and it was shown in the gas-puff-rate scan that τ_{imp} could be varied continuously between long and short, at a given density. The long-confinement mode is an apparent upper limit to this trend.

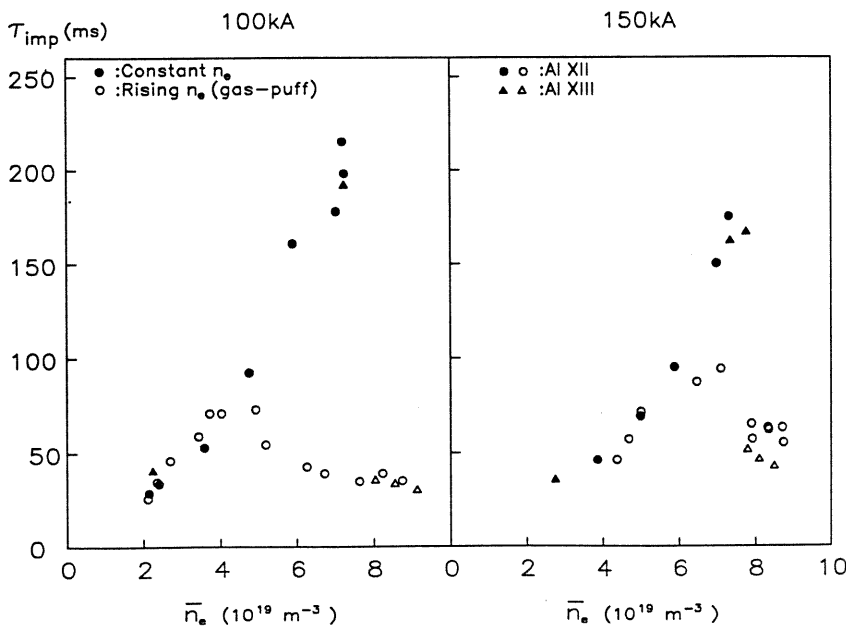


Fig.8.17 Impurity confinement time versus mean line-of-sight density, for 100 kA (left) and 150 kA (right) rail-limiter discharges in helium.

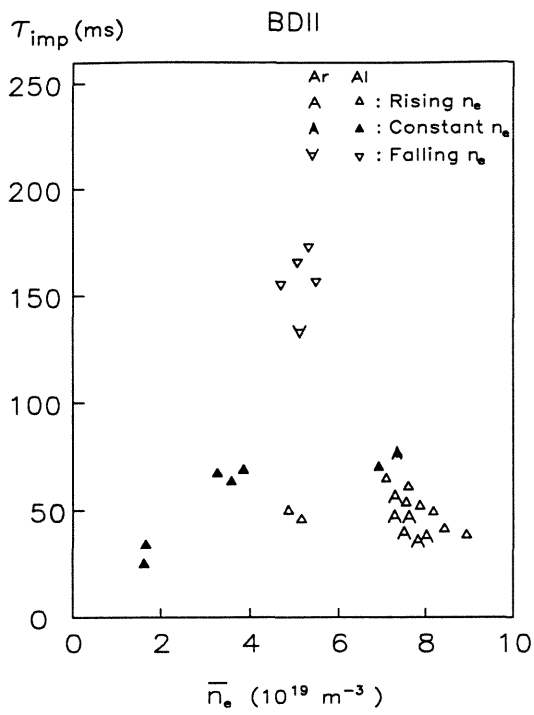


Fig.8.18 τ_{imp} of Al and Ar versus \bar{n}_e , for bundle divertor (BDII) discharges in helium.

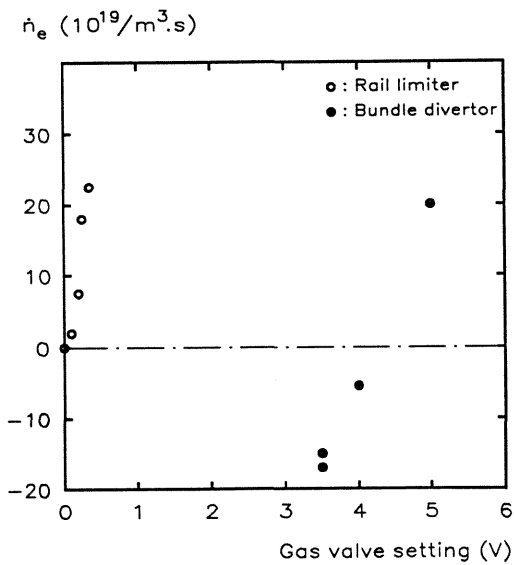


Fig.8.19 Rate of density change versus combined fast gas valve settings (FGV3 + FGV4) for rail limiter and bundle divertor discharges in He.

Fresh gas-feed as the controlling parameter

In general, the rate of density increase will be the difference between the density added by refuelling and that removed by pumping, including such sinks as the vessel walls or a divertor

$$\dot{\bar{n}}_e = \dot{\bar{n}}_{e(\text{refuel})} - \dot{\bar{n}}_{e(\text{pump-out})} \quad (8.26)$$

For helium discharges on the rail limiter, pumping by the vessel walls was negligible, and the density would remain constant when the gas feed was turned off. For discharges with the bundle divertor (BDII), refuelling was necessary to maintain a constant density, resulting in short impurity confinement. The long-confinement mode was not achieved until the density was falling at about $-20 \cdot 10^{19} \text{ m}^{-3} \text{ s}^{-1}$, even though the gas puff was still ten times higher than that required to produce short confinement with the rail-limiter (fig 8.19). If the observed density behaviour of (BDII) discharges is increased by $20 \cdot 10^{19} \text{ m}^{-3} \text{ s}^{-1}$, then the rise and fall times agree very well with the rail limiter data.

Thus, the observed rate of density increase $\dot{\bar{n}}_e$ is not the controlling parameter in the transport change. The quantity that brings together the rail-limiter and bundle divertor data is $\dot{\bar{n}}_{e(\text{refuel})}$ (shortened to $\dot{\bar{n}}_r$ in eq .8.28) the amount of fresh gas entering the plasma

$$\dot{\bar{n}}_{e(\text{refuel})} = \dot{\bar{n}}_e + \dot{\bar{n}}_{e(\text{pump-out})} \quad (8.27)$$

Empirical formula

If all the confinement-time data are plotted together (fig 8.20), an empirical relationship can be found which fits the upper and lower limits (for $\dot{\bar{n}}_r = 0$ and $\dot{\bar{n}}_r = 20 \cdot 10^{19} \text{ m}^{-3} \text{ s}$ respectively) quite well

$$\tau_{\text{imp}} \cong \frac{10 \bar{n}_e^{3/2}}{1 + 10^{-3} \dot{\bar{n}}_r \bar{n}_e^3} \quad (8.28)$$

where \bar{n}_e and $\dot{\bar{n}}_r$ are in units of 10^{19} m^{-3} . It should be emphasized that $\dot{\bar{n}}_r$ is not the rate of density increase, but the rate at which fresh gas enters the plasma.

In the long confinement mode, eq. 8.28 reduces to

$$\tau_{\text{imp}} \cong 10 \bar{n}_e^{3/2} \quad (8.29)$$

This mode could be considered as the "normal" state for a plasma with a quiescent edge, whose impurity confinement increases as $\sim \bar{n}_e^{3/2}$. If, as in the ASDEX IOC, a similar relationship for the energy confinement were to exist, it would be a very significant phenomenon, worthy of further investigation.

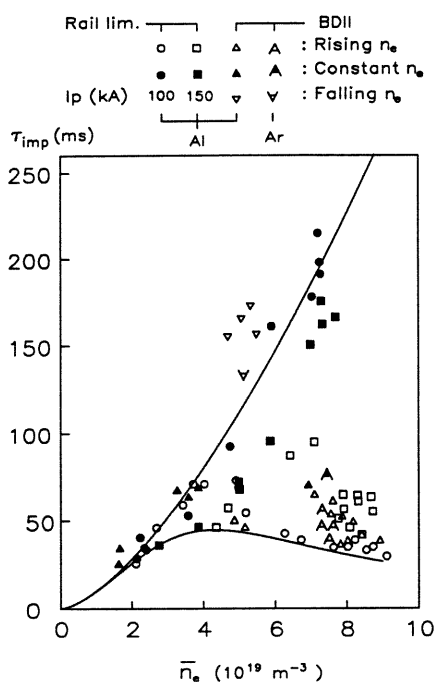


Fig.8.20 Collection of the confinement-time data for 100-150 kA rail-limiter and BDII discharges. All the data, with and without gas puffing, can be fairly well described by a single empirical formula.

Anomalous transport coefficients

Convection parameter S

This measurement is based on the ratio of rise/fall times of the impurity content. As discussed above, analysis was restricted to Al XII, where the ionization time makes only a small contribution to the rise-time.

Discharges were only analysed when \dot{n}_e was constant throughout the rise and fall phases of the ablation. Much of the data was unsuitable because, particularly to reach the highest densities, the density was still rising during ablation before reaching a plateau for the confinement measurement. Because of this, there are no rise-time measurements at constant \dot{n}_e for \bar{n}_e greater than $7 \cdot 10^{19} \text{ m}^{-3}$. It was not possible to make a rise-time measurement for Argon, due to the relatively long duration of the Argon puff, and so it was not possible to compare the convection for differing-Z impurities.

The most consistent set of data (fig 8.21) was obtained from the \dot{n}_e scan with the rail limiter, where the ratio τ_1/τ_0 (≈ 10) is almost constant, with a slight reduction towards short confinement times, corresponding to a reduction in S from about 2.5 to 2.

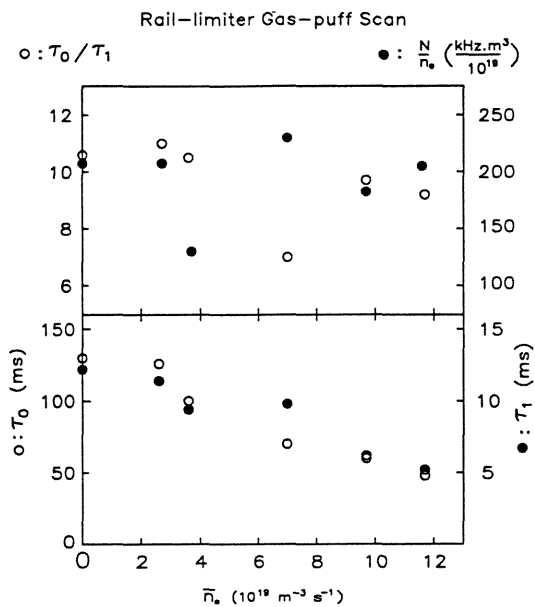


Fig.8.21 Impurity injection time constants and peak intensity (normalized to n_e) for the rail-limiter gas-puff scan.

All the measurable τ_1/τ_0 ratios have been plotted in figure 8.22, together with the corresponding convection parameter S. The scatter in the points may be due to the difficulty of ensuring that the density rate of change was constant during the measurement of τ_1 and τ_0 . To derive \dot{n}_e it was necessary first to plot the interferometer fringe-count from Polaroid photographs, and then measure the gradient - a potentially imprecise differential measurement.

There are insufficient points for long τ_{imp} at the higher densities, so it is difficult to make a strong statement about any change in S between long and short confinement. There is a clear tendency for S to increase with density, suggesting that the plasma changes from being mainly diffusive at low density to an S of about 2 or 2.5 at high density.

There is some evidence that τ_1/τ_0 is slightly lower for short confinement than for long, as shown in figures 8.21, and 8.22. This would be consistent with a shift to increased diffusivity as a result of gas-puffing. The general trend in S is probably more reliable than the absolute values, since they do depend on the assumptions made in eqs. 8.2.

Peak intensity

Further evidence that there is no major change in the convection parameter S , either with density or with gas-puff, is that the quantity of Al reaching the plasma core is remarkably constant for all the discharges. Figure 8.23 shows the peak intensity after ablation (normalized by \bar{n}_e to reflect the abundance) as a function of \bar{n}_e for 100-150 kA rail limiter and BDII discharges. There is no systematic difference between long and short confinement, or between diverted and undiverted discharges.

Another implication of this result is that there is no screening effect due to the gas-puff, even for BDII, where the gas feed rate was ten times higher than for the rail-limiter.

Transport parameters derived from eqs. 8.4-5 and figure 8.3 are shown in figure 8.24 for the gas-puff scan and in figure 8.25 for the density scan. The gas-puff scan represents the most controlled density behaviour during the rise and fall of the injection. Therefore the convection parameter S , on which the derivations of D_a and V_a depend, should be the most reliable. In the smooth change from long to short confinement there is a small decrease in S from about 2.5 to 2, and an increase in D_a from 0.09 to 0.45 m²/s. This implies an increase in V_a from about 3.5 to 7 m/s.

Figure 8.25 shows the density behaviour of D_a and V_a for DITE compared with the edge D_a for ASDEX²⁴ improved (IOC) and saturated Ohmic confinement (SOC). There is a striking similarity between the ASDEX and DITE impurity confinement results, although in ASDEX an improvement in the energy confinement was also observed, which was undetected in DITE.

Code modelling

The above analysis agrees only partially with previous code modelling of the density-scan data²⁵, which used a constant $D = 0.3$ m²/s, and varied from $s \approx 2.5$ for short confinement to about $s \approx 6$ for long confinement. The two methods agree well for short confinement, but not for long confinement. This is because the laser ablation in the early long confinement data took place prior to stabilization of the density, and resulted in apparently near-identical rise-times in long and short confinement. This led to an over estimation of the importance of convection, and an inability to model the signal intensities which were predicted, using a higher convection, to be much higher for long confinement.

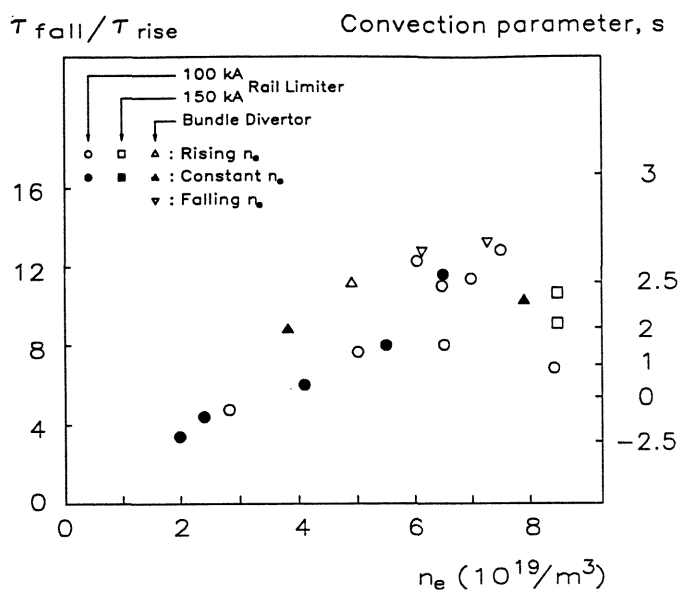


Fig.8.22 The fall-time to rise-time ratio τ_0/τ_1 versus density, with an indication of the corresponding convection parameter S .

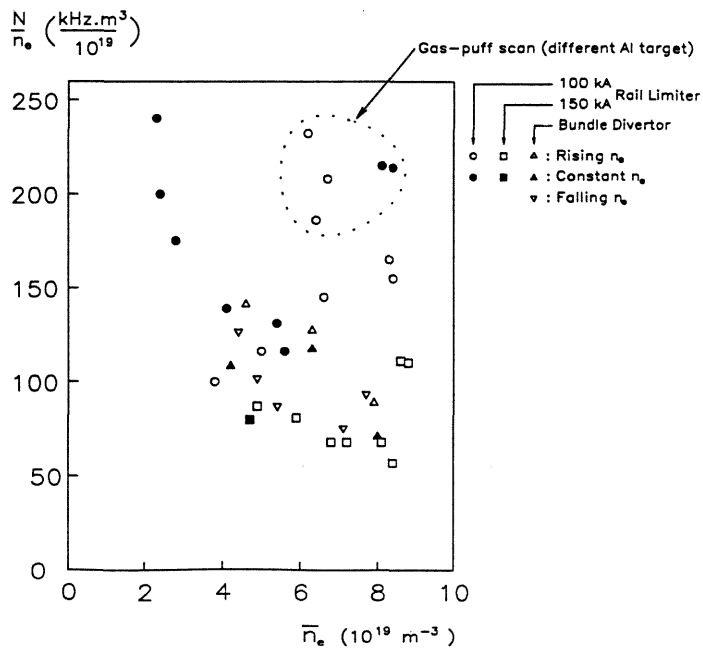


Fig.8.23 The peak intensity after ablation (normalized by \bar{n}_e to reflect the abundance) as a function of \bar{n}_e for 100-150 kA rail limiter and BDII discharges.

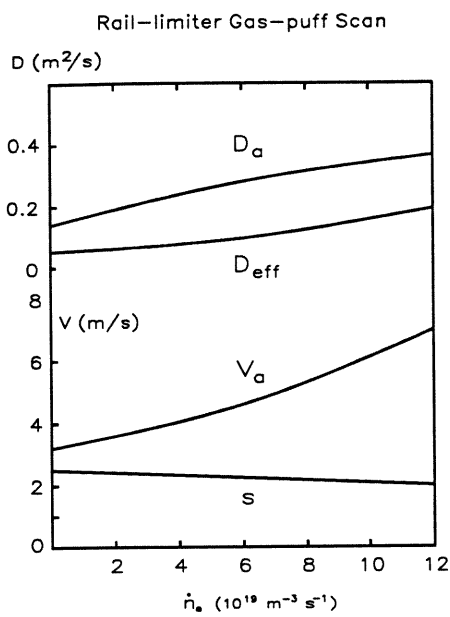


Fig.8.24 The effective diffusion coefficient D_{eff} and the anomalous transport coefficients D_a , V_a and S , derived from the gas puff scan at a constant density of $\sim 6 \cdot 10^{19} \text{ m}^{-3}$.

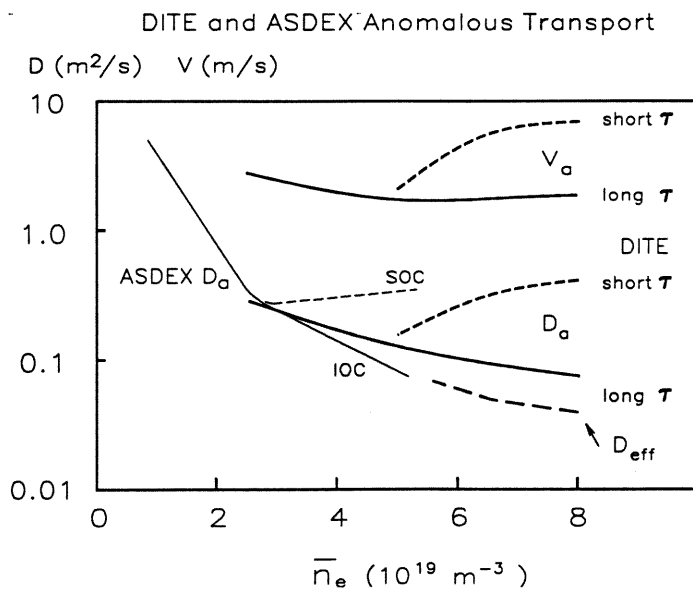


Fig.8.25 The effective diffusion coefficient D_{eff} and the anomalous transport coefficients D_a , V_a and S , for the long and short confinement modes in DITE. Also shown are ASDEX Saturated and Improved Ohmic Confinement (SOC and IOC).

8.7 RADIALLY RESOLVED MEASUREMENTS

The central-chord measurements have allowed us to observe the long/short confinement over a range of plasma conditions, but it is the radially resolved data that give the best insight into the reasons for the difference.

Plasma core

All the evidence suggests that there is no change in the core plasma between long and short confinement.

Aluminium emission

The Al XII and Al XIII profiles inside a radius of 8 cm are almost identical for long and short τ_{imp} (fig 8.13), and their emission is not dominated by the temperature profile (according to the DITE T_e profile in fig 8.4). The similarity of the Al XII/XII emission ratio in the two modes confirms that there is no major change in the central T_e or core T_e profile.

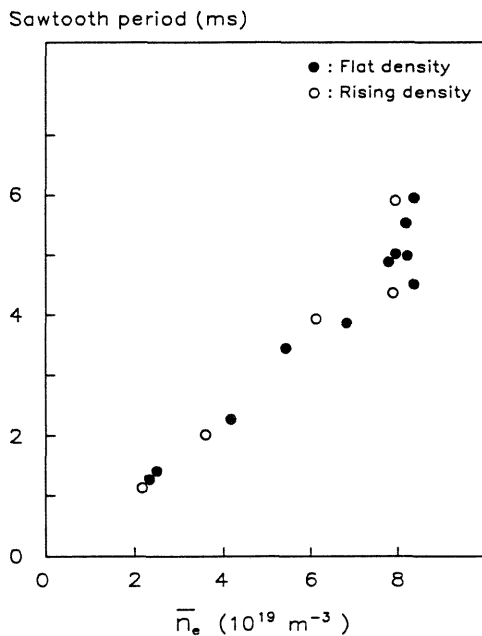


Fig.8.26 The sawtooth period, averaged over 100 ms, as a function of density. There was no significant difference, in either the sawtooth period or inversion radius, between long and short confinement modes.

Sawteeth

The sawtooth period (fig 8.26) increases linearly with density but there is no significant difference between the long and short confinement modes. The gas-puff (leading to reduced impurity confinement) has no effect on the sawtooth inversion radius, as can be seen in figure 8.10. This contrasts with the ASDEX results, which showed an increase in the sawtooth inversion radius during improved Ohmic confinement.

Seguin et al (section 8.2) also consider the effect of sawteeth on transport, and show that, for given values of D_a and S , sawteeth will reduce the inflow and confinement times. The effect is strongest when S is greater than about 5, and when the region affected by sawteeth is a large fraction of the minor radius. In DITE, the sawtooth-affected region was about $0.4 r_L$ which, for the fairly low S of around 2, would give a reduction of not more than 10% in τ_{imp} . This effect has not been included here.

Outer plasma

All the observed changes take place in the outer half of the plasma.

Radiative-recombination lines

As mentioned above, the Al XII and Al XIII profiles in the outer half of the plasma are almost entirely due to recombination of ions leaving the core. The slopes of these profiles vary considerably (fig 8.14), from which changes in the effective edge diffusion can be deduced, as described in section 8.2. The values of D_{eff} derived from the radiative-recombination lines agree quite well with central-chord time decay measurements (table 8.2). This finding is significant because they are independent measurements. The importance of the recombination measurement is that it has allowed a transport change to be unambiguously diagnosed in a specific part of the plasma. This would not have been possible using code modelling of central-chord observations.

Table 8.2 D_{eff} derived from the time decay of central chord radiation, and from the radial decay of radiative-recombination lines.

Source	Parameter	Long τ_{imp}	Short τ_{imp}
(Recomb. Scale Length)	λ (cm)	1.04	1.65
Recomb. Radial Decay	D_{eff} ($m^2 s^{-1}$)	0.035	0.10
Central Chord Time Decay		0.04	0.19

Recombinations per lost ion

The rate at which fully stripped Al ions are lost from the plasma core can be compared with the rate at which they recombine in the outer plasma:

The rate of loss of Al¹³⁺ ions can be estimated from the central total Al abundance Al_{tot}, the Al¹³⁺ fraction f_{Al¹³⁺}, the width r_{Al¹³⁺} of the Al¹³⁺ profile, the plasma major radius R, and the Al confinement time τ_{Al}, such that

$$\frac{dAl^{13+}}{dt} = \frac{Al_{tot} f_{Al^{13+}} V_{Al^{13+}}}{\tau_{Al}} \quad (8.30)$$

where the volume of the Al¹³⁺ region is given by

$$V_{Al^{13+}} = 2 \pi^2 R (r_{Al^{13+}})^2 . \quad (8.31)$$

The total recombination rate into Al¹²⁺ in the outer plasma can be derived by subtracting the calculated coronal equilibrium profile from the measured Al XII profile, using the electron-impact and radiative-recombination excitation profiles shown in figure 8.4. The derived values are shown in table 8.3, and must be considered as estimates only, since they are dependent on the axial fully stripped fraction, which would be strongly temperature dependent, and on the square of the estimate of the radial extent of the fully stripped ions. However, the ratios are not dependent on the instrument absolute calibration, and the ratio of 27/15 for long/short confinement is independent of most of the above uncertainties.

The large number of recombinations per lost ion implies that ions make many trips to outer plasma, recombine there and are transported back to the core to be re-ionized, before they are finally lost. This provides a mechanism for gross changes in the central impurity confinement, caused by transport changes in the outer plasma, even though transport in the core is unaltered.

Table 8.3 An estimate of the number of times a fully stripped ion visits the outer plasma and returns to the core before being lost.

	Long Conf.	Short Conf.
Fully stripped ion loss rate (ion/s)	~ 5 . 10 ¹⁴	~ 6 . 10 ¹⁴
Non-coronal recombinations (ion/s)	≅ 1.3 . 10 ¹⁶	≅ 0.83 . 10 ¹⁶
Recombinations/lost ion	~ 27	~ 15

Screening

These results contradict the hypothesis that gas puffing reduces impurity concentrations by screening impurities at the plasma edge.

Figure 8.23 shows that the gas-puff has a negligible effect on the amount of aluminium reaching the plasma core, even for the ten-fold higher gas-feed needed for BDII (fig 8.20). In these experiments at least, the action of the puff is to cause the rapid removal of impurities already concentrated in the plasma core, as shown in figure 8.10.

Summary

All the impurity confinement time data can be described by an empirical function of density and refuelling rate (eq. 8.28) that has $\sim n_e^{3/2}$ dependence for long confinement, and a smooth shift to short confinement with increased refuelling.

The importance of convection, as described by the convection parameter S , increases with density and decreases very slightly with refuelling.

Refuelling has no screening effect, at least for the Al atoms of a few eV energy produced by laser ablation, but does lead to a rapid release of core impurities.

The plasma is not in a regime where sawteeth significantly affect the impurity confinement, and the almost identical sawtooth behaviour for long and short confinement, combined with the unchanged spectroscopic core profiles, indicates that there is negligible transport change in the core.

There is a five-fold increase in diffusion for short confinement which, by study of radiative-recombination lines, has been shown to occur in the outer plasma.

8.8 CONCLUSION

This chapter has shown how the high sensitivity of a new instrument made possible a novel diagnostic technique which then gave direct information about a newly discovered plasma phenomenon.

There is no substitute for spatially resolved measurements, even from diode arrays. However, the advantage of spectroscopic over broad-band measurements is that the excitation of suitably chosen transitions can be directly interpreted. By contrast, interpretation of broad-band emission requires some model of the ionization balance which, being usually derived from a transport code, involves a circular argument.

Careful choice of an injected impurity can allow some transport parameters to be derived analytically, minimizing reliance on code modelling,

and possibly leading to a better physical understanding. The observed ionization stage should be peaked on axis, its abundance and excitation should be stable against temperature variations, and its ionization time should be short compared with the impurity influx time.

Radiative recombination spectroscopy is an important diagnostic of transport in the outer plasma, and could complement influx measurements of weakly ionized impurities. The radial profile of radiative-recombination lines is much simpler to interpret than the emission from an ion close to ionization equilibrium, since it results from a single atomic process that is relatively insensitive to temperature. It should therefore be easier to observe any abrupt change in transport, for instance at the boundary of an H-mode, or the recombining ions streaming into a divertor.

The discovery of a long impurity confinement mode in DITE was first made, like most other discoveries, in the conditions most favourable for its observation: ohmically heated helium plasmas. These conditions may not have seemed very relevant to nuclear fusion, but since then similar phenomena have been reported in several other machines in deuterium. JET now has sessions devoted to impurity control by gas puffing, and it is possible that the next step device will rely on ohmically heated non-H-mode plasmas. From a fundamental plasma physics point of view, there are advantages in using helium plasmas to study this long confinement mode. Such plasmas appear to make it easier to obtain the long confinement mode (ASDEX required favourable wall conditioning before IOC could be obtained), and extended to higher density; they also eliminate wall and limiter pumping as a variable. The long impurity confinement mode may indeed be the fundamental mode for a stationary, unperturbed plasma.

These results show that the convection parameter S is a more immutable plasma property than diffusion, and is a function more of density than of refuelling rate.

Further experiments could use a high resolution polychromator such as that described in chapter 6 to observe a complete Lyman series in the outer plasma. This would measure the radial profiles of the several parameters: impurity transport from radiative recombination, neutral hydrogen from charge-exchange recombination, ion temperature from Doppler broadening, and electron temperature from the Lyman series decrement.

References

- ¹ K H Burrell et al. Nucl. Fusion 21 (1981) 1009.
- ² W Engelhardt et al, in Plasma Phys. and Contr. Nucl. Fusion Research. (Proc. 7th Int.Conf., Innsbruck, 1978) Vol.1 IAEA, Vienna, (1979) 123.
- ³ G L Jahns et al, Nucl. Fusion 22 (1982) 1049.
- ⁴ M Keilhacker et al, in Plasma Phys. and Contr. Nucl. Fusion Research, (Proc. 10th Int. Conf., London, 1984) Vol.1, IAEA, Vienna (1985) 71.
- ⁵ H Niedermeier et al, in Contr. Fusion and Plasma Heating, (Proc. 13th Eur. Conf.) Vol.9F, EPS Schliersee, Pt.1, (1986) 168.
- ⁶ A A Bagdasarov et al, in Contr. Fusion and Plasma Physics, (Proc. 12th Eur. Conf.) Vol. 9F, EPS, Budapest, Pt.1, (1985) 207.
- ⁷ R C Isler, Nucl. Fusion 24 (1984) 1079.
- ⁸ E A Marmor, J E Rice, J L Terry, F H Seguin, Nucl. Fusion 22 (1982) 1567.
- ⁹ J.Allen, G.E.Austin, K.B.Axon, R.Barnsley, M.Dunstan, D.N.Edwards, K.D.Evans, S.J.Fielding, D.H.J.Goodall, W.Han, N.C.Hawkes, J.Hugill, P.C.Johnson, G.M.McCracken, G.F.Matthews, W.Millar, N.J.Peacock, C.S.Pitcher, J.Pritchard, A.Sykes, M.F.Turner, J.P.Webber. Density limit and impurity transport investigations in DITE Tokamak In: Proc. 11th int. conf. on plasma phys. and contr. nucl. fusion research, Kyoto, Nov.13-20, 1986. Publ. by IAEA, Vienna.
- ¹⁰ J Castracane, Y Demers, L Könen and A Pospieszcyk. Nucl. Fusion, 27noll, (1987) 1921
- ¹¹ F X Söldner, E R Müller, F Wagner et al, Phys. Rev. Let. 61no.9(1988) 1105.
- ¹² V A Vershkov et al (in Russ.) Soviet Journ. Instr. Tech Exp. 6 (1987) 171.
- ¹³ A Gondhalekar et al, Proc. 18th EPS Conf. Contr. Fusion and Plasma Physics, Berlin, (1991).
- ¹⁴ E A Marmor, Rev. Sci. Instrum. 46 (1975) 1149.
- ¹⁵ F H Seguin, R Petrasso and E S Marmor, Phys. Rev. Let. 51no6, (1983) 455-8.
- ¹⁶ N A Krall and A W Trivelpiece. Principles of Plasma Physics, McGraw-Hill (1973).
- ¹⁷ F F Chen, Introduction to Plasma Physics, Plenum Press, New York (1974).
- ¹⁸ J E Rice, E S Marmor, E Källne and J Källne. Phys. Rev. A, 35 no7 (1987) 3033-44.
- ¹⁹ K Brau, S von Goeller et al, Phys. Rev. A, 22 (1980) 2769.
- ²⁰ H Van Regemorter, Astrophys. J. 136 (1962) 906.
- ²¹ H Summers, Rutherford Appleton Lab. report. AL-R-5 (1974)
- ²² J Spence and H Summers, J Phys. B, 19 (1986) 3749-76.
- ²³ C Breton, C de Michelis. EUR-CEA-FC-948, Fontenay-ax-Roses rept.
- ²⁴ O Gehre, G Fussmann, K W Gentle and K Krieger, Proc. 16th EPS Conf.on Contr. Fusion and Plasma Heating. Venice, (1989).
- ²⁵ N C Hawkes, N J Peacock, R Barnsley, S J Fielding, J Hugill, P C Johnson. Proc. 14th EPS Conf.on Contr. Fusion and Plasma Heating. Madrid (1987).

9 SPECTROSCOPIC DIAGNOSTICS OF TEMPERATURE AND DENSITY

9.1	Introduction	194
9.2	Electron Temperature	193
9.3	Electron Density	201
9.4	Ion Temperature	205
9.5	Conclusion	207

Viscount Davidson: *My Lords, though much remains to be done, the latest results from JET have been encouraging. A temperature of 140 million degrees centigrade has been reached. ...*

...

The Earl of Lauderdale: *My Lords, can my noble friend add to what he said about the progress of the JET project when he referred to a temperature of 140 million degrees centigrade having been attained? Can he say whether that has yet exceeded a duration of one-hundredth of a second?*

Viscount Davidson: *No, my Lords,*

...

Earl Ferrers: *My Lords, what kind of thermometer reads a temperature of 140 million degrees centigrade without melting?*

Viscount Davidson: *My Lords, I should think a rather large one.*

Hansard, 19th March 1987, (1517-9)

9.1 INTRODUCTION

Spectroscopic measurements of electron temperature T_e and density n_e depend on the presence of suitable impurities and on a favourable ionization balance, but are often the only means available in astrophysical and high-density laser-produced plasmas. In low-density magnetically-confined plasmas, other, more versatile techniques are available, and spectroscopy is likely to remain a secondary method. Given a careful choice of impurity and parameter range, however, useful results can still be obtained by spectroscopy.

The Bragg rotor spectrometer was particularly useful for these measurements because it was able to measure line-ratios over a wider spectral range than the He-like spectrum normally covered by crystal spectrometers. Moreover, the most favourable density-sensitive transitions lie in the 5 Å to 10 Å band, which has scarcely been monitored in low-density laboratory plasmas.

Some ion temperature measurements are also included here. Although it is very much a primary technique, the implementation of a two-crystal spectrometer was a secondary adaptation of the Bragg rotor spectrometer broadband survey instrument.

9.2 ELECTRON TEMPERATURE

The ionization balance is very a strong function electron temperature, which offers the possibility to measure T_e from the abundance ratio of different ionization stages of a plasma impurity. This technique has been used for the Solar corona but has been less commonly applied to low density laboratory plasma, where T_e can be measured reliably by Thomson scattering, from soft x-ray diode (SXR) measurements of the bremsstrahlung continuum spectrum, and from electron cyclotron emission (ECE).

The spectroscopic technique is theoretically inferior because:

- a) Spectroscopy must rely on uncertain excitation rates, and a modelled ionization balance, whereas Thomson scattering, bremsstrahlung and ECE are physically simpler processes whose spectra can be calculated exactly.
- b) Ion transport can produce ionization balances that are far from coronal equilibrium, making it impossible to interpret line ratios in terms of temperature.

However, there are advantages for spectroscopy:

- a) The signal to noise ratio of the measurement is very good, because the signals from the two ions are restricted to a narrow bandwidth, that is, the convolution of the spectral line width with the spectrometer line-spread function. Typically $\Delta E/E \approx 0.001$ for the line ratio measurement, ≈ 0.1 for the Thomson scattered spectrum, and ≈ 1.0 for the bremsstrahlung and ECE spectra.

b) The good sensitivity of the Bragg rotor spectrometer, which gives count rates of a few MHz in the stronger lines, allows the line ratio to be measured to a few per cent accuracy in about 1 ms.

c) For suitably chosen ionization stages, a doubling of T_e will cause the emission ratio R_ϵ to increase by two orders of magnitude, and even though the absolute value of the measured T_e may be in error, this method is repeatably sensitive to small changes in T .

Much of the data from the Bragg rotor spectrometer contained temperature-sensitive line ratios, and in spite of the possible disadvantages of the spectroscopic technique, it was analyzed for comparison with Thomson scattering results. The primary motivation was to determine what region of the plasma, if any, was in coronal equilibrium so that the ion abundances would be in the ratios predicted by a corona model. Secondly, the technique was evaluated as means of independently measuring T_e , with good results as discussed below.

A commonly used spectroscopic diagnostic of T_e is the ratio of H-like to He-like ions. As shown in figure 1.9, the abundance ratio of Al XIII to Al XII changes by over two orders of magnitude in the T_e range of relevance to DITE. The emission ratio, $R_\epsilon(T_e)$, of a suitable pair of transitions can be calculated from the relevant excitation rates and model of the ionization balance. From chapter 1 we have

$$R_\epsilon(T_e) \equiv \frac{\epsilon_H}{\epsilon_{He}} = \frac{f_H C_H}{f_{He} C_{He}} \equiv \frac{u_H}{u_{He}} \quad (9.1)$$

where ϵ (ph/cm³s) is the volume emissivity, f is the coronal fractional abundance, C (cm³/s) is the excitation rate and u (cm³/s) is the emission function. The function $R_\epsilon(T_e)$ is dominated by the ionization balance, and so the plasma conditions must approximate to the chosen ionization model (coronal equilibrium in this case) for a meaningful T_e to be derivable.

Practical temperature measurement

The function $R_\epsilon(T_e)$ is shown in figure 9.2 for Mg, Al and Si, with an indication of its approximate useful range. Care is required in the choice of impurity, and the T_e range over which it is used as a T_e diagnostic.

Spectrometer calibration

To avoid cross-calibration errors it is clearly desirable to observe both lines with the same crystal. Although the lines are relatively close in the spectrum (fig.9.1), the change in the spectrometer calibration between them must be taken into account, even for a single crystal. This can be done by referring to the overall instrument sensitivity calibration described in

chapter 3. In the absence of a spectrometer calibration, or for spectrometers of insufficient band-pass to simultaneously observe the He-like $1s^2-1s2p$ and H-like $1s-2p$ lines, other pairs of lines from the H-like and He-like series (which usually overlap) have been used¹.

Ion distributions

In a tokamak, the temperature gradients are relatively steep and the effects of ion transport are potentially large. As a result, this line ratio technique is only reliable in a T_e range where the He-like ion fractional abundance is almost constant, and where the H-like fraction is a strong function of T_e . Under these conditions, the emission of both ions will be peaked on axis, making Abel inversion of the radial profiles less demanding, and minimizing the effects of ion transport: this would be a problem if the He-like ion were peaked off-axis. The abundance ratio could not reliably be used to measure T_e in DITE for radii greater than about 10 cm, because the transitions of interest were excited almost entirely by recombination (chapter 8), and coronal equilibrium did not apply.

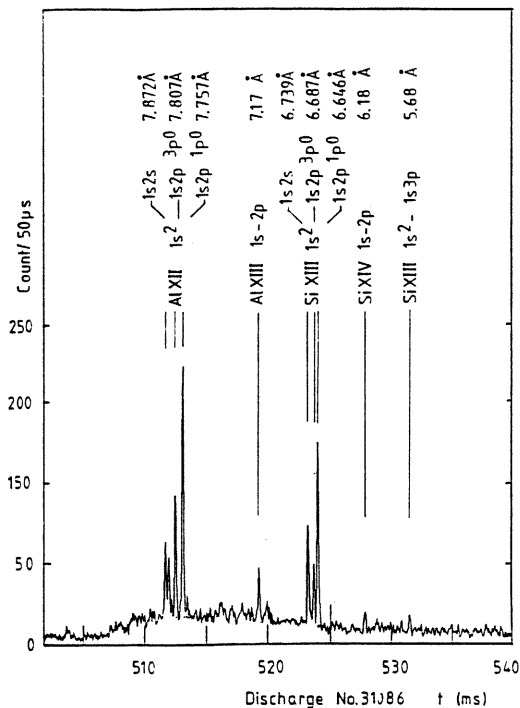


Fig.9.1 A spectrum from the Bragg rotor spectrometer, containing temperature and density sensitive lines of Al and Si.

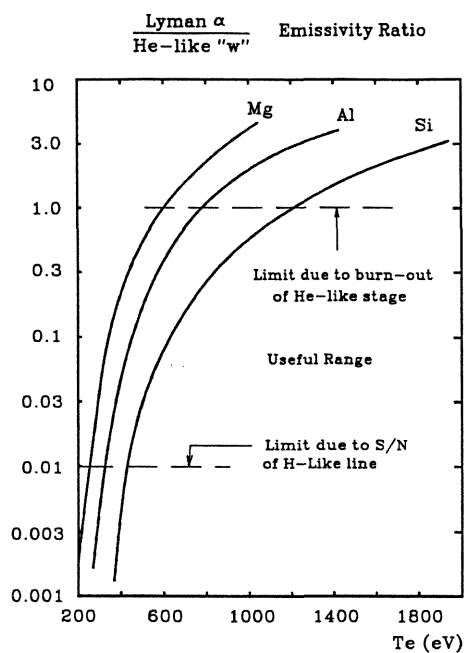


Fig.9.2 The H-like ($1s-2p$) to He-like ($1s^2-1s2p\ ^1P^0$) ratio as a function of electron temperature, showing the useful range for reliable measurement of T_e .

Useful temperature range

The lowest T_e that can be measured depends on the detection threshold of the $\text{Ly}\alpha$ line, which is typically between about 0.01 and 0.05 of the He-like resonance line, giving similar values of R_ϵ . The upper T_e limit is governed by the need to have both ions peaked on axis, and implies a maximum value for R_ϵ of 1.0. Within these constraints there is a small range of impurity Z-number that is suitable for a given T_e range. The useful T_e range for silicon is between about 400 eV and 1200 eV, as shown in figure 9.2. For DITE, Mg, Al and Si were ideal for ohmic discharges.

Radial profiles

Abel-inverted profiles of H-like and He-like emission allow T_e profiles to be derived. Figure 9.3 shows a series of fast survey spectra of Si XIII and Si XIV, recorded at 100 ms intervals during a single discharge where 415 kW of electron cyclotron resonance heating (ECRH) was applied from 330 ms to 530 ms. The Si had been added to the plasma, and these observations made, specifically to measure T_e spectroscopically during experiments with electron cyclotron resonance heating (ECRH)².

The increase in the Si XIV 1s-2p Ly α line at 6.18 Å relative to the Si XIII 1s²-1s2p ¹P⁰ line at 6.65 Å is a clear indication of an increase in T_e. Radial profiles were taken of this spectrum over a series of about 20 identical discharges. These were Abel-inverted, and the Si XIV/XIII ratio used to derive the T_e profiles with and without ECRH. These are compared in figure 9.4 with the Thomson scattering profile without ECRH (none was recorded with ECRH). The two profiles without ECRH agree well, while the profile with ECRH shows that, as well as raising the central T_e, the effect of ECRH was to broaden significantly the T_e profile.

Central-chord observations

As discussed above, for Mg, Al and Si, most of the He-like and H-like line radiation originates from within a minor radius of about 8 cm, allowing T_e profiles within this radius to be measured. Nevertheless, the T_e range in this region is relatively small, and the central-chord intensities alone can give a good measure of the central T_e, provided some estimate is made of the radial extent of the emitting regions for the two ionization stages. This is best done by taking radial profiles of the He-like and H-like emission for the relevant impurity.

The approximate emission ratio R_e is then given by

$$R_e \cong \frac{z_{He} C_{He} N_H}{z_H C_H N_{He}} \quad (9.2)$$

where z is the estimated column depth, C is the spectrometer calibration constant, N the counts in the line, and the suffices refer to He-like or H-like ions. T_e can then be obtained from a plot of R_e(T_e) (fig 9.2).

Electron temperatures were derived from the H-like/He-like intensity ratios of Al and Si in the spectrum shown in figure 9.1, which was recorded in fast survey mode using a PET(002) crystal. Using eq.9.2, the derived temperatures are: T_e(Al) \cong 580 eV and T_e(Si) \cong 670 eV, which is quite good agreement, and which probably slightly underestimates the axial T_e since it is effectively an average over the central emitting region.

Figure 9.5 shows the central T_e measured from the Si XIV/XIII ratio for a series of discharges with 415 kW of ECRH³. The toroidal field (B ϕ) was varied for each discharge in order to shift the position of resonance (and hence absorption of ECRH) outwards along the major radius. Such a series of discharges allowed a determination of the optimum B ϕ for maximum heating, with good sensitivity to small changes in T_e, since R_e is such a strong function of T_e.

Fig.9.3 Si spectra recorded with the Bragg rotor spectrometer, using three PET crystals, on alternate faces of the hexagonal rotor. ECRH was applied between 330 ms and 535 ms, resulting in a Te-induced increase in Si Ly α .

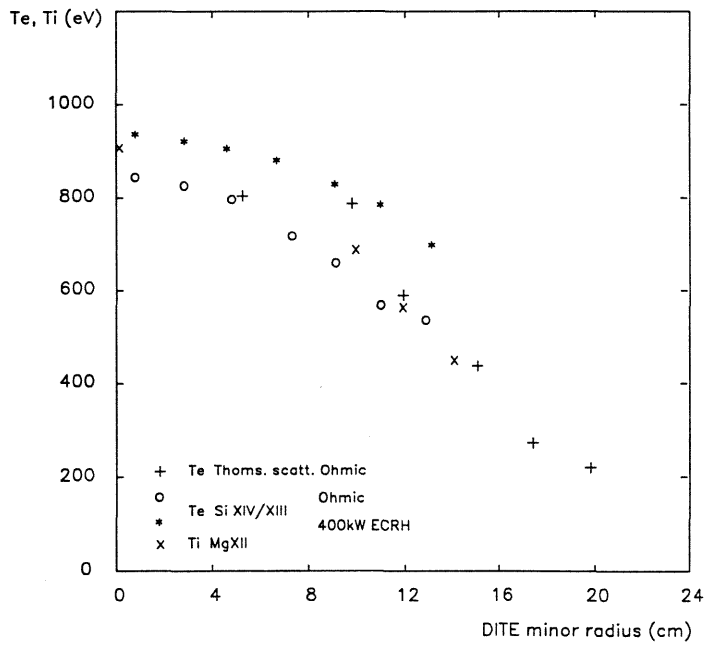
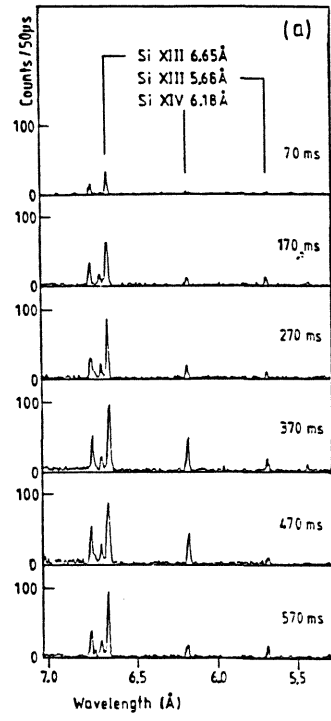


Fig.9.4 DITE Te profiles for Ohmic and ECRH discharges, derived from the Si XIV/XIII ratio. Also shown are the Thomson scattering Te profile and the two-crystal Ti profile for an Ohmic discharge.

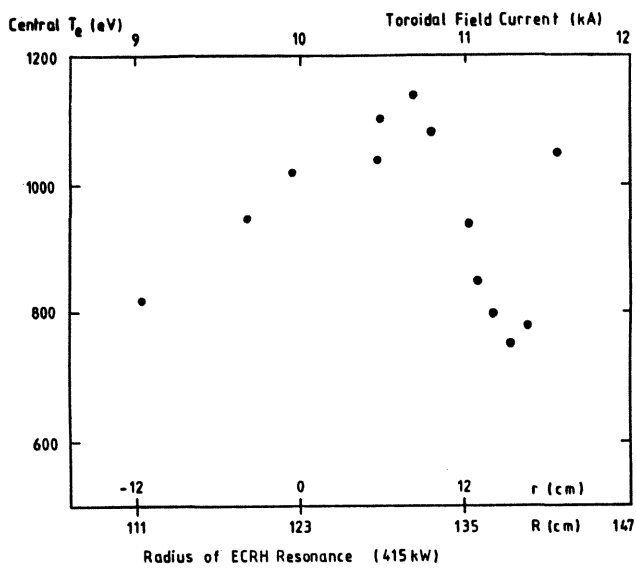


Fig.9.5 The DITE central electron temperature during ECRH, as a function of toroidal field, derived from the Si XIV/XIII ratio. The corresponding radius of maximum absorption of ECRH is also shown.

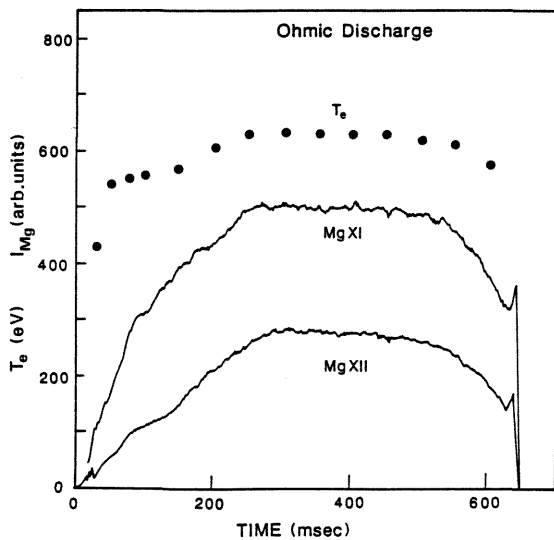


Fig.9.6 Time resolved electron temperature, based on the Mg XII/XI ratio, obtained from monochromatic data from two identical DITE discharges.

Figure 9.6 shows time evolutions (recorded in monochromatic mode) of the 2p resonance lines of Mg XII and Mg XI, as well as the central T_e derived from the ratio Mg XII/Mg XI (table 9.1). This shows the potential for achieving good time resolution, although for time scales of less than a few ms the time taken for the ionization balance to readjust to a change in T_e would become significant.

Table 9.1 Data to derive central T_e from central chord Mg XII/Mg XI Ratio

Transition	Wavelength λ (Å)	Instrument Calibration C_λ (count.rad.cm ² /ph)	Estimated Half Column Depth z (cm)
MgXI 1s ² -1s2p ¹ P ⁰	9.17	4.2 . 10 ⁻¹⁰	9
MgXII 1s-2p	8.42	2.9 . 10 ⁻¹⁰	6.5

Summary

The above results show that, provided a suitable impurity is chosen, T_e profiles of the inner plasma can be derived that agree well with Thomson scattering results. Perhaps more usefully, the central T_e can be estimated quite well from central chord observations alone, with good sensitivity to small changes in T_e , and with much improved time resolution compared with typical Thomson scattering or pulse-height-analysis bremsstrahlung systems. Thus by choosing an impurity to suit a particular temperature range, the spectroscopic technique can be used as a reliable independent measure of T_e , with an error of about 10% relative to Thomson scattering.

9.3 ELECTRON DENSITY

This section describes the investigation of the "R" line-ratio of He-like ions for suitability as an electron density diagnostic. Initially, results for Si XIII⁴ and Mg XI⁵, obtained from the DITE Tokamak, were compared with the R-matrix code calculations of Queens University Belfast. More recently, further results have been obtained from JET for Ne IX⁶ and Cl XVI⁷.

Electron density and temperature can be measured from the R and G line-ratios of He-like ions

$$R = f/i \quad \text{and} \quad G = (f+i)/r \quad (9.3)$$

where f is the 1s² 1S-1s2s ³S forbidden transition, i the 1s² 1S-1s2p ³P_{1,2} intercombination transitions, and r the 1s² 1S-1s2p ¹P₀ resonance transition.

The forbidden line becomes collisionally de-excited with increasing density, providing a means to measure density via the R ratio.

These lines have been extensively observed in tokamaks⁸, but have not been routinely used as n_e and T_e diagnostics. This is partly because other reliable techniques (mainly Thomson scattering and microwave interferometry) are available, and partly because the impurities that are most suitable for the measurement of n_e have their He-like spectra in the band between 5 Å and 10 Å which had scarcely been covered prior to the work described in this chapter.

For this type of density diagnostic to be as sensitive as possible, it is desirable to observe the He-like ion in the density range where the R-ratio is the strongest function of n_e . The density range common to most Tokamaks ($10^{18} < n_e < 10^{21} \text{ m}^{-3}$) restricts the choice of impurity Z-number to the relatively narrow range between Ne and Cl (fig 9.8), which is often further limited by the problem of line-contamination. Although Ne IX was observed in DITE, the spectrum was often complicated by many strong Fe L-shell lines, and the central density in DITE was generally too high for Ne IX to be useful. Ne IX has also been observed in JET⁹, whose Inconel vacuum vessel gave rise to negligible Fe-line contamination. However, since the Ne IX emission was peaked off-axis, it was complicated by profile and transport effects and code modelling of the line ratios was needed.

The Na X lines at around 11 Å would also suffer from Fe-line contamination, and although potentially suitable as a density diagnostic, Na has not been detected as an intrinsic impurity in any of this work. The problem of Fe-line contamination becomes progressively less serious for Mg through to Si, and allows the R-ratio to be measured even with a relatively low intrinsic level of Si.

In principle, the plasma density profile can be derived from the R-ratio by making a radial scan of the He-like spectrum. However, this approach is complicated by the steep T_e profile which means that the density scan would not be at constant T_e . A more serious drawback is the transport of fully stripped and H-like ions from the plasma core to the cooler outer regions, resulting in a non-thermal ionization balance, and a spectrum that is dominated by recombination rather than electron impact excitation. Although it is possible to model successfully the off-axis spectrum⁶, it is no longer possible to claim a direct measurement of the density, as it would be if the emission were peaked on axis.

The need to have the He-like emission peaked on axis, and to use impurities lower in Z than Si or S, limits the applicability of this technique to plasmas with central temperatures less than about 1 keV. Nevertheless, under favourable circumstances the technique provides a very sensitive measurement of the central density.

Results

The results presented here were recorded from many different discharges covering almost the full density range accessible in DITE, so that at each density the ions could be observed in the centre of the plasma, where there was approximate coronal equilibrium. Radial profiles of the Si XIV/Si XIII emission ratio gave good agreement with coronal equilibrium for radii less than about 10 cm (fig 9.4). Examination of the Si XIII emission profile showed that, like the Al profiles in figure 8.13, almost all the emission was from the central region of the plasma, where n_e was almost constant and T_e did not vary significantly. The range of n_e and T_e from which the central chord signal was emitted was similar to the error in the measurement of the central values, that is about 10% for T_e and 5% for n_e . This localization of the emission allowed the R-ratio to be measured from the central chord integrated signal alone, without the need for radial profiles at every plasma density.

In deriving the R ratios, account was taken of the change in spectrometer sensitivity through the spectrum (see chapter 3), which increased by about 7% between the resonance and forbidden lines, mainly due to the change in the Bragg reflection integral of the PET(002) crystal.

Mg XI was detected initially as a result of a fault in DITE (see chapter 7), and later a Mg probe was installed specifically for diagnostic spectroscopy. The Si XIII observations of high density Helium plasmas made use of the intrinsic Si, while those at low density made use of a Si probe that had been fitted as a source for spectroscopic diagnostics during the ECRH programme.

The strong effect of density is illustrated in figure 9.7, which shows Mg XI spectra at two different densities. The Z-dependence of the R-ratio can be seen in figure 9.1, where $R_{Al} = 0.57$ and $R_{Si} = 1.8$, and the results from a range of impurities agree well with the theoretical curves, as shown in figure 9.8. The results for Mg XI and Si XIII were obtained from DITE, where the emission was peaked on axis and the ions were close to coronal equilibrium. In this case the results may be compared directly with the theory, and would allow independent density measurements under similar conditions. The Ne IX⁹ and Cl XVI⁶ results were obtained from JET, where the emission was peaked off-axis. The results are consistent with the theory, after including corrections based on transport-code modelling of the non-coronal ionization balance, as discussed in detail by Coffey⁹.

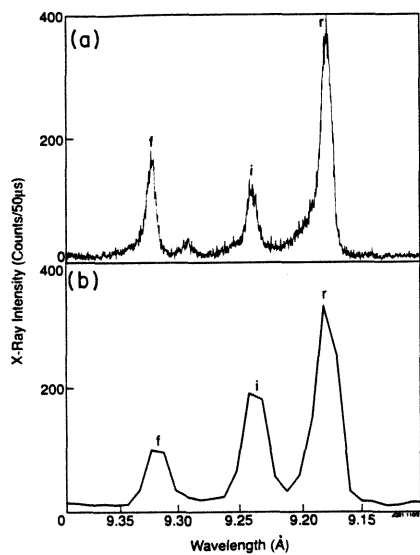


Fig.9.7 Spectra of Mg XI recorded at two different densities in DITE.

- a) $N_e = 1.1 \cdot 10^{13}/\text{cm}^3$, rotor scan speed $40^\circ/\text{s}$
- b) $N_e = 5.5 \cdot 10^{13}/\text{cm}^3$, rotor scan speed $1200^\circ/\text{s}$.

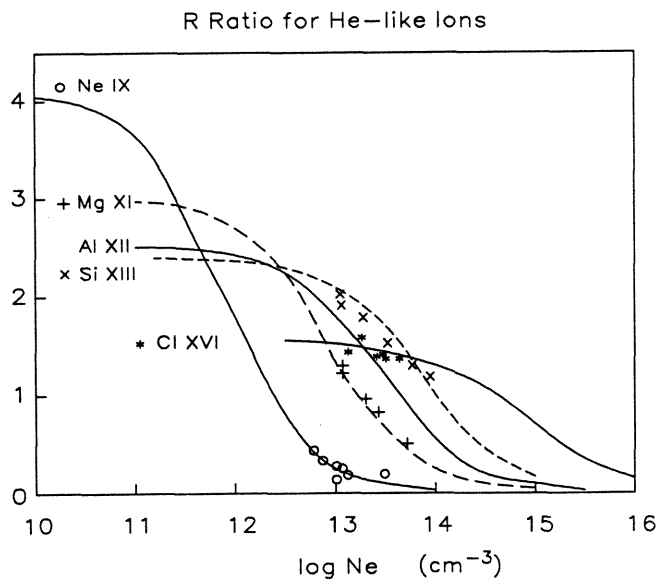


Fig.9.8 The measured R-ratio for Ne IX, Mg XI, Si XII and Cl XVI, compared with QUB R-matrix calculations. (Calculated at the temperature of maximum emissivity of each ion).

9.4 ION TEMPERATURE

As discussed in chapters 1 and 2, the measurement of ion temperature from Doppler broadening of impurity line radiation is a well established technique, and in the soft x-ray region is almost exclusively performed by high-resolution bent-crystal polychromators equipped with position-sensitive detectors. An alternative high-resolution technique is to use a two-crystal spectrometer in the antiparallel, dispersive configuration. This arrangement results in a scanning monochromator, which is theoretically less sensitive than the Johann spectrometer. However, it has the advantages that a position sensitive detector is not needed, the dispersion can be derived simply by measuring the angle between the two crystals, and the resolution need only be limited by the crystal diffraction properties.

Adapted Bragg rotor spectrometer

In order to demonstrate this technique, the Mkl Bragg rotor spectrometer was temporarily adapted by fitting a stationary second crystal and by removing the input collimator (fig.9.9). Two large ($65 \times 65 \text{ mm}^2$) PET crystals were used to observe the Mg XII $\text{Ly}\alpha$ doublet at 8.42 \AA in the DITE Tokamak. This was a compromise arrangement, because the non-rotating second crystal meant that the effective line-of-sight moved relative to the beam-line axis at three times the rate of change of Bragg angle, and thus limited the available Bragg angle range to about 0.6° . The relatively large Bragg angle of 75° allowed the diffracted beam to be directed into the Bragg rotor detector in its normal position. Careful baffling of the beam was necessary to prevent scattered radiation from reaching the detector, particularly since the input collimator was not in place.

Even with two reflections, count-rates up to 1 MHz were obtained, giving good statistics for the Voigt line-fit¹⁰ (fig.9.10), and allowing a radial profile of the ion temperature to be obtained (fig 9.4). The main disadvantage was the need to scan mechanically, which resulted in a relatively long time - about 200 ms - to scan the line.

Although this technique may not be the first choice for a high-resolution spectrometer, very useful results were achieved with minimal modifications to the existing Bragg rotor spectrometer (The second crystal was mounted via a miniature rotary table to a temporary bracket). These were also the first non-photographic crystal-spectroscopic ion temperature measurements from DITE.

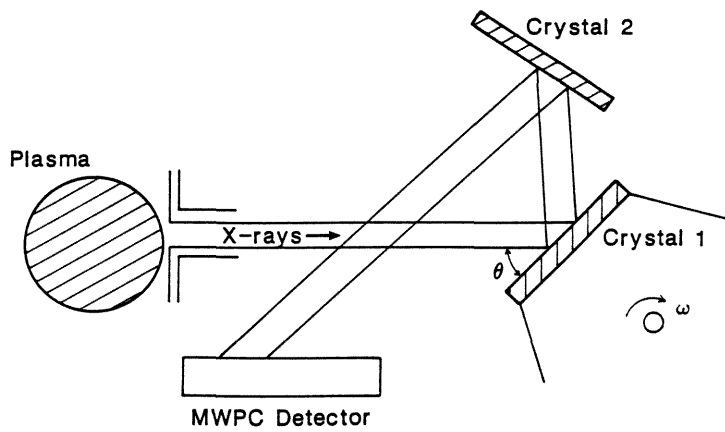


Fig.9.9 Schematic of the Bragg rotor spectrometer two-crystal adaptation.

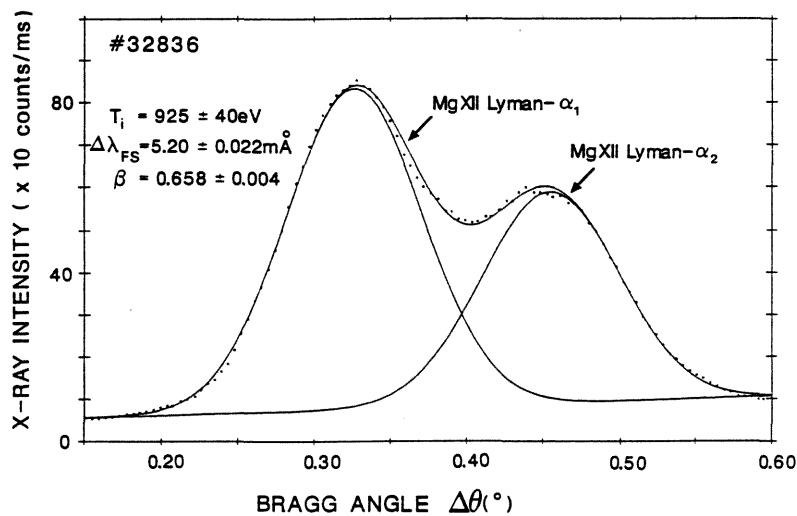


Fig.9.10 The Mg Ly α doublet recorded with two PET crystals in the dispersive (antiparallel) configuration, an adaptation of the Bragg rotor spectrometer. A Voigt fit (Dunn) to the profiles gives an ion temperature of 925 eV.

9.5 CONCLUSION

Although the techniques discussed above may have limited applicability, when used in the relevant parameter range valid results can still be obtained. The T_e profiles based on the Si XIV/XIII ratio were valuable in the ECRH experiment and had better time-resolution than the Thomson scattering system.

The density measurements using He-like ions were, in effect, a calibration of the R-ratio in a plasma of independently measured density. The agreement of the results with the R-matrix calculations suggests that they could be used with confidence to measure the density of other sources, particularly in astrophysics.

The simplicity of adapting the Bragg rotor spectrometer to act as a two-crystal spectrometer demonstrated its versatility. This ability to measure ion temperatures would be invaluable in the absence of a dedicated high-resolution instrument.

References

- ¹ J E Rice, E S Marmor, E Källne, J Källne.
Rev. Sci. Instrum. 57(8) (1986) 2154
- ³ M Ashraf, et al, 12th IAEA Int. Conf. Plasma Phys. and Contr. Nucl. Fusion Res. Nice, Oct 1988.
- ⁴ F P Keenan, S M McCann, R Barnsley, J Dunn, K D Evans, N J Peacock,
Phys. Rev. A, 39, 4092 (1989); UKAEA Culham Lab. Rept. CLM-P854 (1989).
- ⁵ F P Keenan, S M McCann, A E Kingston, R Barnsley, J Dunn, N J Peacock.
Phys. Rev. A, 44 no6, (1991) 3831.
- ⁶ I H Coffey, R Barnsley, F P Keenan, K D Lawson, N J Peacock.
10th Int. colloq. UV and x-ray spectr. of astrophys. and lab. plasmas.
Berkeley, Feb 1992. Proc. publ. by Cambridge Univ. Press, Jun 1993.
- ⁷ I H Coffey, F P Keenan, C E McAdam, R Barnsley, W J Dickson, K D Lawson,
N J Peacock. Physica Scripta, 47 (1993) 169.
- ⁸ R Bartiromo, in: Basic and advanced diagnostic techniques for fusion
plasmas. Varenna (1986) Publ. by International School of PLasma Physics,
"Piero Caldirola" Milano, Italy.
- ⁹ I H Coffey, PhD Thesis, Queens University Belfast, 1993.
- ¹⁰ J Dunn, PhD Thesis, Leicester University, 1990.

10 THE JET PRELIMINARY TRITIUM EXPERIMENT

10.1	Introduction	209
10.2	Instrumentation	210
10.3	Calibration and alignment	213
10.4	Background radiation	213
10.5	Tritium containment and clean-up	222
10.6	Results	226
10.7	Future experiments	227
10.8	Conclusion	229

I at once went to inspect the furnace, and found that the metal had all curdled, had caked as they say. I ordered two of the hands to go over to Capretta, who kept a butcher's shop, for a load of young oak that had been dried out a year or more and had been offered to me by his wife, Ginevra. When they carried in the first armfuls I began to stuff them under the grate. The oak that I used, by the way, burns much more fiercely than any other kind of wood, and so alder or pinewood, which are slower burning, are generally preferred for casting artillery. Then, when it was licked by those terrible flames, you should have seen how that curdled metal began to glow and sparkle!

...

Then I had someone bring me a lump of pewter, weighing about sixty pounds, which I threw into the furnace on to the caked metal. By this means, and by piling on the fuel and stirring with pokers and iron bars, the metal soon became molten. And when I saw that despite the despair of all my ignorant assistants I had brought the corpse back to life, I was so reinvigorated that I quite forgot the fever that had put the fear of death into me.

*The Life
Benvenuto Cellini c1588*

10.1 INTRODUCTION

To be useful for a reactor-relevant plasma such as JET, and for a future reactor, any diagnostic installation must operate in the presence of tritium, and with a high background flux of neutrons and γ -rays. The design of a crystal spectrometer for such conditions can involve severe compromises in sensitivity and spectral range. It is important therefore to evaluate the performance of spectrometers in the relevant conditions to ensure that no more concessions are made to shielding than are absolutely necessary.

This chapter describes the techniques used to monitor soft x-ray line emission from all impurities in the JET Tokamak plasma throughout the 1991 Preliminary Tritium Experiment¹ (PTE). The shielding performance of the Bragg rotor spectrometer was compared with that of the purpose-built JET active-phase double-crystal monochromator. The main objective was to obtain unique impurity data from the PTE, particularly since many related diagnostics were inoperable due to high background or to their lack of tritium compatibility. These included the VUV-XUV grating spectrometers, the soft x-ray pulse-height analyzer, and the soft x-ray tomography.

The two Bragg spectrometers were situated outside the JET torus hall and shared a beamline that was tritium compatible and well shielded against neutrons (fig 10.1). These instruments monitored all the main intrinsic impurities (Be, C, O, Cl and Ni) as well as checking against unexpected influxes of any other impurity such as Ne, F, Al, P, S, Ar, Cu and Zn, all of which had previously been observed.

The PTE was also an opportunity to evaluate the spectroscopic performance, neutron shielding and tritium containment of the instruments, with a view to possible improvements for the full JET active phase, and to aid the design of a diagnostic system for the next-step fusion device. To this end, procedures were tested for safe operation and clean-up of the beamline and spectrometer chamber in the presence of tritium, and the background radiation was measured and compared with the original design study.

The experiment was successful in that useful data were obtained from all the PTE discharges, resulting in a valuable contribution to the understanding of the impurity behaviour, particularly the higher-Z ions.

As expected, the shielding of the double-crystal monochromator was excellent, and it was shown that even the poorly-shielded Bragg rotor spectrometer could be used in this and future JET D-T experiments.

10.2 INSTRUMENTATION

The two spectrometers sharing the beamline were set up so that between them they gave the best available time resolution of all the main intrinsic impurities, and of most other occasionally-occurring impurities.

A series of JET discharges began with pure deuterium plasmas with additional heating from positive ion neutral beam injectors (PINIs), followed by a few discharges with a 1% mixture of tritium in deuterium in one PINI. Finally two discharges were made with 100% tritium in two PINIs. The two instruments gave useful data throughout these discharges.

Active phase double-crystal monochromator

This instrument² used two identical crystals in the parallel (1,-1) mode, a configuration resulting in a fixed detector position for all accessible wavelengths (fig 10.2). This allowed a labyrinth to be built around the x-ray beam path, shielding the detector against neutrons and γ -rays. Although the shielding of this instrument was excellent, as demonstrated below, its physical scale made the scan time relatively slow. It was therefore important to choose a spectral range that would yield the best possible time resolution of the largest number of impurities.

A pair of TIAP ($2d = 2.5757$ nm) crystals was scanned between 1.15 nm and 1.65 nm, as a compromise between a relatively narrow spectral range and a time resolution of about 1 s. This scan (fig 10.3) monitored H-like lines of O VIII and F IX, and Ne-like lines from metals ranging from Fe XVII to Zn XXI. Second-order lines of Al XII and Al XIII could also be monitored.

Bragg Rotor spectrometer

This instrument, described in detail in chapter 3, was fitted with a selection of crystals and multilayer mirrors to give almost full coverage from 0.2 nm to 11 nm, enabling it to monitor all the main impurities in JET. The full survey mode was used occasionally to check the condition of the vessel but, since the fast time resolution of the parallel-channel monitor was not available at the time, the rotor was reciprocated over a narrower range for most discharges. This included OV120 ($2d = 11.7$ nm), OV44 ($2d = 4.4$ nm) multilayers and a LiF crystal ($2d = 0.4027$ nm), and maximized the time resolution for Be IV, C VI and Cl XVI respectively.

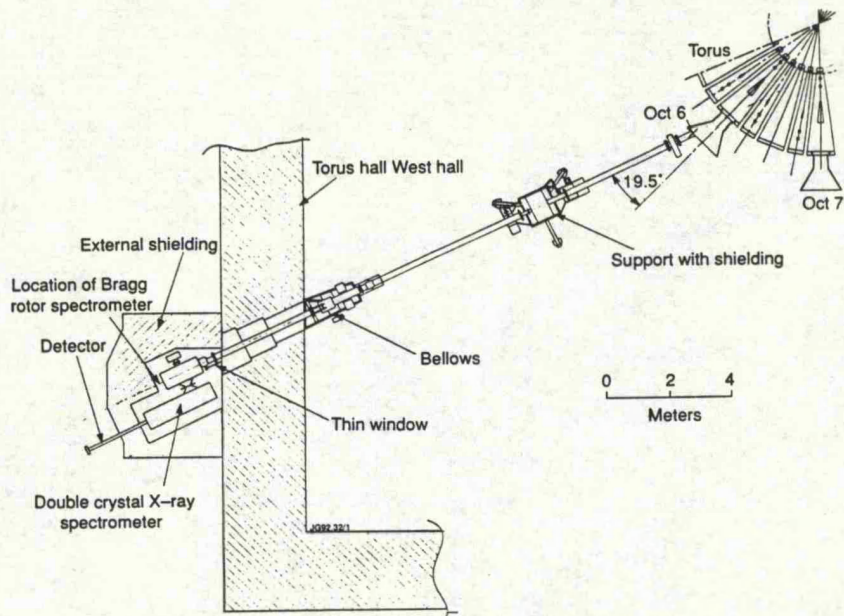


Fig 10.1 Location outside the torus hall of two Bragg spectrometers used during the JET preliminary tritium experiment.

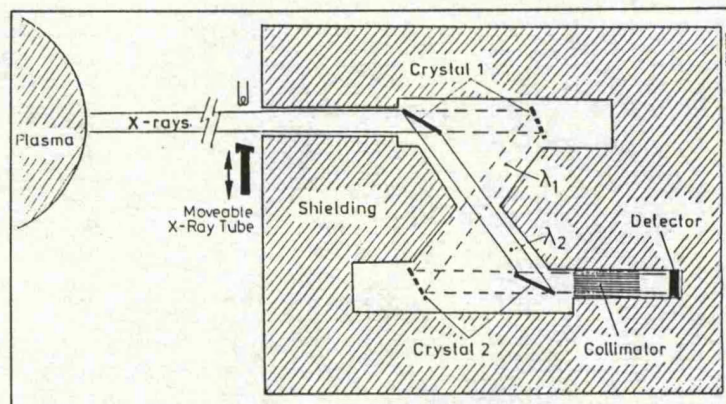


Fig 10.2 Schematic of the active phase double-crystal monochromator.

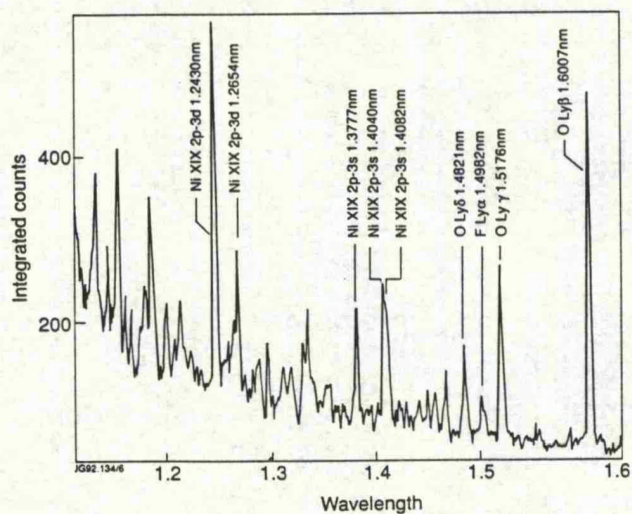


Fig 10.3 The double-crystal monochromator spectrum between 1.15 nm and 1.65 nm, recorded using TIAP crystals. This relatively narrow spectral range was used to monitor O VIII, F IX, Ni XIX and Zn XXI.

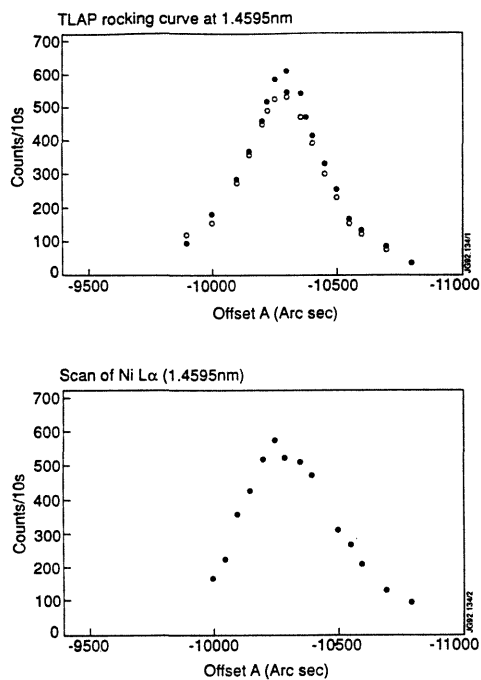


Fig 10.4 Crystal alignment data for the double-crystal monochromator at a wavelength of 1.4595 nm ($\text{Ni L}\alpha$). a) Two crystal (1,-1) rocking curve of the TLAP crystals (points before PTE; circles after PTE). b) A scan through $\text{Ni L}\alpha_{1,2}$. The offsets are arbitrary angles relative to the encoder datum.

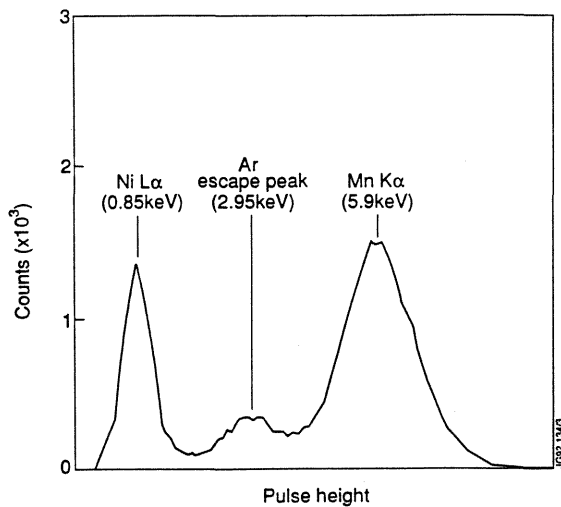


Fig 10.5 Detector energy calibration of the double-crystal monochromator, showing superimposed pulse-height spectra of $\text{Mn K}\alpha$ from the ^{55}Fe source, and $\text{Ni L}\alpha$ from the beamline x-ray tube.

10.3 CALIBRATION AND ALIGNMENT

Crystal alignment

A consequence of the double-crystal monochromator configuration is that during a Bragg angle scan the crystals must be kept parallel, with an error much less than the width of their combined diffraction profile; otherwise, gross changes in the sensitivity can occur. This alignment was checked regularly by means of a remotely deployable x-ray tube in the beamline. Figure 10.4a shows the rocking curve for TIAP (obtained by rotating the first crystal through the reflection peak while keeping the second crystal fixed) taken immediately before and after the PTE. There is no measurable change in the position or the width, and the FWHM of 370 arcsec agrees well with previous measurements³. No change in the profile due to neutron damage was expected for the relatively low extra dose accumulated during D-T discharges. The absolute wavelength reference for the instrument was defined by scanning both crystals in parallel through Ni L α (fig 10.4b).

Detector calibration

Figure 10.5 shows the detector energy calibration for the double-crystal monochromator. This is a superimposition of the spectrum from the ⁵⁶Fe source in the detector with the diffracted Ni L α signal from the beamline source. The energy scale is slightly non-linear as a result of operating the detector at a relatively high gas-gain to overcome electrical noise.

10.4 BACKGROUND RADIATION

The integrated neutron production for each of the two D-T discharges was about $7 \cdot 10^{17}$ neutrons, with a peak production rate of $6 \cdot 10^{17} \text{ n s}^{-1}$. This corresponds to a direct flux at the crystal of $2 \cdot 10^7 \text{ n.cm}^{-2}.\text{s}^{-1}$. The two spectrometers probably represented the worst-case and best-case shielding arrangements, and so a comparison of their background performance gives a guide to what limits can be achieved.

Double crystal monochromator

For the PTE this instrument was not fitted with its ultimate shielding, which will consist of a close-fitting concrete wall between the two crystal modules (fig 10.1), a concrete plug on the roof of the bunker, and containers of paraffin wax filling most of the unused spaces inside the vacuum chamber.

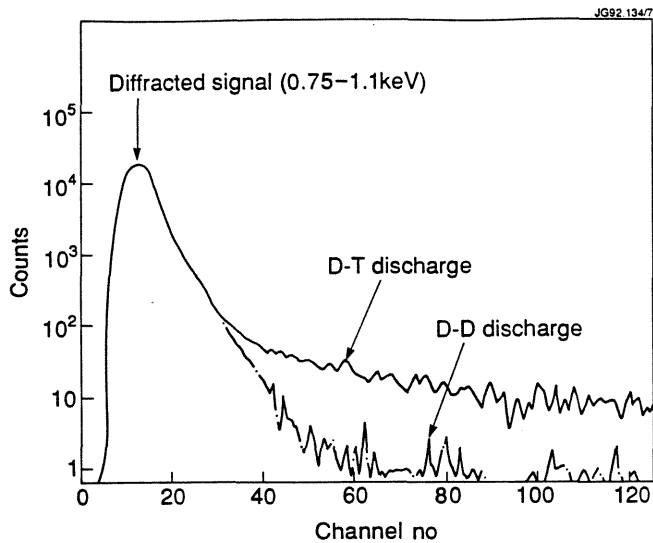


Fig 10.6 Pulse-height spectra from the double-crystal monochromator integrated throughout D-D (dotted line) and D-T (solid line) discharges. The total diffracted signal is about $2 \cdot 10^5$ counts, while the background is about 100 counts for D-D and 2000 counts for D-T.

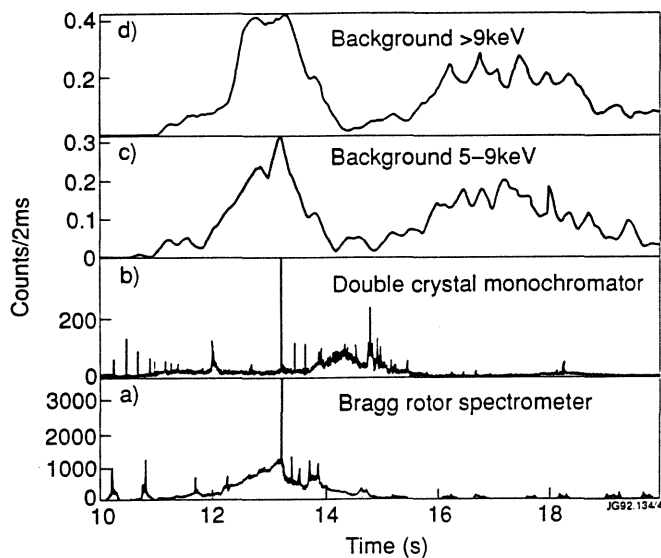


Fig 10.7 Raw data of reciprocating wavelength scans from both spectrometers, recorded during peak D-T neutron production at 13 s. The Bragg rotor spectrometer scan (a) shows a large background increase, and the signal-to-noise ratio for the weaker lines is less than unity. Three energy bands from the double-crystal monochromator show the diffracted spectrum (b), and the background counts in the ranges 5-9 keV (c) and > 9 keV (d). The first background peak at 13 s coincides with the peak in D-T neutron production.

Advantage was taken of the energy resolution of the gas proportional counter to give a time-resolved record of the background in a range of energy bands. To achieve this, the preamplifier signal was fed in parallel to five separate single-channel analysers, which were set to a range of energy windows including that of the diffracted signal. Thus, most noise pulses were not only discriminated against, but also stored in separate memory locations for later assessment of the signal-to-noise performance of the system.

As well as storing a range of energy bands from the detector, full pulse-height spectra were integrated during each discharge using a multichannel analyzer, and are shown in figure 10.6 for pure deuterium (D-D), and deuterium-tritium (D-T) discharges. The spectrum for a D-D discharge shows that the signal is almost entirely due to diffracted x-rays in the energy band of the scan, with a negligible contribution from scattering, fluorescence or background radiation. It follows that the base-line signal in the wavelength spectrum is due to diffracted continuum radiation. The pulse-height spectrum for the D-T discharge shows a broad-band background of about 2000 counts.

Raw data from the double crystal monochromator are shown in figure 10.7, where (b) shows the diffracted signal energy window, with two higher energy windows in (c) and (d). The peak in D-T neutron production occurred at about 13 s, and leads to a corresponding peak in the two background channels. These have been heavily smoothed, since there was on average less than one count per 2 ms sample. The diffracted signal shows no increase during the high neutron yield. The increase in the diffracted signal at 13.5 s is due to an increase in bremsstrahlung continuum as the plasma Z_{eff} increased with the fall in neutron production.

The background during D-D discharges was extremely low - only slightly above the natural background - and only the > 9 keV channel was sufficiently far from the tail of the diffracted pulse-height distribution to allow a noise analysis. To reveal the background during D-D and 1% tritium discharges, it was necessary to add together the background from several discharges, and to bin the data at 1 s intervals (fig 10.8).

Figure 10.9 shows a more detailed comparison between the summed background above 5 keV and the D-T neutron production for a PTE discharge. The best agreement is achieved after multiplying the normalized peak background by 0.8. The delayed peak must be due to secondary activation, although its origin has not yet been identified.

The background count-rate in the energy band of the diffracted signal is estimated from the pulse-height distribution to be the same as that above 5 keV, so that figure 10.9 is a good estimate of the background level in the spectrum (fig 10.7b). Typical integrated counts in the lines O VIII and Ni XIX range from 50 to 500, with the lines being scanned in about 10 ms.

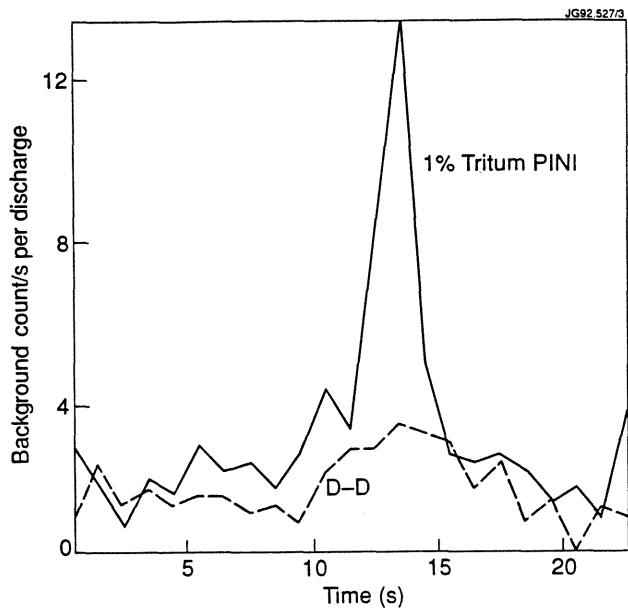


Fig 10.8 Background in the detector of the double crystal monochromator during D-D and 1% tritium PINI discharges. Due to the extremely low background it was necessary to average the data from about 10 discharges in each case.

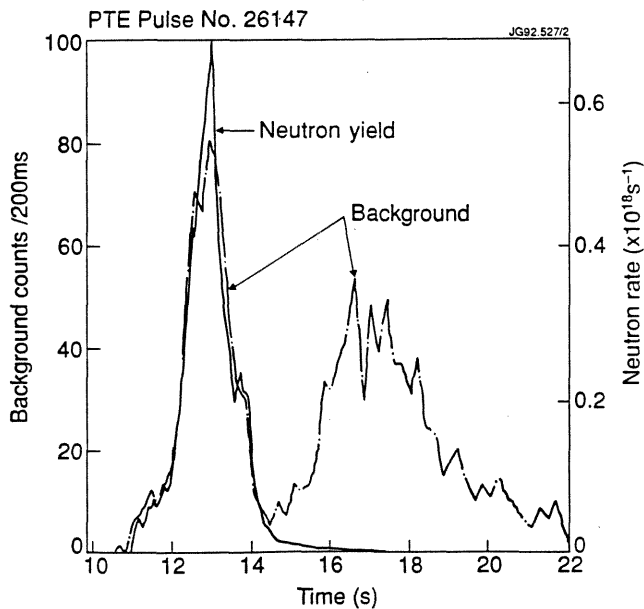


Fig 10.9 The double-crystal monochromator background above 5 keV (integrated over 200 ms but not smoothed) compared with the D-T neutron production for the PTE discharge 26147.

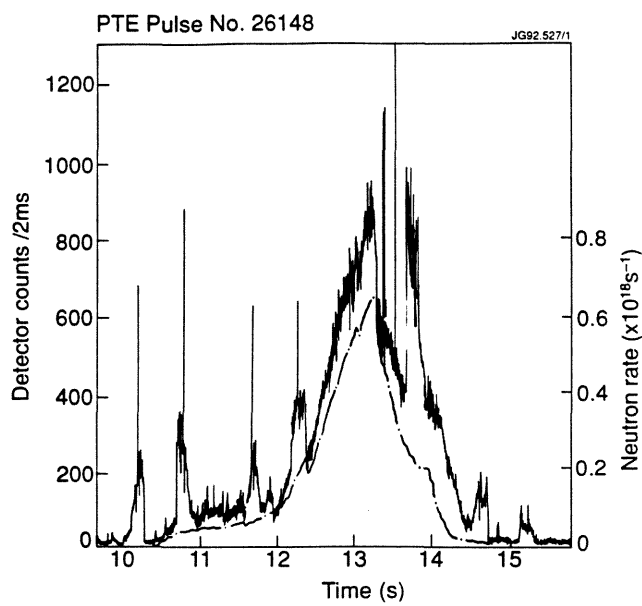


Fig 10.10 The signal from the Bragg rotor spectrometer compared with the neutron yield for a D-T discharge (26148). The neutron level has been scaled to indicate its probable contribution to the noise level.

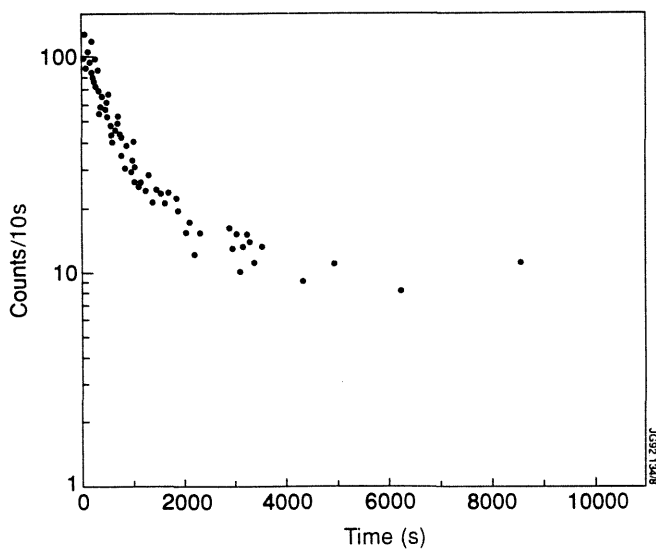


Fig 10.11 The background count-rate in the detector of the Bragg rotor spectrometer following a D-T discharge.

The peak background rate is 80 count/s, or 0.8 count during a line scan, making the background negligible and leaving the bremsstrahlung continuum as the effective noise level for the line intensities. The background sensitivity is equivalent to $7.5 \cdot 10^{-16}$ count/neutron (ct/n) for the prompt background only, and $1.5 \cdot 10^{-15}$ ct/n if the delayed background is included. The total background rate was about 2.5 times that in the > 5 keV band, giving a total background sensitivity of about $4.0 \cdot 10^{-15}$ ct/n. For D-D discharges, the total background was about $2.0 \cdot 10^{-15}$ ct/n, which is similar to the D-T prompt background. The background rates in the D-D and 1% tritium discharges were too low to make a definitive statement, but it appears that the delayed background only results from D-T neutrons.

Bragg rotor spectrometer

The configuration of this instrument was probably the worst case for neutron-induced background because the detector was only a few mm from the direct beam to the plasma, and had an area about 7 times greater than the crystal aperture. Its background sensitivity is therefore interesting as an upper limit which can be improved upon by almost any other instrument.

It was not possible to store multiple energy channels from this instrument, which had a system of five parallel preamplifier-amplifier-discriminator channels designed to process a high count-rate. The signal-to-noise ratio was less than optimum, due to the large energy range between Be Ly α (163 eV) and Cl XVI (3.4 keV), and the consequently wide pulse-height window. The signal (fig 10.10) shows a large increase in background that almost exactly follows the neutron yield, although the stronger lines still have a useful signal-to-noise ratio. After the D-T discharges, the detector background count-rate showed a considerable increase due to short-term activation (fig 10.11).

The background as estimated from figure 10.10 was equivalent to $5 \cdot 10^{-12}$ ct/n, which gave a crude signal-peak to background-peak ratio of about 1.0. However, provided the background is varying smoothly, the signal-to-noise (S/N) ratio is determined by the statistical variations in the background level during the time taken to scan a spectral line. The typical time to scan a line was about 10 ms, giving a worst background integral of 3000 counts, and a statistical variation of $\sqrt{3000} \approx 55$. The strong lines such as Cl XVI and Be IV had over 1000 integrated counts (fig 10.10), and hence have S/N ratios of about 20. For C VI, which had only about 50 integrated counts during the peak neutron production, the S/N ratio is barely 1.0. This is a weakness in the data, since Carbon is such an important impurity for these discharges. However, several improvements are possible for future experiments at JET, and are discussed below in section 10.7. It was not

possible to estimate the D-D neutron background in this instrument, because the signature of the D-D neutron yield could not be identified in the raw data in the same way as it was for the D-T discharges (fig 10.10).

Table 10.1 Signal and noise characteristics of the Bragg spectrometers

	Bragg rotor	Two-crystal
Peak D-T total background (ct/s)	$\sim 10^6$	1000
D-T backgrnd in sig. ΔE window (ct/s)	$6 \cdot 10^5$	400
Signal energy window (keV)	3.8	0.25
D-T backgrnd ct/s per keV bandwidth	$1.5 \cdot 10^5$	320
Typical int. signal counts in a line	500	100
Total backgrnd cts per D-D neutron	a	$2 \cdot 10^{-15}$
Total backgrnd cts per D-T neutron	$5 \cdot 10^{-12}$	$4 \cdot 10^{-15}$
Counts/neutron incident on crystal	10^{-3}	$2 \cdot 10^{-6}$

a: not measurable

Comparison with design calculations

As part of the design study for the double-crystal monochromator, R B Thom of UKAEA Winfrith Laboratory made an extensive Monte Carlo simulation⁴ of the neutron-shielding properties of the instrument and bunker. The relevant results are shown in figure 10.12, where the original figure has been modified from Rem/yr to show $\mu\text{Sv}/10^{18}$ D-T neutrons. To help assess the validity of this study, the background outside the bunker was measured using a Geiger counter, and dose estimates were also made based on the background count-rates in the proportional counters of the spectrometers themselves.

An integrating Geiger counter (Phychem Gammalog) was placed outside the bunker, directly behind the beamline penetration. It was zeroed about 20 min before each discharge and read about 5 min after each discharge. After subtracting the natural background of about $0.1 \mu\text{Sv} \cdot \text{hr}^{-1}$, the recorded additional background for the two tritium discharges 26147-8 was about $0.1 \mu\text{Sv}$ and $0.15 \mu\text{Sv}$ respectively, with the accuracy limited by the resolution of the Geiger counter.

The integrated background in the detector of the double-crystal monochromator was about 2000 counts, with a mean pulse energy of about 7.5 keV, absorbed in Argon gas at 500 mb pressure, in an active volume of 148 cm^3 . This gives a dose of $1.4 \cdot 10^5 \text{ MeV} \cdot \text{kg}^{-1}$, or $2.2 \cdot 10^{-8} \text{ Gy}$. Due to the incomplete shielding, the detector would have been exposed to γ -rays and partially thermalized neutrons from within the bunker, so a value of $Q = 5$ has been estimated in the relationship

$$\text{Human dose equivalent (Sv)} = Q \cdot \text{Absorbed dose (Gy)}$$

giving a dose of 0.11 μSv . This is in good agreement with the value from the Geiger counter, which was in a similar position. Both values are about 200 times higher than the design study value of 0.0005 μSv . This discrepancy can almost certainly be accounted for by the incomplete shielding.

The integrated background in the detector of the Bragg rotor spectrometer was about $5 \cdot 10^5$ counts with a mean pulse energy of about 10 keV, absorbed in Argon gas at atmospheric pressure, in an active volume of 48 cm^3 . This gives a dose of $5.6 \cdot 10^7 \text{ MeV} \cdot \text{kg}^{-1}$, or 9.4 μGy . Assuming $Q = 10$ for high energy neutrons in the bunker, this gives a dose equivalent of 94 μSv , which is somewhat lower than the value of 550 μSv calculated in the design study, though not for exactly the same position in the bunker. The doses derived from the proportional counter background signals can only be approximate because the absorption mass was taken to be that of the gas only, and there may have been some contribution from the chamber walls. The above results are summarized in table 10.2.

Table 10.2 Background levels in and around the bunker for PTE D-T discharges.

Location in fig. 10.12	Detector	Meas. dose ^a ($\mu\text{Sv}/10^{18} \text{ n}$)	Calc. dose ^b ($\mu\text{Sv}/10^{18} \text{ n}$)
Outside bunker at "A"	Geiger counter	0.12	0.0008
Outside bunker at "B"	Prop. counter	0.11	0.0005
Inside bunker at "C"	Prop. counter	94	
Inside bunker at "D"			550

a: Incomplete shielding.

b: Calculated for full shielding.

These results are qualitatively consistent, and the readings inside the bunker, where the absence of the full shielding is not very significant, suggest that the calculated doses are at least safe, and may even have over-estimated the actual doses. On this basis, fitting the full shielding can be expected to reduce the background in the detector of the double crystal spectrometer by a factor of about 200, resulting in a total neutron sensitivity of $2 \cdot 10^{-17} \text{ ct/n}$, and about $8 \cdot 10^{-18} \text{ ct/n}$ in the diffracted energy window. Improvements to the detector and pulse processing can be foreseen that might reduce this to about 10^{-18} ct/n , implying a count-rate of 10 count/s for the full JET active phase, and 1000 count/s for an ignited Tokamak such as ITER.

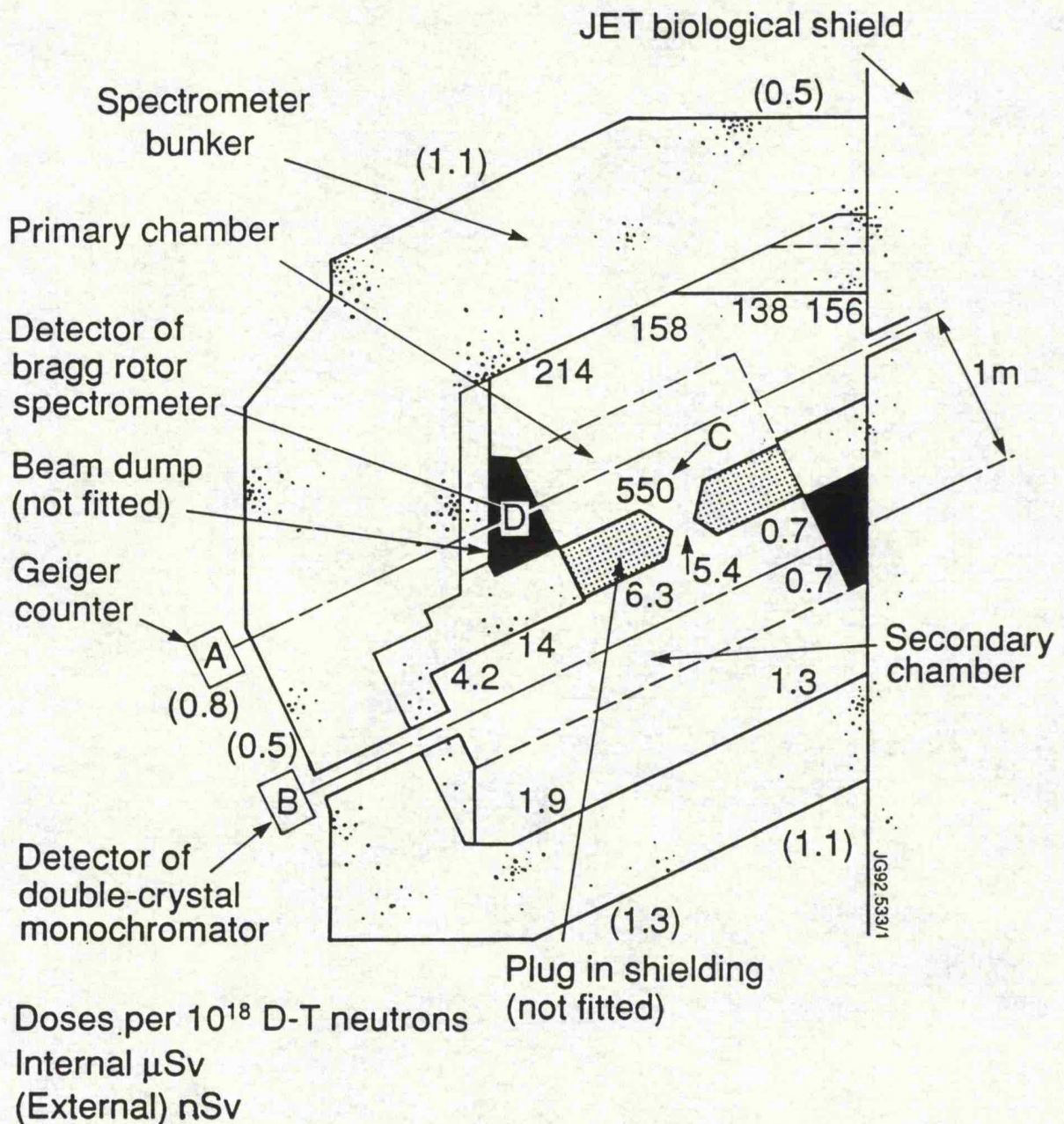


Fig 10.12 Calculated radiation doses in and around the spectrometer bunker for a JET PTE D-T discharge of 10^{18} n.

From the background point of view, the full shielding is not strictly necessary for the final active phase of JET, because a factor ten increase in the noise level could easily be accommodated. However, in view of the importance of shielding for future D-T plasma spectrometers, the ultimate performance of this system should be tested and compared with the design calculations.

10.5 TRITIUM CONTAINMENT AND CLEAN-UP

Since the double-crystal monochromator was designed for the full active-phase of JET, it was important for future operation to devise and test safe procedures for the operation and subsequent clean-up in the presence of tritium, and to quantify the tritium retention of the beamline and the chamber.

Beamline

The beamline (fig. 10.13) had no window at the torus end, and was isolated from the spectrometer vacuum chamber by a 1 μm polypropylene window. This window was protected against pressures up to 5 bar on either side by fine steel meshes supported by steel ribs.

For the full D-T phase of JET, the beamline turbo-pumps will be connected to a backing crown which will form part of the tritium recovery circuit, but for the PTE this system was not commissioned. Since it was not possible to allow the normal beamline backing pump to exhaust tritium into the torus hall, it was decided to operate the beamline with its backing line valved off, and its turbo-pumps in standby. This was done using an electro-pneumatic valve V10 which could be controlled from the diagnostic area (fig 10.13). During the PTE the air line to this valve was removed making it impossible to open unintentionally.

This mode of operation made it possible to close and re-open the main beamline/torus valve V1 in case of any failure, while ensuring that all accumulated tritium was eventually returned to the torus.

With the beamline operating in this mode, the backing line pressure settled at about 10^{-1} mb, and the beamline at about $5 \cdot 10^{-6}$ mb, with the system effectively being stabilized by the Torus. The backing line was regenerated most nights by shutting down the turbo-pumps, leaving V1 open and allowing the Torus to pump the system through to the backing line. When returning to normal operation, the volume of about 20 l between V2/V3 and V10 would be vented to the torus hall.

During a normal regeneration of the beam-line at 19:09 hr on 24th November 1991, release into the torus was monitored on the torus pressure and mass spectrometer. No release of tritium was detectable on the torus mass spectrometer.

Spectrometer chamber

Leakage of tritium from the beamline into the spectrometer chamber was restricted by a thin foil, but there was also a small by-passed interspace between the sight-line valve V4 and the foil, which alternated its communication between the beamline and the chamber whenever V4 was cycled.

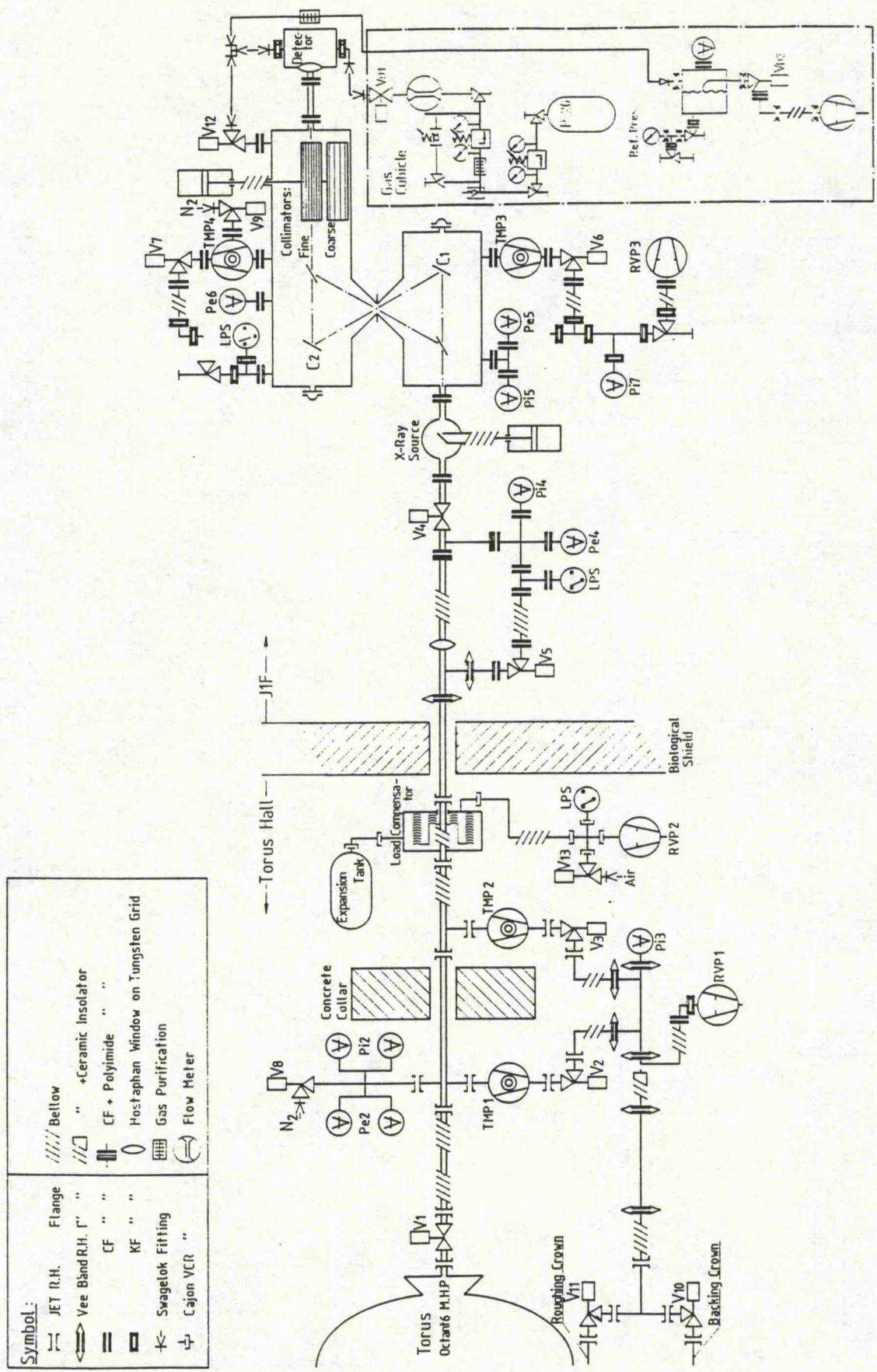


Fig 10.13 Schematic of the beamline and spectrometer vacuum systems.

It was estimated that the tritium transferred by this interspace when V4 opened at the start of a discharge was more significant than permeation through the foil.

The beamline foil used for the PTE was 1 μm polypropylene, which for a given thickness had been found (when used as detector window material) to have at least as low a leak rate as Hostaphan. Diffusion through a 1 μm foil would be expected to be four times higher than through 2 μm , but for these estimates a factor ten increase over the value for Hostaphan was assumed.

The foil leakage estimates have been based on experiments carried out at IPP Garching⁵, which gave a tritium leak rate equivalent to $4 \cdot 10^4 \text{ Bq} \cdot \text{s}^{-1} \text{ mb}^{-1}$ for a 2 μm Hostaphan polyester foil.

Two modes of operating the beamline were considered:

a) V4 Opened only during discharge:

Leakage through foil $\sim 80 \text{ Bq} / \text{shot}$ ($2 \times 10^{-6} \text{ mb}$ for 40 s)
 Transfer via interspace $\sim 0.4 \text{ MBq} / \text{shot}$ ($2 \times 10^{-7} \text{ mb} \times 10 \text{ l}$)

b) V4 open throughout tritium operation (4 hrs):

Leakage through foil $\sim 6000 \text{ Bq}$
 Transfer via interspace $< 0.4 \text{ MBq}$

In spite of the apparent lower tritium ingress in mode b, it was decided to operate in mode a, which is much safer in case of any failure.

Table 10.3 Estimates of tritium retention in the beam-line.

Backing line volume	20 l
Estimated Tritium partial pressure	$< 0.01\%$ of total
Daytime backing line pressure (~14 hr)	10^{-1} mb
Tritium trapped in backing line:	$< 2 \cdot 10^{-3} \text{ mb.l}$ (400 MBq)*
Overnight backing line press. (~10 hr)	10^{-4} mb
Tritium trapped in backing line	$< 2 \cdot 10^{-7} \text{ mb.l}$ (40 kBq)*

* Based on 1 mb.l T₂ $\Leftrightarrow 1.9 \cdot 10^{11} \text{ Bq}$

Any tritium that leaked into the chamber would have been pumped out and collected from the backing line by the JET tritium circuit. The chamber volume was about 1 m^3 with a pumping speed of 660 l/s, giving a time constant of about 1 s for gas retention. Estimates using a tritium diffusion code (TCCC) indicated that the amount of tritium retained in the chamber and on surfaces would be negligible.

The detectors of the two spectrometers were flow proportional counters with 2 μm polypropylene or Mylar windows. Their flow was vented to the atmosphere, but in view of the relatively low leak rate of tritium through their windows, and the high pumping speed of the chamber, tritium release to the atmosphere via this path was estimated to be negligible.

The air in the spectrometer bunker was sampled by a silica gel absorption monitor, which could differentiate between HT and HTO molecules. The recorded levels were so low that it was difficult to distinguish between the periods before and after the PTE:

Tritium monitor in bunker:		HT (Bq m^{-3})	HTO (Bq m^{-3})
Before PTE	(7 Oct - 5 Nov)	20	0.3
After PTE	(5-18 Nov)	2	22

Clean-up

The following procedure was followed after the PTE and before the spectrometer chamber and beamline were cleared for normal operation:

Chamber:

- i) Purge the backing line by using the ballast valve on the backing pump, while monitoring the tritium recovery stack.
- ii) Vent the chamber and draw a sample of the air inside the chamber through a tritium monitor via a sealed tube connected to the chamber vent valve.
- iii) Remove a flange. Monitor the air inside the chamber and take a swab from the inside of the flange.

Throughout this procedure no airborne tritium was detected above background, nor subsequently on the surface swabs.

Beamline:

- i) Wait for the pumping system of the torus to be returned to normal.
- ii) Reconnect air-line to remote control temporary backing line valve V10.
- iii) Open torus valve V1, shut down beamline pumps and allow torus to pump out the beamline through to the backing-line. Tritium pressure in the backing line would then be at its 'overnight' level.
- iv) Close the torus valve V1, and the normal backing line valves V2/V3.
- v) Open backing-line valve V10 locally.
- vi) Monitor tritium release locally and in tritium recovery stack.

At no time during this procedure was any tritium detected by monitoring instruments.

These results confirm that the tritium safety of the system was more than adequate for the PTE. For the full JET D-T phase, the beamline and spectrometer chamber backing lines will be connected to the tritium recovery circuit, further adding to security. The low level of tritium leakage through the thin foil should lead to negligible retention in the chamber and so allow relatively free access for crystal changes and maintenance.

10.6 RESULTS

The main purpose of this chapter has been to describe the techniques and subsidiary measurements necessary to obtain valid soft x-ray spectroscopic data from a D-T plasma. Within that context, the successful monitoring of all impurities throughout the PTE was itself the main result.

The data were analysed using similar techniques to those developed for the VUV/XUV grating spectrometers, as discussed in chapter 7.

Line intensities were derived from the raw data by taking the integral counts in a line above the background. An example of the time evolution of the main impurity line intensities throughout a D-T discharge is shown in figure 10.14. The impurity behaviour was broadly similar for the D-D and D-T discharges. The modest time resolution was sufficient to reveal the gross impurity behaviour, but at least a factor ten improvement to ~ 100 ms is required to give useful data on the timing of influxes.

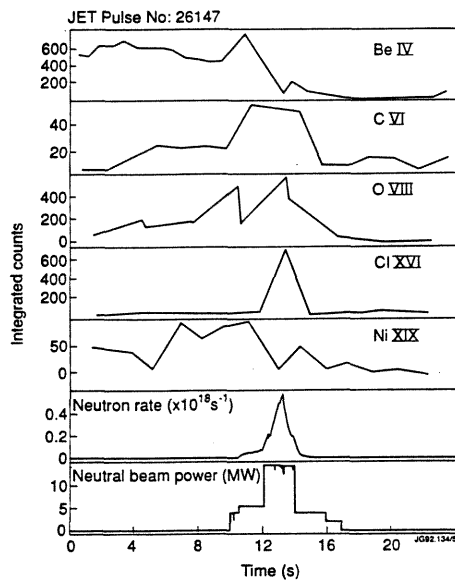


Fig 10.14 Time evolutions of the main impurity line intensities during a D-T discharge. The neutral beam power and neutron production rates are also shown.

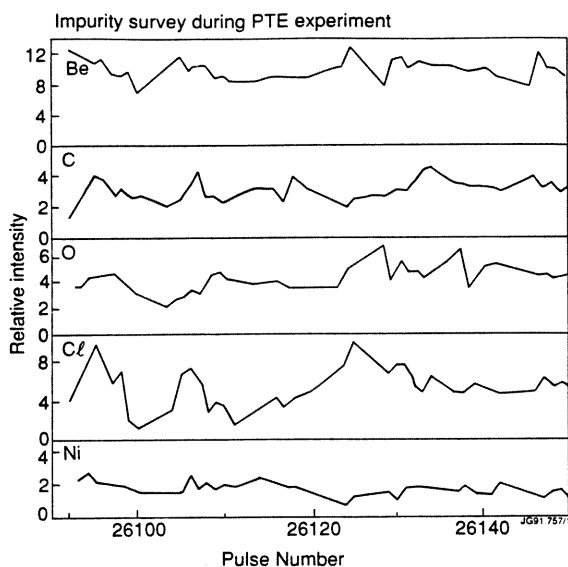


Fig 10.15 Impurity survey during the JET preliminary tritium experiment, measured in the early ohmically heated part of each discharge.

A guide to the general impurity trend during the week of the PTE is shown in figure 10.15, where the line intensities were measured at the same time in the early, ohmically heated, part of each discharge.

10.7 FUTURE EXPERIMENTS

Extrapolation to JET full D-T phase

For the full D-T phase of JET operation, we can expect a tenfold increase in neutron production relative to the PTE: about 10 MW to 20 MW of D-T neutrons.

For the PTE, the Double-crystal monochromator was not fitted with its ultimate shielding, which, according to the design study discussed above, is expected to give at least a further factor 200 background reduction. A further signal-to-noise improvement could easily be obtained by matching the detector area to that of the crystals. The detector was larger than the effective crystal aperture by about a factor three, due to the aperture-sharing with the Bragg rotor spectrometer and to an avoidable reduction in the size of the second TIAP crystal. If necessary, improvements to the detector energy resolution and pulse processing might yield a further factor three background reduction, resulting in about a factor 2000 gain overall, relative to the system as used for the PTE.

The Bragg rotor spectrometer was on the limit of acceptable background level during the peak neutron production of the PTE, and would require a factor 10 improvement in signal-to-noise ratio to be useful during the full D-T phase of JET. This should be possible with the upgraded Bragg rotor spectrometer now installed at JET and described in chapter 5. It has four separate narrow-band impurity-monitor channels with improved sensitivity, time resolution and much narrower pulse-height windows than the prototype. The high-rate pulse processing system is capable of handling an expected factor ten increase in background count-rate. A further background reduction, probably at least a factor ten, can be achieved by moving the detector back from the rotor by about 0.5 m to 1 m. This would reduce the working Bragg angle range to about 5° , which is sufficient to encompass suitable lines of the main impurities. The short-term activation shown in figure 10.11 is unlikely to pose a problem.

Extrapolation to ITER

The neutron rate for ITER is expected to be about 1000 MW of D-T neutrons, which is 1000 times higher than for the JET PTE.

The results presented here confirm the conclusion of a previous study⁶ that the Double crystal monochromator has the shielding potential to be operable on ITER. Due to the detector location (fig 10.1) and the small divergence (~ 0.3 deg) of the x-ray beam, the background can be further reduced almost at will by moving the detector back from the second crystal.

A single reflection instrument such as the Bragg rotor spectrometer, with close-coupled detector, is unlikely to be usable for the ignition phase, due to high background radiation during the discharge, and to activation of the detector. However, its simplicity, flexibility and high sensitivity would be useful in the commissioning phase, when impurity identification, monitoring and control will be important.

Other approaches

The technique of multiple reflections clearly provides excellent shielding. However, the use of a crystal for the first reflection, with its associated narrow band-pass, imposes penalties in sensitivity and alignment. An alternative approach would be to use a range of curved graphite and multilayer first diffractors, each deflecting a relatively broad wave-band through an angle of several degrees, resulting in significant attenuation of neutrons and gamma rays. These beams would be matched to an array of compact curved-crystal polychromators with solid-state detectors such as the instrument described in chapter 6. Such a system would monitor all the impurities, and give routine ion temperatures from Doppler broadening of spectral lines.

10.8 CONCLUSION

The Bragg spectrometers at JET were able to monitor all the major intrinsic impurities, and can offer a viable alternative to grating instruments, particularly in D-T experiments, where a shielded low f-number beamline is desirable. At the present level of analysis, the derived components of P_{rad} and Z_{off} for the light impurities (Be and C) are useful only in the Ohmic phase, and are complementary to charge-exchange spectroscopy. In future, the improved time resolution (~20 ms) of the completed Bragg rotor spectrometer will increase its value as a survey monitor and allow a deeper analysis of the impurity time behaviour.

Most of the key elements necessary for the spectroscopic diagnosis of an ignited thermonuclear plasma have been demonstrated in this work. Adequate shielding, spectral coverage, sensitivity and tritium containment were all achieved, using a thin foil to isolate tritium, and a low f-number beamline.

The other crucial factor, that of diffractor life in a high neutron flux, remains to be demonstrated, and the two-axis diffractometer described in chapter 2 is an ideal instrument to begin a programme of diffractor selection. Other areas, such as real-time data reduction, will be indispensable in future large experiments.

A system using multiple Bragg reflections will almost certainly offer the best solution for a future reactor such as ITER. For future experiments, the challenge will be to improve not so much the shielding, which has been shown to be more than adequate, but the sensitivity and time resolution. Some possibilities for ITER, based on experience with the instrumentation at JET, are discussed in the next chapter.

References

- ¹ The JET Team (many authors), Nucl. Fus. **32** (Feb 1992) 187.
- ² R Barnsley, U Schumacher et al, Rev Sci Instrum, **62**(4) (Apr. 1991) 889-898.
- ³ M Lewis, PhD Thesis, Leicester University, 1981.
- ⁴ R B Thom, Radiation levels in the vicinity of the KS1 x-ray spectrometer. AEE Winfrith report RPD/RBT/1107, December 1985.
- ⁵ IPP-JET private communication.
- ⁶ R Barnsley, R Giannella, M Stamp and P Thomas. Visible, grating VUV/XUV and crystal spectroscopy on ITER. ITER-IL-PH-7-0-80, July 1990.

11 DIAGNOSTICS FOR REACTOR CONDITIONS

11.1	Introduction	231
11.2	Neutron and tritium factors	233
11.3	Preselectors	234
11.4	Spatial resolution	235
11.5	Spectrometers	240
11.6	Conclusion	242

In 1955, the Austrian refugee physicist Richter was imprisoned in Argentina after failing to provide Peron with the fusion device he had promised. When asked about his welfare, his captors replied that he was perfectly happy: "We just keep him supplied with blank sheets of paper and he spends all day writing proposals."

11.1 INTRODUCTION

As has been illustrated in the previous chapters, impurity spectroscopy is important for all the parameters in the product $n_i \tau_E T_i$, which characterizes the performance of a fusion reactor. For a next-step device such as ITER, passive x-ray spectroscopy will be especially important, since the conditions for charge-exchange recombination spectroscopy will be less favourable than on JET (due to reduced beam penetration and increased bremsstrahlung continuum), particularly if ITER has mainly Ohmic heating.

Operation of the Bragg spectrometers during the JET PTE demonstrated that an instrument with multiple reflections could have adequate sensitivity, shielding and tritium containment. However, the penalty was poor time resolution and considerable mechanical complexity. Based on the JET experience, a reactor-relevant soft x-ray spectroscopy system using multiple reflection polychromators is proposed.

Design philosophy

The overriding consideration is to avoid the siting of any sensitive component in the plasma-facing chamber of the diagnostic.

Although the activation in the primary chamber will be orders of magnitude lower than in the torus primary containment, it will not be negligible. It seems undesirable to expect physicists and technicians to don radiation or tritium protection to adjust or replace precision components in the "hot" side of the installation. Therefore it should be unnecessary or even impossible for personnel to enter the primary chamber.

Ideally the plasma-facing chamber would contain no moving parts, thin windows or electronics. Plasma-facing diffractors would not be deployed in such a way that their degradation could affect the spectral resolution of the system.

The philosophy of starting with full active-phase design is questionable, firstly because a heavily-shielded design loses a lot of data in the early years (and it will be years), and secondly because by the time the machine is active, better techniques may be available. The strategy proposed in the design study for JET¹ was to have available a progressively increasing level of shielding that would only be incorporated when the background radiation dictated it. This means that the sensitivity and flexibility are never unnecessarily compromised, and seems as relevant for ITER as it did for JET.

Design principle

The use of a crystal, multilayer or grazing incidence mirror to deflect the incoming beam, and thus eliminate the line-of-sight neutron and γ -ray fluxes is the key to x-ray and XUV spectroscopy of an active tokamak.

The crystal method has been implemented successfully at JET, but necessarily reflects a narrow bandwidth and requires precise alignment control of moving parts. In contrast, the use of multilayer or grazing incidence mirrors would pass a broad band from a static installation, but still with the advantage of deflecting the x-ray beam through a relatively large angle of between 20° and 30° .

The first beam-deflecting chamber (fig 11.1) would contain only broadband diffractors and mirrors, whose alignment and diffraction widths would not be critical to the performance of the down-stream spectrometers. The primary chamber need contain only an easily retractable module, supporting a prealigned combination of mirrors, multilayers and low-resolution crystals such as graphite. In the early stages of ITER, for as long as the neutron flux would allow, these instruments could view the plasma directly, giving better sensitivity and flexibility. This was argued in the 1982 recommendation for JET. All the elements necessary to design the beamline are available at present, but it would be adaptable to future improvements in dispersive elements and detectors, over the expected 20-year time span of ITER.

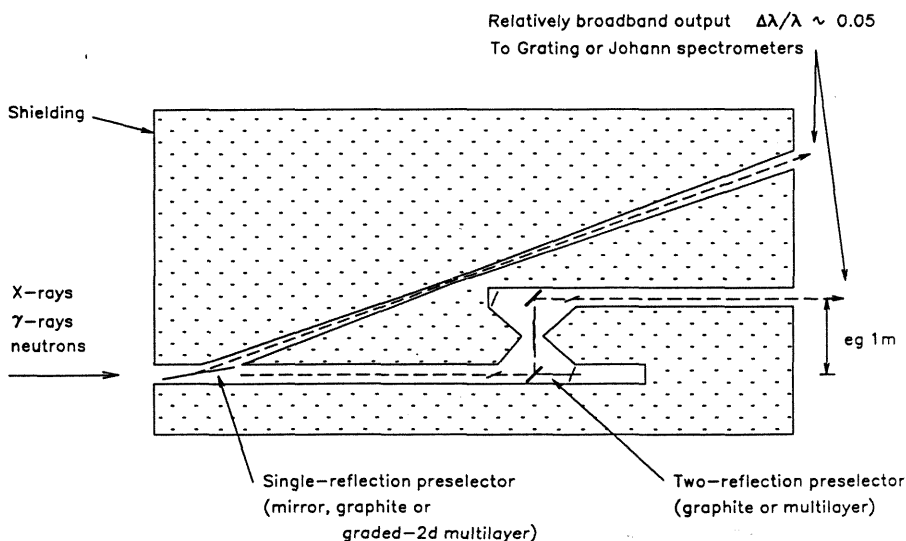


Fig.11.1 The general principle of a well-shielded primary chamber, containing only fixed mirrors and broad-band Bragg preselectors. Standard grating and crystal instruments analyse the deflected beam.

11.2 NEUTRON AND TRITIUM FACTORS

Results from the double-crystal monochromator during the JET PTE (chapter 10) showed that, as far as detector background was concerned, its shielding was sufficient even for the neutron levels expected from ITER. We can therefore go on to improve the original design in terms of sensitivity, spectral coverage and time resolution, with confidence that the detector shielding will be adequate. Similar extrapolations cannot be made for diffractor damage, which has not yet been tested at the neutron levels experienced at JET.

Neutron damage to crystals

Before considering any type of crystal spectrometer for diagnosis of an ignited plasma, it is necessary to be sure that the crystal exposed to the plasma will have a useful life.

In a test at Harwell² a Si diode detector had degraded energy resolution after bombardment with 14 MeV neutrons at a dose of 10^{13} n/cm². Given that a dose of 10^{17} n/cm² results in several displacements per atom, it is believed that the following levels of damage can be expected.

Neutron Dose (n/cm ²)	Effect
10^{13}	Si detector degraded but functional.
10^{15}	Probable dose for significant (but not destructive) damage to a crystal.
10^{17}	Several displacements per atom ie lattice may become amorphous.

The neutron flux at the first diffractor was estimated using the following assumptions:

- 1000MW of 14MeV neutrons, $\dot{n} \approx 4.5 \cdot 10^{20}$ n/s
- Major Radius R = 8 m, Burning core $\Delta z \approx 1.5$ m dia.
- \therefore Burning volume, $V_b \approx 2 \pi R \pi (\Delta z/2)^2 = 89 \text{ m}^3$
- \therefore Neutron emissivity, $\epsilon_n \approx \dot{n}/V_b \approx 5 \cdot 10^{12}$ n/cm³ s
- Distance of crystal from plasma, D \approx 25m
- Size of window to plasma, $d^2 \approx 0.2 \cdot 0.2 \text{ m}^2$
- Plasma solid angle seen by crystal $\Omega = \psi_x \cdot \psi_y = d^2/D^2$

$$\text{Flux at crystal} = \frac{\epsilon_n \Delta z d^2}{4\pi D^2} \approx 4 \cdot 10^9 \text{ n/cm}^2 \text{ s}$$

$$\text{Time for dose of } 10^{15} \text{ n/cm}^2, \quad T = 0.6 \cdot 10^6 \text{ s} \approx 130 \text{ hr.}$$

The estimated flux is similar to a more complete estimate made by the TFTR group³. However, the TFTR study used an estimated damage threshold of 10^{17} n/cm², which is 100 times greater than that used here. The resulting discrepancy in predicted crystal life is critical, because it influences the decision whether to make the first crystal a high-resolution analyser or a low-resolution pre-disperser. Experiments are necessary to evaluate the type and scale of neutron damage to crystals and multilayers, although this initial estimate suggests that a useful life could be achieved. An order of magnitude shorter life would be manageable, while two orders would become a problem.

A diffractor close-coupled to the plasma would receive a flux of about 10^{13} n/cm²s. This would seem to rule out any space-resolving Bragg optics except during the early, non-tritium, phases of operation.

Tritium containment

The previous chapter has demonstrated that a 1 μ m polypropylene foil is sufficient to isolate the spectrometer from tritium in the beamline. However, the first-window problem on ITER will be more severe, and tests will be necessary to find a suitable thin foil which could withstand direct exposure to the plasma, if such a window is unavoidable. An alternative is to include the first chamber in the tritium circuit and to have the thin foil in the path of the reflected beam, with a consequent large reduction in the neutron loading on the foil. A thin foil, supported by a mesh and ribs, has been tested to failure at 6 bar at JET. With some loss in sensitivity imposed by a stronger structure, the same principle should be suitable for a 20 bar safety margin which may be adopted for ITER.

11.3 PRESELECTORS

The main purpose of the first reflection is to deflect the desired photon beam away from the neutron and gamma-ray flux from the plasma. At soft x-ray wavelengths, unless extreme grazing angles are used, this requires a bandwidth-limiting Bragg reflection.

Mirrors

A doubly curved mirror with a grazing angle of 7.5° will focus all wavelengths longer than about 30 \AA through a small aperture in the shielding. The f-number of the mirror can match standard VUV and XUV grating instruments. As shown in figure 11.2, grazing angles of around 0.5° are necessary to reflect the full spectrum down to 1 \AA . A mirror will be more radiation-resistant than a

crystal, and could be a low-mass (hence low neutron scattering) and cheaply replaceable plastic replica. While such a mirror may be necessary for a broad-band pulse-height-analysis diagnostic³, a system using Bragg reflections should be more practical for Bragg spectroscopy, as discussed below.

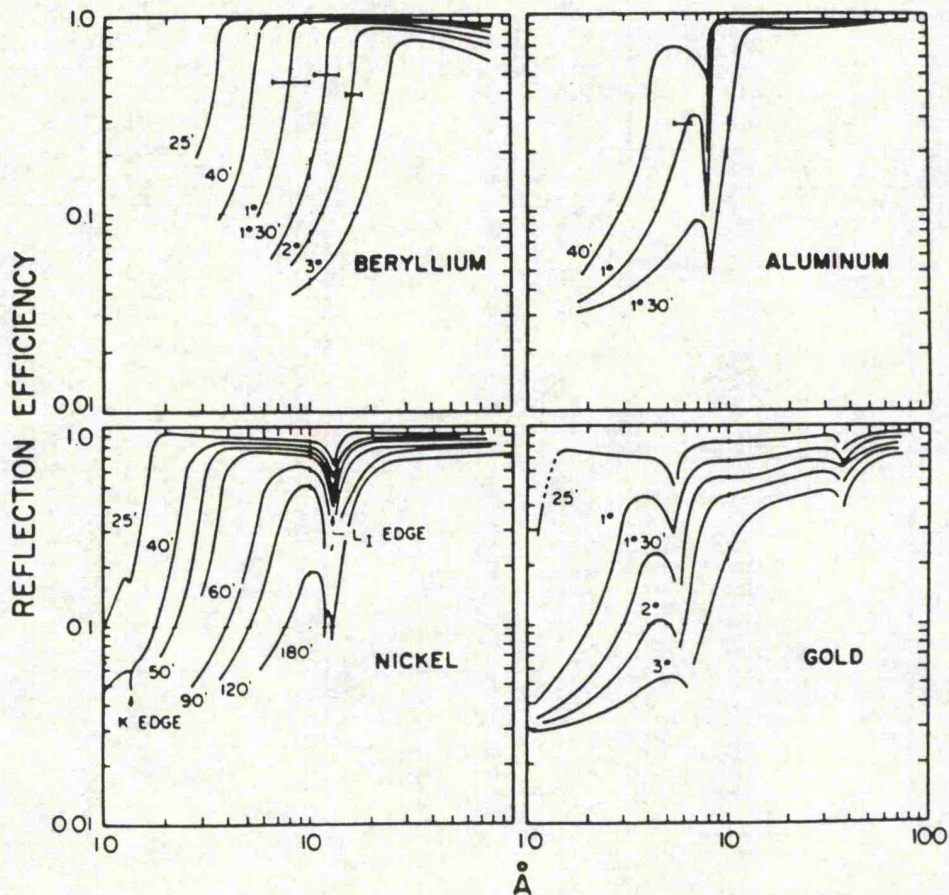


Fig.11.2 Calculated reflectivity of various materials as a function of grazing-angle and wavelength⁴.

Multilayers

As discussed in chapter 5, multilayers are commercially produced in a wide range of 2d-spacings, and to some extent the bandwidth can be tailored to suit the application. The reflectivity and bandwidth of typical multilayers are shown in figure 11.3, and are suitable for reflection into a higher resolution grating or crystal polychromator. Present-day multilayers range in 2d-spacings from about 40 Å to 300 Å, but this range might be extended in both directions in future, particularly if resolution is not the main priority.

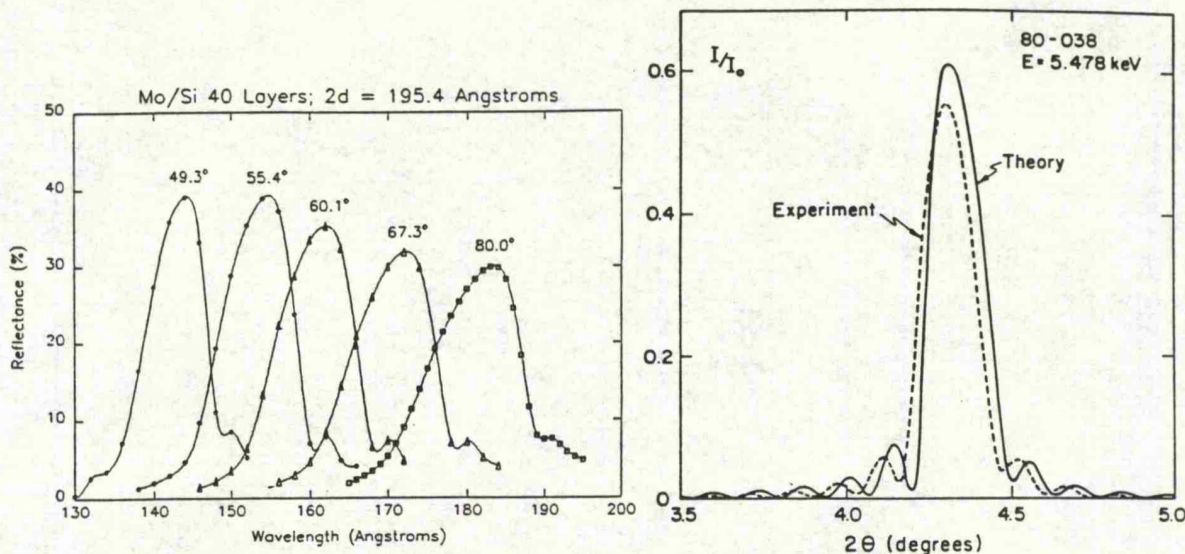


Fig.11.3 Peak reflectivity and diffraction widths for multilayer mirrors. Left: Mo-Si ($2d=195.4 \text{ \AA}$)⁵ at a range of Bragg angles. The band-pass would suit a 3 m grating instrument. Right: W-C ($2d=61.8 \text{ \AA}$)⁶ at a Bragg angle of about 2° , suitable as a preselector for a high-resolution Johann spectrometer.

Constant-deviation Bragg preselector

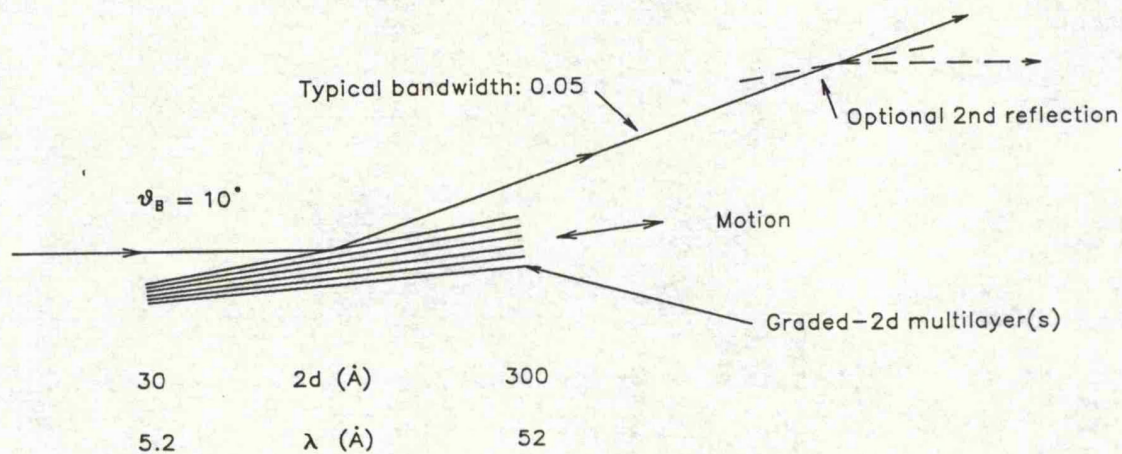


Fig.11.4 A constant-deviation Bragg preselector using a graded- $2d$ multilayer. The same multilayer operating at 2° would cover from about 1 \AA to 10 \AA .

An attractive possibility for a tunable constant-deviation Bragg preselector is shown in figure 11.4. This requires the development of a multilayer with a varying layer spacing across its surface. The constant angle of deviation allows more effective shielding and much faster scanning than would a double-reflection variable Bragg-angle design. A combination of two such preselectors operating at Bragg angles of say, 2° and 10° , would cover all the necessary spectrum below the cut-off of the Fresnel mirror.

Crystals

Graphite has several advantages as a preselector: it has high reflectivity and a broad diffraction profile (fig 11.5), its $2d$ of 6.71 \AA is well matched to the spectral region of interest for high resolution spectroscopy, and it has good resistance to high temperature. Due to its naturally broad diffraction width, graphite is probably less sensitive to neutron damage than most crystals, though this has yet to be demonstrated. For example, the diffraction width of graphite⁷ (002) can be as high as 1.5° , which is sufficient to reflect simultaneously the H-like Ni Ly α lines at 1.53 \AA , and the He-like Ni group at around 1.58 \AA . The Bragg angle of 13.4° results in a beam deflection of 26.8° .

A double reflection graphite preselector (fig 11.6) can be combined with a high resolution Johann spectrometer. For high resolution, the overall sensitivity is midway between that of a direct-viewing Johann spectrometer and the JET double-crystal monochromator, because the losses (~ 10 - 30) due to the graphite reflections would be partly compensated by the gain of the Johann optics relative to a high resolution collimator (~ 100). The alignment tolerance for a double-reflection preselector using graphite or multilayers is only a few arcmin, compared with the precision of a few arcsec required by the JET double-crystal monochromator, greatly simplifying its design.

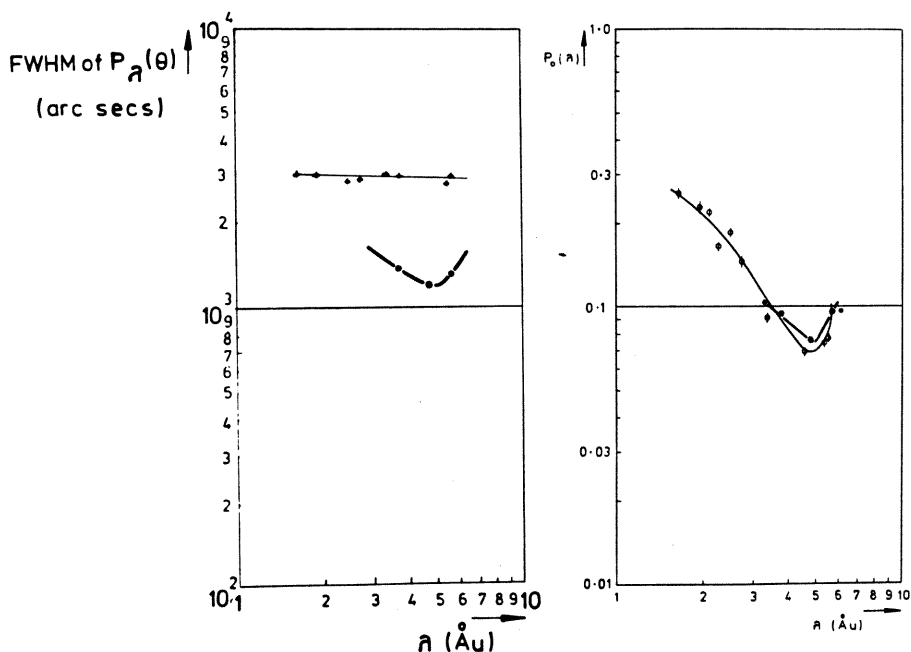


Fig.11.5 Diffraction width and peak reflectivity of graphite (002) $2d=6.71 \text{ \AA}$. These are two-reflection calibrations for x-ray astronomy satellites. Solid points are Ariel 5 data⁷. Crosses and open circles are Columbia data⁸.

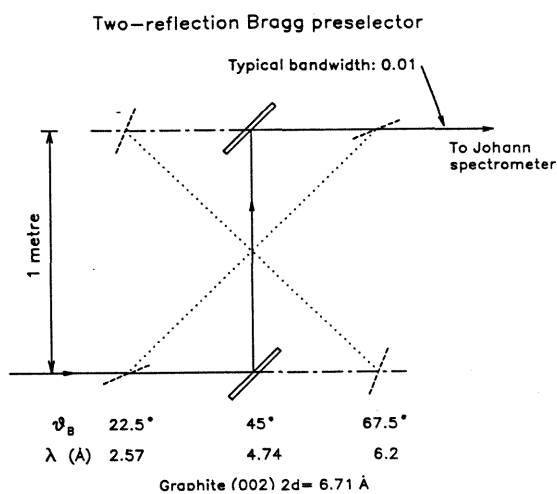


Fig.11.6 A two-reflection Bragg preselector. This is based on the JET double crystal monochromator, but using low-resolution crystals without a collimator. The bandwidth ($\Delta\lambda/\lambda \approx 0.01$) suits a high-resolution Johann spectrometer.

11.4 SPATIAL RESOLUTION

In view of the importance of profile data, it is worth considering what could be achieved on ITER. A system with either multiple lines of sight or a close-coupled spatial-scan mechanism would seem to be impractical.

A possible solution is to use a curved graphite panel, as illustrated in figure 11.7. Though not ideal, it requires no moving parts and gives information from all radii, albeit at a different wavelength for each radius. The reflected spectrum has each chord coded by wavelength, so that each spectral line or point on the continuum can be related to a different plasma chord.

Mica is also a possibility because it withstands high temperatures, is easy to form into a curved panel, and gives a useful wavelength range from 6 Å to 12 Å. Multilayers may be possible to observe longer wavelengths, from the outer plasma or from the divertor.

Diagnostic potential

Even if the "mirror" is necessarily dispersive, forcing us to view each chord at a different wavelength, at least the spectral region offered by the first and higher orders of graphite still enables us to perform some valuable diagnostics. The spectrum below about 4 Å contains almost exclusively H- and He-like lines of medium-Z elements from Cl upwards, well separated by continuum.

Spatial information without moving parts

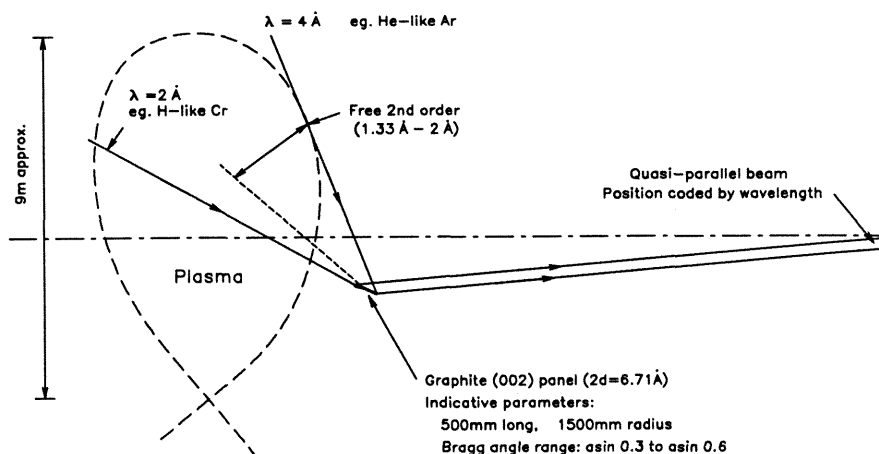


Fig.11.7 A curved graphite panel to obtain spatial information from a low f-number beamline, with no moving parts close to the plasma. Mica ($2d=19.84 \text{ \AA}$) is another possibility.

Ion temperature profiles

The graphite panel technique is not suitable for radial profiles of a single transition, but does give as many radial T_1 points as there are suitable lines in the spectrum. It is fortunate that the available wavelength range (between about 2 \AA and 4 \AA) contains lines from ions which radiate from almost the full spatial extent of the plasma. For example, the emissivity of H-like Cr ($\lambda \sim 2 \text{ \AA}$) peaks at about 15 keV and could be used to measure the central ion temperature. Near the plasma edge, He-like Ar and Cl are well excited at 500 eV, and have lines around 4 \AA . By observing suitable ionization stages of intrinsic and injected impurities, we can expect at least ten points on the ion temperature profile.

Pulse-height analysis - T_e and Z_{eff} profiles

The continuum spectrum between the lines is, of course, also spatially coded and will yield information that may not be available from the more usual means. Provided overlapping diffraction orders are avoided (fig 11.7), the broadband spectrum (from, say, a pulse-height-analysis system) will contain two energies for each chord, allowing the T_e profile to be derived. Analysis of the spatially-coded spectrum, together with the full central-chord integrated spectrum, will allow derivation of the Z_{eff} profile.

Soft x-ray "tomography"

By redispersing the spectrum spatially (as for example in figure 11.8), a diode array can be placed in positions corresponding to the continuum, to record a soft x-ray continuum profile. The complications introduced by the energy variation across the profile should not prevent its analysis for such phenomena as impurity accumulation.

An array of proportional counters with well-developed background rejection would be more suitable than a diode array in this application. To date at JET, only pulse-height analysis has been used for proportional counters, giving about 90% rejection of background events (chapter 10). X-ray astronomy uses more advanced background-rejection techniques. In space, large-area proportional counters are used to record pulse-height spectra of galactic x-ray sources. Such detectors⁹ use pulse-height and pulse-shape analysis, as well as anti-coincidence background rejection from "guard anodes" surrounding the main chamber. By these means¹⁰, spectra can be recorded with raw signal-to-noise ratios of around 1:1000.

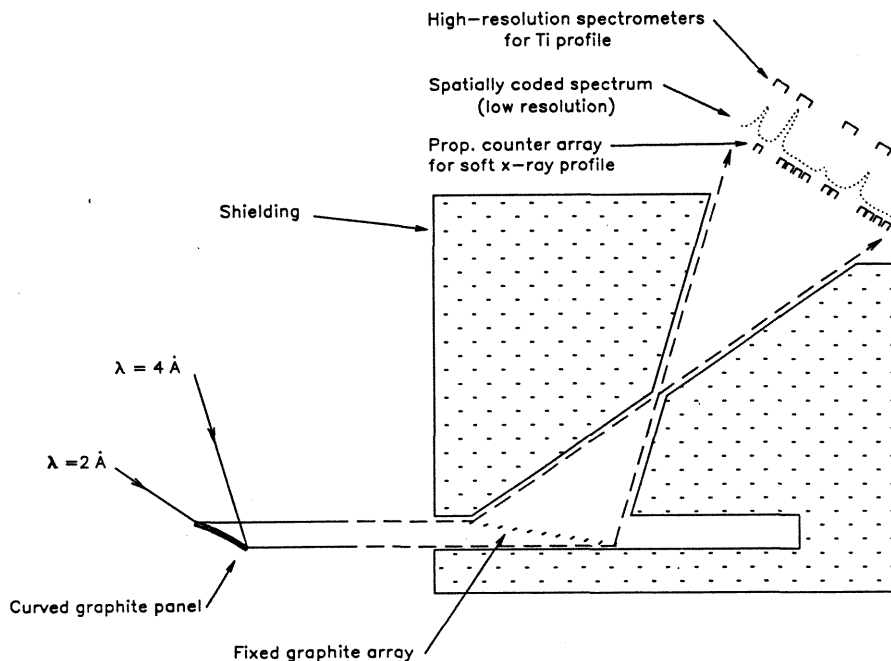


Fig.11.8 Analysis of the spectrum from a curved graphite panel. Each spectral line, or point on the continuum, can be related to a different plasma chord.

11.5 SPECTROMETERS

A major consequence of using the preselectors described above, is that the spectrometers themselves can be "standard", and can be used to view the plasma directly in the early years of the project. A list of possible instrumentation capable of covering the complete spectrum from about 1 Å through to the visible is given in table 11.1.

Survey instruments

From the visible down to about 30 Å, standard normal and grazing incidence grating instruments can be used. Back-thinned or open-electrode CCD arrays are likely to replace channel-plate detectors in the VUV/XUV range.

Between about 1 Å and 100 Å a Bragg rotor spectrometer is almost ideal for full spectral coverage with medium resolution. A graded-2d multilayer could be scanned fast enough, and in synchronism with the rotor scan, to achieve adequate time resolution for the full spectrum.

For survey work, the Johann instrument has no overriding advantage, because the sensitivity is only higher by the ratio of the beamline divergence to that of the Bragg rotor collimator (~500/200), and it is more difficult to scan a wide spectrum. Nevertheless, the free spectral range of the Johann configuration is well matched to that of a multilayer preselector, and the use of a CCD array allows a compact versatile instrument to be built. One possible design is shown in figure 11.9, where the full Bragg angle range can be accessed by a simple double-arm mechanism. This can be geared from a single rotary table if desired. This principle would find applications on other sources.

High resolution

For line-profile measurements, the sensitivity advantage of a Johann instrument, compared to a flat-crystal high-resolution collimator combination, is overwhelming, being about 100 (the ratio of the beamline divergence to the product of the collimator divergence and transmission). Although the detector-shielding properties of a large radius instrument, such as that used at JET, are likely to be adequate for ITER, it is less clear whether or not the crystal life will be acceptable, as discussed above. As well as the crystal degradation, activation of the focusing jig and alignment system must be considered. It may be better to accept the losses due to the ~30% reflection from a single multilayer or graphite preselector.

Table 11.1 Indicative parameters of a VUV, XUV and X-ray spectroscopy system for ITER.

	Wavelength range		
	> 30 Å	5 Å - 50 Å	0.6 Å* - 6 Å
Preselector			
Material	Gold mirror	Graded multilayer	Graphite
Grazing angle	7°	10°	22° - 68°
Tunable spectrum	n/a	5 Å - 50 Å	0.6 Å - 6 Å
Free bandwidth	> 30 Å	5%	1%
Analyser 1	Norm. Inc. Grtg.	Bragg rotor	Johann/CCD
Tunable spectrum	> 1000 Å	5 Å - 50 Å	0.6 Å - 6 Å
Free bandwidth	5%	n/a	1%
Analyser 2	7° grating	Johann/CCD	*Using higher orders
Tunable spectrum	100 Å - 1000 Å	5 Å - 25 Å	
Free bandwidth		2%	
Analyser 3	2° grating		
Tunable spectrum	30 Å - 300 Å		
Free bandwidth	5%		
Radial profiles from curved "mirror"			
Spectral range	Metal		Graphite
	> 1000 Å		2 Å - 4 Å

Compact Johann Survey Spectrometer

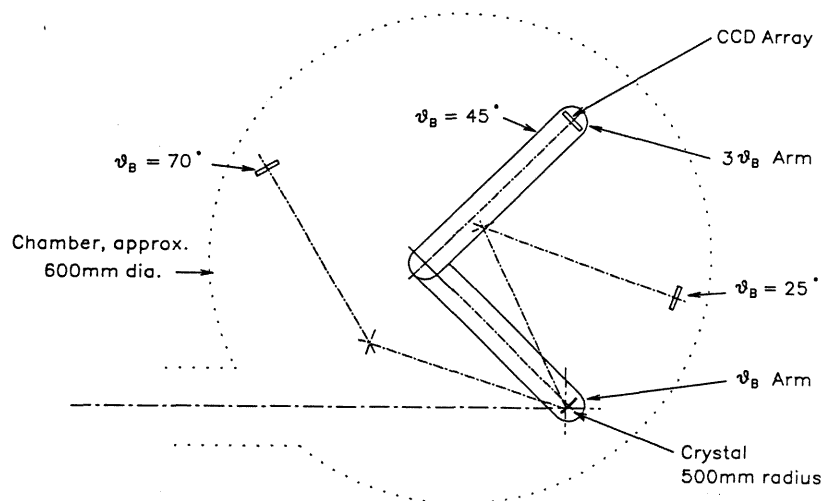


Fig.11.9 A compact Johann survey spectrometer using only two rotary motions. The free spectral range is well-matched to a multilayer or graphite preselector, and the full Bragg angle range can be easily accessed.

11.5 CONCLUSION

Most of the techniques necessary for crystal spectroscopy of an active tokamak have been demonstrated at JET. The most important outstanding requirement is for measurements of neutron damage to diffractors and thin windows. The diffractometer outlined in chapter 2 is designed to make such measurements.

The principle of separating the two functions of beam deflection and spectral analysis gives more flexibility of operation than is available with the JET double-crystal monochromator. The development of graded-2d multilayers for a constant-deviation preselector would improve the shielding and sensitivity of the overall system.

The use of a curved graphite panel to relay a wavelength-coded spatially resolved spectrum may offer a partial solution to the seemingly intractable problem of obtaining any kind of radial profile information.

References

- ¹ R Barnsley, K D Evans, W Griffin, N C Hawkes, N J Peacock.
JET Design Study 12.6, (1982).
- ² D West, UKAEA Harwell report, AERE-R11481 (1984).
- ³ K W Hill et al, Rev. Sci. Instrum. 63(10) (Oct 1992) 5032.
- ⁴ M V Zombeck, AIP conf. proc. 75. Low energy x-ray diagnostics.
Eds. D T Attwood and B L Henke (1981).
- ⁵ W Moos et al, Rev. Sci. Instrum. 61(10) (1990) 2733-37.
- ⁶ T W Barbee Jr. AIP conf. proc. 75. Low energy x-ray diagnostics.
Eds. D T Attwood and B L Henke (1981).
- ⁷ K D Evans, R Hall, M Lewis, D Underwood, B Cooke.
Space Sci. Instrum. 2 (1976) 313-323.
- ⁸ H L Kestenbaum, Appl. Spectr. 27 (1973) 454.
- ⁹ G W Fraser, X-ray Detectors in Astronomy, Cambridge Univ. Press (1989).
- ¹⁰ M J L Turner et al, Publ. Astron. Soc. Japan. 41 (1989) 345-372.

CONCLUSION

*When the conjunctions of matter are working in your favour a moment
Go and live happily, you did not choose your lot;
Keep company with men of science, since your bodily properties
Are as a speck of dust joined with a puff of air,
a mote with a gasp of breath.*

*The Ruba'iyat
Omar Khayyam c1120*

The Bragg rotor spectrometer and the Johann-CCD spectrometer are together capable of almost every diagnostic measurement possible in the soft x-ray band, ranging from broad-band monitoring of all impurities, through general spectroscopy and plasma transport studies, to high-resolution Doppler measurements. Although much work remains to be done, it is now possible, as a result of the increase in spectral coverage of the instrumentation, to make quantitative analyses of the radiation from all impurities. Required calibration data, particularly of diffractors, can be supplied by the new fixed-source diffractometer.

The use of radiative-recombination-excited line-radiation to spatially resolve plasma transport phenomena is a novel technique which will be useful on other machines, particularly where the spectroscopically observed effects can be correlated with other measurements such as plasma temperature and density profiles.

Probable future developments include the use of a low-energy CCD array in the focus of a flat-field grating, routine use of multilayer gratings to improve resolution and dispersion between 10 Å and 200 Å, variable 2d multilayers for improved focusing of curved optics and for a possible tunable constant-Bragg-angle reflector, and cryogenic x-ray calorimeters for high resolution energy dispersive spectroscopy. An important area that remains to be fully developed is that of plasma imaging and spectroscopic tomography. The CCD array will prove useful for this purpose, either with crystal or multilayer optics, or as an imaging spectrometer in its own right. Regardless of the type of instrument, spatially-resolved measurements almost always repay the effort taken to obtain them.

This work has demonstrated all the techniques necessary for the soft x-ray spectroscopic diagnostics of a reactor-relevant plasma. Experience with the JET preliminary tritium experiment has been valuable for the optimization of the instruments for future tritium experiments at JET. It is now possible to predict the performance a soft x-ray diagnostic system for a next-step device such as ITER.